Tracing the origin of heavy elements through metal-poor stars

A thesis
submitted for the degree of

Doctor of Philosophy

in

The Department of Physics,
Pondicherry University,
Puducherry - 605 014, India

by

Pallavi Saraf
Indian Institute of Astrophysics,
Bangalore - 560 034, India

November 2024

Title of the thesis	:	**Tracing the origin of heavy elements through metal-poor stars**
Name of the author	:	**Pallavi Saraf**
Address	:	Indian Institute of Astrophysics II Block, Koramangala Bangalore - 560 034, India
Email	:	pallavi.saraf@iiap.res.in
Name of the supervisor	:	**Prof. Sivarani Thirupathi**
Address	:	Indian Institute of Astrophysics II Block, Koramangala Bangalore - 560 034, India
Email	:	sivarani@iiap.res.in

Declaration of Authorship

I hereby declare that the matter contained in this thesis is the result of the investigations carried out by me at the Indian Institute of Astrophysics, Bangalore, under the supervision of Prof. Sivarani Thirupathi. This work has not been submitted for the award of any other degree, diploma, associateship, fellowship, etc. of any other university or institute.

Signed: Pallavi Saraf

Date: 18/11/2024

Certificate

This is to certify that the thesis entitled **'Tracing the origin of heavy elements through metal-poor stars'** submitted to the Pondicherry University by Ms. Pallavi Saraf for the award of the degree of Doctor of Philosophy, is based on the results of the investigations carried out by her under my supervision and guidance, at the Indian Institute of Astrophysics. This thesis has not been submitted for the award of any other degree, diploma, associateship, fellowship, etc. of any other university or institute.

Signed:

Date: 18/11/2024

Acknowledgements

I am deeply honored to convey my heartfelt gratitude to all those who have contributed to the successful completion of my doctoral journey. This section encapsulates the culmination of many emotions and significant moments experienced throughout my Ph.D. endeavour.

I extend my profound thanks to my supervisor, Professor Sivarani Thirupathi, for her invaluable support and encouragement. Her guidance has been instrumental in my academic development, and I am particularly grateful for the freedom she afforded me to work independently and for her openness to my ideas during our discussions.

My gratitude also goes to my esteemed doctoral committee members, Professor C. Muthumariappan and Professor R. Sivakumar, whose insightful feedback and constructive suggestions significantly enhanced the quality of my research.

Special acknowledgment is given to Professor Carlos Allende Prieto for his generosity in providing us with data from the Gran Telescopio CANARIAS (GTC), which was pivotal in publishing my first paper. I am also thankful to Professor Timothy Beers for his insightful comments on my work.

I appreciate the distinguished faculty from various institutes in Bangalore who enriched my PhD coursework, including (in alphabetical order)- Professors Arun Mangalam, Prof. Banibrata Mukhopadhyay, Prof. Biman Nath, Prof. C S Stalin, Prof. C. Kathiravan, Prof. Maheswar Gopinathan, Prof. Nirupam Roy, Prof. Prateek Sharma, Prof. Pravabati Chingangbam, Prof. Sharanya Sur, and Prof. US Kamath.

I would also like to extend my gratitude to several faculty members at IIA. Although I have not directly worked with them, their affection and encouragement have been invaluable. I am particularly thankful to Tonmay Dada, Wagessh Misra, Shudhakar Reddy, Veema Reddy, Sashi kumar Raja, Smitha Subramanium, Paul

Rajaguru, and Arkaprabha Sarangi. A special thanks to Tonmay Dada and Sashi Anna for inviting us to their home for a party.

Heartfelt thanks to the Director and the Dean of IIA, the BGS IIA, and the entire administrative and support staff for creating an enabling environment for my research. I am thankful for the assistance provided by the academic, administrative, library, and store staff, as well as the Computer Centre staff—Fayaz, Anish, Ashok, Prakash and others—for their invaluable support.

I am grateful to the observing assistants at Hoskote—Pramod, Sujith, Kiran, Mulchand, Srikant, Yogita, Aditya and Surya for their assistance.

I owe a special thank you to individuals who were pivotal in the early days of my PhD: Raghu Bhaiya, Sudhakar Reddy, and Ankit. Ankit, in particular, has been a steadfast companion during challenging times and his family's love for me is unbelievable.

I am fortunate to have the support of close friends, seniors, and juniors—Ankit, Suman, Swastik, Manju, Phanindra—and my Rakhi brothers at Bhaskara, Aritra Dada, Samrat Dada, Sudheer Bhaiya, Manju and Satyajeet. Additionally, I am deeply grateful to all the Bhaskaramates for their love and support, including Prasanta dada, Meenakshi di, Bhoomika di, Piyali di, Partha, Pavan bhaiya, Sonith, Reena, Shivani, Hrishav, Payel, Swagata, Sushant, Savitha, Puja, and Sunit. I also want to thank my batchmates Swastik, Rishabh, Ravi, Sioree, and Anohita for their companionship during our coursework.

I extend my gratitude to the postdocs at IIA, specifically Gaurav Bhaiya, Archita di, Hema di, and Sudheer bhaiya, for their care and support. I am also thankful to the TMT employees, particularly Sarang and Sudharsan, as well as the staff in the optics lab and the electricians at IIA.

Thanks to my roommates, Annu Jacob and Aratrika, for their unwavering support during challenging times, and to my groupmates—Sushmita di, Avrajit Dada, Devika di, Athira, Arun, Manju, Parvathy, and Drisya di—for their teamwork and support. The sisterly behavior of Athira, Devika Di, and Drisya Di holds a special place in my heart. I thank Lokesh, an intern, for his insightful questions on the first two chapters of my thesis, which gave me valuable insight into how newcomers perceive my subject.

A heartfelt appreciation goes to Shankar Sir and Sriram Sir for their love and guidance. During the final year of my PhD, I had the pleasure of interacting with several interns at IIA. I am deeply touched by their affection. Among them are Kamil, Satyajeet, Mukund and Lokesh.

I want to express my heartfelt gratitude to all the Bhaskara staff—supervisors, cleaning ladies, security guards, cooks, and drivers who took me to observations. Your love and care have overwhelmed me with gratitude. Special thanks to Vimal Anna (cook) and Haseena aunty (cleaning lady) for their exceptional care and affection. They both hold a special place in my heart. I also want to thank Manju Bhaiya, the institute canteen supervisor, for his constant care and love.

I extend my gratitude to all my teachers who have imparted valuable knowledge. I offer special remembrance to my late B.Sc. Physics teacher, Nigam Sir, and my late college Chemistry teacher, Swain Sir.

I also want to thank my friends outside of my PhD circle—Krushna Bhai, Premchand, Suman, Chinmay, Rubi, and Sugyan—for their constant motivation. Special thanks to the blind students at Ravenshaw University— Oosi, Madhuri, Nagendra, and Rajeswari— whose love and support during my MSc years were beyond measure.

I am also thankful to my family members, including my grandparents, uncles, aunts, and cousins, for their continual support. My little brother Subham holds a special place in my heart.

Lastly, a profound thank you to my parents for their unwavering love, sacrifices, and encouragement. Without their support, my journey to achieve my dreams would not have been possible.

I express my heartfelt gratitude to all the doctors, especially during the COVID times, for their help. I salute the army and navy forces of India for their service at the border. Because of their sacrifices, we are living a peaceful life.

Last but not least, I would like to thank those who have helped during this beautiful journey, and I forgot to mention it here. Finally, I would like to take this opportunity to thank the almighty for being with me every step of the way during this wonderful journey.

Data Usage

The work presented in this thesis utilized data from several ground-based telescopes, including the 10-meter class Gran Telescopio Canarias (GTC), the 8.4-meter class Very Large Telescope (VLT), and the KECK telescope. I am grateful to the instrument teams for making this data publicly available, and I acknowledge their contributions to this work.

Additionally, we extensively used data from the 2-meter Himalayan Chandra Telescope (HCT), maintained by the Indian Institute of Astrophysics in Bangalore. The Hanle Echelle Spectrograph (HESP) was instrumental in acquiring the spectrum of various objects.

We also employed archival data from the European Southern Observatory (ESO), and I would like to thank ESO for making this data accessible to the public.

Furthermore, we utilized archival data from the Large Sky Area Multi-Object Fibre Spectroscopic Telescope (LAMOST). I appreciate the LAMOST team for providing access to this valuable data.

List of Publications

1. **Decoding the compositions of four bright r-process-enhanced stars**
   Saraf Pallavi., Allende Prieto C., Sivarani T., Bandyopadhyay A., Beers T. C., Susmitha A.,
   MNRAS, 164, 60 (2023)

2. **Chemodynamic analysis of four r-process enhanced stars observed with GTC**
   Saraf Pallavi., Sivarani T.,
   BINA Conference Proceedings, 166, 91 (2023)

3. **Survey of the metal-poor stars with 2m Himalayan Chandra Telescope**
   Saraf Pallavi., Sivarani T.,
   Metals 2023 Conference proceeding, 2023

4. **Probing the distinct chemical history of the Milky Way halo and old thick disk through HESP-GOMPA survey**
   Saraf Pallavi., Sivarani T., Bandyopadhyay A.,
   EPJ Web of Conferences, 2024

5. **Differential abundance analysis of r-process stars using VLT**
   Saraf, Pallavi, Sivarani T., et al.,
   to be submitted to Astronomy & Astrophysics

6. **Kinematics and chemical abundances of different classes of RPE stars**
   Saraf Pallavi., Sivarani T., et al.,
   to be submitted to Journal of Astronomy & Astrophysics

7. **A chemodynamical analysis of bright metal-poor stars from the HESP-GOMPA survey – Indications of a non-prevailing site for light r-process elements**
   Bandyopadhyay A., Beers T. C., Ezzedine R., Sivarani T., Nayak P. K., Pandey J. C., **Saraf Pallavi**., Susmitha A.,
   MNRAS, 164, 181 (2024)

8. **Possibilities of Identifying Members from Milky Way Satellite Galaxies using Unsupervised Machine Learning Algorithms**
Divakar Devika K., **Saraf Pallavi**., Sivarani T., Doddamani V H.,
Journal of Astronomy and Astrophysics, 161, 114 (2023)

Oral Presentations

1. 2024, September 2nd - 5th: Oral presentation at **Astrophysical Origin of Carbon**, Tokyo, Japan
2. 2024, February 26th - March 1st: Oral presentation at **National Space Science Symposium**, Goa University, Mumbai
3. 2023, November 13 - 17th: Oral Presentation at **Metal Production and Distribution in a Hierarchical Universe – II**, ESO-Santiago, Chile
4. 2023, October 29th - November 4th: Oral Presentation at **International Symposium on Nuclear Astrophysics**, Manipal, Karnataka, India
5. 2023, March 21st - 25th: Oral presentation at **Indo-Belgium conference (BINA)**, Aries, India
6. 2023, March 1st - 5th: Oral presentation at **41st meeting of The Astronomical Society of India** at IIT Indore, India.
7. 2022, 31st January - 3rd February: Oral presentation at **21st National Space Science Symposium (NSSS)**, IISER Kolkata, India

Poster Presentations

1. 2024, January 31st - February 4th: Presented poster at **42nd meeting of The Astronomical Society of India at Indian Institute of Science**, Bengaluru, India.

2. 2023, July 17 - 21st: Presented poster online mode in **Massive Triples, Binaries and Mergers 2023** meeting at Leuven, Belgium.

3. 2023, February 9 - 12th: Poster at **Indo-French CEFIPRA Astronomy Meeting (IFCAM)-III**, Indian Institute of Astrophysics, Bengaluru, India.

4. 2022, November 9 - 13th: Flash poster talk at **Young Astronomer's meet** at Aries, Nainital.

5. 2022, March 25 - 29th: Poster presentation at **40th meeting of The Astronomical Society of India** at IIT Roorkee, India.

6. 2021, February 18th - 23rd: Online Poster presentation at **XXXIXth meeting of the Astronomical Society of India (ASI)** hosted jointly by ICTS - TIFR Bengaluru, IISER Mohali, IIT Indore and IUCAA Pune, India.

Dedicated to

My Grand Mother Late Premsila Saraf

My parents Apurna Chandra Saraf and Reeta Saraf and My brother Subham Saraf for their love and sacrifices to impart the best possible quality of education to me

Abstract

The hierarchical mass assembly of galaxies and the formation timescales of their substructures are important topics in astrophysics and cosmology. These aspects can be explored in the local universe by studying resolved stars. By analyzing individual stars and stellar populations, one can estimate their ages. Although the color-magnitude diagram of co-evolved stellar populations aids in age determination, dating field stars is more complex. Typically, the iron content (or metallicity) of stars serves as an age indicator. However, metallicity is influenced by the history and rate of star formation. Analyzing multiple chemical elements can provide additional insights. Yet, using elements heavier than iron, particularly those formed by rapid neutron capture, hinges on understanding their astrophysical origins. Identifying these origins remains a significant challenge and a key question in nuclear astrophysics.

This thesis investigates chemical compositions of metal-poor stars, aiming to understand their origins and chemical evolution. Halo stars, which are some of the Galaxy's oldest, offer insights into the astrophysical sites of element production due to their minimal pollution by progenitor stars. Utilizing high-resolution spectroscopic analysis through telescopes such as the 10-m GTC, 8.4-m VLT, 10-m KECK, and 2-m HCT, and supplementing with low-resolution spectra from LAMOST, this study analyzes the detailed abundances of approximately 50 stars. These stars, with metallicities ranging from -3.2 to -1.8, include many classified as very metal-poor and extremely metal-poor, with their chemical compositions examined for the first time. The findings are systematically presented across the thesis.

The initial findings of the thesis include a comprehensive abundance analysis of four r-process enhanced (RPE) stars, utilizing the HORuS spectrograph at 10-m GTC.

These stars are in the metallicity range of -2.3 to -1.9. The high SNR of the spectrograph enable determining the abundances of 16 light elements and 20 neutron-capture elements, including thir peak element, Os. We identified Th in two objects, with [Th/Fe] values of 0.65 and 0.6, respectively, which helped us estimate their ages. The study discusses the metallicity trends of elements such as Mg, Sr, Ba, Eu, Os, and Th in both r-II and r-I objects, using a compilation of RPE objects from existing literature.

We carried out a detailed line-by-line differential analysis comparing a moderately RPE object (r-I: HD107752) with an extremely RPE object (r-II: CS31082-0001) to explore the potential shared origins of their heavy element nucleosynthesis. This part of the study utilized high-resolution and high SNR spectra from the ESO-VLT's UVES instrument, sourced from the ESO data archive. We identified three distinct patterns in the differential abundance analysis. The similar abundances of light elements up to zinc in both stars suggest a shared origin for these elements, with no odd-even variation observed. In the case of neutron-capture elements, r-I stars exhibit slightly depleted light r-process elements and more significantly depleted heavier r-process elements, challenging the theory of a single production site. We also provide plausible scenarios for their r-process enrichment.

Additionally, we performed a kinematic analysis of nearly 466 r-process-enhanced stars compiled from literature, examining their origins and locations within the Milky Way. We compare the significance of our orbit-based classification of stars into different Galactic components with the Toomre diagram-based classification. Our findings indicate that RPE stars are equally distributed between the disk and halo of the Galaxy.

We also utilized archival data from the ESO and KECK telescopes to explore similarities between CEMP-r/s and r-process objects and to investigate the origin of thorium in CEMP-r/s stars using machine learning algorithms. We observed that r-I and r-II stars do not distinctly separate into two groups; rather, there is an intermediate group that may consist of diluted or mixed stars. Our analysis indicate that CEMP-r/s and RPE stars are separate classes of objects.

Additionally, we used the HESP, installed on the Himalayan Chandra Telescope to observe some metal-poor stars (the HESP-GOMPA Survey). This led to the discovery of numerous very metal-poor, extremely metal-poor, CEMP-r, and RPE stars. We also study the kinematics of these stars. These findings are detailed in Chapter 7 of the thesis. Our study indicates that within our range of metallicities, neutron stars mergers and supernovae are the primary sites contributing to the chemical composition of halo stars.

Contents

Abstract **i**

List of Figures **ix**

List of Tables **xix**

Abbreviations **xxiii**

1 Introduction and Motivation **1**
1.1 The Milky Way 2
1.2 Galactic components 3
1.2.1 The Bulge 4
1.2.2 The disk 6
1.2.3 The stellar halo 7
1.3 Formation of galaxy 8
1.3.1 Top-down model 9
1.3.2 Bottom-up model 9
1.4 Nucleosynthesis: Origin of elements 11
1.4.1 Galactic Chemical Evolution (GCE) 11
1.4.2 Primodial nucleosynthesis 12
1.4.3 Fusion: Nucleosynthesis up to iron peak 12
1.4.4 Neutron-capture nucleosynthesis: Beyond iron peak 16
1.5 Galactic archaeology 20
1.5.1 Metal-poor stars and their classification 21
1.5.2 *r*-process enhanced (RPE) stars 22
1.5.3 EMP and CEMP stars 23
1.6 Proposed sites for *r*-process 25
1.6.1 Neutrino-driven winds 25
1.6.2 Electron-capture supernovae 25
1.6.3 Magnetorotational supernovae with jets 26
1.6.4 Collapsars 27
1.6.5 Neutron star mergers 27

1.7 Thesis aim 28
1.8 Thesis outline 29

2 Methodology 33
2.1 Introduction 33
2.2 Telescopes and spectrographs 34
2.3 Data acquisition 37
2.3.1 Candidate metal-poor stars selection 37
2.3.2 Observing facilities used 39
2.4 Preparation of science ready spectra 45
2.4.1 Data Reduction 45
2.4.2 Radial Velocity 48
2.5 Characterization of stellar atmosphere 48
2.5.1 Linelist 48
2.5.2 Model atmosphere 51
2.5.3 Codes used for modeling 52
2.5.4 Stellar parameters estimation 53
2.6 Elemental abundance measurement 58
2.6.1 Equivalent width method (EW Method) 58
2.6.2 Spectral synthesis method 59
2.6.3 Uncertainties in abundance calculation 60

3 Decoding the compositions of four bright *r*-process enhanced stars with GTC 63
3.1 Introduction 64
3.2 Observation and data preparation 66
3.3 Stellar parameter estimation and abundance calculation 68
3.4 Abundance Interpretation 71
3.4.1 Light elements: Carbon and Nitrogen (molecular bands) . . 71
3.4.2 Alpha-elements 72
3.4.3 Odd-Z Elements 73
3.4.4 Iron-peak Elements 74
3.4.5 Neutron-capture Elements 75
3.4.6 Uncertainties in abundances 83
3.5 Discussion 84
3.5.1 Level of r-process enhancement and classification 84
3.5.2 Evolution of light elements with RPE stars 85
3.5.3 Evolution of Heavy-element Abundance Ratios for RPE Stars 90
3.5.4 Evolution and Production of third r-process peak 92
3.5.5 The r-process pattern 95
3.5.6 Age estimation 96
3.6 Conclusion 103

4 Differential abundance analysis of *r*-process stars using VLT 105
4.1 Introduction . . . 106
4.2 Sample selection and data acquisition . . . 108
4.3 Stellar Parameters . . . 110
4.3.1 Stellar parameters estimation of standard stars . . . 110
4.3.2 Line-by-line differential stellar parameters of program star . 112
4.3.3 Error in stellar parameters . . . 114
4.4 Abundance Analysis . . . 114
4.4.1 Differential abundances of light and Fe-peak elements . . . 115
4.4.2 Differential abundances of neutron-capture elements . . . 116
4.4.3 Uncertainties in abundance calculation . . . 116
4.5 Discussion . . . 118
4.5.1 Abundance pattern of elements up to Zn . . . 118
4.5.2 Neutron-capture abundance pattern . . . 119
4.5.3 Formation scenario of *r*-I stars . . . 121
4.5.4 Comparison with Literature . . . 124
4.5.5 More in the context of universality . . . 127
4.5.6 Orbital kinematics . . . 129
4.6 Summary and conclusions . . . 131

5 Kinematics and chemical abundances of different classes of RPE stars 137
5.1 Introduction . . . 138
5.2 The sample . . . 140
5.2.1 The sample selection . . . 140
5.2.2 Orbit calculation . . . 140
5.2.3 Galactic bulge, disk, and halo . . . 141
5.3 Results . . . 142
5.3.1 Orbit based association of RPE stars to Galactic components 142
5.3.2 Galactic components in Toomre diagram . . . 144
5.3.3 In-situ and ex-situ origin of RPE stars . . . 146
5.3.4 R-process enrichment of Galactic components . . . 148
5.4 Conclusions . . . 150

6 Probing the origin of *r*-process elements in CEMP-*r/s*, and assessing the classification of *r*-process rich stars using clustering algorithms. 153
6.1 Introduction . . . 154
6.2 Osmium and Thorium abundance in CEMP-*r/s* . . . 155
6.2.1 Synthesis of Thorium and Osmium . . . 156
6.3 Classification of RPE stars . . . 158
6.4 Machine learning Algorithms . . . 160
6.4.1 Gaussian Mixture Model . . . 160

6.5 Results . . . 162
6.5.1 Revisiting r-I and r-II classes using GMM . . . 162
6.5.2 Are CEMP-r/s and RPE stars the same? . . . 165
6.6 Conclusions . . . 167

7 New metal-poor stars from HESP-GOMPA survey-II: stellar parameters, abundances and kinematics 169
7.1 Introduction . . . 170
7.2 Sample Selection, data preparation and radial velocity estimation . 172
7.3 Stellar parameter Estimation . . . 175
7.4 Abundance Calculation . . . 175
7.4.1 Light, alpha and iron-peak elements . . . 178
7.4.2 Neutron-capture elements . . . 181
7.5 Results and Discussion . . . 183
7.5.1 C to Zn abundance variation . . . 183
7.5.2 Heavy element variation . . . 187
7.5.3 New r-Process Stars and Their Origins . . . 188
7.5.4 Yoon diagram and new cemp stars . . . 192
7.6 Kinematic analysis . . . 194
7.6.1 r_a vs z_{max}: association to Galactic components . . . 194
7.6.2 Toomre diagram . . . 196
7.6.3 Di Matteo diagram . . . 197
7.6.4 Metallicity Distribution of Stars in Galactic Components . . 198
7.7 Conclusions . . . 200

8 Thesis Conclusions and Future work 203
8.1 Thesis conclusion . . . 203
8.2 Future work . . . 206

Bibliography 209

Appendix 233
A Fe-I and Fe-II lines information . . . 233
B Other Lines List . . . 238
C Elemental abundances of objects presented in Chapter 7 . . . 246

List of Figures

1.1 The figure depicts the artistic face on view of the Milky Way galaxy. It is showing two main spiral arms Perseus and Scutum-Centaurus, extend from the ends of the central bar. Image credit: NASA/JPL-Caltech/R. Hurt (SSC/Caltech) 3
1.2 The solar system occupy a position in the plane of the Milky way. When we look through the disk, where stars are densely clustered, they line up across the distance to form a luminous band in the sky known as the Milky Way. Beyond this band, both above and below the disk, star density diminishes swiftly, resulting in a sky speckled with isolated stars. All the stars visible to us, whether with the naked eye or through the majority of telescopes, are constituents of the Milky Way. Credits: NASA, Richard Powell, with additional contributions by Bob King. 4
1.3 Figure depicts the different Galactic components of MW galaxy. . . 5
1.4 Evolution of [α/Fe] versus [Fe/H] for thin, thick and halo stars. . . 7
1.5 An schematic diagram of the Bottom-up model of the galaxy formation 10
1.6 Galactic Chemical Evolution plot 12
1.7 Internal structure depiction of AGB star. Picture courtesy: Karakas (2010). 14
1.8 An illustration of evolutionary stage of low, intermediate and high mass stars. Image Credit: https://www.britannica.com/science/star-astronomy/Star-formation-and-evolution 15
1.9 Classification of CEMP into different sub-groups. Picture courtesy: Zepeda et al. (2022) 24

2.1 A schematic diagram of echelle spectrograph. Standard grating disperse the light slightly, then echelle grating disperse it further into perpendicular direction. Picture Courtesy: Wikipedia. 36

2.2 The overplot showcases LAMOST spectra overlaid with synthetic spectra. The black solid lines represent the low-resolution LAMOST spectra with a resolution of R $\sim$ 1800, while the red solid lines depict the synthesis. The top panel displays the synthesis of whole spectrum, while the middle panel exhibits the overplot of the Ca H and K regions alongside carbon band regions. Finally, the bottom panel illustrates the synthesis of the Mg triplet and Ca Triplet regions. 38
2.3 Figure depicts the High Optical Resolution Spectrograph (HORuS) installed at GTC. Image Credit: [HORuS website] 40
2.4 Figure depicts the UVES installed at VLT of ESO. Image Credit: [UVES website] 41
2.5 Figure depicts the Hanle Echelle Spectrograph design mounted on HCT telescope. Image Credit: [HESP website] 43
2.6 Spectrograph layout for the High Resolution Echelle Spectrometer. Image Credit: [HiRES website] 44
2.7 Flow chart of the spectroscopic data analysis. 46
2.8 Figure depicts the definition of equivalent width. Image Credit: [Equivalent width website] 50
2.9 The top panel illustrates the variation in iron abundance with respect to lower excitation potential (LEP). Meanwhile, the bottom panel displays the iron abundance plotted against the normalized equivalent width. 53
2.10 The H-alpha wing fitting results for one of our program stars. The blue color corresponds to the best fit achieved at a temperature of 4700 K. Additionally, deviations of $\pm$150 K from the best fit are highlighted in green and red colors, providing insight into the sensitivity of the fit to variations in effective temperature. 54
2.11 Estimation of temperature through Spectral Energy Distribution (SED) fitting for one of our program stars. The observed SED is denoted by black downward triangles connected by a black line, while the fitted SED is indicated by red upward triangles along with the corresponding red curve. 55
2.12 The Mg-triplet wing fitting results obtained for one of our program stars are illustrated in the figure. The best-fit line is represented in blue, while $\pm$0.3 dex variations from the best fit are highlighted using green and red lines. 55
2.13 The plot illustrates the relationship between surface gravity ($\log g$) and effective temperature ($\log T_{eff}$) for the program stars. Each black diamond represents a program star, with measurement uncertainties indicated. The colored curves correspond to isochrones spanning ages from 8 to 12 Gyr. 56

2.14 This figure showcases micro-turbulence velocity estimation using dispersion in the abundances of Fe I lines for a program star. The crossing point of vertical and horizontal lines indicates the minimum of the distribution. The micro-turbulence value corresponding to this crossing point is considered as the estimate in the stellar atmosphere. 57
2.15 Flowchart describing steps used in the spectrum synthesis method. . 60

3.1 C and N abundance estimation for one of our program stars, HD 263815, using the spectrum-synthesis method. The top and bottom panels show the C and N synthesis, respectively. The black dots represents observation, and blue colour shows the best match. The green and red colours indicate ± 0.5 dex deviations. 73
3.2 Synthesis of the Na-absorption feature. The black dotted points represent the observed spectra and the solid blue colour shows the best fit. Green and red colours indicate ± 0.5 dex deviations. 74
3.3 Synthesis of Sr, Ba, Eu, Tb, Os, and Th. The black dotted points represent the observed spectra and the solid blue colour shows the best fit. Green and red colours indicate ± 0.5 dex deviations from the best fit. 77
3.4 Synthesis of regions containing Os and Lu lines. The black dots display observation, and the blue colour shows best match. The green and red colours indicate dispersion of ± 0.5 dex. 83
3.5 Distribution of limited-r (yellow colours), r-I (cyan colours), and r-II (magenta colours) stars in [Ba/Eu] vs [Eu/Fe] plane. The four black diamonds indicate the r-I (cyan) and r-II (magenta) from this study. For data reference, see Saraf et al. (2023). 85
3.6 Light elements abundance evolution limited-r (yellow colour), r-I (cyan colour), and r-II (magenta colour) with metallicity. The four black diamonds indicate the r-I (cyan) and r-II (magenta) from this study. References for the r-process stars are given in the caption of figure 3.5. Normal metal-poor halo stars, indicated with grey filled circles. The grey horizontal lines represent the solar values. For data reference, see Saraf et al. (2023). 86
3.7 Relation between the N and C abundances for limited-r (yellow colour), r-I (cyan colour), and r-II (magenta colour). The four black diamonds indicate the r-I (cyan) and r-II (magenta) from this study. References for the RPE stars are given in the caption of Figure 3.5, and references for the normal metal-poor halo stars, indicated with grey filled circles, are listed in the caption of figure 3.6. The grey horizontal line represents the solar value. 87

3.8 Alpha-element enhancements in limited-r (yellow colour), r-I (cyan colour), and r-II (magenta colour). The four black diamonds indicate the r-I (cyan) and r-II (magenta) from this study. References for the RPE stars are given in the caption of Figure 3.5. The black line is fitting after removing the 1σ outliers denoted by overlaid crosses. The grey horizontal line represents the solar value. 88
3.9 Evolution of the [Eu/Zn] in limited-r (yellow colour), r-I (cyan colour), and r-II (magenta colour) with metallicity. The four black diamonds indicate the r-I (cyan) and r-II (magenta) from this study. For references, see Figure 3.5, and references for normal metal-poor halo stars, indicated by grey-filled circles, are listed in the caption of Figure 3.6. The grey horizontal lines indicate solar value. 90
3.10 Evolution of neutron-capture abundance ratios of limited-r (yellow colour), r-I (cyan colour), and r-II (magenta colour) with iron and europium. The four black diamonds indicate the r-I (cyan) and r-II (magenta) from this study. References for the RPE stars are given in the caption of Figure 3.5, and references for normal halo stars are listed in the caption of Figure 3.6. 91
3.11 Comparison of metallicity, C, Sr, and Ba abundance distribution in limited-r (blue color), r-I (red), and r-II (green). References for these objects are given in the caption of Figure 3.5. 93
3.12 Evolution of ratios of Th with different elements as a function of metallicity. The r-I are displayed with open cyan circles, and r-II are displayed by magenta crosses. The four black diamonds indicate the r-I (cyan) and r-II (magenta) from this study. The cyan and magenta lines represent fitting to r-I and r-II, respectively. Their corresponding dispersions are shown with the shaded regions. For data reference, see Saraf et al. (2023). 94
3.13 Top: Black line shows the solar r-process pattern. The elemental abundances of our program stars are scaled to the solar Eu abundance. Bottom: The residual abundances calculated as the difference between scaled stellar abundance and solar abundance. The solar pattern is adopted from Arlandini et al. (1999a) 96
3.14 Th II 4019 Å line synthesis in TYC 1191-918-1 for two different values of $\log gf$, -0.228 and -0.651. The dotted line represents observation and the blue line is the best match model spectrum. The green and red curves show 0.5 dex deviations from the best-fit line. 98

3.15 The log ϵ (Th/Eu) evolution with metallicity for RPE stars with measured Th. The r-I are displayed using cyan circles, and the r-II with magenta crosses. The black diamonds indicate the r-I (cyan) and r-II (magenta) from this study. The black line represents the best fit for the data, and the shaded swath is its dispersion. The references for stars with detected Th are given in the caption of Figure 3.12 99

4.1 Comparison of program and reference star spectra in the Eu region. 109
4.2 Stellar parameter estimation of HD107752 using differential abundance analysis with respect to CS31082- 0001 111
4.3 Comparison of program and reference star spectra in H_β and H_α regions, indicating similarities in the stellar parameters 111
4.4 Differential abundance pattern of r-I star (HD107752) with respect to r-II star (CS31082-0001). 119
4.5 A schematic diagram illustrating the expected differential abundance pattern of HD107752 relative to CS31082-0001, if the r-process elements are from same kind of progenitor sites 120
4.6 A schematic diagram explaining the expected differential abundance pattern of HD107752 with respect to CS31082-0001 if the lighter and main r-process elements originate from different types of progenitor sites. This is similar to the observed differential abundance. 120
4.7 A schematic diagram to explain the dilution of ejecta. 122
4.8 A scenario to explain the pre-enriched ISM. 123
4.9 A separate site scenario to explain the abundance of r-I and r-II. . 125
4.10 The evolution of Sr, Y, Zr with r-process enhancement enhancement for limited-r (yellow colours), r-I (cyan colours), and r-II (magenta colours) stars. The black straight line is the fittings to the data, and shaded gray regions display 1σ dispersion. The fitted equations are shown above the respective panels. The gray horizontal lines represent solar values. For reference, see Saraf et al. (2023) and Saraf & Sivarani (2023b). 126
4.11 Evolution of [Sr/Eu] with [Eu/Fe] to infer the separate sites of r-I and r-II. The gray, yellow, cyan, and magenta colors respectively represents normal halo stars, limited-r stars, r-I stars, and r-II stars. The solid black line is the straight line fittings to the data, and shaded gray region displays 1σ dispersion. For reference, see Saraf et al. (2023) and Saraf & Sivarani (2023b). 127
4.12 Evolution of [Sr/Eu] ratio with Eu enhancement in limited-r (yellow colours), r-I (cyan colours), and r-II (magenta colours) stars. The black straight line is fittings to the data, and shaded gray regions display 1σ dispersion. Green color lines show the mixing of NSM ejecta of Fujibayashi et al. (2017) models into different metallicity ISM. 128

4.13 Top panel compares the mean r-process abundance pattern of r-I stars (cyan color), r-II stars (magenta color), and the Sun (black color). We use stars with $[Fe/H] < -2.0$ For the mean abundance pattern is calculation. Bottom panel compares the mean differential abundance pattern of r-I stars with respect to r-II stars, and the differential abundance pattern of HD107752 (r-I star) with respect to S31082-0001 (r-II star) 129
4.14 Orbits of standard and program stars in MW Potential. The black arrow in each panel shows the present location and direction of the star. 130
4.15 Comparison of some of the light, alpha, and iron-peak element regions for standard and target stars. 134
4.16 Comparison of some of the heavy element regions for standard and target stars. 135

5.1 Bulge, disk, and halo classification: The apocenter distance (r_a) as a function of maximum vertical height (z_{max}) of the stellar orbits. For better visibility, we have set the axes scale to log-scale. The vertical black line at z_{max} = 3 kpc and horizontal black lines at r_a = 3 kpc and r_a = 15 kpc separate RPE stars into five different Galactic components namely, bulge, inner disk, inner halo, outer disk, and outer halo. Open cyan circles show r-I, r-II are displayed by magenta crosses, and limited-r stars are displayed with yellow down triangles. 142
5.2 Example orbits of two stars in the Milky Way potential (MW Potential). The top panel shows the star orbiting in disk plane and bottom panel shows the star orbiting in the stellar halo. 143
5.3 Toomre diagram for RPE stars, where the large red circle with a radius of 180 km/s around LSR is used to separate the disk stars from halo stars. The black vertical line separates the stars on retrograde and prograde motions. Open cyan circles show r-I stars , r-II stars are represented by magenta crosses, and limited-r stars are displayed with yellow down triangles. 145
5.4 Same as Figure 5.3 for RPE stars categorized as in Section 5.2.3. . . 145
5.5 Orbital eccentricity of r-process-enhanced stars as a function of azimuthal velocity. Stars are color-coded with different galactic components as defined in Section 5.2.3. Colors of different Galactic components are shown in the legend at the top of the figure. 146
5.6 This is the specific angular momentum diagram for RPE stars, where the black dotted line delineates retrograde and prograde objects. The vertical red line at l_z = 1000 kpc km s^{-1}, and horizontal red line at $l_\perp$ = 1300 kpc km s^{-1} separate in-situ, ex-situ and mixed stars. Open cyan circles show r-I stars, r-II are marked by magenta crosses, and limited-r stars are displayed with yellow down triangles. 147

5.7 Metallicity ([Fe/H]) distribution of RPE stars in different Galactic components. 147
5.8 The [Eu/Fe] evolution in RPE stars metallicity for various Galactic components categorized in this work. 149
5.9 Apocenter distance of RPE stars with metallicity for Galactic components categorized in this work. 150

6.1 Top: Osmium synthesis in HD 224959. Bottom: Osmium synthesis in HD 187861. Red curves show best fit to the observed black color curves. Blue and green curves represent synthesis with a 0.3 dex difference. 159
6.2 Examples of Gaussian Mixture Model (GMM) for cluster identification. Top: GMM application for one dimensional dataset. Bottom: GMM application for two dimensional dataset. 161
6.3 Classification of r-I and r-II objects using Gaussian Mixture Model in five dimensional plane of shown elements. 162
6.4 Categorization of r-I and r-II objects using Gaussian Mixture Model in five dimensional plane of shown elements. 163
6.5 The same groups from Figure 6.3 in [Sr/Eu]−[Fe/H] plane. 164
6.6 Grouping of r-I, r-II, CEMP-r/s objects using Gaussian Mixture Model in five dimensional plane of shown elements. 165
6.7 Grouping of r-I, r-II, CEMP-r/s objects using GMM in the [X/H] vs [Fe/H] plane. 166

7.1 Left: Vmag distribution of the SAGA database. The cyan bars represent all the metal-poor stars, while the magenta bars represent stars with accurate abundances of alpha, iron peak, and neutron capture elements. Right: Metallicity distribution of the same stars from the SAGA database. It is evident that only around 10% of the sample has detailed abundances, leaving 90% without detailed abundance measurements. 172
7.2 Surface gravity ($\log g$) versus effective temperature ($\log T_{\text{eff}}$) for our program stars. The black diamonds show the locations of the program stars along with the measurement uncertainties. Different color curves shows isochrones ranging 8 to 12 Gyr in age. 179
7.3 Synthesis of carbon band for three CEMP stars. Blue color shows the best fit to the observed points shown in black. Green and red colors represent 0.5 dex scatter from the best fit curve. 180
7.4 Synthesis of Ba, Eu, and Sr lines in TYC 224-475-1, TYC 267-308-1, and TYC 665-522-1. Black dots are observed spectra and blue curves are best fit. Green and red colors represent 0.5 dex scatter from the best fit curve. 181

7.5 Synthesis of Ba, Eu, and Sr lines in TYC 975-2188-1, TYC 1120-1253-1, and TYC 1170-642-1. Black dots are observed spectra and blue curves are best fit. Green and red colors represent 0.5 dex scatter from the best fit curve. 182
7.6 Synthesis of Ba, Eu, and Sr lines in TYC 1465-1148-1, TYC 3474-142-1, and TYC 195-1636-1. Black dots are observed spectra and blue curves are best fit. Green and red colors represent 0.5 dex scatter from the best fit curve. 183
7.7 Synthesis of Ba, Eu, and Sr lines in TYC 1576-1703-1, TYC 3534-57-1, and TYC 279-1113-1. Black dots are observed spectra and blue curves are best fit. Green and red colors represent 0.5 dex scatter from the best fit curve. 184
7.8 Evolution of light, alpha, and iron-peak elements with metallicity ([Fe/H]). The magenta color asterisk are from this study and grey circles are from literature (Abohalima & Frebel 2018; Suda et al. 2008). 185
7.9 Evolution of ([Si/Fe] + [Ca/Fe] + [Ti/Fe])/3 − [Mg/Fe] as a function of [Mg/Fe]. Objects from this study are shown with asterisk symbols and color coded with their respective metallicities. The grey filled circles represent sample from literature (Abohalima & Frebel 2018; Suda et al. 2008). We find a clear enhancement of Si, Ca and Ti in Mg poor stars. 186
7.10 Evolution of heavy elements Sr, Ba and Eu with metallicity. Magenta color asterisks show stars from this study and grey circles represent objects compiled from literature (Abohalima & Frebel 2018; Suda et al. 2008). Horizontal dashed lines depict reference for solar abundances. 189
7.11 Evolution of [Sr/H]+[Ba/H] as a function of [Eu/H]. Magenta color asterisks show stars from this study and grey circles represent objects compiled from literature (Abohalima & Frebel 2018; Suda et al. 2008). 190
7.12 Distribution of limited-r (yellow colours), r-I (cyan colours), and r-II (magenta colours) stars in [Ba/Eu] vs [Eu/Fe] plane. The diamond symbols show objects from this study. See Saraf et al. (2023) for literature reference of compiled sample. 191
7.13 Evolution of the [Mg/Eu] in limited-r (yellow colour), r-I (cyan colour), and r-II (magenta colour) with metallicity. The diamonds show objects from this study. Grey symbols show normal halo stars. See Saraf et al. (2023) for literature reference of compiled sample. . 192

7.14 Yoon-Beers diagram for our sample stars. Grey asterisks represent samples from literature (Abohalima & Frebel 2018; Suda et al. 2008), red asterisks are carbon normal stars from this study, magenta asterisks are CEMP-r, and blue asterisk is CEMP-r/s. The slant line separates normal and carbon enhanced stars at [C/Fe]=0.7, whereas horizontal lines represent centers of Group I and Group III from Yoon et al. (2016) at A(C)$\sim$8.0 and A(C)$\sim$6.3 respectively. . . 193
7.15 CEMP-r/s star showing thin disc kinematics in three different orbital plane x, y and z. 194
7.16 Apocenter distance (r_a) vs maximum vertical height (z_{max}). Stars from this study are shown with black diamonds and literature sample is shown with open circles. Thick disk, inner halo and outer halo are respectively represented with cyan, magenta, and yellow colors. The literature sample is obtained from Gudin et al. (2021). . 195
7.17 Toomre diagram for our program stars shown with black diamonds. The open circles represents objects collected from literature. All the objects are color coded with cyan, magenta, and yellow colors to respectively indicate thick disk, inner halo, and outer halo stars are categorized in Section–7.6.1. The solid and dotted semicircles respectively enclose thick disk and thin disk stars. The vertical line separates retrograde and prograde stars. The literature sample is obtained from Gudin et al. (2021). 196
7.18 Place of our program stars (black diamonds) on Di Matteo diagram. Open circles represents sample compiled from literature. Our orbital parameter based thick disk, inner halo, and outer halo components are respectively shown cyan, magenta, and yellow colors. The maroon lines divide the image into in-situ, ex-situ, and mixed zone regions of star formation. The black vertical line at $l_z = 0$ separates prograde and retrograde components of the Galaxy. The literature sample is obtained from Gudin et al. (2021). 198
7.19 Metallicity distribution of thick disc, inner halo and outer halo components for the complete sample (literature + HESP GOMPA survey). Cyan histogram shows thick disk stars, magenta histogram displays inner halo stars, and yellow histogram shows outer halo stars. 199

8.1 Figure illustrating the synthesis of the strontium region in a LAMOST spectrum within a 300 Å spectral range. 207
8.2 Synthesis of the Sr line in LAMOST spectra at 4077 Å. 207

List of Tables

1.1 Classification of RPE metal-poor stars from Beers & Christlieb (2005a), Holmbeck et al. (2020), and Cain et al. (2020). 22

3.1 Basic information for our program stars. The spectral coverage is 3800−6900 Å, and exposure times for each object were 1800 seconds, with two exposures of 900 seconds. The equinox and epoch for the coordinates is J2000. 68
3.2 RVs of our program stars. 68
3.3 Estimate of effective temperature ($T_{\rm eff}$, in K) of our program stars, using different photometric and spectroscopic methods. 69
3.4 Estimates of micro-turbulence velocity (ξ) of our program stars using the methods described in the text. 70
3.5 Final adopted stellar parameters. 70
3.6 Dilution of carbon corrected according to Placco et al. (2014), and r-process classification of our program stars from Holmbeck et al. (2020). 72
3.7 Line list used for the spectrum synthesis of Th II lines in the 4019.129 Å region. 78
3.8 Detailed composition TYC 3431-689-1. 79
3.9 Detailed composition HD 263815. 80
3.10 Detailed composition of TYC 1716-1548-1. 81
3.11 Detailed composition of TYC 1191-918-1. 82
3.12 Age estimation of TYC 3431-689-1. 100
3.13 Age estimation of TYC 1191-918-1. 101

4.1 Basic information of our program stars. 109
4.2 Stellar parameters of standard and program stars. 113
4.3 Detailed differential abundances of HD107752 with respect to CS31082-0001. 117

4.4 Orbital parameters of standard and program stars in MW Potential. U, V, and W are velocities towards Galactic center, Galactic rotation and North Galactic pole respectively. The l_x, l_y, and l_z are specific angular momentum compoenents along x, y, z-axis respectively. The r_{peri} is pericenter distance, r_{apo} is apocenter distance, z_{max} is the maximum vertical height, and *ecc* is the eccentricity of the orbit. . . . 131

6.1 Basic information for the program stars. . . . 156
6.2 Estimated Thorium and Osmium abundances of CEMP-r/s stars. . 157

7.1 Basic observational information for our program stars. . . . 173
7.2 RV of our program stars. . . . 174
7.3 Estimates of temperatures of our program stars using different methods. . . . 176
7.4 Estimates of surface gravities of stars in this study using different methods. . . . 177
7.5 Final adopted stellar parameters for our program stars. . . . 178
7.6 Dilution of carbon corrected according to Placco et al. (2014), and r-process classification of our program stars from Holmbeck et al. (2020). . . . 191

A.1 Information about the Fe line list. . . . 234
B.1 Information about the line list. . . . 238
C.1 Detailed abundance determination for UCAC4 488-001423. . . . 247
C.2 Detailed abundance determination for TYC 1795-438-1. . . . 247
C.3 Detailed abundance determination for TYC 665-522-1. . . . 248
C.4 Detailed abundance determination for TYC 1939-202-1. . . . 248
C.5 Detailed abundance determination for TYC 195-1636-1. . . . 249
C.6 Detailed abundance determination for TYC 23-815-1. . . . 249
C.7 Detailed abundance determination for TYC 2985-737-1. . . . 250
C.8 Detailed abundance determination for TYC 1404-1448-1. . . . 250
C.9 Detailed abundance determination for TYC 1406-971-1. . . . 251
C.10 Detailed abundance determination for TYC 243-502-1. . . . 251
C.11 Detailed abundance determination for TYC 3443-1105-1. . . . 252
C.12 Detailed abundance determination for LP 491-46. . . . 252
C.13 Detailed abundance determination for TYC 1436-366-1. . . . 253
C.14 Detailed abundance determination for TYC 2533-1475-1. . . . 253
C.15 Detailed abundance determination for TYC 1465-1148-1. . . . 254
C.16 Detailed abundance determination for TYC 1192-20-1. . . . 254
C.17 Detailed abundance determination for TYC 2014-552-1. . . . 255
C.18 Detailed abundance determination for TYC 3474-142-1. . . . 255
C.19 Detailed abundance determination for TYC 1501-1445-1. . . . 256
C.20 Detailed abundance determination for TYC 1760-1284-1. . . . 256

C.21 Detailed abundance determination for TYC 2601-637-1. 257
C.22 Detailed abundance determination for TYC 975-2188-1. 257
C.23 Detailed abundance determination for TYC 1576-1703-1. 258
C.24 Detailed abundance determination for TYC 3534-57-1. 258
C.25 Detailed abundance determination for TYC 1653-657-1. 259
C.26 Detailed abundance determination for TYC 1170-642-1. 259
C.27 Detailed abundance determination for TYC 1988-1110-1. 260
C.28 Detailed abundance determination for UCAC4 430-119026. 260
C.29 Detailed abundance determination for TYC 1120-1253-1. 261
C.30 Detailed abundance determination for TYC 224-475-1. 262
C.31 Detailed abundance determination for TYC 1741-618-1. 262
C.32 Detailed abundance determination for TYC 267-308-1. 263
C.33 Detailed abundance determination for TYC 279-1113-1. 263

Abbreviations

AU	**A**stronomical **U**nit
GAIA	**G**lobal **A**strometric **I**nterferometer for **A**strophysics
GCE	**G**alactic **C**hemical **E**volution
HCT	**H**imalayan **C**handra **T**elescope
HD	**H**enry **D**raper
HESP	**Hanle E**chelle **SP**ectrograph
HIRES	**HI**gh **R**esolution **E**chelle **S**pectrograph
IAO	**I**ndian **A**stronomical **O**bservatory
IRAF	**I**mage **R**eduction and **A**nalysis **F**acility
LAMOST	**L**arge **A**rea **M**ulti **O**bject **S**pectroscopic **T**elescope
NASA	**N**ational **A**eronautics and **S**pace **A**dministration
NIST	**N**ational **I**nstitute of **S**tandards and **T**echnology
SNR	**S**ignal to **N**oise **R**atio
GTC	**G**ran **T**elescopio **C**anarias
VLT	**V**ery **L**arge **T**elescope
SDSS	**S**loan **D**igital **S**ky **S**urvey
ESO	**E**uropean **S**outhern **O**bservatory
HORuS	**H**igh **O**ptical **R**esolution **S**pectrograph
UVES	**U**ltraviolet and **V**isual **E**chelle **S**pectrograph
MW	**M**ilky **W**ay
CCD	**C**harge **C**oupled **D**evice

Chapter 1

Introduction and Motivation

Precision astrometry from Gaia accompanied with chemical composition of stars helping us revealing several substructure, which contributed significantly in the assembly of the Milky Way (MW). The early history of galaxy formation is preserved in the atmosphere of low-mass metal deficient stars which formed just after Big Bang (BB), and survived till date due to their slow evolution. These nearby objects act as the tool to understand early cosmology giving rise to a field known as near-field cosmology.

The concept of near-field cosmology, as described by Freeman & Bland-Hawthorn (2002), emphasizes how stars in the MW can provide valuable information of the early Universe, shortly after the BB. This field became important for scientists studying the universe's earliest epochs. The slow-evolving, metal-poor (MP) stars offer insights into several key areas: their chemical compositions and peculiar elemental abundance patterns reveal the chemical enrichment of the Universe, the early interstellar medium, the early stellar mass function, the star formation history, the activity of stellar nucleosynthesis over time, the astrophysical environments for heavy element formation, among other. This thesis aims to utilize the potential of metal deficient stars to investigate the metal enrichment of the MW, particularly the heavy elements.

1.1 The Milky Way

The Sun is positioned approximately 25,000 light-years from the Galactic center. Astronomers believe that the MW likely has two main spiral arms, the Perseus and the Scutum-Centaurus, along with several spurs and small arms. Our Sun is located on the Orion spur/arm, branching off from the Sagittarius arm. The Sun takes about 220 million years to complete one revolution in the Galaxy.

The MW exhibits a graceful structure that shows both order and complexity. Recent studies reveal it as a large barred spiral galaxy, home to billions of stars. Its structure comprises three main components: a flat disk-shaped region with spirals, a thick stellar distribution in the center referred to as the bulge or BPX(boxy/peanut/-X-shaped) structure, and a several kiloparsecs extended halo. The MW disk has a radius of approximately 10 kiloparsecs, which harbors most of its stars (Binney & Tremaine 2008). The illustrations in Figure 1.1, and Figure 1.2 respectively depict face-on, and edge-on perceptions of the MW. The face-on view offers a detailed artistic portrayal of the Galaxy, showcasing its central bar, and spiral arms. On the other hand, the edge-on view illustrates the extent of the disk and the dense concentration of stars in the central region. Now, let us discuss about the different parts of the MW.

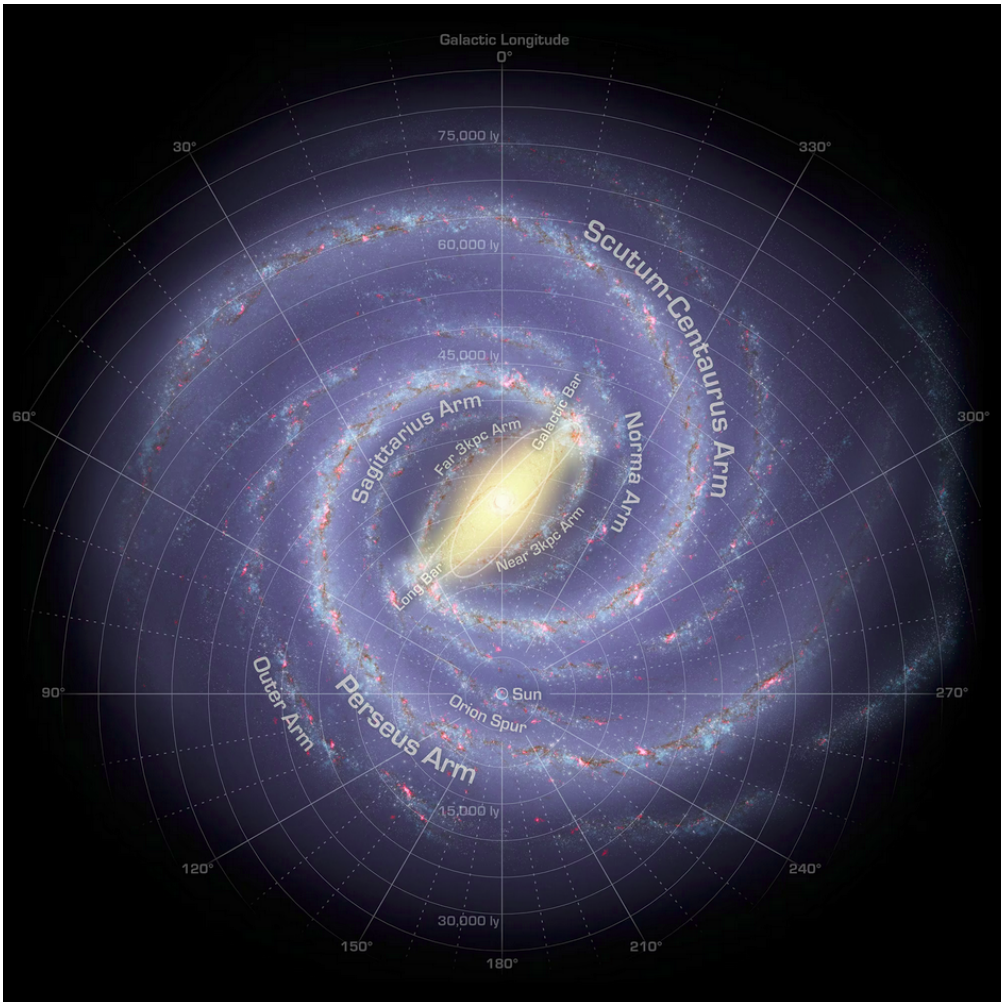

FIGURE 1.1: The figure depicts the artistic face on view of the Milky Way galaxy. It is showing two main spiral arms Perseus and Scutum-Centaurus, extend from the ends of the central bar. Image credit: NASA/JPL-Caltech/R. Hurt (SSC/Caltech)

1.2 Galactic components

The Galaxy comprises of three main components: the central bulge, flat disk, and stellar halo. In Figure 1.3, we illustrate different galactic components and their characteristic properties.

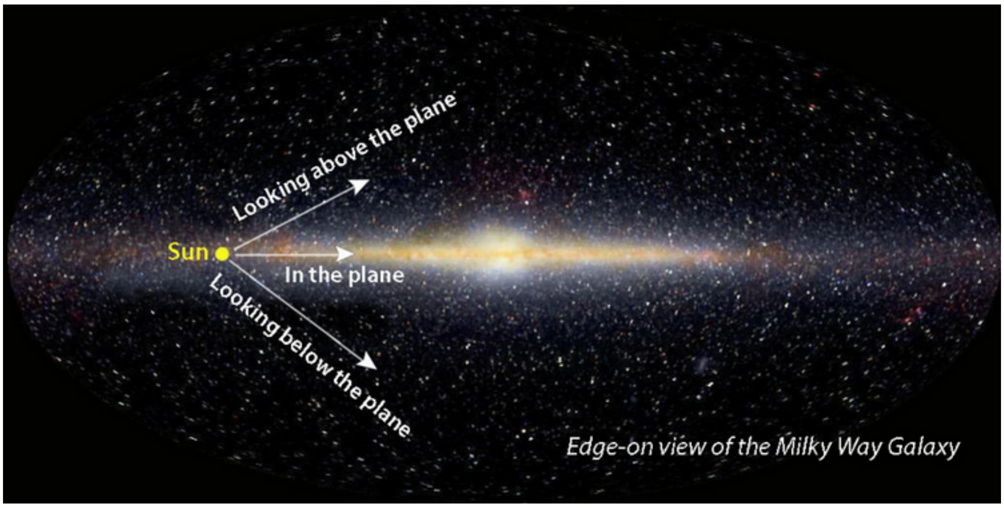

FIGURE 1.2: The solar system occupy a position in the plane of the Milky way. When we look through the disk, where stars are densely clustered, they line up across the distance to form a luminous band in the sky known as the Milky Way. Beyond this band, both above and below the disk, star density diminishes swiftly, resulting in a sky speckled with isolated stars. All the stars visible to us, whether with the naked eye or through the majority of telescopes, are constituents of the Milky Way. Credits: NASA, Richard Powell, with additional contributions by Bob King.

1.2.1 The Bulge

The dense aggregation of stars in the central spheroidal region is called bulge. It primarily consists of old stellar population along with a substantial amount of gas and dust. The presence of dust poses difficulties in observing bulge stars, contributing to uncertainties in age determination. Baade's window, an area of relatively lower gas and dust density in the sky spanning approximately 2 degrees in diameter, facilitates observations of the bulge (Fulbright et al. 2006).

The stellar population within the Milky Way bulge is predominantly ancient, with most stars exceeding 8-10 billion years in age (see, Zoccali et al. (2003) and (Clarkson et al. 2008)). It includes a bar at the centre. Majority of stars in the bulge are metal-rich with a few metal-poor stars. This population displays a varied distribution of metallicity, spanning from -2.0 to +0.6 with multiple peaks indicating a mix of stellar population towards the MW center (Bensby et al. 2013).

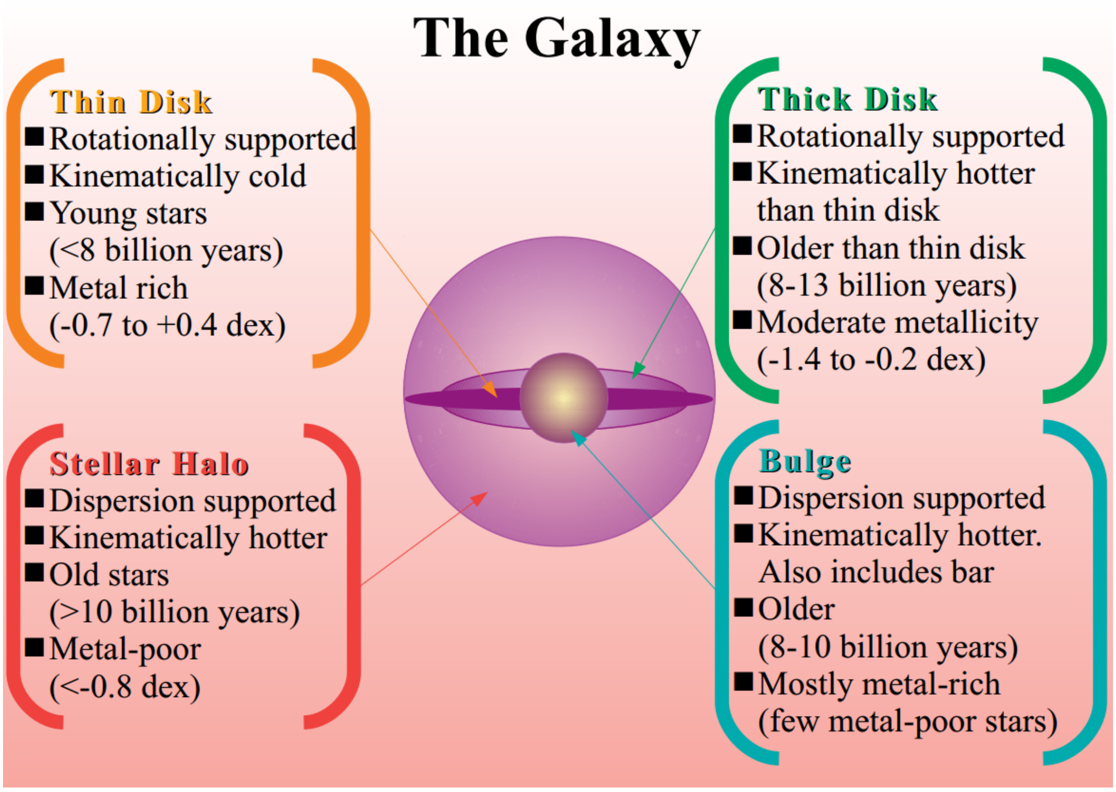

FIGURE 1.3: Figure depicts the different Galactic components of MW galaxy.

The MW bulge exhibits rotation (Kunder et al. 2012), characterized by a max velocity of roughly 75 $km\ s^{-1}$, and notable velocity dispersion reaching 120 $km\ s^{-1}$, which diminishes with increasing Galactocentric distance (Minniti & Zoccali 2008; Kunder et al. 2012). It is dispersion supported and kinematically hotter. Despite ongoing research, the formation of the bulge remains incompletely understood. Studies suggests two primary processes: (1) a rapidly star forming spheroid, as indicated by high [α/Fe] relative to other populations in the MW, and (2) the gradual formation of stars over an extended period through dissipational collapse (Meléndez et al. 2008). The bulge represents the central convergence zone of the MW, where diverse stellar populations intersect (Bensby et al. 2013).

1.2.2 The disk

Our Milky way's spiral disk is a flattened, rotationally supported structure, containing a total mass of approximately 6×10^{10} solar masses, comprised of gas, dust, stars, and open clusters (Sofue et al. 2009). It predominantly contains young and intermediate stellar populations, orbiting symmetrically around the galactic center. Observations toward the Galactic North Pole by Gilmore & Reid (1983) revealed two distinct components within the Galactic disk – (1) the thin disk and (2) the thick disk. The thin disk stretches outward radially to approximately 15 kpc (Ruphy et al. 1996) showing 3.4 kpc scale length and 0.3 kpc scale height (Jurić et al. 2008; Cheng et al. 2012). It represents the youngest Galactic component with stellar population younger than 9 billion years. In contrast, the thick disk comprises very old stars spanning ages ranging from approximately 8 to 13 billion years (Fuhrmann 1998; Reddy et al. 2006).

The thin disk of the MW contains metal-rich stars whose metallicity spans over a range of -0.7 to $+0.4$, peaking at around -0.2 (Nordström et al. 2004). In the solar vicinity, its mean metallicity is approximately -0.06 ± 0.22, while at a distance of 11 kiloparsecs, it drops to -0.48 ± 0.12, indicating a significant abundance gradient (Bensby et al. 2011). It is rotationally supported showing circular velocity of $\sim 210\ km\ s^{-1}$, and kinematically cold showing vertical velocity dispersion of $\sim 20\ km\ s^{-1}$ (Soubiran et al. 2003).

In contrast, the thick disk consists of old stars, spanning ages from approximately 8 to 13 billion years (Fuhrmann 1998; Reddy et al. 2006) and metallicities ranging from -2.2 to 0.0 (Bensby et al. 2007). The scale length of thick component is approximately 1.8 kpc and scale height is about 1.3 kpc (Binney et al. 1998; Reddy & Lambert 2008; Cheng et al. 2012). In comparison to thin disk, thick disk stars display higher dispersion and lower rotation support (Soubiran et al. 2003; Wyse et al. 2006). The [α/Fe] increases with increasing vertical height making thin disk

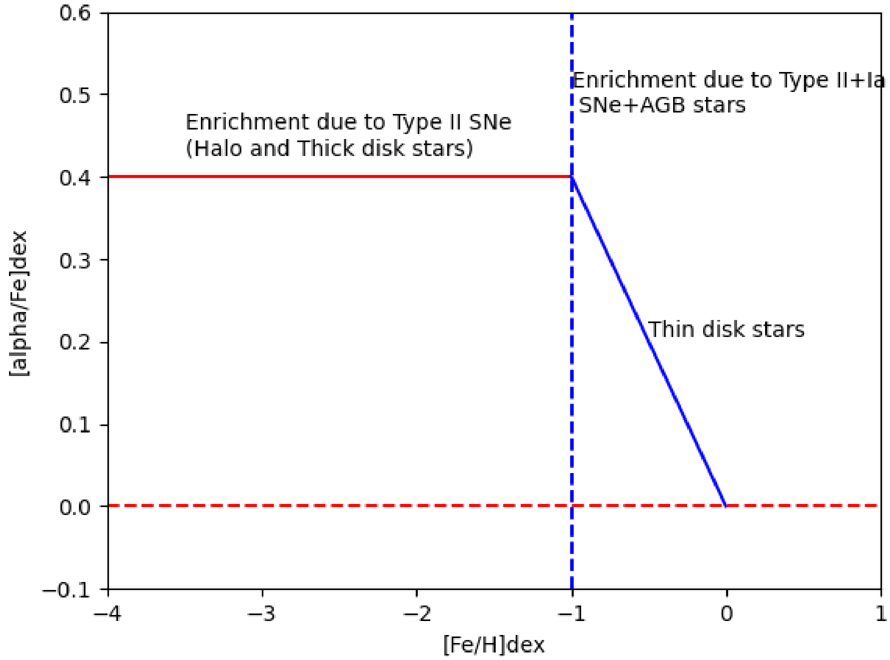

Figure 1.4: Evolution of [α/Fe] versus [Fe/H] for thin, thick and halo stars.

[α/Fe]-poor and thick disk [α/Fe]-rich (Bensby et al. 2011). Figure 1.4 portrays the [α/Fe] trend with [Fe/H] in the MW. For thin disk [α/Fe] started decreasing at metallicity around -1.0 dex, while for thick disk [α/Fe] ratios remain constant until approximately -1.0 dex.

1.2.3 The stellar halo

The stellar halo constitutes the outer visible part of the Galaxy. It primarily comprise of metal deficient stars, and globular clusters. The matter density of halo is notably low in comparion to other components. However, it comprises of huge amount of dark matter, constituting approximately 90% of its dynamical mass.

Several surveys conducted over recent decades have demonstrated differences in the inner and out part of the halo (Carollo et al. 2007, 2010) leading further division of the halo. The inner halo reaches about 10 to 15 kpcs from center and outer halo bounds between $10 - 20$ kpcs. The inner halo density follows a power-law distribution, $\rho_{\mathrm{in}} \sim r^{-\alpha}$, with an exponent α ranging between 2 and 3 (Bell 2008). It exhibits a moderately flattened shape, and has an average metallicity of [Fe/H] ~ -1.6 dex. Stars in inner halo exhibit a predominant eccentric and prograde orbits. Some studies suggests that the inner halo is formed during protogalactic gas collapse event Carollo et al. (2007); Jofré & Weiss (2011). More recent findings by Helmi et al. (2018) depict the inner halo as primarily composed of Gaia-Enceladus debris.

In contrast, the outer halo density follows power-law distribution, $\rho_{out} \sim r^{-\alpha}$, with an exponent α between 3 and 4. Compare to the inner halo, the outer halo exhibits near spherical shape, and has metallicity distribution peaking approximately at -2.0 (Bell 2008; Carollo et al. 2007). A major part of the outer halo stars displays retrograde orbits, offering crucial insights into the accretion and merging events that have shaped the MW. The similarity of chemical composition between outer halo stars and dwarf galaxies further support their accretion origin Battaglia et al. (2017).

1.3 Formation of galaxy

The understanding of how galaxies and larger structures come into existence within the Universe entails two distinct approaches: top-down approach and bottom-up approach.

1.3.1 Top-down model

The top-down approach, also termed the monolithic collapse theory, emerged from the research of (Eggen et al. 1962) [ELS theory], who investigated the formation of the Milky Way galaxy. According to the ELS theory, a massive cloud collapses until reaching equilibrium, balancing inward gravitational force with outward centrifugal force to preserve angular momentum. The dissipation of large gas clouds in dark matter halo show rapid star formation, lasting a timescale comparable to free fall time. Subsequently, the galactic disk forms from the cooling of remaining gas into a disk. While this theory is insufficient in explaining some phenomena like retrograde orbits in the halo and multi-age population in globular clusters.

1.3.2 Bottom-up model

In bottom-up theories (also termed the ΛCDM model), it is assumed that smaller systems or star clusters collapse first, and then assemble through collisions and mergers, combining over extensively large time scales to eventually form large structures such as galaxies. It is widely accepted model for explaining various observed properties of the Cosmos (Madriz Aguilar et al. 2017). This model account for dark energy, dark matter and baryonic matter in the Universe (Solà & Gómez-Valent 2015). In this model, first dark matter clumps to form minihalos. Then gas accretion begins into the minihalos. Subsequent gravitational collapse within subhalos facilitated the formation of protogalaxies. This process of merging continued, progressively forming larger systems, in what is referred to as hierarchical merging.

An illustration of bottom-up model is shown in Figure 1.5. First-row panels show the gravitational collapse of metal-poor gas in the dark matter halos. If the gas

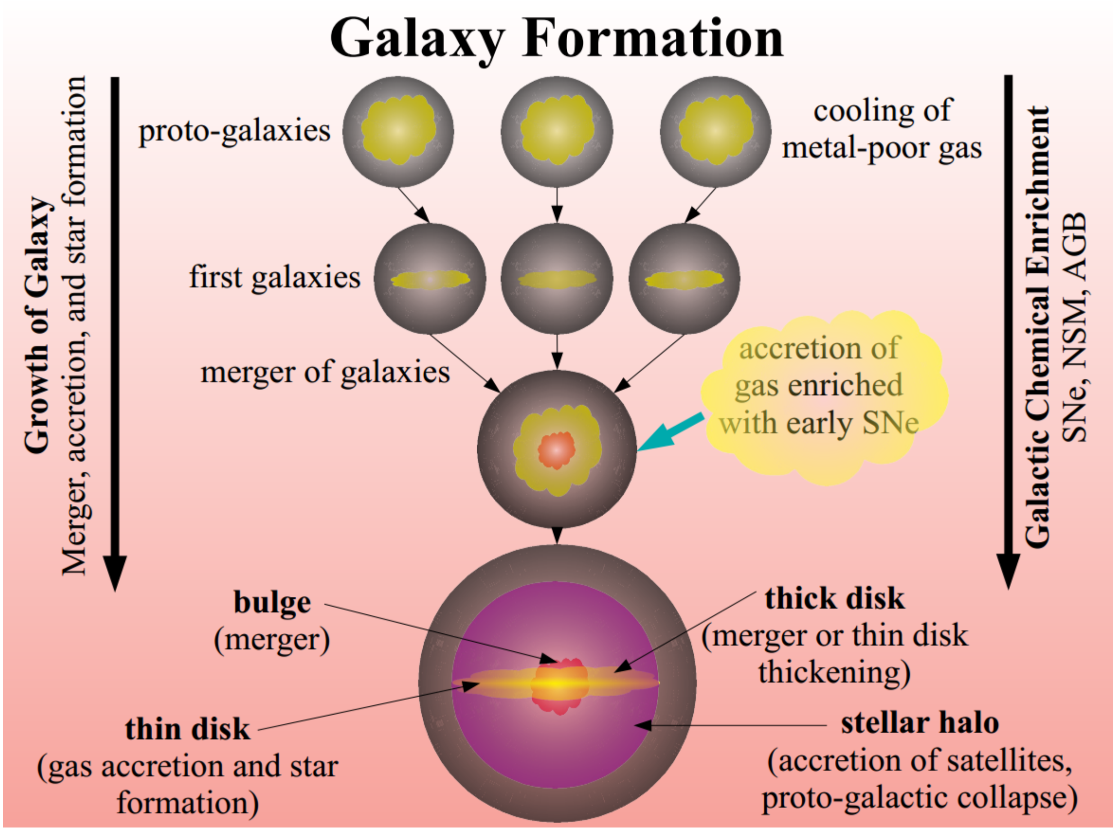

FIGURE 1.5: An schematic diagram of the Bottom-up model of the galaxy formation

has significant initial angular momentum, it settles in the form of a disk. These are the first galaxies where massive pop-III star forms. The merger of the first galaxies gives rise to a dispersion-supported bulge. The accretion of gas enriched from SNe ejecta of pop-III stars forms a new disk surrounding the bulge as you can see in the bottom panel. This gas gives birth to pop-II stars. The metal-poor stars we see today are low-mass pop-II stars. Later on, inter stellar medium (ISM) metal content keeps increasing due to neutron star mergers (NSM), type-Ia SNe and AGB stars. After several merger/accretion events, we see a massive galaxy with different components, as seen here at the bottom.

1.4 Nucleosynthesis: Origin of elements

Nucleosynthesis is the process through which new heavy nuclei are formed from pre-existing light nucleons (protons and neutrons) and nuclei. It occurs in various cosmic environments, such as during the early stages of the Universe (Big Bang nucleosynthesis), in stars (stellar nucleosynthesis), and during explosive stellar events like supernovae (supernova nucleosynthesis). This process is crucial for the production of elements beyond hydrogen and helium, which are the abundant elements in the Cosmos.

1.4.1 Galactic Chemical Evolution (GCE)

On the periodic table, Astronomers classify all the elements except H and He as metals. Just 3 seconds after the BB, the Universe consists solely of H, He, and a small portion of Li. The first stars, forming from pristine, metal-free gas, are exceptionally massive due to the absence of heavy elements to cool the ISM. These stars rapidly evolve into supernovae, enriching the ISM with elements beyond carbon. This process gives rise to the second generation of low-mass Pop-II stars, known as metal-poor stars. The cycle of stellar evolution continues, progressively generating heavier elements.

In this manner, subsequent generations of stars contribute to the metal content of the Universe. Figure 1.6 presents an artistic depiction illustrating known chemical evolution. We will explore the chemical evolution of stars in greater detail in the next section.

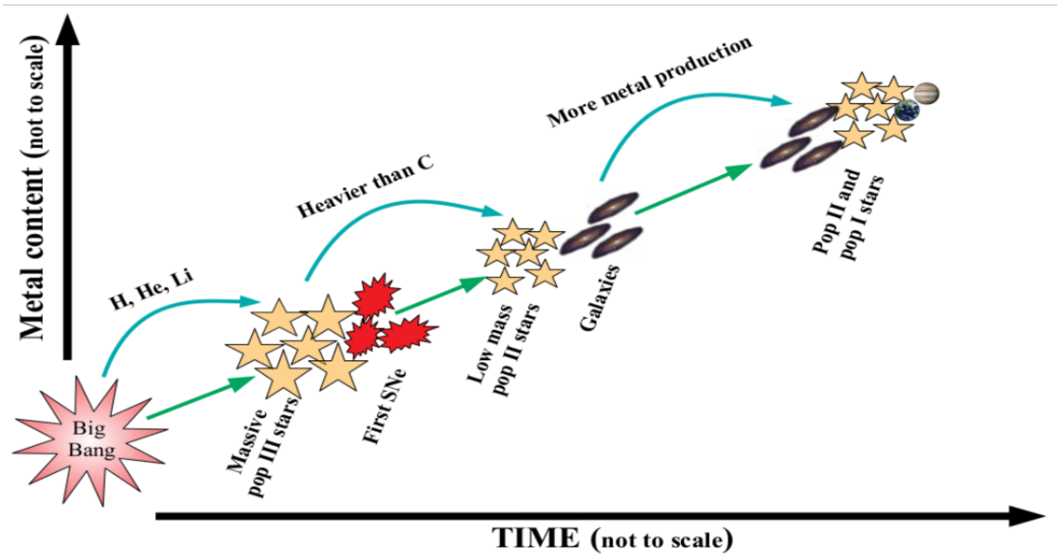

FIGURE 1.6: Galactic Chemical Evolution plot

1.4.2 Primodial nucleosynthesis

Big Bang nucleosynthesis (BBN), also referred to as primordial nucleosynthesis. Alpher et al. (1948) (Alpher-Bethe-Gamow) performed calculations on the production of light elements in the early Universe. Once the temperature of Universe reduced enough ($\sim 10^9$ K) during first minute of BB, it leads to the formation of stable neutrons and protons (Maoz 2016; Dodelson & Schmidt 2020). These particles then combined to form deuterium, eventually producing other light elements such as hydrogen-1, deuterium, tritium, helium-3, helium-4, lithium-7, and beryllium-7. Notably, tritium and beryllium-7, being unstable, subsequently decayed into helium-3 and lithium-7, respectively. The remaining heavier elements were synthesized in stars or during stellar explosions.

1.4.3 Fusion: Nucleosynthesis up to iron peak

After a protostar forms in the interstellar medium, its core temperature rises due to gravitational collapse. Once the core temperature reaches a critical point, hydrogen fusion begins, leading to the formation of helium. Depending on the stellar mass and density, this fusion process occurs either through the PP chains or the CNO cycle. In solar mass stars, the PP chain operates at a core temperature of approximately 4×10^6 K, while the CNO cycle occurs in stars with a mass greater than 1.3 solar masses, at a core temperature of approximately 15×10^6 K. The radiation produced during nucleosynthesis supports further collapse of gas leading to a hydrostatic equilibrium. This stage is known as stellar main sequence (MS).

The high gravity of massive stars requires a larger pressure to maintain hydrostatic equilibrium, resulting in increased core temperature and luminosity, causing fuel to burn more rapidly. Consequently, the lifespan of massive stars is shorter than low-mass stars. On the depletion of core hydrogen, the star undergoes gravitational collapse and enters the giant phase. During this phase, hydrogen starts burning in the shell above the core, while the contracting helium core accumulates more helium from the hydrogen shell. The outer stellar surface expand, and cool, causing star to move in the direction of lower temperatures on the Hertzsprung-Russell (HR) diagram. Now star becomes sub-giant.

In this stage, convection transports the newly formed material on the surface of the star and changes outer stellar composition. This event is know as First Dredge-Up (FDU). Subsequently, while moving on the giant branch, the core continues to contract until it reaches a temperature of approximately 10^8 K, triggering He ignition and the formation of C through the triple-α reaction.

Helium in low mass stars ignites under degenerate conditions, leading to a rapid helium burning known as helium flash. Conversely, helium in high mass stars ignites quiescently under non-degenerate conditions, marking the termination of the RGB phase. At 0.02 metallicity, the degenerate and non-degenerate delineating boundary is 2.25 $M_{\odot}$(Karakas 2010). Further, star contracts as its luminosity reduces, causing the core temperature to rise. Eventually, He burning begins in

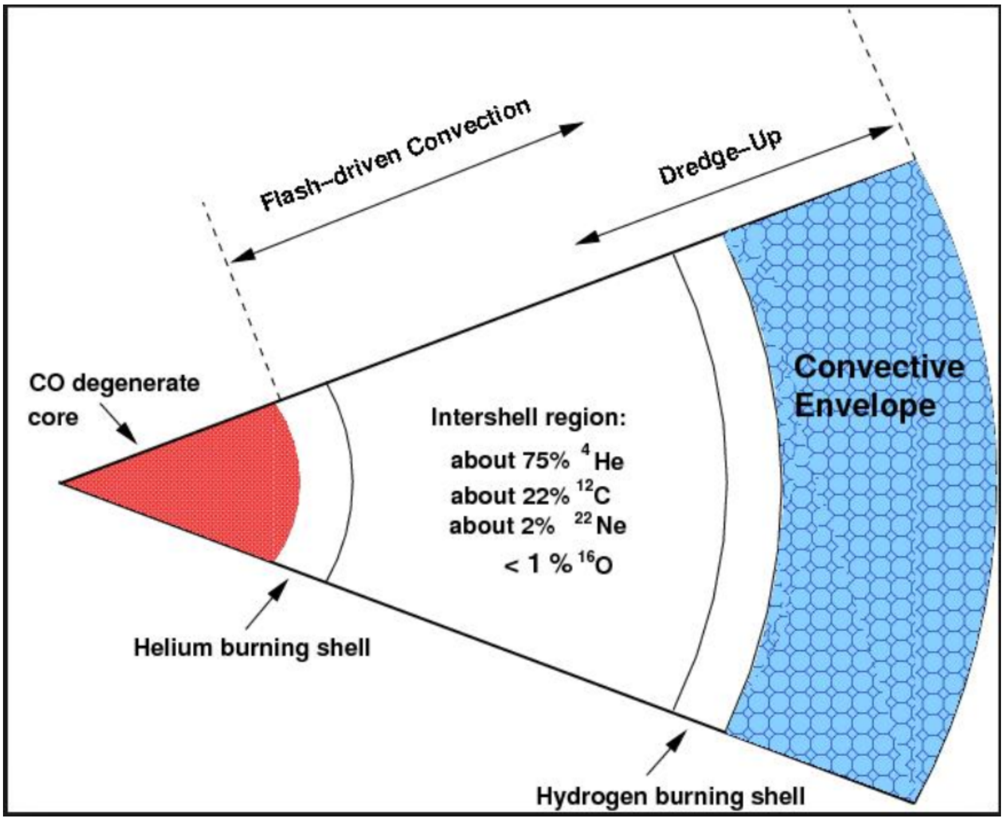

FIGURE 1.7: Internal structure depiction of AGB star. Picture courtesy: Karakas (2010).

the core and star become Horizontal Branch (HB) star. Upon exhaustion of He in the core, $0.8 - 8$ solar mass stars moves on giant branch for the second time which is know as asymptotic giant branch (AGB).

During the AGB phase, stars possess an inert carbon-oxygen core, a helium shell, a hydrogen shell, and a convective envelope. A schematic diagram of AGB star with CO degenerate core is shown in Figure 1.7. As nuclear burning transitions to a helium shell, star expands, the hydrogen shell extinguishes, and convection deepens. It causes mixing of surface material, and alters ^{4}He and ^{14}N, marking the Early-AGB (E-AGB) stage of stellar evolution. This mixing is known as Second Dredge-Up (SDU).

Following the SDU, the stellar contraction resumes hydrogen-shell burning, leading

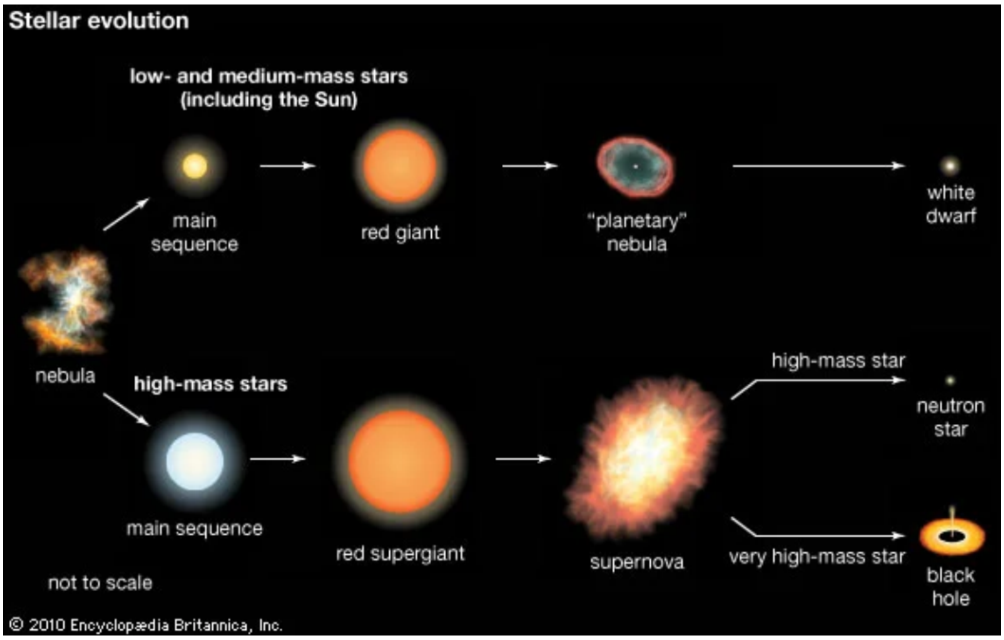

FIGURE 1.8: An illustration of evolutionary stage of low, intermediate and high mass stars. Image Credit: https://www.britannica.com/science/star-astronomy/Star-formation-and-evolution

to the thinning of the helium shell. Accumulation of helium during hydrogen-shell burning triggers explosive helium burning in the helium shell, known as a helium-shell flash, marking the onset of the Thermally Pulsing AGB (TP-AGB) phase. During this phase, the helium-shell flash, or thermal pulse (TP), lasts for a few hundred years, while the hydrogen-shell burning, or interpulse (IP), persists for approximately 10^4 years. The TP generates luminosity of up to approximately 10^8 solar luminosities, causing stellar layers' expansion and the extinction of the hydrogen shell.

The Thermal Pulse phase triggers the convective region formation within the helium shell, known as the He-intershell (IS) region. This convective activity, driven by the flash, effectively unifies the composition within the IS region. As the flash subsides, the convective envelope migrates inside towards the already mixed region by the previous flash. This inward movement results in the mixing of carbon and other He burning products to the stellar exterior, a phenomenon referred to as the Third Dredge-Up (TDU). Subsequently, the star undergoes contraction, re-ignition of the hydrogen shell, and the cycle repeats. The successive occurrences of TP-TDP-IP significantly alter the surface composition of AGB stars. The stellar metallicity and initial mass significantly influence the final exterior composition. Though TDU has the potential to transform a star into a carbon star, additional mixing mechanisms, e.g., Hot-Bottom Burning (HBB) and Cool-Bottom Processing (CBP), prevent the carbon star formation. These additional processes occur when the convective envelope penetrates the hydrogen-burning shell. During HBB, reactions such as the Ne-Na and Mg-Al cycle operate depending on the temperature, altering the surface abundances of elements like lithium, nitrogen, fluorine, sodium, magnesium, and aluminum. The significant expansion and contraction of the AGB star's envelope lead to considerable mass loss, enriching the ISM with nucleosynthesis products. The outer layer shedding eventually ceases the TP-AGB phase. $0.8 - 8$ solar mass stars end their lives as C-O white dwarfs due to insufficient temperature for C burning. Conversely, massive stars (> 11 solar masses) go through successive stages of carbon, neon, oxygen, and silicon burning. Ultimately, they develop an iron core and culminate in a core-collapse supernova (CCSN) explosion. Figure 1.8 illustrates the diverse stages of stellar evolution for different stellar masses.

1.4.4 Neutron-capture nucleosynthesis: Beyond iron peak

Traditional nucleosynthetic mechanisms, such as proton capture and alpha processes, are insufficient to account for the presence of elements heavier than iron because of highest binding energy of iron (Fe). Beyond iron, elements are synthesized through neutron-capture processes (n-capture processes). These processes are classified into three categories according to neutron flux on seed nuclei: (1) the slow neutron-capture process (*s*-process), (2) the rapid neutron-capture process (*r*-process), and (3) the intermediate neutron-capture process (*i*-process).

***s*-process:** In case of s-process, the neutron capturing rate onto the seed nuclei is slower than the beta decay rate, i.e., the time of capturing neutrons onto the seed nuclei is larger than the beta decay time. Theoretical calculations suggest that in the case of the s-process, the seed nuclei capture one neutron in thousands of years. This process occurs at a neutron-density of around 10^7 cm^{-3} (Busso et al. 1999), resulting in three distinct peaks in the abundance pattern. The first peak emerges at $N = 50$, generating elements like ^{86}Kr, ^{87}Rb, ^{88}Sr, ^{89}Y, and ^{90}Zr, forming the light-s process peak. The second peak, occurring at $N = 82$, constitutes elements such as ^{138}Ba, ^{139}La, ^{140}Ce, ^{141}Pr, ^{142}Nd, and ^{144}Sm, forming the heavy-s process peak, attributed to the main s-process component. The third peak stems from the strong component of the s-process, and comprises Pb and Bi at $N = 128$. Ba is used as the representative element for the s-process.

The s-process takes place in the intershell region between H and He burning shells of AGB stars. The H and He shell burning causes multiple thermal pulses (TPs) until the convective envelope is entirely sheds into ISM. The time interval between two consecutive TPs termed as interpulse period ($\sim 10^5$ years). During the interpulse period, protons (hydrogen nucleus) near the upper boundary of the intershell region are mixed with inner material, phenomenon knowns 'partial mixing of protons'. This leads to the production of ^{13}C from ^{12}C capturing protons, eventually forming a ^{13}C pocket in the same region via the β-decay of ^{13}N. The temperature conditions ($\sim 10^8$ K) favor the temperature-sensitive reaction ^{13}C (α, n) ^{16}O, acting as a neutron-source for the slow neutron-capture (n-capture) process (Karakas & Lattanzio 2014).

Additionally, another neutron-source, ^{22}Ne (α, n) ^{25}Mg, operates at temperatures around 3×10^8 K for stars with initial masses exceeding approximately $3M_\odot$ (Lugaro et al. 2012). However, this neutron-source remains active for a brief period and thus cannot produce sufficient neutron exposure to generate the heavy s-process peak (Gallino et al. 1998). Hence, the primary neutron source in the intershell region of AGB stars is the ^{13}C (α, n) ^{16}O reaction. Several mechanisms, such as rotation, convective overshooting, and gravity waves, have been proposed in the literature to elucidate the process by which protons are mixed into the intershell region for ^{13}C pocket formation, yet the precise workings of this mixing process remain incompletely understood (Karakas & Lattanzio 2014).

During each TP, the AGB star gradually loses its envelope. The material enriched with *s*-process elements by successive TDU episodes in the convective envelope is transferred to the binary companion (secondary star) via Roche Lobe Overflow (RLOF) or wind accretion (Abate et al. 2013). Consequently, the secondary star manifests as an *s*-process enriched star, while the primary star culminates its evolution as a white dwarf.

***r*-process:** In case of *r*-process, the neutron capturing rate onto the seed nuclei is faster than the beta decay rate i.e., the time of capturing neutrons onto the seed nuclei is smaller than the beta decay time. The process occurs at a neutron-density exceeding 10^{22} cm^{-3} (Frebel 2018a). Unlike the timescale of the *s*-process, which spans hundreds to thousands of years, the *r*-process occurs within seconds. The representative element of the *r*-process is Europium(Eu) due to its ease of spectroscopic detection. The *r*-process constitutes approximately 95% of the solar Eu (Arlandini et al. 1999b). Despite variations in enhancement levels from star to star, the *r*-process abundance pattern remains consistent for $56 \leq Z \leq 70$ elements, a phenomenon referred to as 'universality of main *r*-process' (Roederer et al. 2012).

However, there are noticeable deviations among some RPE stars, particularly, the scatter of first peak elements and actinides. For instance, the scatter of Sr can reach about 1.5 dex in some RPE stars (Frebel 2018a). This variation is viewed as an evidence for multiple astrophysical sites for *r*-process (Travaglio et al. 2004a; Hill et al. 2017a). The process producing primarily light r-process elements is coined as weak r-process or limited r-process (Wanajo et al. 2001; Cowan et al. 2021; Frebel 2018a). The proposed sites for the r-process include core-collapse supernovae, magnetorotational magnetohydrodynamical (MHD)-jet supernovae or collapsars, neutron stars − neutron stars (NS-NS) merger, and neutron star − black hole (NS-BH) merger (Schramm 1973; Lattimer & Schramm 1974a; Symbalisty et al. 1985; Eichler et al. 1989; Qian & Woosley 1996; Fujimoto et al. 2008a; Ono et al. 2012; Eichler et al. 2015; Wu et al. 2016; Thielemann et al. 2017; Obergaulinger et al. 2018).

Detection of NS-NS merger and associated kilonova event (Abbott et al. 2017; Villar et al. 2017a), has provided support for the aforementioned third production site (NS-NS). Nevertheless, many details regarding these sites remain unclear. The abundant population of RPE stars in dwarf galaxies such as Reticulum II and Tucana III is anticipated to enhance our comprehension of element production sites within the realm of galactic archaeology (Ji et al. 2016; Hansen et al. 2017; Ji & Frebel 2018a; Frebel 2018a; Marshall et al. 2019; Cowan et al. 2021).

***i*-process:** The i-process operates at neutron-density around 10^{15} cm^{-3} (Dardelet et al. 2014; Roederer et al. 2016b; Hampel et al. 2016). It lies between the neutron-densities associated with the s-process and r-process. Cowan & Rose (1977) initially demonstrated the potential for achieving such high neutron-densities by introducing hydrogen into the convective intershell region of AGB stars through simulations. This process, now termed proton ingestion episodes (PIEs), purportedly facilitates the mixing of protons into specific He-rich convective regions, where ^{12}C captures protons to yield ^{13}C. Subsequently, the neutron-source ^{13}C (α, n) ^{16}O generates neutron-densities adequate for i-process operation. It's worth noting that the same neutron-source in a radiative environment yields neutron-densities conducive to the s-process.

Theoretical calculations of i-process yields have been conducted by Dardelet et al. (2014); Hampel et al. (2016). Dardelet et al. (2014) successfully replicated the abundance patterns of three CEMP-r/s stars, while Hampel et al. (2016) matched the observed abundances of twenty CEMP-r/s stars, including those previously studied by Dardelet et al. (2014).

Despite advancements, the exact sites of i-process occurrence, where PIEs can occur, remain contentious. Proposed stellar sites include the intershell regions of very metal-poor AGB stars (Campbell & Lattanzio 2008; Cristallo et al. 2009; Campbell et al. 2010; Stancliffe et al. 2011), super-AGB stars (Doherty et al. 2015; Jones et al. 2016), the very late thermal pulse (VLTP) phase in post-AGB stars (Herwig et al. 2011), low-metallicity massive stars (Clarkson et al. 2018; Banerjee et al. 2018), and rapidly accreting white dwarfs (Denissenkov et al. 2017; Côté et al. 2018; Denissenkov et al. 2019).

1.5 Galactic archaeology

Galactic (or stellar) archaeology focuses on the early composition of the Universe by examining metal-poor population. Essentially, it utilizes chemical abundances of ancient stars to uncover patterns in element distribution. By studying these stars, we gain insights into their metal-free, Population III ancestors. This investigation sheds light on various phenomena, including galaxy formation, early star birth, stellar and supernova nucleosynthesis, and halo formation processes. These observations, combined with theoretical models, offer comprehensive insights about the conditions under which they formed and the characteristics of their predecessors (Sneden et al. 2000b; Beers & Christlieb 2005b; Frebel & Norris 2015a; Frebel 2018a).

1.5.1 Metal-poor stars and their classification

Metal-poor stars are old and low-mass Population II (Pop II) objects that born in the ISM polluted by the leftover of Population III (Pop III) stars. These stars are typically in giant or main-sequence phase. They are important because their atmospheres have not changed much over time, so they still hold clues of birth ISM and early synthesis mechanisms.

These objects are categorized in various groups depending on the metal content in the star. Conventionally, absolute elemental content is measured relative to hydrogen on a logarithmic scale. It is calculated using the formula

$$\log \epsilon(A) = \log_{10}\left(\frac{N_A}{N_H}\right) + 12$$

,

where N_A is atom counts of element A, and N_H is hydrogen atom counts. This definition assumes 10^{12} hydrogen atoms as base. In astronomy, the abundance ratio of two elements is usually represented with respect to the Sun. For elements A and B with atom counts respectively N_A and N_B, the abundance ratio is given as follows,

$$[A/B] = \log_{10}\left(\frac{N_A}{N_B}\right)_* - \log_{10}\left(\frac{N_A}{N_B}\right)_\odot$$

.

The term metallicity represents the stellar metal content, traditionally indicated by the iron content $[Fe/H]$ because of ubiquitous presence of iron features in the visible region. By convention, the solar metallicity is zero. Objects with positive $[Fe/H]$ are classified metal-rich, whereas those having $[Fe/H] < -1.0$ are called metal-poor, having 10 times less metals than the Sun. Similarly, metallicity less than -2.0 means star contains 100 times less metal than the Sun and so on. So

subclass	Definition
r-I	$0.3 <$ [Eu/Fe] $\leq +0.7$ and [Ba/Eu] < 0
r-II	[Eu/Fe] $> +0.7$ and [Ba/Eu] < 0
r-III	[Eu/Fe] $> +2.0$ and [Ba/Eu] < 0
limited-r	[Eu/Fe] $< +0.3$, [Sr/Ba] $> +0.5$, and [Sr/Eu] > 0.0
CEMP	[C/Fe] $> +0.7$
s	[Ba/Fe] $> +1.0$ and [Ba/Eu] $> +0.5$
r/s	$0.0 <$ [Ba/Eu] $< +0.5$

TABLE 1.1: Classification of RPE metal-poor stars from Beers & Christlieb (2005a), Holmbeck et al. (2020), and Cain et al. (2020).

far, stars with a wide range of metallicity have been identified for $[Fe/H]$ from $+0.7$ to -7.3. The current record holder metal-poor star is the SMSS J0313–6708 whose metallicity is -7.3 (Keller et al. 2014).

Now, we will delve into the distinct categories of chemically peculiar stars, which are pertinent to our investigation.

1.5.2 r-process enhanced (RPE) stars

Stars with excess r-process elements, such as Europium, are rare objects called RPE stars. They originate from ISM that underwent mixing with the ejecta of an events rich in r-process. The shape of the abundance distribution observed in these stars, particularly after the first r-process peak, follows that of the solar r-process pattern. Such findings suggest a universal event of main r-process elements.

The RPE stars are classified into several subclasses according to different enhancement levels of r-process material. This r-process excess is characterized by the europium abundance. We list different subclasses of RPE stars in Table 1.1.

The potential birthplaces of these objects are the Ultra Faint Dwarf galaxies, from where they later accreted into the MW. The establishment of the r-process Alliance (RPA) collaboration has led to a surge in their discoveries. Finding more of these objects is crucial to characterize the sites of heavy element synthesis and their evolution.

1.5.3 EMP and CEMP stars

Extremely Metal-poor (EMP) stars represent a class of objects with [Fe/H] < -3.0. They are very important for inferring the compositions and nature of the young Universe. An interesting fact about studying these EMP stars is that the ratio of carbon to iron ([C/Fe]) tends to increase with reducing metallicity. Objects showing [C/Fe] $> +0.7$ are labeled as Carbon Enhanced Metal Poor (CEMP) stars. The excess of neutron-capture material in CEMP leads their further division:

CEMP-*s*: These objects display an enrichment of s-process product such as Ba, likely due to mass transfer from a binary companion during their Asymptotic Giant Branch (AGB) phase. Studies of binary systems support this idea.

CEMP-*r*: These objects have an excess of r-process elements such as Eu and are rare in the halo. The source of these elements could be faint supernovae, but this remains uncertain. Discovering more of these stars would greatly benefit research in this area.

CEMP-*r*/*s*: These objects exhibit excess of s- and r-process elements simultaneously, such as Ba and Eu, are present in excess in these stars. The origin of the s-process is likely AGB stars or Fast Rotating Massive Stars (FRMS), while the source of the r-process is less apparent.

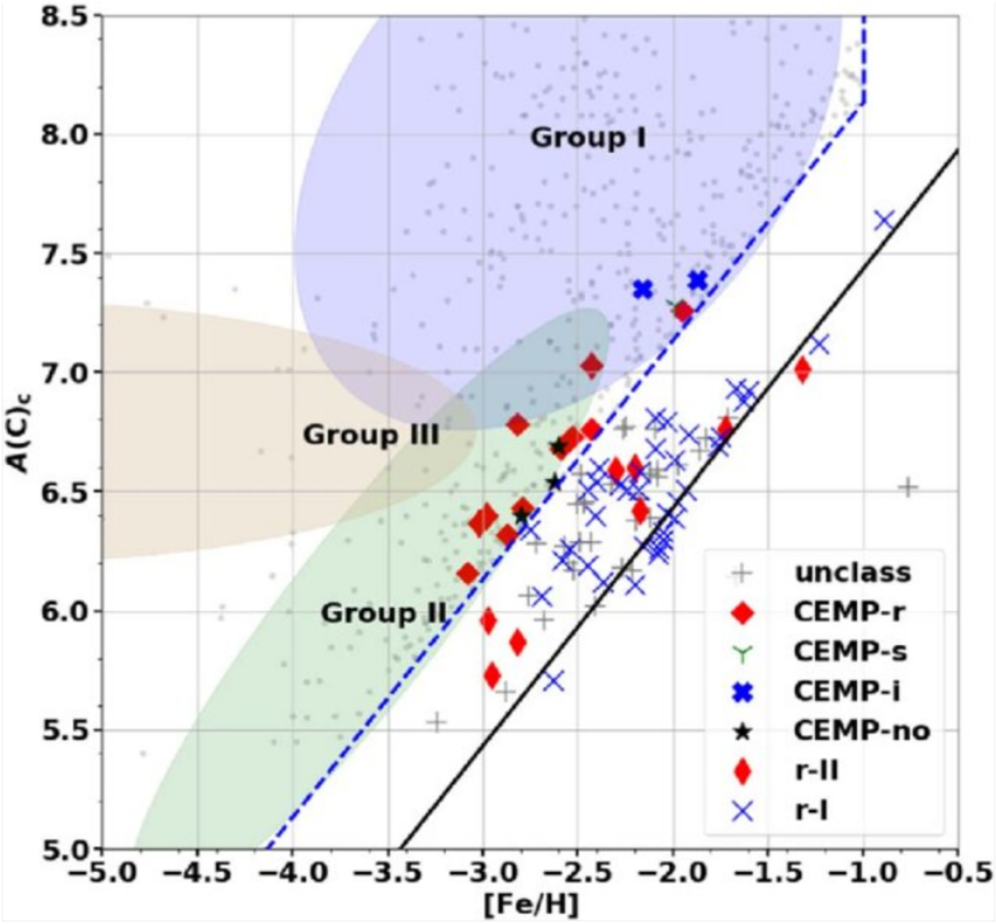

FIGURE 1.9: Classification of CEMP into different sub-groups. Picture courtesy: Zepeda et al. (2022)

CEMP-no: In contrast to above sub-groups, these objects exhibit no surplus of neutron-capture product. They may originate from mixing and fallback supernovae or spinstars. Their frequency increases as metallicity decreases, and they become more prevalent at lower metallicities. In addition to [C/Fe] ratios, CEMP stars can also be classified based on absolute carbon abundances. The Yoon-Beers diagram in Figure 1.9 illustrates this classification, with CEMP-*s* stars in the higher band and CEMP-no stars in the lower band.

1.6 Proposed sites for *r*-process

There are various proposed sites for the nucleosynthesis of *r*-process, but none of them are well constrained. Some of the proposed sites are given below.

1.6.1 Neutrino-driven winds

After the collapse of massive star into a neutron star, a high intensity neutrino flux emerge from hot neutron star. This neutrino flux interacts with the nearby neutron-rich material, and carries the material outward. These neutrino-driven winds are thought to have sufficient neutron density to initiate *r*-process. Although these winds may produce lighter *r*-process nuclei, recent studies suggest that they may not reach the extreme neutron richness required for the heaviest elements. Nonetheless, it remains a plausible source.

Simulations have demonstrated that the hot proto-neutron star enters what is known as the Kelvin-Helmholtz cooling phase, which lasts for about 10s, following the start of the supernova explosion. Neutrinos of different flavours are released during this phase as a result of deleptonization. These neutrinos are essential for producing the neutrino-driven wind, an outflow of matter (Duncan et al. 1986).

1.6.2 Electron-capture supernovae

It is a special kind of supernova which occur in 8-10 $M_{\odot}$ stars with cores composed mostly of oxygen, neon, and magnesium, which do not reach the high temperatures necessary for typical iron-core collapse. As the star ages, electrons in the core are captured by magnesium and neon nuclei, reducing the core's electron pressure and triggering a sudden collapse under gravity. This process leads to a supernova explosion, releasing a burst of neutrons that can create conditions favorable for the r-process (Jones et al. 2014). Although they might not be the primary site for the heaviest elements, they contribute to the diversity of nucleosynthesis processes that enrich galaxies with essential elements (Kitaura et al. 2006; Wanajo et al. 2009, 2011; Mirizzi et al. 2016).

1.6.3 Magnetorotational supernovae with jets

Magnetorotational supernovae or Magnetars are driven by intense magnetic fields (10^{15} G) and rapid stellar rotation (Kasen & Bildsten 2010; Nicholl et al. 2017). In these events, as a massive star's core collapses, its rotation and magnetic fields focus the explosion's energy into narrow jets along the rotational axis. These jets are both highly energetic and extremely neutron-rich, ideal conditions for r-process occurance. Within this environment, atomic nuclei rapidly capture neutrons, building up heavier. The jets eject these newly formed elements into space, contributing to the enrichment of the surrounding interstellar medium. These supernovae are thought to be a viable alternative astronomical source of the r-process.

3D MHD simulations of highly magnetic and rotating massive stars show formation of jet like structures (Marek et al. 2006; Winteler et al. 2012). These simulations show successful production of heavy elements upto third r-process peak.

1.6.4 Collapsars

Collapsars are a unique kind of core-collapse supernovae which formed after the evolution of first generation massive stars. In essence, these are revolving black holes with accretion disks $\approx 0.1\,M_\odot\,\mathrm{s}^{-1}$ that can produce lGRBs or hypernovae, also known as collapsars, under specific circumstances (high magnetic fields). Woosley (1993a) was the first to propose this collapsar model. In thier MHD simulations, Siegel & Metzger (2017); Janiuk (2019); Siegel et al. (2019) claimed that collapsars can eject more than $0.1\,M_\odot$ of r-process material. It will be sufficient to describe the entire pattern of solar r-process abundance. They also observed from their calculations that 1000–10000 core-collapse supernovae are equivalent to one collapsar event.

1.6.5 Neutron star mergers

The 2017 detection of gravitational waves, GW170817, provides strong evidence that neutron star mergers are key astronomical sites for r-process. In such events, as two neutron stars come closer, tidal forces begin to strip material from their surfaces. This neutron-rich material, ejected in the form of tidal spirals during the merger, is known as dynamical ejecta. At the point of merger, the material becomes extremely heated and is expelled as shock ejecta. Following the merger, an accretion disk may form around black hole (BH) or neutron star (NS), which can also release material through winds known as accretion disk outflows.

The r-process production varies with the electron fraction of the ejecta (Y_e). Lower Y_e value indicates neutron rich ejecta which produce larger r-process material. The Y_e value of different ejecta is related with the following inequality equation,

$$Y_{e,\text{dynamical}} < Y_{e,\text{accretion}} < Y_{e,\text{shock}}$$

It means that majority of r-process occur in dynamical ejecta. The NSM can eject about order of $10^{-2} M_{\odot}$ r-process material which is enough to explain observations in the Galaxy.

1.7 Thesis aim

The thesis targets on studying the metal composition of bright metal-poor stars with $V < 13$ mag, falling within the metallicity range of $-3.2 < [Fe/H] < -1.5$. This specific metallicity range encapsulates crucial stages in the MW formation. It is pivotal in understanding the timescales associated with neutron star mergers in comparison to other astrophysical sites. Moreover, this moderate metallicity range also includes globular clusters, which provide significant insights into the connections and counterparts they share with the halo population. Exploring this metallicity regime allows for a better understanding of the connection between different components of the MW, providing detailed picture of the chemical evolution processes.

The selection of target stars is carried out from various surveys, including the LAMOST DR8, HESP-GOMPA, and other archival datasets, ensuring a diverse and representative sample for analysis. Observations were conducted using a range of telescopes, including 10m class telescope GTC, 8.2m class telescopes VLT & KECK telescope, and 2m class telescope HCT. The detailed descriptions of these observational procedures are outlined in chapter 2 of the thesis.

The primary focus of the thesis work involves obtaining high-resolution spectra of metal-poor stars and conducting detailed abundance analyses to interpret the results. Specifically, the thesis investigates abundance trends in r-process-rich stars, aiming to constrain their astrophysical sites. Additionally, kinematic analyses of metal-poor stars were performed to discern their birth environments, providing insights into their formation mechanisms.

Furthermore, the thesis work resulted in the discovery of numerous RPE stars, CEMP stars, and spectroscopic binary systems, contributing significantly to the understanding of stellar populations in the halo. Comparative analyses of heavy and light element abundances among different halo stars were conducted to elucidate the nature of first stars and their impact on galactic chemical evolution.

1.8 Thesis outline

Chapter 1: Introduction: It presents a concise introduction to the MW, including its substructure and models of galaxy formation. It also covers fundamental aspects of stellar evolution and nucleosynthesis, focusing on metal-poor stars and their classifications. Additionally, the chapter outlines the objectives and structure of the thesis.

Chapter 2: Methodology and Techniques: Observational facilities data reduction and analysis tools are described in this chapter. We use observations from the Himalayan Chandra Telescope (HCT) of more than 40 metal-poor stars that were pre-selected from the Large Sky Area Multi-Object Fibre Spectroscopic Telescope (LAMOST) survey. Some data used in the thesis are collected from observations/archive from 8-10m telescope facilities. We also discuss tools and methods of stellar atmospheric parameters and abundance estimation.

Chapter 3: Decoding the composition of four bright RPE stars: We use the 10m GTC-HORuS spectrograph to obtain accurate abundances of approximately 20 neutron-capture elements, including Osmium and Thorium, for four stars that were enhanced by the r-process event. By analyzing the abundance trends of these stars and comparing them with a comprehensive list of RPE stars from existing literature, we found that α-elements were not produced by the sites of r-process. There was no correlation between alpha abundance and Eu-enhancement. We also observed a mild depletion of α-elements in stars enriched by the r-process (r-II stars), possibly due to the mixing of ejecta that was rich in the r-process and depleted in α-elements. We discovered that Strontium, Yttrium, and Zirconium were co-produced with Europium. Additionally, we found that the ratio of Thorium to Europium decreased as the metallicity increased, which suggests that the production-ratio of the r-process is dependent on metallicity. This finding can be used to improve the accuracy of the thorium-based cosmochronometer, where the production ratio is considered constant for all metallicities.

Chapter 4: Differential abundance analysis of RPE stars: The main motivation of this chapter is to derive the precise abundances of r-I and r-II stars using differential abundance technique to show whether the two classes of stars can be explained by single astrophysical site for n-capture production with different dilution factors. We found that the differential abundances of light, α elements and Fe-peak elements are close to zero and there is no clear odd-even trend, confirming same origin. However, the light neutron-capture elements show higher differential abundances than the main-peak elements indicating a single site cannot produce whole r-process pattern. We show that simple dilution cannot explain the observed differential abundance pattern. To explain the observed pattern, we have proposed several scenarios. For further confirmation of the observed results, we calculated mean abundance pattern of r-I and r-II stars from literature and showed that the observed results are consistent for their average abundance

Chapter 5: Elemental trends of RPE stars in different Galactic components:

This chapter focuses on the kinematics of RPE stars to investigate the r-process enrichment in different Galactic components. We calculate the orbital parameters of a sample of 488 metal-poor RPE stars ($[Fe/H] < -1.0$) from the literature and associate them to bulge, disk and halo components using a physically motivated definition of Galactic components based on apocenter distance(r_a) and maximum absolute vertical height ($z_{\rm max}$) of the orbit. We find that the Toomre diagram does not separate stars in disk and halo components when they are on highly eccentric and/or retrograde orbits. Disk and halo share a similar fraction of RPE stars in contrast to the earlier perception that the majority of RPE stars belong to the halo. We found all the most probably accreted stars are from halo. However, 3/4 stars lies in mixed-zone. The inner disk, inner halo and outer halo stars show similar abundance trends of n-capture elements.

Chapter 6: Origin of r-process elements in CEMP-r/s stars using Thorium abundance and probing them using the Clustering algorithms:

Using archival data from the ESO and KECK telescopes, this chapter investigates the similarities between CEMP-r/s stars and r-process stars and explores the origin of thorium in CEMP-r/s stars utilizing machine learning techniques. The research identifies that r-I and r-II stars are not distinctly categorized into two separate groups; instead, an intermediate group exists, likely consisting of diluted or mixed stars. It was also found that CEMP-r/s stars and RPE stars represent distinct classes of objects. The findings suggest that future studies incorporating additional elements and similar methodologies could lead to more precise classifications based on elemental ratios, which would reflect the underlying physical processes rather than relying on arbitrary thresholds.

Chapter 7: New metal-poor stars from HESP-GOMPA survey-II: stellar parameters and abundances: Bright, very metal-poor stars ($V < 12$,

$[Fe/H] < -2.0$) present valuable opportunities for investigating the initial stages of star formation and the chemical enrichment processes across various Galactic components. We conduct abundance analyses of light and neutron-capture elements for 33 recently identified bright metal-poor stars obtained from the HESP-GOMPA survey. These stars were initially selected from low-resolution LAMOST spectra through automated spectrum synthesis. The majority of these targets reside within the metallicity range of -3.2 to -1.5, a critical range where notable shifts in abundance trends of key elements occur, signifying significant milestones in galactic evolution or the emergence of new nucleosynthesis mechanisms. This chapter uncovers numerous RPE stars, carbon-enhanced metal-poor (CEMP) stars, and extremely metal-poor (EMP) stars, and conducts comparative analyses with halo stars to infer the characteristics of their progenitor massive stars. Many of these bright stars with detailed abundances could form benchmark stars for future metal-poor star surveys.

Chapter 8: Conclusions and future work: This chapter provides an overview of the thesis's outcomes and discoveries. Additionally, it outlines the forthcoming endeavors subsequent to the submission of the thesis.

Chapter 2

Methodology

Abstract

In this chapter, we discuss the details of the observation facilities and the data source. We also discuss the data reduction methods and data analysis tools.

2.1 Introduction

Until the detection of gravitational waves, our understanding of the Galaxy (or even the Universe) is based only on the electromagnetic radiation we receive from stellar objects. Different treatments of electromagnetic radiation provide us with different information about stellar objects. In this thesis, I will be focusing on the spectroscopic treatment of the radiation. Spectroscopy helps us reveal the characteristics of stellar objects by dividing radiation into its constituent wavelengths, which is called spectrum. The spectrum of any object contains several dark (or bright) regions known as the absorption (or emission) spectral lines. These spectral lines are like our finger prints as they uniquely represent the composition of that object.

Stellar spectroscopy focuses on these spectral lines to study the mass, temperature, surface gravity, chemical make-up, and more. In the next section, we briefly discuss the astronomical tools used to obtain the spectrum of the stellar objects.

2.2 Telescopes and spectrographs

Being at farther distances, stellar objects look very faint which makes them nearly impossible to study. Thanks to the technological advancements, we have various sophisticated astronomical telescopes around the globe. Telescopes act like a giant artificial eyes to see through the cosmos. The basic concept of an astronomical telescope includes primary and secondary mirrors. To avoid optical aberrations, mechanical complications mirrors are preferred over lens. The big mirror facing towards the sky is called primary mirror and the smaller one which collects light from the primary mirror is called secondary mirror.

The primary mirror of a telescope is the key factor which decide how faint and resolved objects it can see. The faint limit of a telescope (in magnitude) is defined by following expression:

$$m_L = N + 5\log(D), \tag{2.1}$$

where D is the primary mirror's diameter in inches and N is a constant which ranges from 7 to 9 depending on the observer's pupil size, telescope transmittance, etc (Bowen 1947; Garstang 2000). The Larger the value of m_L, the fainter the telescope can see. Similarly, the angular resolution of the telescope at any wavelength λ is defined as,

$$\Delta\theta = 1.22\frac{\lambda}{D}. \tag{2.2}$$

The smaller the value of $\Delta\theta$, the closer objects telescope can resolve.

The light collected by the primary mirror falls on the secondary mirror. Secondary mirror directs the light to instrument of astronomical purpose. Here, we are interested in spectroscopy, therefore, we will discuss briefly a spectrograph.

The basic functionality of a spectrograph is to disperse the light into its constituent wavelength components utilizing a diffracting grating or prism. The grating choice depends on the science case we are interested in i.e., whether we need low dispersion grating or high dispersion grating. The dispersion quality of a spectrograph is quantified by the resolution of the spectrum at any wavelength λ as follows:

$$R = \frac{\lambda}{\Delta\lambda}, \tag{2.3}$$

where $\Delta\lambda$ is the minimum wavelength difference spectrograph can distinguish i.e., its resolving power. For detailed analysis, we use high-resolution spectrograph. The high-resolution spectrograph uses a special type of grating know as Echelle grating.

Figure 2.1 shows the working principle of echelle spectrograph. Unlike traditional gratings where the grooves are spaced at regular intervals, echelle gratings have a relatively large groove spacing in one direction (the "groove direction") and a much finer spacing in the perpendicular direction (the "cross-dispersion direction"). This design allows an echelle grating spectrograph to achieve high spectral

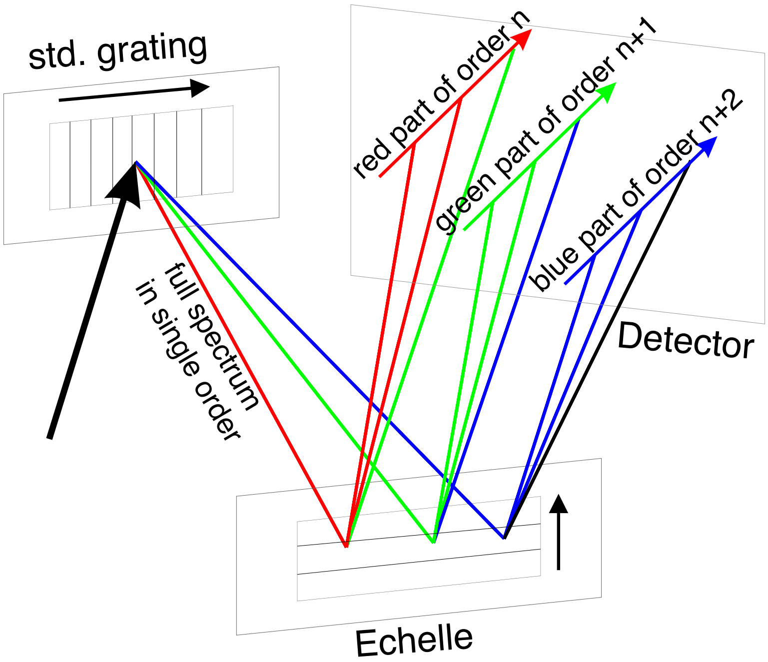

FIGURE 2.1: A schematic diagram of echelle spectrograph. Standard grating disperse the light slightly, then echelle grating disperse it further into perpendicular direction. Picture Courtesy: Wikipedia.

resolution by dispersing the light twice: once along the grooves (the "echelle dispersion") and then again perpendicular to the grooves (the "cross-dispersion"). By combining these two dispersions, echelle spectrographs can achieve very high spectral resolutions over a wide wavelength range.

Next, we describe selection of candidate metal-poor stars and brief overview of observational facilities utilized in this thesis as a part of data acquisition.

2.3 Data acquisition

2.3.1 Candidate metal-poor stars selection

Given the vast number of stars in the Galaxy, a systematic study requires the selection of candidate stars from low-resolution spectroscopic survey for high-resolution follow-up. For this purpose, we make use of existing spectroscopic surveys, such as, SDSS/MARVEL and LAMOST. Our effort in this direction begins in 2017 as a part of HESP-GOMPA (Hanle Echelle Spectrograph Galactic Observation of Metal-Poor stArs) survey. The previous HESP-GOMPA run is based on SDSS/-MARVEL survey and the present run, which is the part of this thesis, is based on the LAMOST survey. The following subsections outline our candidate selection procedure:

Signal-to-noise ratio (SNR) threshold: Our initial selection involve stars exhibiting a SNR greater than 20. This criterion is implemented to mitigate the inclusion of spectra prone to inaccuracies in estimating stellar parameters, thereby ensuring the reliability of our candidate selection process.

Magnitude constraints: A further criterion was imposed based on magnitude, ensuring that selected stars are observable using the Hanle Echelle Spectrograph (HESP), which is stationed at the Himalayan Chandra Telescope (HCT). This step guarantees that our observations align with the capabilities of the instrumentation at our disposal, facilitating subsequent analysis and follow-up observations.

Metallicity threshold: We restricted our candidate selection to stars exhibiting a metallicity below $[Fe/H] < -1.5$. This stringent criterion serves multiple purposes: it enables investigations into the temporal dynamics of neutron

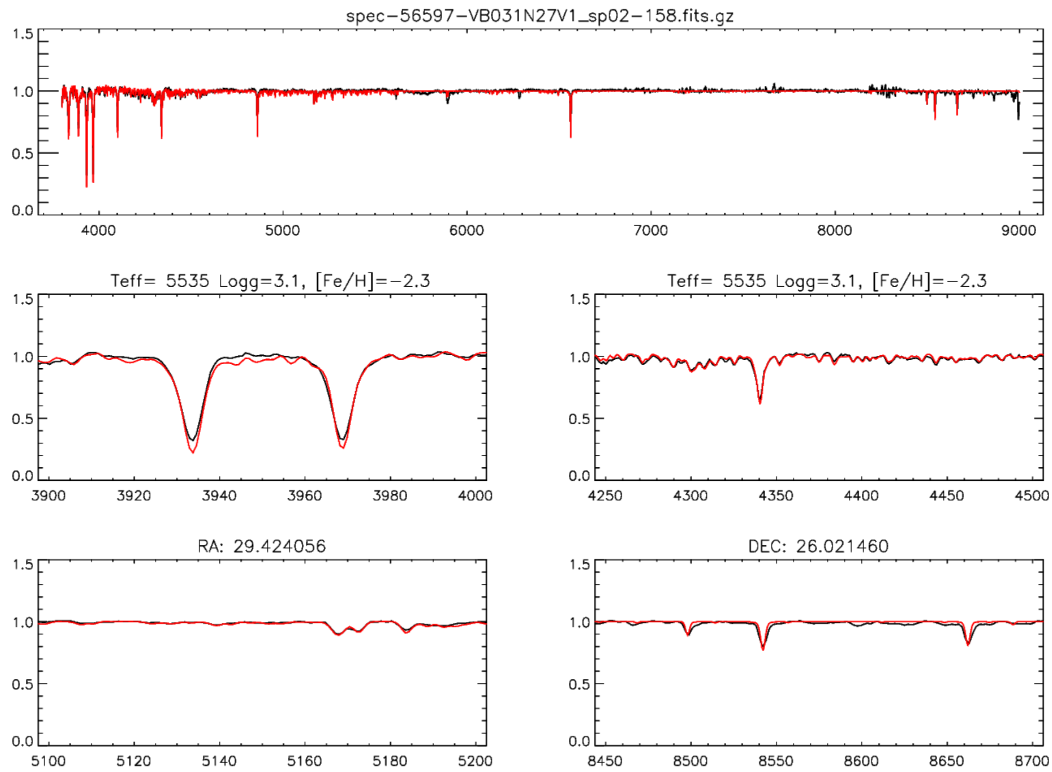

FIGURE 2.2: The overplot showcases LAMOST spectra overlaid with synthetic spectra. The black solid lines represent the low-resolution LAMOST spectra with a resolution of R $\sim$ 1800, while the red solid lines depict the synthesis. The top panel displays the synthesis of whole spectrum, while the middle panel exhibits the overplot of the Ca H and K regions alongside carbon band regions. Finally, the bottom panel illustrates the synthesis of the Mg triplet and Ca Triplet regions.

star merger (NSM) events, facilitates the search for Globular cluster escapees, as these objects typically exhibit similar metallicity, and provides insights into the formation mechanisms underlying different Galactic components.

Spectral fitting: Upon satisfying the aforementioned criteria, we conducted detailed spectral fitting analyses. Figure 2.2 is an example illustrating the spectral fitting applied to one of the LAMOST spectra. Subsequently, approximately 70 new metal-poor candidates were identified for further scrutiny and follow-up observations utilizing the high-resolution spectrograph HESP. This final step ensures the selection of the most promising candidates for in-depth investigation and contributes to expanding our understanding of metal-poor stellar populations.

2.3.2 Observing facilities used

The subsequent list delineates several telescopes alongside their associated instruments utilized to achieve the objectives outlined in this thesis:

GTC/HORuS: The Gran Telescopio CANARIAS (GTC) is one of the largest and cutting-edge optical telescope around the globe. Its primary mirror comprises of 36 hexagonal segments. The light-gathering capacity of the GTC is equivalent to that of a telescope with a 10.4m diameter monolithic mirror. It is situated at the Roque de los Muchachos Observatory on La Palma Island. Its coordinates are Latitude: 28° 45´ 24´´ N and Longitude: 17° 53´ 31´´ W, positioned approximately 2300 meters above sea level [GTC-HORuS website].

The High Optical Resolution Spectrograph (HORuS) is a state-of-the-art instrument integrated into the Gran Telescopio CANARIAS (GTC) at Nysmyth focal plane (Tabernero et al. 2020; Allende Prieto 2021). HORuS works on a remarkable spectral resolution of 25000, spanning the wavelength range from 3800 to 6900 Angstroms. Utilizing a 3×3 integral field unit (IFU) with microlenses, it efficiently gathers light, which is then channeled through optical fibers to form a pseudo-slit at the entrance of the spectrograph. This setup ensures nearly continuous coverage across the spectrum. Since its installation in March 2019, HORuS has significantly enhanced the GTC's suite of instruments, enabling comprehensive spectroscopic observations with unparalleled spectral coverage and resolution. Figure 2.3 shows the HORuS spectrograph.

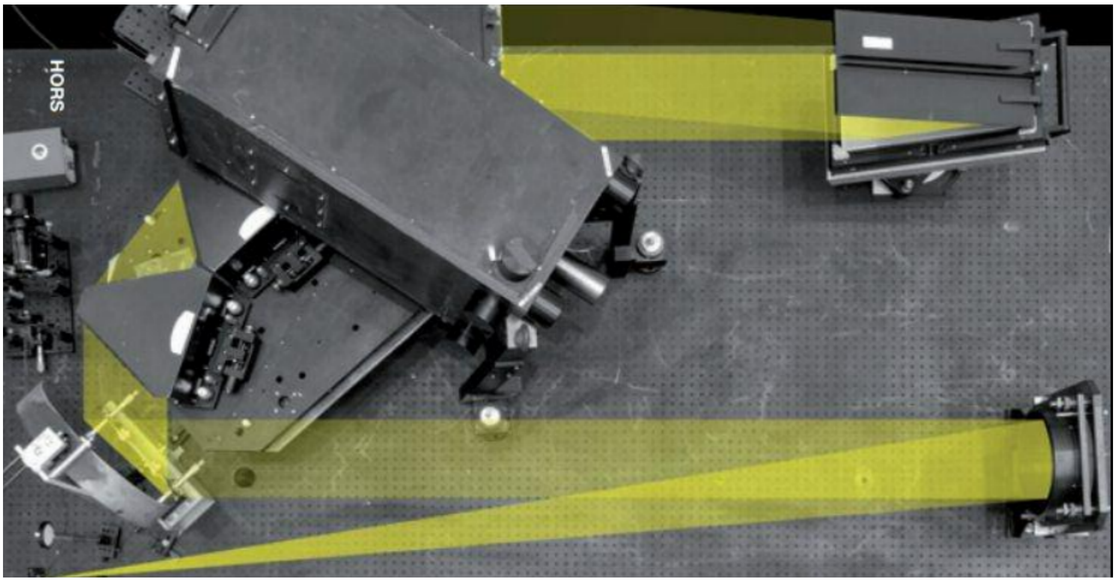

FIGURE 2.3: Figure depicts the High Optical Resolution Spectrograph (HORuS) installed at GTC. Image Credit: [HORuS website]

VLT/UVES: The Very Large Telescope (VLT) is a group of four big telescopes run by the European Southern Observatory. They are perched up on Cerro Paranal in the dry Atacama Desert in Chile. Each of these telescopes, also called Unit telescopes, has a massive mirror that is 8.2 meters across. They go by the names Antu, Kueyen, Melipal, and Yepun, which are all words from the Mapuche language for celestial bodies [VLT-ESO website].

These telescopes can work separately or together to get really sharp images. Besides these, there are also four smaller telescopes called Auxiliary Telescopes (ATs) with 1.8-meter mirrors. The Unit telescopes are built in a specific way called Ritchey-Chrétien design with a Cassegrain-Nasmyth focus. This setup allows them to be used on their own, but when all of them work together, they form what is called the ESO Very Large Telescope Interferometer.

The VLT can see both visible light and infrared light. Each telescope is super sensitive, able to pick up objects that are about four billion times fainter than what we can see with just our eyes. When all four telescopes work together, they can see things with an incredibly sharp detail, about

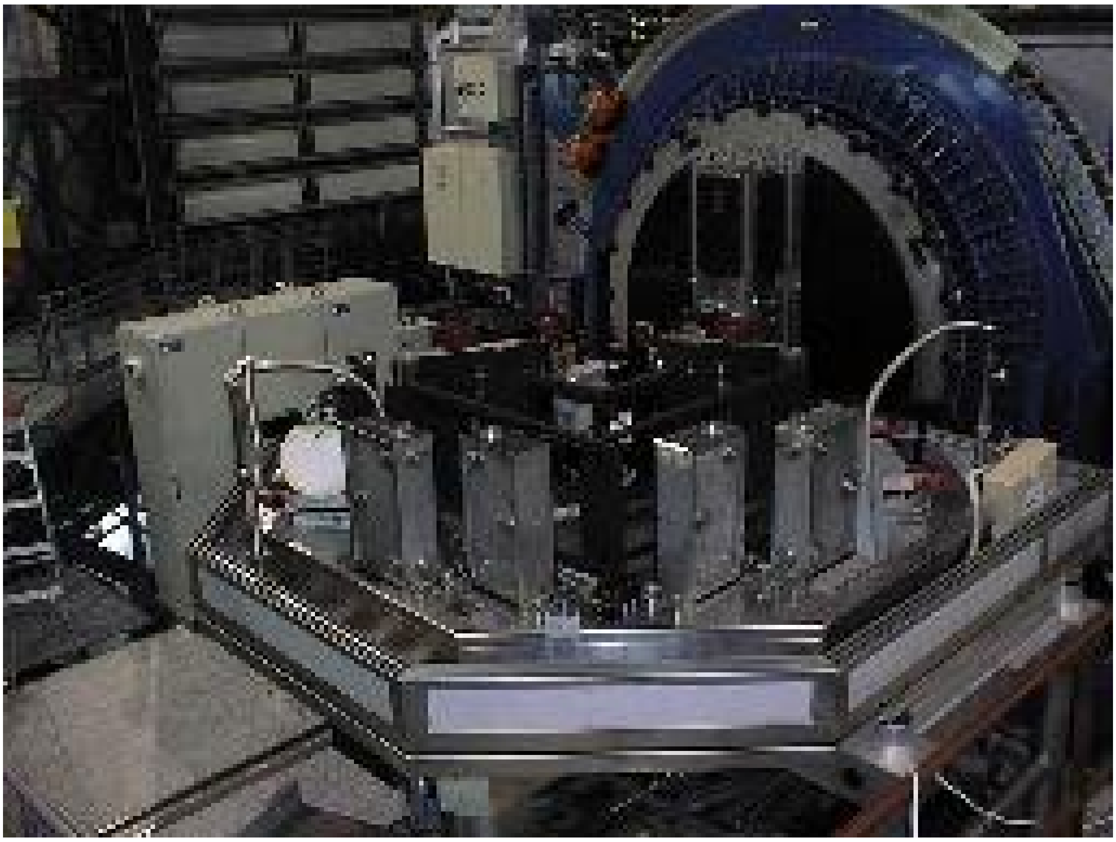

FIGURE 2.4: Figure depicts the UVES installed at VLT of ESO. Image Credit: [UVES website]

0.002 arcsecond. On their own, each telescope can still see quite sharply, with an angular resolution of around 0.05 arcsecond.

Ultraviolet and Visual Echelle Spectrograph (UVES) serves as the high-resolution optical spectrograph stationed at the Nasmyth B focus of UT2 (Kueyen) within the Very Large Telescope. It operates as a cross-dispersed echelle spectrograph. It is designed to efficiently cover a broad wavelength range from 300 to 1100 nanometers, utilizing CCD detectors. The instrument splits the incoming light beam into two arms, dividing the ultraviolet to blue wavelengths and the visual to red wavelengths. These arms can function independently or concurrently using a dichroic beam splitter. UVES achieves notable resolving power of approximately 40,000 with one arcsecond slit. In optimal conditions, the maximum resolution reaches 110,000 in the red arm and 80,000 in the blue arm, utilizing narrow slits [VLT ESO website].

Additionally, UVES features three image slicers to enhance resolution while minimizing slit loss. Notably, the instrument ensures mechanical stability and facilitates precise wavelength calibration. For observations demanding exceptional radial velocity accuracy, an iodine cell can be introduced into the light beam. Figure 2.4 shows the picture of UVES instrument.

HCT/HESP: The Himalayan Chandra Telescope (HCT), also known as the Indian Astronomical Observatory (IAO), sits atop Mt. Saraswati in Ladakh region of India, at a height of 4500 meters above the sea level [IIAP website]. It is managed by the Indian Institute of Astrophysics in Bangalore. The telescope, named in honor of Nobel laureate Subrahmanyam Chandrasekhar, has a diameter of 2.01-meters and employs a modified Ritchey-Chretien system with a primary mirror crafted from ULE ceramic, designed to withstand the extreme cold temperatures it encounters. The telescope houses three scientific instruments: the Himalayan Faint Object Spectrograph (HFOSC), TIFR near-infrared spectrometer and Imager (TIRSPEC), and Hanle Echelle Spectrograph (HESP).

The telescopes Operates even in sub-zero winter temperatures. It is controlled remotely via an INSAT-3B satellite link. This allows its operation from the Centre for Research and Education in Science and Technology (CREST), located approximately 35 kilometers northeast of Bangalore, ensuring continuous astronomical observations despite the harsh conditions.

Hanle Echelle Spectrograph (HESP) is a dual fiber-fed, high-resolution spectrograph with resolving powers of 30000 and 60000 [IIAP Website]. The spectrograph design includes a white pupil concept, enabling continuous spectral coverage, and utilizes a 4K $\times$ 4K detector (single CCD) to capture detailed spectra. With its capability to cover wavelengths from 350 to 1000 nanometers, it enables precise measurements of chemical abundances crucial for understanding stellar evolution. Figure 2.5 shows the instrumental design of the HESP.

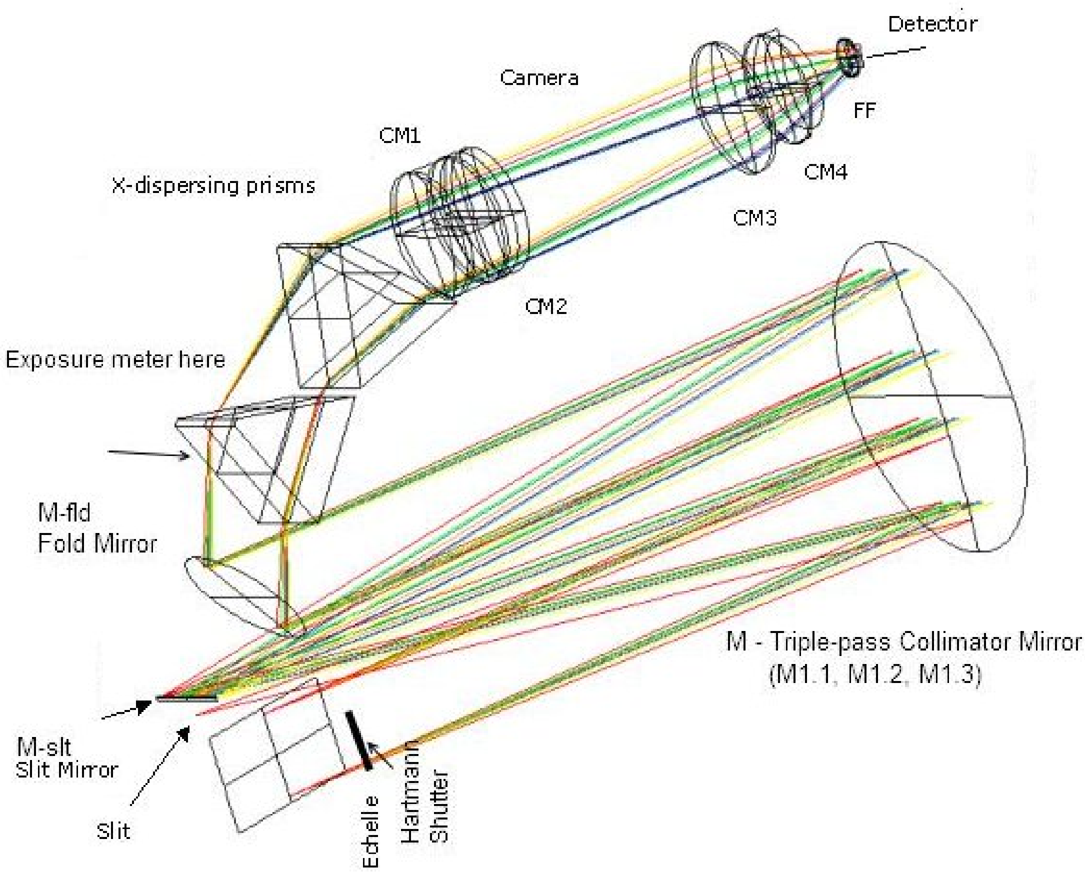

FIGURE 2.5: Figure depicts the Hanle Echelle Spectrograph design mounted on HCT telescope. Image Credit: [HESP website]

Its robust mechanical stability and dual-fiber mode facilitate accurate radial velocity measurements, essential for various research programs like exoplanet studies and astroseismology. Operating with a spectral resolution of 30000 without an image slicer and 60000 with an image slicer, it ensures high precision in radial velocity measurements, achieving an accuracy of 20 meters per second. The spectrograph also maintains an efficiency of over 20 percentage within the wavelength range of 450 to 800 nanometers. It is equipped with observing modes such as Object/ThAr, Object/Sky, and ThAr/ThAr, it can detect objects as faint as V-band magnitude 11 under typical seeing conditions.

To ensure long-term stability, the instrument is thermally controlled with a precision of ±0.1°C at a constant temperature of 16°C throughout the year.

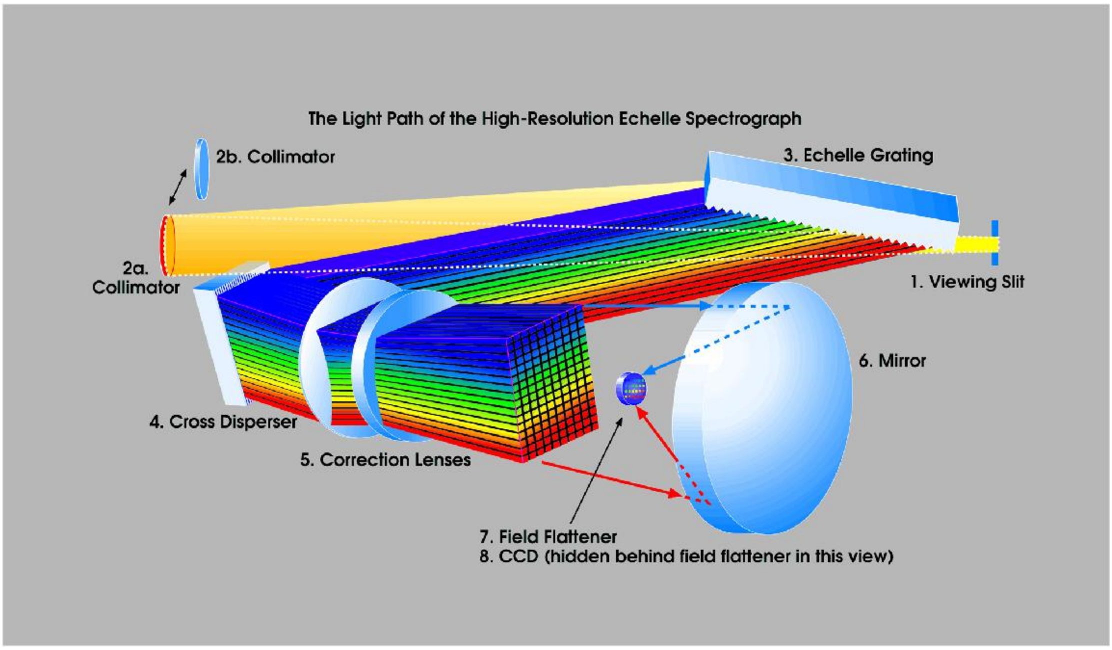

FIGURE 2.6: Spectrograph layout for the High Resolution Echelle Spectrometer. Image Credit: [HiRES website]

This control minimizes systematic errors, maintaining stability at approximately 200 meters per second, further enhancing the reliability and accuracy of observations.

Keck/HiRES: The W. M. Keck Observatory is a leading astronomical facility located at an altitude of 4145 meters near the summit of Mauna Kea in Hawaii, USA. It is Positioned at a longitude of 155 ° 28´ 28´´ W and a latitude of 19° 49´ 35´´ N. It specializes in observing the optical-infrared wavelength region.

Equipped with two telescopes having 10-meter aperture primary mirrors, the Keck Observatory initially held the title of the world's largest optical reflecting telescopes upon completion in 1993 (Keck 1) and 1996 (Keck 2). Each telescope operates on an alt-azimuth mount. It is managed by the California Association for Research in Astronomy, a non-profit organization. The Keck Observatory's oversight includes representation from esteemed institutions such as Caltech and the University of California.

The High Resolution Echelle Spectrograph (HiRES) is permanently installed at the right Nasmyth focus of the Keck-1 telescope and was put into operation in 1993. HiRES was crafted to offer versatility across the optical spectrum, spanning from 300 to 1000 nanometers, achieved through interchangeable optical components optimized for both the blue and red sides of the bandpass. This design allows users to exercise precise control over the imaged spectrum.

In 2004, HiRES underwent a significant upgrade to its detector system. The upgrades have led to significant improvements in several key areas: enhancing the blue/UV response shortward of 3800 Å by approximately eight-fold, expanding the wavelength coverage for a single instrument setting, providing finer sampling of the point-spread function (PSF), and reducing both CCD readout noise and readout time. Figure 2.6 depicts HiRES instrument on the Keck Telescope.

2.4 Preparation of science ready spectra

After observation, we process the raw data for science purpose. It involves the correction of dark, bias, scatter light, cosmic rays, radial velocity, etc. Figure 2.7 shows the steps used in spectroscopic data preparation.

2.4.1 Data Reduction

In this doctoral work, we have adopted the standard data reduction tool IRAF (Image Reduction and Analysis Facility) to transform 2-D raw data into 1-D data suitable for subsequent analysis. This tool offers a range of packages designed to perform tasks and analyze raw data files.

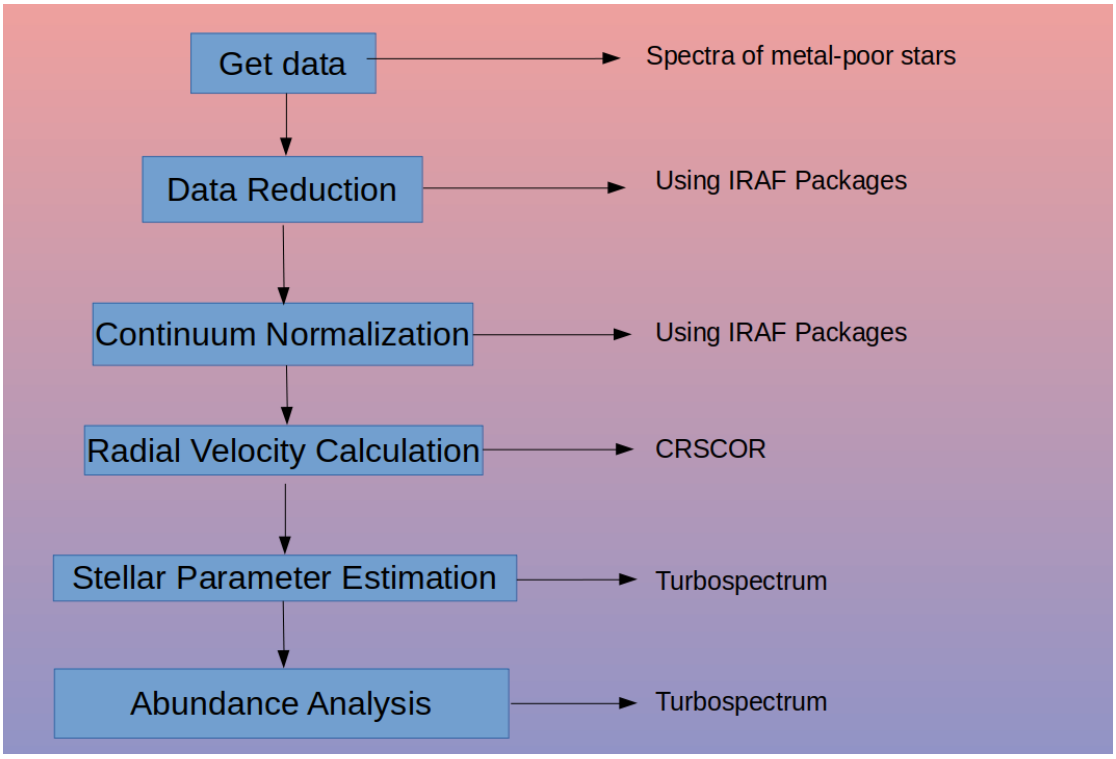

FIGURE 2.7: Flow chart of the spectroscopic data analysis.

The data captured by the CCD is influenced by various factors such as effect of atmosphere, the sensitivity of CCD and spectrograph optics. To mitigate these effects, additional image frames are obtained alongside the object frames. These frames, which include bias, flat, and dark frames, serve to minimize the impact of such disturbances on the final spectra. Before analysis, all image frames undergo trimming to isolate the area containing only useful data.

To eliminate the thermal noise from the CCD, we acquire dark frames with exposures matching those of the object frames during observation. These frames are captured when the CCD is shielded from light, with the shutter closed. Additionally, bias frames are obtained with zero exposures to correct the detector's zero level. These bias frames are median combined to create a master bias utilizing the $ZEROCOMBINE$ task.

Many spectroscopic datasets contain areas that are not exposed to light, known as overscan regions, typically found at the edges of the image. To enhance spectral quality, these regions are trimmed from all images using the $CCDPROC$ task in IRAF.

Since the sensitivity of light varies across each pixel, we capture flat frames by exposing the CCD to a continuous light source such as a halogen lamp. All flat frames are then combined using the $FLATCOMBINE$ command. Subsequently, we subtract master bias from all frames (flat, object, and dark frames) using the $IMARITH$ task. The scattered light from both object and flat frames is further subtracted using the $APSCATTER$ task.

Next, the bias-subtracted master flat files are normalized using the $APNORM$ task. Then, object frames are divided by these normalized flat frames using $CCDPROC$ task. Subsequently, we extract the spectra using the $APALL$ command, resulting in spectra in the form of counts vs pixels.

To convert these spectra into a wavelength vs flux format, we capture a Th-Ar arc spectrum. Using the $ECIDENTIFY$ task and an identification atlas, we identify the lines in the extracted Th-Ar spectrum. The $REFSPEC$ task is used to wavelength-calibrate the object frames by utilizing these arc frames as references. After calibration, the $DISPCOR$ task is applied to correct the dispersion of the wavelength-calibrated images.

Finally, the spectra undergo continuum fitting using the $CONTINUUM$ task, rendering them ready for further analysis.

2.4.2 Radial Velocity

Due to the motion of the objects with respect to the observer, their spectra shifts from the original. This shift in the spectra is known as Doppler shift, and the component of object's velocity along the observer's line-of-sight is referred to as radial velocity (RV). For Doppler correction of the spectra, we measure RV using following relation:

$$v_r = \frac{\lambda_{\text{obs}} - \lambda_{\text{lab}}}{\lambda_{\text{lab}}} \times c, \tag{2.4}$$

where 'c' is light speed. λ_{obs} and λ_{lab} indicates the observed and laboratory wavelengths respectively. A negative radial velocity indicates motion towards the observer, while a positive value suggests movement away from the observer.

To determine the radial velocity, we conduct cross-correlation between observed and synthetic spectra with IDL routine, *CRSCOR*. The RV obtained is then adjusted for heliocentric motion with the *RVCORRECT* task within IRAF. Subsequently, the continuum-fitted spectra undergo RV correction with the *DISPCOR* task within IRAF, preparing them for science purpose.

2.5 Characterization of stellar atmosphere

2.5.1 Linelist

The light coming from stellar interior interacts with the stellar atmosphere. Thus, different elements present in the stellar atmosphere give rise to different atomic transitions and spectral lines form. Boltzmann equation describes population density of an atom in two energy states:

$$\frac{n_2}{n_1} = \frac{g_2}{g_1} \exp\left(-\frac{E_2 - E_1}{kT}\right) \tag{2.5}$$

where:

n_1, n_2: Number of atoms in lower and higher energy state

g_1, g_2: Degeneracy of lower and higher energy state

E_1, E_2: Energy of lower and higher energy state

k: Boltzmann constant

T: Temperature,

and its population density in two ionization states is determined by Saha equation:

$$\frac{n_{i+1}}{n_i} = \frac{2}{n_e} \left(\frac{2\pi m_e kT}{h^2}\right)^{3/2} \frac{Z_{i+1}}{Z_i} \exp\left(-\frac{\chi_i}{kT}\right) \tag{2.6}$$

where:

n_i, n_{i+1}: Number density of ions in i-th and (i+1)-th ionization stage

n_e: Number density of electrons

m_e: Mass of an electron

k: Boltzmann constant

T: Temperature

h: Planck constant

Z_i, Z_{i+1}: Partition function for i-th and (i+1)-th ionization stage

χ_i: Ionization energy of the i-th ionization stage.

The intensity of a spectral line relates with the number of atoms available in the stellar atmosphere. Therefore, when we have science ready spectrum, we identify the spectral lines of different elements and measure their strength in terms of the equivalent width. It is the measure of a rectangle's width whose height equal to the line's continuum level and area equal to that enclosed by the line. Mathematically,

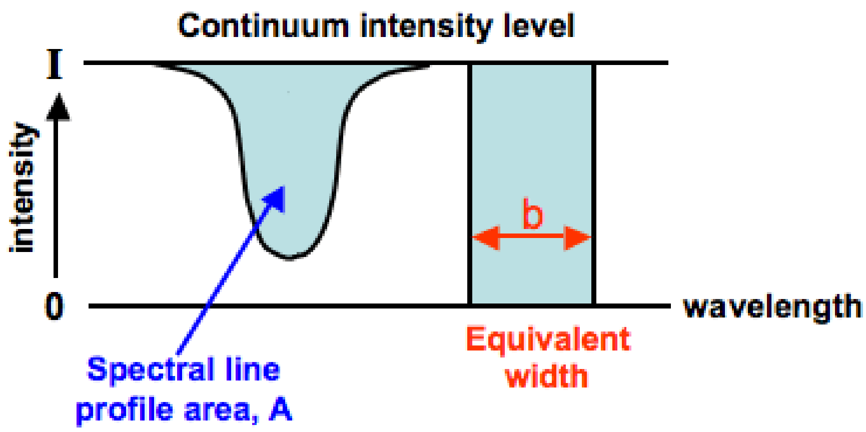

FIGURE 2.8: Figure depicts the definition of equivalent width. Image Credit: [Equivalent width website]

it is expressed as

$$W_\lambda = \frac{1}{F^c_\lambda} \int_{\lambda_1}^{\lambda_2} (F^c_\lambda - F_\lambda) d\lambda, \tag{2.7}$$

where F^c_λ, and F_λ respectively represent flux at the continuum, and at the wavelength λ. Figure 2.8 illustrates the definition of the equivalent width. Higher equivalent width indicates strong line.

We consider following precautions while selecting lines for measuring equivalent widths:

1. Blended and asymmetric lines are avoided, due to potential contamination by other lines or species.

2. Lines without clear continua are avoided, due to the difficulty of modeling the overly crowded regions of the spectrum.

3. Lines with equivalent widths below 10 mÅ and above 120 mÅ are avoided; below 10 mÅ the lines are often dominated by noise, and above 120 mÅ they can approach saturation.

The final linelist consists of the central wavelength, equivalent width, and some theoretical/experimental parameters that characterize the line formation such as lower excitation potential, oscillator strength, etc.

2.5.2 Model atmosphere

For a systematic analysis of the stellar spectrum, we generate theoretical model atmosphere. These models are based on various crude assumptions listed below.

Plane parallel: Despite stars being spherical, we assume a plane parallel atmosphere due to the fact that the photosphere's thickness (ΔR) is significantly smaller than stellar radius (R) i.e., $\frac{\Delta R}{R} << 1$.

Homogeneity: The effect of granules, spots, and other stellar activities are not considered. The stellar atmosphere is assumed homogeneous.

Steady state: We consider a steady atmosphere ignoring the rotation, pulsation and other dynamic activities.

Radiative equilibrium: The energy generated in the core of the star leaves the photosphere maintaining a constant flux at any depth. This flux is given by Stefan-Boltzmann law

$$F = \sigma T_{eff}^4, \tag{2.8}$$

where $\sigma = 5.67 \times 10^{-8}\ W\ m^{-2}\ K^{-4}$ is Stefan-Boltzmann constant.

Hydrostatic equilibrium: Pressure supports the gas against gravitational collapse.

$$\frac{dP}{dr} = -\rho g, \tag{2.9}$$

where ρ is the gas density and g is the gravity.

Local Thermodynamic Equilibrium: Although temperature varies across the atmosphere, a local thermodynamic equilibrium (LTE) can be assumed within a small region of unit optical depth. This assumption simplify the representation to a single temperature and optical depth.

2.5.3 Codes used for modeling

Model atmosphere code - ATLAS9: In this thesis work, we have used ATLAS9 for stellar atmospheric models. ATLAS9 models, developed by Kurucz (1993b) and Castelli & Kurucz (2003), provide a comprehensive grid of stellar atmospheric models. These models utilize a set of pre-calculated tabulated opacity data known as Opacity Distribution Functions (ODF) to handle line opacity. With 72 plane parallel layers ranging from $log\tau_{Ross} = -6.875$ to $+2.00$ at intervals of $\Delta\log\tau_{Ross} = 0.125$, each layer encompasses various crucial parameters. These include mass depth, temperature, gas pressure, electron density, absorption coefficient, radiation pressure, microturbulent velocity, convective flux, convective velocity, and sound velocity.

Spectrum synthesis code - Turbospectrum: For spectrum synthesis, we have utilized Turbospectrum (Alvarez & Plez 1998; Plez 2012). It enhances the spectral generation process by evaluating continuous opacities and solving radiative transfer equations through an opacity sampling technique. It is capable of efficiently managing millions of spectral lines within a reasonable computational time frame. By inputting the desired models, Turbospectrum synthesizes stellar spectra, calculating radiative transfer equations based on specified parameters such as temperature, gravity, metallicity, and microturbulent velocity.

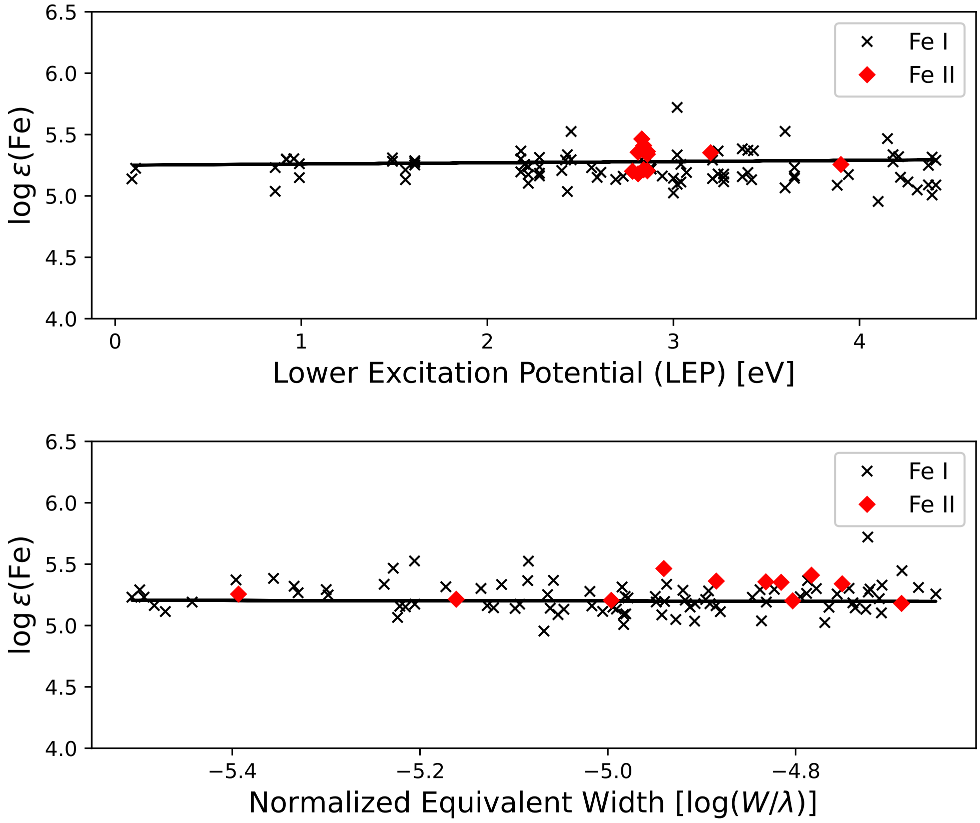

FIGURE 2.9: The top panel illustrates the variation in iron abundance with respect to lower excitation potential (LEP). Meanwhile, the bottom panel displays the iron abundance plotted against the normalized equivalent width.

2.5.4 Stellar parameters estimation

Stellar atmosphere is mainly characterized by four basic parameters: effective temperature (T_{eff}), surface gravity ($\log g$), micro-turbulence (ξ), and metallicity ($[Fe/H]$).

Effective temperature: To estimate the temperature using photometric methods, we employ color-temperature calibration equations derived by Alonso et al. (1999). Utilizing photometric magnitudes from SIMBAD, we calculate the photometric temperature for our program stars as an initial guess for deriving the spectroscopic effective temperature.

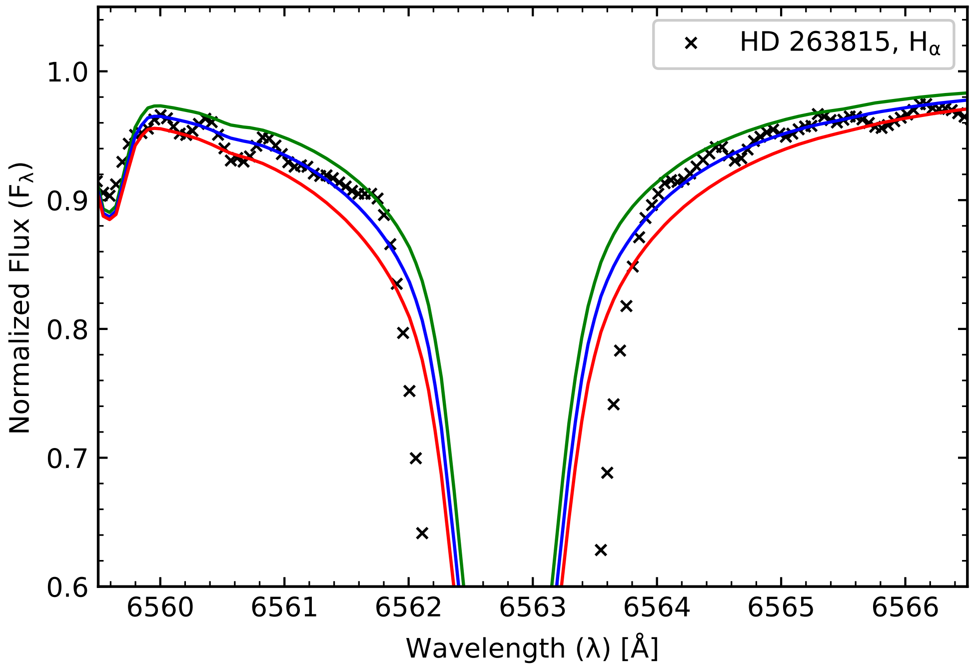

FIGURE 2.10: The H-alpha wing fitting results for one of our program stars. The blue color corresponds to the best fit achieved at a temperature of 4700 K. Additionally, deviations of ±150 K from the best fit are highlighted in green and red colors, providing insight into the sensitivity of the fit to variations in effective temperature.

The spectroscopic effective temperature was determined using the excitation balance method, ensuring the slope of abundances from Fe I lines versus excitation potentials is zero. Figure 2.9 shows the spectroscopic method for estimating effective temperature for one of our program star.

The Hα line is also utilized in determining temperature, as its wings are highly sensitive to small variations in temperature. Figure 2.10 shows the fitting of H_α wings for estimating effective temperature. Additionally, we employed VOSA SED fitter (Bayo et al. 2008) *, to determine temperatures using available photometry. Figure 2.11 is an illustration of SED fitting for one of our program star.

Surface gravity: Stellar surface gravity is estimated presuming the ionization balance of an element, i.e., by forcing the abundance of an element in its

*http://svo2.cab.inta-csic.es/

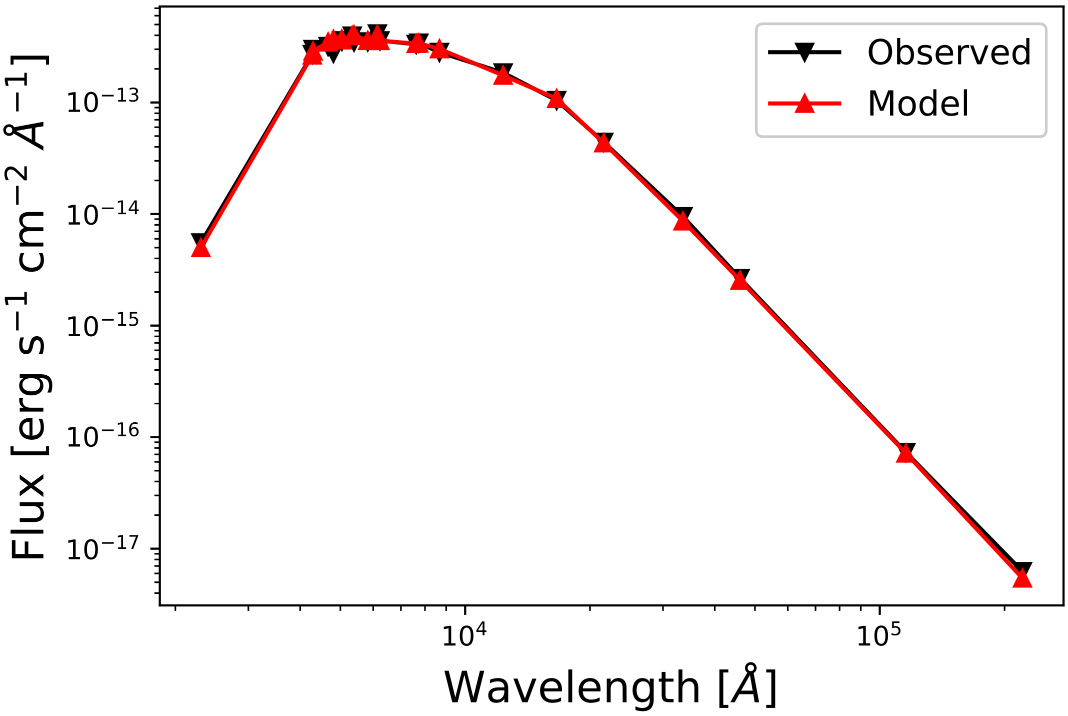

FIGURE 2.11: Estimation of temperature through Spectral Energy Distribution (SED) fitting for one of our program stars. The observed SED is denoted by black downward triangles connected by a black line, while the fitted SED is indicated by red upward triangles along with the corresponding red curve.

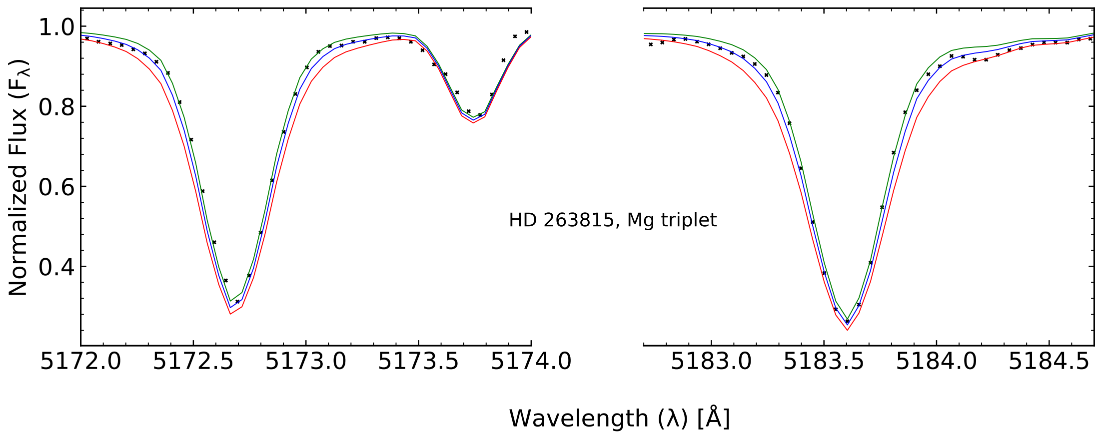

FIGURE 2.12: The Mg-triplet wing fitting results obtained for one of our program stars are illustrated in the figure. The best-fit line is represented in blue, while ±0.3 dex variations from the best fit are highlighted using green and red lines.

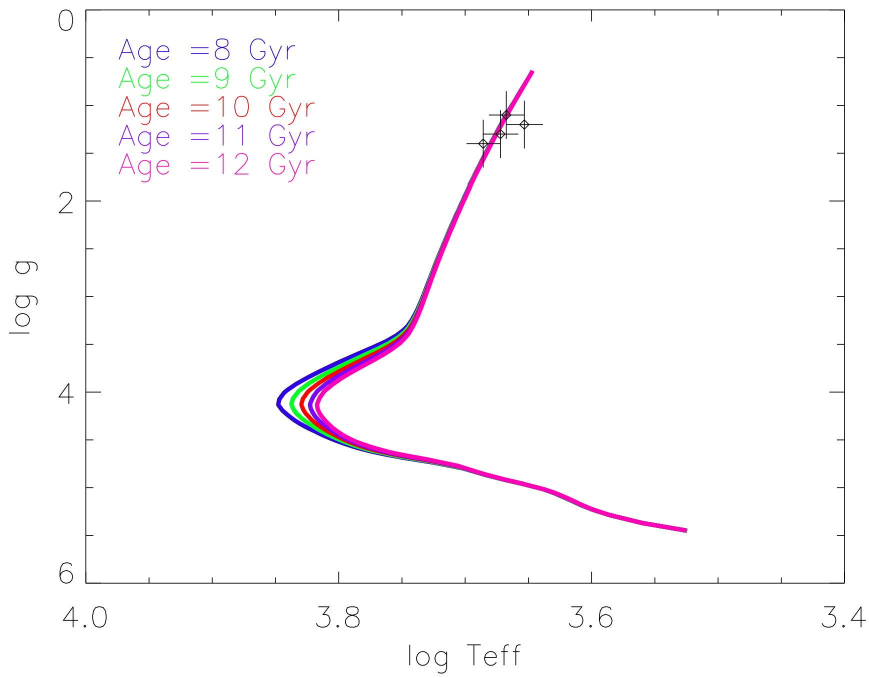

FIGURE 2.13: The plot illustrates the relationship between surface gravity ($\log g$) and effective temperature ($\log T_{eff}$) for the program stars. Each black diamond represents a program star, with measurement uncertainties indicated. The colored curves correspond to isochrones spanning ages from 8 to 12 Gyr.

neutral state (Fe I) and ionized state (Fe II) to be equal by changing surface gravity. We have also shown the fitting of the Mg triplet profile (5167 Å, 5172 Å, 5187 Å), as the wings are highly sensitive to small changes in surface gravity. See Figure 2.12 for the fitting of Mg-triplet wings. We have also placed the stars on the evolutionary track for the consistency check. In Figure 2.13, we show the placement of some of our program stars on the surface gravity ($\log g$) vs effective temperature ($\log T_{eff}$) plane along with the theoretical isochrones ranging in age from 8 to 12 Gyr. These isochrones are obtained from the CMD 3.6 website, which uses PARSEC and COLIBRI tracks (Bressan et al. 2012; Marigo et al. 2013).

Micro-turbulence: To calculate the micro-turbulence velocity, we force the abundance of neutral iron lines (Fe I) to be independent of reduced equivalent

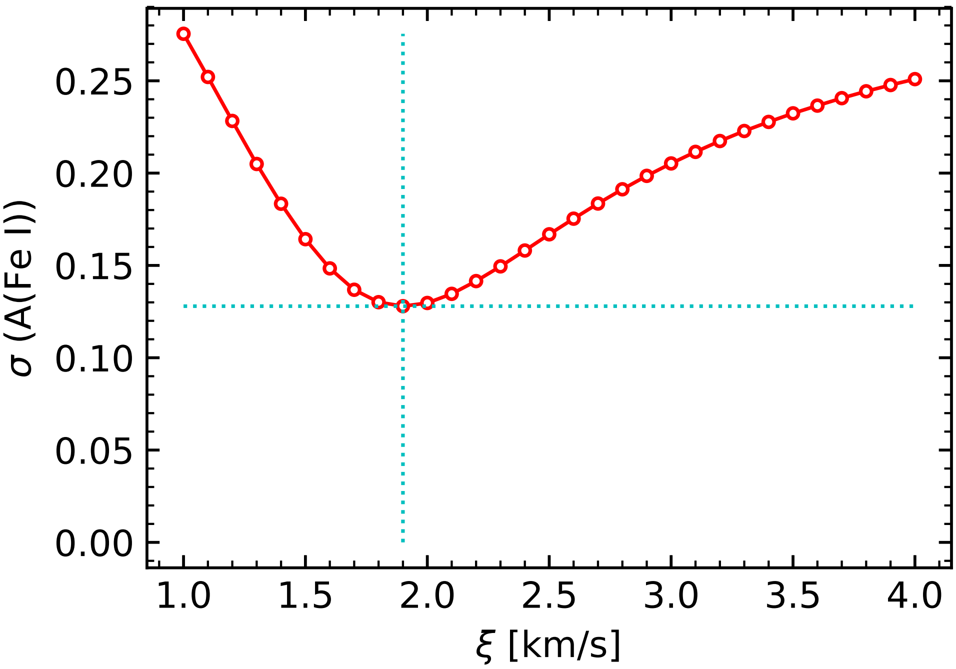

FIGURE 2.14: This figure showcases micro-turbulence velocity estimation using dispersion in the abundances of Fe I lines for a program star. The crossing point of vertical and horizontal lines indicates the minimum of the distribution. The micro-turbulence value corresponding to this crossing point is considered as the estimate in the stellar atmosphere.

width ($\log[EW/\lambda]$). The bottom panel of Figure 2.9 illustrates the micro-turbulence measurement method. For an consistency check, we also calculate an estimate of the micro-turbulence velocity using the method described in Şahin & Lambert (2009), Reddy et al. (2012), and Molina et al. (2014a), which makes use of the dispersion in the abundance of an element. The value of micro-turbulence where the dispersion becomes a minimum is taken as the micro-turbulence velocity of the atmosphere. For this analysis, we used the abundances of Ti, Cr, Fe, and V species, depending on the presence of significant count of clean lines in the spectra. For example, Figure 2.14 displays the dispersion in the elemental abundance of Fe I lines for one of our program stars. The minimum of the distribution is the estimated micro-turbulence velocity in the stellar atmosphere.

Metallicity: In astronomy, metallicity refers to the abundance of elements heavier than helium (He). Despite oxygen (O) being one of the most abundant elements in the universe after hydrogen and helium, the abundance of iron is used to assess a star's metallicity. This preference arises from the ubiquitous presence of iron lines in the optical spectrum, facilitating precise and accurate measurements of metal abundance. Metallicity is denoted by the notation [Fe/H], indicating the abundance of iron relative to hydrogen. It is measured as the average of Fe I and Fe II abundances from all the lines used.

2.6 Elemental abundance measurement

One of the primary objectives in stellar spectroscopy is to accurately determine chemical abundances, crucial for understanding the GCE. The essential prerequisites for this analysis include a comprehensive line-list and a well-defined model atmosphere. The process involves indirect methods based on spectral line intensities, comparing observed data with theoretical models. The accuracy of these comparisons relies heavily on the postulates of model atmosphere generation and line formation modeling. There are two methods to measure the abundances of elements, facilitated by the Turbospectrum software:

2.6.1 Equivalent width method (EW Method)

Spectral lines without blending are selected from the spectra, and their equivalent widths are computed utilizing IRAF task *SPLOT*. This task employs a Gaussian fitting approach to determine the profile's width. To enhance measurement accuracy, equivalent widths were measured three times, and the median of these values are considered the final equivalent width. These calculated equivalent widths serve as inputs for synthetic spectrum generation codes, which then compute abundances using the input equivalent widths.

2.6.2 Spectral synthesis method

This method entails generating a grid of synthetic or lab spectra using model atmospheres and radiative transfer codes, each corresponding to different abundances of the element of the interest. Then observed spectrum is compared with this grid, and the best-fit model abundance is determined using a χ^2 minimization technique. The χ^2 value is calculated using the following formula:

$$\chi^2 = \frac{1}{\mathrm{DOF}} \sum_{i=1}^{m} \left(\frac{O_i - S_i}{\sigma_i} \right)^2 , \tag{2.10}$$

where, DOF (degrees of freedom) represents the number of data points minus the number of parameters being estimated. O_i is the observed flux at the ith pixel. S_i is the synthetic flux at the ith pixel, calculated from the model spectra. σ_i is the scatter associated with the observed flux at ith pixel.

The χ^2 value is computed for the whole grid of spectra. The goal is to find the model spectrum that minimizes χ^2, indicating the best match between spectra. The abundance of the model spectrum which minimizes χ^2 is considered as the abundance of the element. The flow-chart in Figure 2.15 shows the steps involved in the spectrum synthesis method for abundance measurement.

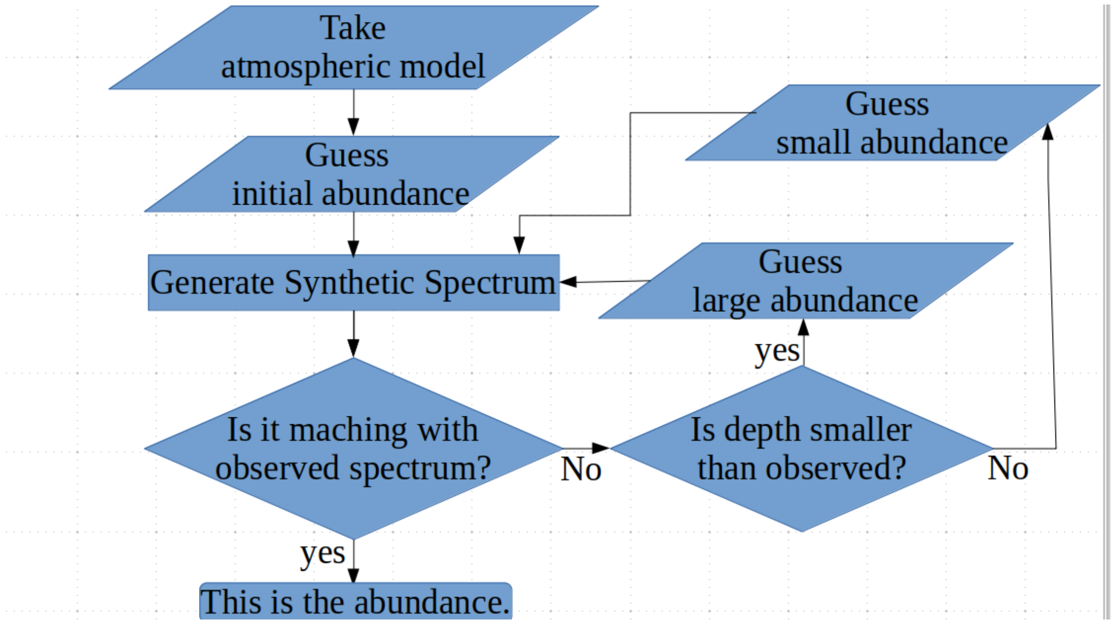

FIGURE 2.15: Flowchart describing steps used in the spectrum synthesis method.

2.6.3 Uncertainties in abundance calculation

The total error in the abundance analysis comprises random and systematic errors. The random error comes particularly from the uncertainty in EW measurement, oscillator strength, and contribution of blends. However, the systematic error appears due to uncertainty in stellar parameter estimation. The sum of all the errors in quadrature returns total uncertainty in the abundance.

$$\begin{aligned} \sigma^2_{\log\epsilon} &= \sigma^2_{\rm rand} + \sigma^2_{\rm sys} \\ \sigma^2_{\log\epsilon} &= \sigma^2_{\rm rand} + \left(\frac{\partial \log\epsilon}{\partial T}\right)^2 \sigma^2_T + \left(\frac{\partial \log\epsilon}{\partial \log g}\right)^2 \sigma^2_{\log g} \\ &+ \left(\frac{\partial \log\epsilon}{\partial \xi}\right)^2 \sigma^2_\xi + \left(\frac{\partial \log\epsilon}{\partial [Fe/H]}\right)^2 \sigma^2_{[Fe/H]} \end{aligned} \tag{2.11}$$

where $\sigma^2_{\rm rand}$ and $\sigma^2_{\rm sys}$ are the random and systematic errors, respectively. If we use N lines to measure the abundance of a species, its random error is defined as $\sigma/\sqrt{N}$. The typical errors in the stellar parameters are considered ($\sigma_{T_{\rm eff}}$, $\sigma_{\log g}$, σ_ξ, $\sigma_{\rm [Fe/H]}$) $\approx$ ($\pm$150 K, $\pm$0.25 dex, $\pm$0.25 km s^{-1}, $\pm$0.1 dex).

We estimate the uncertainties in abundance by adjusting each stellar atmospheric parameter individually to its respective uncertainty, while keeping all other parameters constant, and then calculating the resulting changes in the abundances.

Chapter 3

Decoding the compositions of four bright *r*-process enhanced stars with GTC

Abstract

Metal-poor stars with peculiar abundance patterns give the possibility of studying the nature of progenitor stars that polluted them. RPE metal-poor stars are rare, and these numbers have increased recently through the RPA collaboration. However, detailed abundance data covering various neutron capture peaks remain limited. Variations in the r-process pattern and third peak element abundances are expected to provide further insights into the nature of these sites. In this study, we conduct a thorough abundance analysis of four bright RPE metal-poor stars

identified in the HESP-GOMPA survey, using a high SNR data from the HORuS spectrograph at the 10-m class Gran Telescopio CANARIAS (GTC) telescope in Spain. We derive abundances for 21 neutron-capture elements, including osmium and thorium. Thorium (Th) detection in two stars enables age estimation. We delve into the metallicity evolution of select elements in r-II and r-I stars, along with compiled data from the literature. The trend in Sr, Y and Zr abundance relative to europium suggests a possible need for an additional production site for these elements. Furthermore, we suggest a potential time delay between r-II and r-I star formation based on [Mg/Th].

3.1 Introduction

Studying heavy elements formation stands as one of the important topics in stellar astronomy. The rapid r-process has been recognized as one of the prominent mechanisms driving the synthesis of heavy elements (Burbidge et al. 1957; Cameron 1957). Yet, despite advancements, the precise r-process sites in the Galaxy remain elusive. Very metal-poor (VMP: $[Fe/H] \leq -2.0$) stars preserve the nucleosynthesis signatures of the first generations of stars in the galaxy (Beers & Christlieb 2005a; Frebel et al. 2005; Frebel & Norris 2015b). Hence, detailed high-resolution spectroscopic analysis of VMP stars, polluted by fewer progenitor stars, allows more insights into their formation and the origins of their elements.

Beers & Christlieb (2005a) categorized the RPE stars into two groups, namely r-I and r-II (see Table 1.1). These distinctions rely on europium (Eu) as r-process tracer due to its dominant synthesis in r-process and the presence of strong transitions in the optical spectra. The inclusion of barium (Ba) serves to mitigate potential contamination from s-process contribution. Another subset within RPE stars is the limited-r category (see Table 1.1), introduced to address the dispersion observed among first r-process peak elements (Sneden et al. 2000a; Travaglio et al. 2004b; Frebel 2018b). Among all identified metal-poor stars (up to [Fe/H] ≈ -1.0), limited-r constitute only about 2 %, while r-I and r-II stars account for $\sim 15\%$ and $\sim 5\%$, respectively (Frebel et al. 2016). Presently, the known population includes 46 limited-r, 426 r-I, and 155 r-II (Gudin et al. 2021; Shank et al. 2023).

Numerous potential sources for the r-process production have been proposed. These include neutrino-driven winds in Type-II supernovae, (Takahashi et al. 1994; Arcones et al. 2007; Wanajo et al. 2018), the prompt explosion of low-mass supernovae (Wheeler et al. 1998; Sumiyoshi et al. 2001; Wanajo et al. 2003), NS-NS or NS-BH mergers (Lattimer & Schramm 1974b, 1976; Symbalisty & Schramm 1982; Meyer 1989; Goriely et al. 2011; Rosswog et al. 2014; Bovard et al. 2017), and collapsars (Woosley 1993b; Fujimoto et al. 2008b; Siegel et al. 2019). However, each of these scenarios presents challenges. For instance, the neutrino-driven winds in Type-II supernovae tend to excessively generate elements around atomic mass A$\sim$90 and require entropy levels higher than those predicted by hydrodynamical simulations (Takahashi et al. 1994). The problem with the prompt explosions of low-mass supernovae model is whether it really explodes or not (Bethe 1990; Sumiyoshi et al. 2001). Furthermore, collapsars is considered a promising site for r-process-element production (Siegel et al. 2019). Nevertheless, all proposed sites face limitations yet to be validated by observations and simulations. Consequently, the astrophysical sites or sites responsible for r-process enrichment remain a topic of interest.

Observations of the electromagnetic counterparts of NS-NS mergers detected by the LIGO–Virgo collaboration exhibited a kilonova-like behaviour (Arcavi et al. 2017; Tanvir et al. 2017). Notably, the excess red emission observed in the kilonova lightcurve, coupled with the identification of a distinct strontium (Sr) spectral feature, serves as compelling evidence supporting neutron star mergers as prominent sites for r-process (Chornock et al. 2017; Drout et al. 2017; Metzger 2017; Shappee et al. 2017; Tanaka et al. 2017; Villar et al. 2017b; Watson et al. 2019). A single neutron star merger (NSM) event can enrich a large number of objects with r-process element ejecta, as observed in Reticulum II (Ret II) galaxy (Ji et al. 2016, 2022; Roederer et al. 2016a). Study by Ji et al. (2022) indicate that more than 70 % of stars in Ret II, subject to high-resolution spectroscopic scrutiny, exhibit pronounced enrichment by r-process elements. However, there remain several difficulties in our understanding. The long delay between the first supernovae explosions that produce Mg, Fe-peak elements, and ejection of r-process material from NSMs, for instance, does not support the observed r-process enhancement by NSM in a pristine galaxy (Wehmeyer et al. 2015; Tarumi et al. 2021). Nonetheless, there have been efforts to explain the r-process enrichment at low metallicity through accretion of stars from dwarf galaxies of low mass (Hirai et al. 2015, 2022) and neutron star natal kicks (Banerjee et al. 2020).

In this work, we derive elemental abundances of 20 neutron-capture species in four bright RPE stars. By studying their abundance patterns with those of both RPE and typical halo stars compiled from various literatures, we aim to discern distinctive trends in abundance ratios, potentially shedding light on intriguing astrophysical phenomena.

3.2 Observation and data preparation

In this study, we have selected four relatively bright ($V < 12$) VMP stars enhanced in r-process from Bandyopadhyay et al. (2020c) [part of HESP–GOMPA survey (Bandyopadhyay et al. 2020a)] to acquire high SNR spectra, including the bluer spectral wavelengths that previously had too low SNRs for detailed study, to determine elemental abundances and upper limits of as many elements as possible, and to probe the rare-Earth peak elements. radial velocity survey (Ge et al. 2015). Observations were carried out using GTC/HORuS spectrograph (Tabernero et al. 2020; Allende Prieto 2021). HORuS is located at the Nasmyth focal plane of the telescope, and provides simultaneous wavelength coverage 3800 − 6900 Å at a spectral resolution of $R \sim 25000$. All the details about the telescope are thoroughly described in Chapter 2. The observations were obtained in the month of December 2019. During the observations, we obtained the sets of bias and flat frames required for data-reduction procedure. All the data reduction steps were carried out using the IMRED, CCDRED, and ECHELLE packages within NOAO's Image Reduction and Analysis Facility (IRAF). All the data reduction procedure is elaborately given in Chapter 2. Finally, we normalized the continuum of the spectra to unity. The details of observations are tabulated in Table 3.1.

We calculate the radial velocities (RVs) of our program stars relative to the observer's frame by cross-correlating the observed spectra with a template spectrum with similar stellar parameters. This cross-correlation is performed using the IDL routine CRSCOR for each spectral order across the entire range from 3800 to 6900 Å. We determine the geocentric RV of each star by taking the median of these RVs, and we use their standard deviation (σ) as the measurement error. All the continuum-normalized spectra were corrected for the Doppler shift due to the RVs of the stars using the IRAF task DOPCOR. Table 3.2 represents both the geocentric and heliocentric RVs of our program stars, corrected for Earth's orbital motion around the sun. Our RVs are compared with the Gaia Collaboration et al. (2021a) and those reported by Bandyopadhyay et al. (2020c), which were initially geocentric. We have recalculated their RVs to reflect heliocentric values. Our RV measurements align closely with the latest Gaia DR3 data, showing no significant RV variations that could suggest the presence of no binaries among our targets.

TABLE 3.1: Basic information for our program stars. The spectral coverage is 3800−6900 Å, and exposure times for each object were 1800 seconds, with two exposures of 900 seconds. The equinox and epoch for the coordinates is J2000.

Star name	RA	DEC	V mag	SNR	Date of Observation (UT)
TYC 3431-689-1	09:21:57.28	+50:34:04.5	11.75	102 (4500 Å)	2019/12/22
HD 263815	06:48:13.33	+32:31:05.2	9.92	161 (4500 Å)	2019/12/23
TYC 1191-918-1	00:43:05.28	+19:48:59.1	9.90	107 (4500 Å)	2019/12/26
TYC 1716-1548-1	23:19:23.84	+19:17:15.4	11.57	126 (4500 Å)	2019/12/26

TABLE 3.2: RVs of our program stars.

Star name	Geocentric RV (km/s)	Heliocentric RV (km/s)	Error (km/s)	RV GAIA DR3$^{(a)}$ (km/s)	RV HESP$^{(b)}$ (km/s)
TYC 3431-689-1	−127.98	−112.95	0.28	−110.75±0.44	−111.96±0.50
HD 263815	133.99	139.33	0.52	138.74±0.23	136.13±0.41
TYC 1191-918-1	−158.01	−186.96	0.19	−187.46±0.18	−189.26±0.51
TYC 1716-1548-1	−250.00	−278.27	0.43	−277.10±0.20	−277.89±0.47

[a] Gaia Collaboration (2022)

[b] Bandyopadhyay et al. (2020c) [we have listed here heliocentric RVs after correction.]

3.3 Stellar parameter estimation and abundance calculation

Throughout this work, we make use of ATLAS9 (Kurucz 1993b; Castelli & Kurucz 2003) for atmospheric model computation and TURBOSPECTRUM (Alvarez & Plez 1998; Plez 2012) for abundance estimation. We use FeI and FeII lines for the estimation of spectroscopic parameters.

Effective Temperature: To estimate the initial temperature, we use various photometric colors such as V-K, J-H, and J-K, which serve as indicators for determining the temperature of the stars. Additionally, for temperature estimation based on Spectral Energy Distribution (SED), we use an online tool called VOSA (Virtual Observatory Sed Analyzer; Bayo et al. (2008)). For obtaining stellar parameters using spectroscopic method, we identify Fe I and Fe II specific absorption lines in the spectra, following our selection criteria detailed in Chapter 2. We use

TABLE 3.3: Estimate of effective temperature (T_{eff}, in K) of our program stars, using different photometric and spectroscopic methods.

Star name	Hα	V-K	J-K	J-H	Fe-I	SED	GAIA
TYC 3431-689-1	4900	5017	4938	4754	4850	5000	5450
HD 263815	4700	4872	4809	4874	4700	4750	5016
TYC 1191-918-1	4700	4690	4613	4756	4650	4750	4877
TYC 1716-1548-1	4550	4522	4286	4362	4500	4500	4644

110 Fe I and 17 Fe II for TYC 3431-689-1, 102 Fe I and 18 Fe II for HD 263815, 111 Fe I and 20 Fe II for TYC 1716-1586-1, and 106 Fe I and 21 Fe II for TYC 1191-918-1. We calculate equivalent width (EW) of each line interactively through Gaussian fitting within the SPLOT task of IRAF. For verification, we also determine the EWs using an automated tool, the Automatic Routine for line EWs in Stellar Spectra (ARES: Sousa et al. 2007). Thanks to the high SNR spectra, both methods yield consistent results.

Spectroscopic temperature estimates are obtained by assuming excitation equilibrium among the neutral iron lines, i.e, by demanding that the abundance of Fe I lines is independent of the LEP, as detailed in the Chapter 2. We fit the wings of the Hα line to check the consistency in temperature estimates (Şahin & Lambert 2009; Matsuno et al. 2017) using our LTE models. As an illustration, the Hα wing-fitting is shown in the Chapter 2. All the temperature estimation with different methods is tabulated in Table 3.3.

Surface Gravity: Stellar surface gravity is estimated presuming the ionization balance of an element, i.e., by forcing the abundance of an element in its neutral state (Fe I) and ionized state (Fe II) to be equal by changing surface gravity. We also fit the wings of the magnesium (Mg) triplet (5167 Å, 5172 Å, 5187 Å) to obtain an estimate of log g, because the Mg-triplet wings are sensitive to small changes in surface gravity. To ensure consistency, we placed our program stars in

TABLE 3.4: Estimates of micro-turbulence velocity (ξ) of our program stars using the methods described in the text.

Star name	using abundance of Fe I & Fe II (km/s)	using dispersion of Fe I abundance (km/s)
TYC 3431-689-1	1.80	2.00
HD 263815	1.85	1.90
TYC 1191-918-1	1.95	2.10
TYC 1716-1548-1	1.95	2.00

TABLE 3.5: Final adopted stellar parameters.

Star name	$T_{\rm eff}$ (K)	$\log g$	[Fe/H]	ξ (km/s)
TYC 3431-689-1	4850	1.4	−2.05	1.80
HD 263815	4700	1.3	−2.22	1.85
TYC 1191-918-1	4650	1.1	−1.90	1.95
TYC 1716-1548-1	4500	1.2	−2.15	1.95

a color-magnitude diagram (CMD). All these methods yield consistent results and exhibit good agreement with one another. These methods are discussed in detail in Chapter 2.

Micro-turbulence: To determine the micro-turbulence velocity, we ensure that the abundance of the neutral iron line (Fe I) does not depend on its reduced equivalent width. For additional verification, we calculate the micro-turbulence velocity using methods from earlier studies (Şahin & Lambert 2009; Reddy et al. 2012; Molina et al. 2014b), which involve measuring the dispersion in the element's abundance. We identify the micro-turbulence velocity as the value that minimizes this dispersion. We also include a comparison of micro-turbulence velocities determined by different methods in Table 3.4. We adopt spectroscopic parameters for further analysis. Table 3.5 presents adopted stellar parameters for the objects in this study.

Abundance Analysis: In this study, we use a combination of EW analysis and spectrum synthesis methods for elemental-abundance estimates. For the lighter elements, up to Zn, we easily find unblended lines in our spectra. Thus, we use the equivalent-width method, but also carried out spectrum synthesis for some of the lines to check the consistency. In the case of heavier elements, most of the absorption features contain contributions from many atomic transitions, thus spectrum synthesis is performed for them. In the equivalent-width analysis, we select lines with EWs < 120 mÅ, which are on the linear region of the Curve of Growth, and are not sensitive to wings broadening. In contrast to the lower limit on EWs used in Fe line list preparation, for other elements, we use any identifiable clear line to study as many elements as possible. For each element, we take the solar values from Asplund et al. (2009). We have also incorporated the hyperfine splitting information for Sc, V, Mn, Cu, Ba, La, Pr, Nd, Sm, and Eu. Solar isotopic ratios are employed. We compute 16 light elements (C, N, Mg, Si, Ca, Ti, Na, Al, Sc, V, Cr, Mn, Fe, Co, Ni, Cu, and Zn) and 20 neutron-capture elements (Sr, Y, Zr, Ba, La, Ce, Pr, Nd, Sm, Eu, Gd, Tb, Dy, Ho, Er, Tm, Lu, Hf, Os, and Th) in four of our program stars because of their excellent SNR (Saraf et al. 2023).

3.4 Abundance Interpretation

3.4.1 Light elements: Carbon and Nitrogen (molecular bands)

We derive carbon (C) abundances utilizing spectrum-synthesis of CH *G*-band molecular region near 4313 Å for all program stars. Line lists from Masseron et al. (2014) were utilized for CH band synthesis. Figure 3.1, illustrates observed

TABLE 3.6: Dilution of carbon corrected according to Placco et al. (2014), and r-process classification of our program stars from Holmbeck et al. (2020).

Star name	[Fe/H]	$[C/Fe]_{LTE}$	$\Delta[C/Fe]^a_{cor}$	$[C/Fe]_{cor}$	[Sr/Fe]	[Ba/Fe]	[Eu/Fe]	[Ba/Eu]	[Sr/Ba]	Class
TYC 3431-689-1	−2.05	−0.60	+0.55	−0.05	+0.15	+0.25	+0.80	−0.55	−0.10	r-II
HD 263815	−2.22	−0.58	+0.63	+0.05	−0.18	−0.13	+0.52	−0.65	−0.05	r-I
TYC 1191-918-1	−1.90	−0.70	+0.66	−0.04	−0.10	−0.14	+0.55	−0.69	+0.04	r-I
TYC 1716-1548-1	−2.15	−0.35	+0.62	+0.27	+0.15	+0.17	+0.80	−0.63	−0.02	r-II

[a] https://vplacco.pythonanywhere.com/.

spectrum (black dots) and synthetic model spectra (blue line), with green and red indicating ± 0.5 dex deviations. Additionally, we constrain the $^{12}C/^{13}C$ ratio through spectral synthesis in regions around 4211 Å, 4230.30 Å and 4231.45 Å. Our analysis shows, $^{12}C/^{13}C$ ratios of 3.0, 3.5, 5.5, and 5.5 for the stars TYC 3431-689-1, HD 263815, TYC 1191-918-1, and TYC 1716-1548-1, respectively. High SNRs of our program stars allows us to calculate the nitrogen (N) abundance in the blue region, adopting line lists from Plez & Cohen (2005) for CN band synthesis around 3883 Å. Example CN-band synthesis is illustrated in Figure 3.1 (bottom panel). The program objects exhibit low surface carbon abundances, consistent with their evolutionary stages as red giants. We employ the method proposed by Placco et al. (2014) to correct observed carbon abundances for stellar evolutionary states. Table 3.6 presents LTE values of observed C abundances alongside corrected values from our analysis.

3.4.2 Alpha-elements

We have detected α-elements Mg, Si, Ca, and Ti in our program objects. Abundances of Ti were calculated using the equivalent-width method due to the presence of numerous clean Ti I and Ti II lines in all stars. Although significant numbers of unblended Ca I lines are present in the spectra, we used both the equivalent-width and spectrum synthesis methods for Ca abundance estimation.

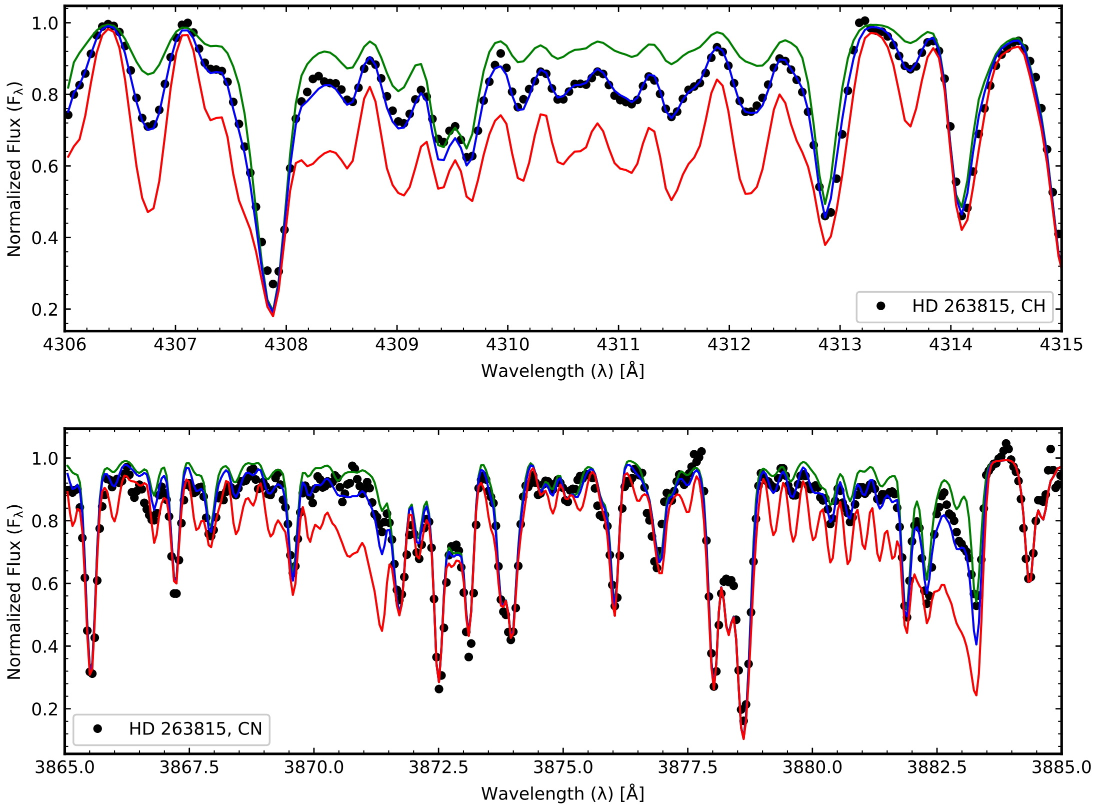

FIGURE 3.1: C and N abundance estimation for one of our program stars, HD 263815, using the spectrum-synthesis method. The top and bottom panels show the C and N synthesis, respectively. The black dots represents observation, and blue colour shows the best match. The green and red colours indicate $\pm$ 0.5 dex deviations.

Spectrum-synthesis methods were used for Mg and Si abundance determination, with Si abundance derived from the 4102 Å and 6155 Å lines.

3.4.3 Odd-Z Elements

We determined the abundances of sodium (Na) and aluminium (Al) among the odd-Z elements. Na abundance was calculated using the sodium D1 and D2 at 5890 Å and 5896 Å, respectively, while Al abundance was derived from resonance lines at 3941 Å and 3961 Å. These Na and Al lines are strongly affected by NLTE effects, so we have taken into account these corrections (Baumueller & Gehren

1997; Gehren et al. 2004; Andrievsky et al. 2007). Synthesis of the Na I line at 5890 Å is illustrated in Figure 3.2, demonstrating spectral synthesis with consideration for collisional broadening following the method by Barklem & O'Mara (2001). We have also verified the consistency of our estimated Na and Al abundances with those of other halo stars.

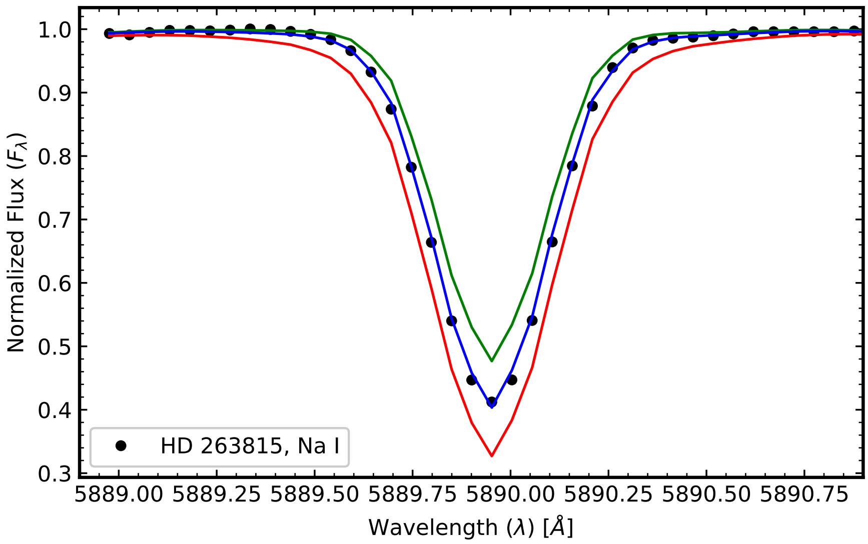

FIGURE 3.2: Synthesis of the Na-absorption feature. The black dotted points represent the observed spectra and the solid blue colour shows the best fit. Green and red colours indicate ± 0.5 dex deviations.

3.4.4 Iron-peak Elements

We determined abundances for several iron-peak elements, including Sc, V, Cr, Mn, Fe, Co, Ni, Cu, and Zn species. A combination of both the EW method and the synthesis method is used for abundance estimation. Hyperfine splitting is also considered as required. Fe I and Fe II content were obtained using the EW method during stellar-parameter estimation.

Abundances of Co, Cu, and Zn are determined using the spectrum synthesis method. We found only one line, at 5105.53 Å, useful for Cu abundance estimation while Co abundance was evaluated from lines at 5020.82 Å, 4110.53 Å, and 4121.31 Å. Zn abundance was derived using lines at 4810.52 Å and 4722.15 Å.

Tables 3.8, 3.9, 3.10, and 3.11 present estimated abundances of iron-peak elements and the number of lines used. All obtained abundances are consistent with previous estimates for halo stars.

3.4.5 Neutron-capture Elements

We utilize the synthesis method for estimating the abundances of heavy elements as these lines are often blended with other elements, and often possessing several isotopes and hyperfine structures. We have identified, 20 neutron-capture elements Sr, Y, Zr, Ba, La, Ce, Pr, Nd, Sm, Eu, Gd, Tb, Dy, Ho, Er, Tm, Lu, and Hf, along with important third r-process peak elements Os and Th, some elements may or may not be present in all program stars. Notably, this study reports the abundances of 10 elements (Pr, Gd, Tb, Ho, Er, Tm, Lu, Hf, Os, Th) for the first time in our program stars.

3.4.5.1 First-peak elements

We measure absorption lines for three first r-process peak elements: Sr, Y, and Zr. Sr abundance is determined from two lines at 4077 Å and 4215 Å, both yielding similar results. However, the Sr I line at 4607 Å provides significantly lower abundance due to NLTE effects (Bergemann et al. 2012), thus not considered for average abundance calculation. Y and Zr abundances are estimated using 7 transitions for each element. Figure 3.3(a) illustrates the synthesis of the Sr line at 4215 Å. Nonetheless, similar to many RPE stars, the first r-process peak does not align well with the scaled-solar r-process pattern (See Figure 3.13).

3.4.5.2 Second-peak elements

In the second r-process peak, we detect 15 elements: Ba, La, Ce, Pr, Nd, Sm, Eu, Gd, Tb, Dy, Ho, Er, Tm, Lu, and Hf. However, Pr and Hf measurements were not possible in TYC 1716-1548-1, and Gd, Ho, and Er measurements were not feasible in TYC 1191-918-1. Tb was only measured in HD 263815 and TYC 3431-689-1 (See the synthesis in Figure 3.3(d)), while Tm was only available in HD 263815. Details of identified lines are listed in Appendix B. Ba abundance is estimated using lines at 4554 Å, 4934 Å, 5853 Å, 6142 Å, and 6496 Å. We corrected the abundance derived from the 4554 Å line for NLTE effects according to Short & Hauschildt (2006a). The Eu abundance primarily comes from lines at 4129 Å and 4205 Å, both yielding similar estimates. Tb and Lu abundances are estimated from lines at 3976 Å and 5476 Å, respectively. Abundance details for all second-peak r-process elements are listed in Tables 3.8, 3.9, 3.10, and 3.11, aligning well with the scaled-solar r-process pattern (see Figure 3.13).

3.4.5.3 Third-peak elements

We estimated the abundances of Os and Th, key elements in the third r-process peak. Os abundance is derived from lines at 4420 Å and 4265 Å, the spectral synthesis is shown in Figure 3.3(e) and 3.4(a). Th abundance is estimated from a strong line at 4019 Å, blended with other lines and the CH G-band. We took care of all the blends while synthesizing Th. Table 3.7 lists lines used for Th II 4019 Å synthesis. We obtained an upper limit for Pb in three stars. Figure 3.3(f)

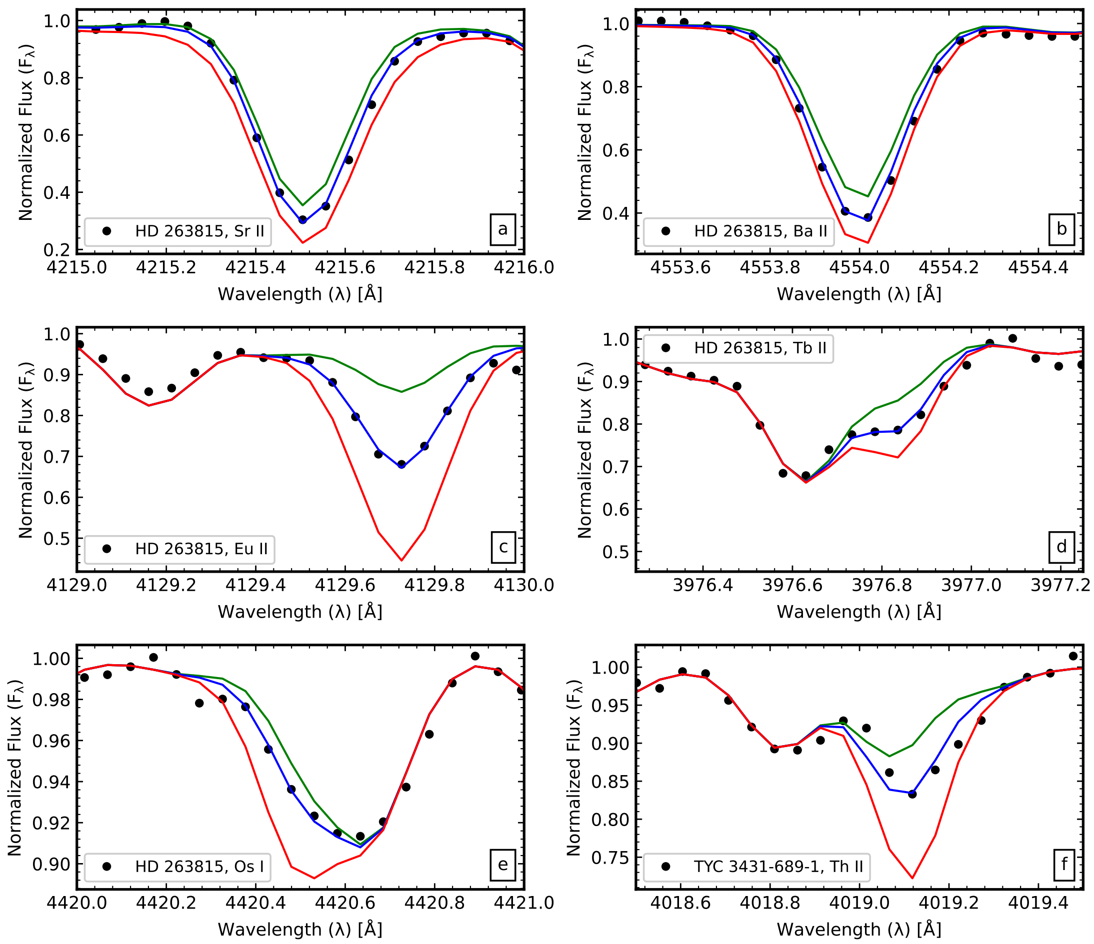

FIGURE 3.3: Synthesis of Sr, Ba, Eu, Tb, Os, and Th. The black dotted points represent the observed spectra and the solid blue colour shows the best fit. Green and red colours indicate ± 0.5 dex deviations from the best fit.

demonstrates Th synthesis in TYC 3431-689-1. To test the robustness of our Th determination in the spectra, we compute equivalent widths of contributing elements in the 4019.00−4019.44 Å range, finding Th contributions of 44 percent and 59 percent for TYC 3431-689-1 and TYC 1191-918-1, respectively. Due to low SNR (< 15) in the 3959 Å region, U detection was not possible. Highly RPE stars with low [C/Fe] may be suitable for U detection using GTC.

Table 3.7: Line list used for the spectrum synthesis of Th II lines in the 4019.129 Å region.

Species	wavelength (Å)	log gf	LEP (eV)
Nd II	4018.823	−0.899	0.064
Cr I	4018.826	−2.629	3.648
Cr I	4018.863	−2.822	4.440
V I	4018.929	−0.651	2.581
Mn I	4018.999	−1.497	4.354
V II	4019.036	−2.704	3.753
Fe I	4019.042	−2.780	2.608
Fe I	4019.052	−2.78	2.608
Ce II	4019.057	−0.213	1.014
Ni I	4019.058	−3.174	1.935
Fe II	4019.110	−3.102	9.825
Co I	4019.126	−2.270	2.280
Th II	4019.129	−0.228	0.000
V I	4019.134	−1.999	1.804
Co I	4019.163	−3.136	2.871
Fe II	4019.181	−3.532	7.653
Co I	4019.289	−3.232	0.582
Co I	4019.299	−3.769	0.629
Cr II	4019.289	−5.604	5.330
^{12}CH	4019.440	−7.971	1.172

TABLE 3.8: Detailed composition TYC 3431-689-1.

Element	species	atomic no.	N-lines	Solar	$A(X)_{syn}$	[X/H]	[X/Fe]	σ
C	CH	6	1	8.39	5.74	−2.65	−0.60	0.23
N	CN	7	1	7.78	6.78	−1.00	+1.05	0.18
Na	Na I	11	2	6.17	4.72	−1.45	+0.60	0.25
Mg	Mg I	12	7	7.53	5.93	−1.60	+0.45	0.17
Al	Al I	13	2	6.37	4.17	−2.20	−0.15	0.14
Si	Si I	14	2	7.51	5.71	−1.80	+0.25	0.13
Ca	Ca I	20	14	6.31	4.6	−1.71	+0.34	0.12
Sc	Sc I	21	1	3.17	0.67	−2.50	−0.45	0.31
Sc	Sc II	21	9	3.17	1.07	−2.10	−0.05	0.10
Ti	Ti I	22	18	4.90	3.07	−1.83	+0.22	0.19
Ti	Ti II	22	31	4.90	3.18	−1.72	+0.33	0.08
V	V I	23	4	4.00	1.6	−2.40	−0.35	0.23
V	V II	23	2	4.00	1.9	−2.10	−0.05	0.11
Cr	Cr I	24	13	5.64	3.31	−2.33	−0.28	0.19
Cr	Cr II	24	5	5.64	3.54	−2.10	−0.05	0.08
Mn	Mn I	25	8	5.39	2.82	−2.57	−0.52	0.19
Co	Co I	27	3	4.92	3.02	−1.90	+0.15	0.24
Ni	Ni I	28	16	6.23	4.03	−2.20	−0.15	0.13
Cu	Cu I	29	1	4.21	1.05	−3.16	−1.11	0.19
Zn	Zn I	30	2	4.60	2.65	−1.95	+0.10	0.08
Sr	Sr II	38	2	2.92	1.02	−1.90	+0.15	0.13
Y	Y II	39	7	2.21	0.01	−2.20	−0.15	0.10
Zr	Zr II	40	7	2.58	0.88	−1.70	+0.35	0.10
Ba	Ba II	56	5	2.17	0.37	−1.80	+0.25	0.13
La	La II	57	4	1.13	−0.57	−1.70	+0.35	0.11
Ce	Ce II	58	3	1.70	−0.35	−2.05	+0.00	0.12
Pr	Pr II	59	1	0.58	−0.72	−1.30	+0.75	0.07
Nd	Nd II	60	6	1.45	−0.12	−1.57	+0.48	0.12
Sm	Sm II	62	3	1.00	−0.5	−1.50	+0.55	0.12
Eu	Eu II	63	2	0.52	−0.73	−1.25	+0.80	0.03
Gd	Gd II	64	2	1.11	−0.39	−1.50	+0.55	0.15
Tb	Tb II	65	1	0.28	−0.82	−1.10	+0.95	0.23
Dy	Dy II	66	3	1.14	−0.29	−1.43	+0.62	0.12
Ho	Ho II	67	1	0.51	−0.69	−1.20	+0.85	0.02
Er	Er II	68	2	0.93	−0.57	−1.50	+0.55	0.11
Lu	Lu II	71	1	0.06	−1.24	−1.30	+0.75	0.12
Hf	Hf II	72	2	0.88	−0.72	−1.60	+0.45	0.15
Os	Os I	76	2	1.25	−0.15	−1.40	+0.65	0.21
Pb	Pb II	82	1	2.00	<0.1	–	–	–
Th	Th II	90	1	0.06	−1.34	−1.40	+0.65	0.1

TABLE 3.9: Detailed composition HD 263815.

Element	species	atomic no.	N-lines	Solar	$A(X)_{syn}$	[X/H]	[X/Fe]	σ
C	CH	6	1	8.39	5.59	−2.80	−0.58	0.25
N	CN	7	1	7.78	6.28	−1.50	+0.72	0.18
Na	Na I	11	2	6.17	4.22	−1.95	+0.27	0.26
Mg	Mg I	12	7	7.53	5.83	−1.70	+0.52	0.17
Al	Al I	13	2	6.37	3.87	−2.50	−0.28	0.15
Si	Si I	14	2	7.51	5.71	−1.80	+0.42	0.11
Ca	Ca I	20	14	6.31	4.43	−1.88	+0.34	0.14
Sc	Sc I	21	1	3.17	0.39	−2.78	−0.56	0.31
Sc	Sc II	21	9	3.17	0.96	−2.21	+0.01	0.09
Ti	Ti I	22	14	4.90	2.9	−2.00	+0.22	0.19
Ti	Ti II	22	33	4.90	3.0	−1.90	+0.32	0.08
V	V I	23	4	4.00	1.50	−2.50	−0.28	0.24
V	V II	23	3	4.00	1.90	−2.10	+0.12	0.08
Cr	Cr I	24	13	5.64	3.12	−2.52	−0.30	0.22
Cr	Cr II	24	5	5.64	3.44	−2.20	+0.02	0.06
Mn	Mn I	25	8	5.39	2.66	−2.73	−0.51	0.21
Co	Co I	27	3	4.92	2.92	−2.00	+0.22	0.27
Ni	Ni I	28	16	6.23	4.08	−2.15	+0.07	0.14
Cu	Cu I	29	1	4.21	1.01	−3.20	−0.98	0.21
Zn	Zn I	30	2	4.60	2.55	−2.05	+0.17	0.05
Sr	Sr II	38	2	2.92	0.52	−2.40	−0.18	0.13
Y	Y II	39	7	2.21	−0.29	−2.50	−0.28	0.09
Zr	Zr II	40	7	2.58	0.48	−2.10	+0.12	0.14
Ba	Ba II	56	5	2.17	−0.18	−2.35	−0.13	0.13
La	La II	57	4	1.13	−1.04	−2.17	+0.05	0.12
Ce	Ce II	58	3	1.70	−0.8	−2.50	−0.28	0.14
Pr	Pr II	59	2	0.58	−1.02	−1.60	+0.62	0.1
Nd	Nd II	60	6	1.45	−0.51	−1.96	+0.26	0.13
Sm	Sm II	62	3	1.00	−1.00	−2.00	+0.22	0.13
Eu	Eu II	63	2	0.52	−1.18	−1.70	+0.52	0.01
Gd	Gd II	64	2	1.11	−0.79	−1.90	+0.32	0.14
Tb	Tb II	65	1	0.28	−1.22	−1.50	+0.72	0.2
Dy	Dy II	66	3	1.14	−0.86	−2.00	+0.22	0.16
Ho	Ho II	67	2	0.51	−1.19	−1.70	+0.52	0.01
Er	Er II	68	2	0.93	−0.97	−1.90	+0.32	0.14
Tm	Tm II	69	1	0.0	−1.5	−1.50	+0.72	0.1
Lu	Lu II	71	1	0.06	−1.54	−1.60	+0.62	0.14
Hf	Hf II	72	2	0.88	−1.02	−1.90	+0.32	0.14
Os	Os I	76	1	1.25	−0.45	−1.70	+0.52	0.22
Pb	Pb II	82	1	2.00	< -0.1	< -2.1	<0.12	–
Th	Th II	90	1	0.06	< -2.04	–	–	–

TABLE 3.10: Detailed composition of TYC 1716-1548-1.

Element	species	atomic no.	N-lines	Solar	$A(X)_{syn}$	[X/H]	[X/Fe]	σ
C	CH	6	1	8.39	5.89	−2.50	−0.35	0.27
N	CN	7	1	7.78	6.58	−1.20	+0.95	0.20
Na	Na I	11	2	6.17	4.17	−2.00	+0.15	0.32
Mg	Mg I	12	7	7.53	5.9	−1.63	+0.52	0.23
Al	Al I	13	2	6.37	4.17	−2.20	−0.05	0.17
Si	Si I	14	2	7.51	5.81	−1.70	+0.45	0.15
Ca	Ca I	20	14	6.31	4.36	−1.95	+0.20	0.19
Sc	Sc I	21	1	3.17	0.46	−2.71	−0.56	0.3
Sc	Sc II	21	9	3.17	0.92	−2.25	−0.1	0.05
Ti	Ti I	22	15	4.90	2.92	−1.98	+0.17	0.28
Ti	Ti II	22	29	4.90	3.27	−1.63	+0.52	0.06
V	V I	23	4	4.00	1.55	−2.45	−0.30	0.28
Cr	Cr I	24	13	5.64	3.24	−2.40	−0.25	0.28
Cr	Cr II	24	5	5.64	3.49	−2.15	+0.00	0.09
Mn	Mn I	25	8	5.39	2.63	−2.76	−0.61	0.26
Co	Co I	27	3	4.92	2.72	−2.20	−0.05	0.29
Ni	Ni I	28	16	6.23	3.91	−2.32	−0.17	0.17
Cu	Cu I	29	1	4.21	1.08	−3.13	−0.98	0.26
Zn	Zn I	30	2	4.60	2.55	−2.05	+0.10	0.04
Ga	Ga I	31	1	2.88	0.48	−2.40	−0.25	–
Sr	Sr II	38	2	2.92	0.92	−2.00	+0.15	0.05
Y	Y II	39	7	2.21	0.01	−2.20	−0.05	0.07
Zr	Zr II	40	7	2.58	0.98	−1.60	+0.55	0.07
Ba	Ba II	56	7	2.17	0.19	−1.98	+0.17	0.04
La	La II	57	4	1.13	−0.72	−1.85	+0.30	0.07
Ce	Ce II	58	3	1.70	−0.55	−2.25	−0.10	0.08
Pr	Pr II	59	2	0.58	−0.42	−1.00	+1.15	0.1
Nd	Nd II	60	3	1.45	−0.05	−1.50	+0.65	0.07
Sm	Sm II	62	2	1.00	−0.75	−1.75	+0.40	0.1
Eu	Eu II	63	2	0.52	−0.83	−1.35	+0.80	0.02
Gd	Gd II	64	2	1.11	−0.49	−1.60	+0.55	0.17
Dy	Dy II	66	3	1.14	−0.43	−1.57	+0.58	0.09
Ho	Ho II	67	2	0.51	−0.99	−1.50	+0.65	0.1
Er	Er II	68	2	0.93	−0.47	−1.40	+0.75	0.13
Lu	Lu II	71	1	0.06	−1.33	−1.39	+0.76	0.11
Os	Os I	76	2	1.25	−0.15	−1.40	+0.75	0.19
Pb	Pb II	82	1	2.00	<0.1	< −1.9	<0.25	–

TABLE 3.11: Detailed composition of TYC 1191-918-1.

Element	species	atomic no.	N-lines	Solar	$A(X)_{syn}$	[X/H]	[X/Fe]	σ
C	CH	6	1	8.39	5.79	−2.60	−0.70	0.24
N	CN	7	1	7.78	6.78	−1.00	+0.90	0.19
Na	Na I	11	2	6.17	4.47	−1.70	+0.20	0.26
Mg	Mg I	12	7	7.53	6.15	−1.38	+0.52	0.18
Al	Al I	13	2	6.37	4.07	−2.30	−0.40	0.13
Si	Si I	14	2	7.51	5.91	−1.60	+0.30	0.13
Ca	Ca I	20	14	6.31	4.72	−1.59	+0.31	0.15
Sc	Sc II	21	9	3.17	1.12	−2.05	−0.15	0.12
Ti	Ti I	22	17	4.90	3.19	−1.71	+0.19	0.23
Ti	Ti II	22	22	4.90	3.4	−1.50	+0.40	0.10
V	V I	23	4	4.00	1.81	−2.19	−0.29	0.24
V	V II	23	1	4.00	2.1	−1.90	+0.00	0.13
Cr	Cr I	24	13	5.64	3.44	−2.20	−0.30	0.24
Cr	Cr II	24	5	5.64	3.72	−1.92	−0.02	0.1
Mn	Mn I	25	8	5.39	2.89	−2.50	−0.60	0.17
Co	Co I	27	3	4.92	2.92	−2.00	−0.10	0.29
Ni	Ni I	28	16	6.23	4.20	−2.03	−0.13	0.15
Cu	Cu I	29	1	4.21	1.31	−2.90	−1.00	0.21
Zn	Zn I	30	2	4.60	2.70	−1.90	+0.00	0.07
Sr	Sr II	38	2	2.92	0.92	−2.00	−0.10	0.12
Y	Y II	39	7	2.21	0.21	−2.00	−0.10	0.13
Zr	Zr II	40	5	2.58	0.84	−1.74	+0.16	0.12
Ba	Ba II	56	3	2.17	0.13	−2.04	−0.14	0.15
La	La II	57	4	1.13	−0.52	−1.65	+0.25	0.14
Ce	Ce II	58	3	1.70	−0.35	−2.05	−0.15	0.15
Pr	Pr II	59	2	0.58	−0.82	−1.40	+0.50	0.12
Nd	Nd II	60	6	1.45	−0.08	−1.53	+0.37	0.15
Sm	Sm II	62	3	1.00	−0.6	−1.60	+0.30	0.14
Eu	Eu II	63	2	0.52	−0.83	−1.35	+0.55	0.03
Tb	Tb II	65	1	0.28	−1.82	−1.10	+0.80	0.12
Dy	Dy II	66	3	1.14	−0.39	−1.53	+0.37	0.15
Ho	Ho II	67	2	0.51	−0.89	−1.40	+0.50	0.13
Er	Er II	68	2	0.93	−0.58	−1.51	+0.39	0.12
Hf	Hf II	72	1	0.88	−0.82	−1.70	+0.20	0.16
Os	Os I	76	2	1.25	−0.1	−1.35	+0.55	0.21
Th	Th II	90	1	0.06	−1.24	−1.30	+0.60	0.12

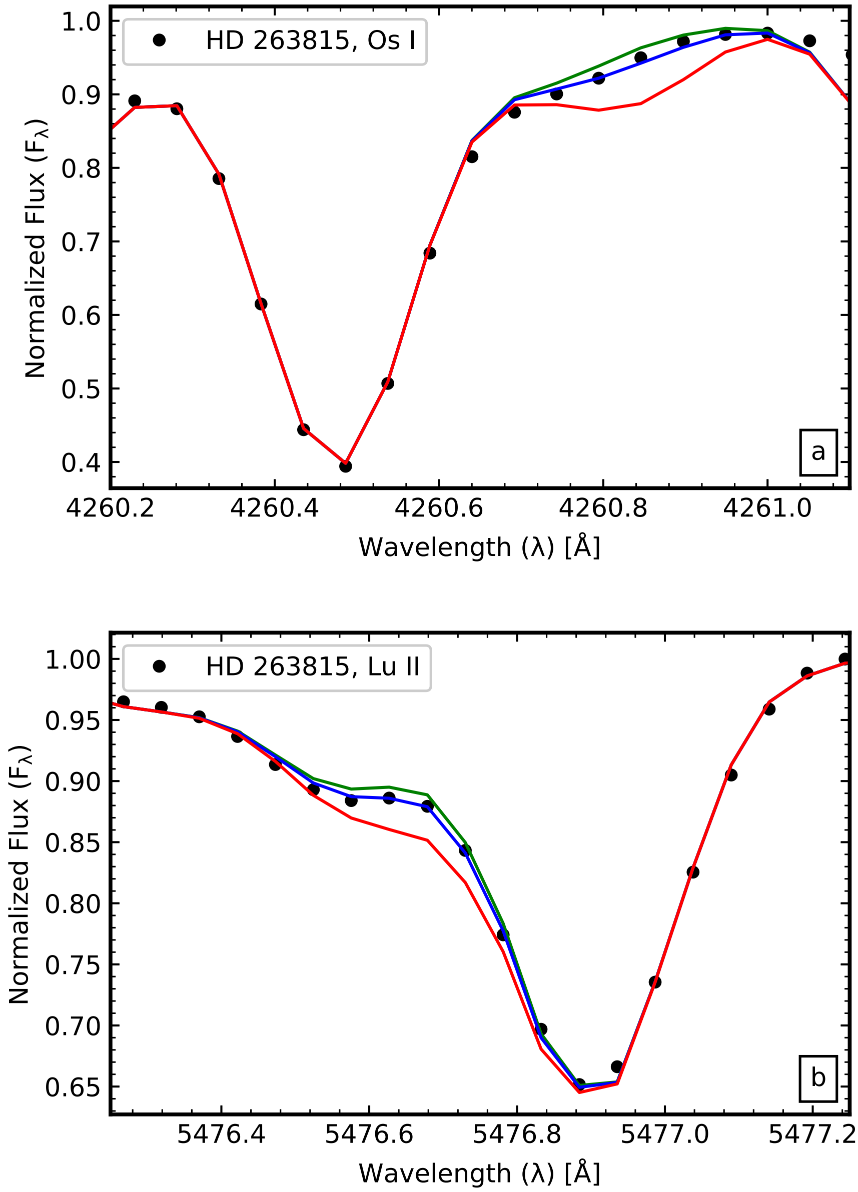

FIGURE 3.4: Synthesis of regions containing Os and Lu lines. The black dots display observation, and the blue colour shows best match. The green and red colours indicate dispersion of $\pm$ 0.5 dex.

3.4.6 Uncertainties in abundances

To calculate elemental abundances, we require stellar parameters and a line list as inputs. Spectroscopic methods that determine these parameters also rely on an atomic line list. Each line in the list carries inherent uncertainties in its atomic or molecular data and parameters, which influence the final abundance estimates. Additionally, SNR affects the uncertainty of these estimates Cayrel (1988). In our analysis, we estimate errors by assuming a 150 K uncertainty in effective temperature ($T_{\rm eff}$) and a 0.25 dex uncertainty in surface gravity ($\log g$). We calculate errors associated with the SNR using the method described by Cayrel (1988). The overall error in elemental abundance is then calculated as the quadratic sum of all individual errors.

3.5 Discussion

3.5.1 Level of *r*-process enhancement and classification

Traditionally, metal-poor stars are classified based on the abundance levels of C, Fe, Sr, Ba, and Eu. Europium (Eu) typically indicates r-process enrichment, while Barium (Ba) indicates s-process enrichment. Initially the classifications criteria was proposed by Beers & Christlieb (2005a) and later modified by Frebel (2018b). Cain et al. (2020) introduced r-III class to include extremely RPE stars with [Eu/Fe] $> +2.0$. Recently, Holmbeck et al. (2020) updated r-process classification using RPE stars from the RPA survey, the most notably shifting the r-I and r-II division to [Eu/Fe] $= +0.7$ based on a statistical analysis, which we adopt for the rest of this paper. Table 1.1 lists r-process class.

Some mildly RPE stars show elevated abundances of the first r-process peak elements, potentially due to a limited-r process. The frequent occurrence of carbon enhancement in VMP stars has led to the designation of CEMP stars, initially characterized by [C/Fe] $> +1.0$ (Beers & Christlieb 2005a) and later revised to [C/Fe] $> +0.7$ by various researchers, a criterion we use in this paper.

For classifying our program stars, we first calculate their carbonicity ([C/Fe]), finding that all our stars have [C/Fe] $< +0.7$. We also measured the [Eu/Fe] and [Ba/Eu] ratios to calculate the excess of r- and s-process enhancements. Figure 3.5 illustrates the positions of our program stars on the [Ba/Eu] vs. [Eu/Fe] plane. According to the classification criteria of Beers & Christlieb (2005a), all our stars are categorized as r-I. However, using the updated criteria from Holmbeck et al. (2020), which we adopt in this study, two stars (HD 263815 and TYC 1191-918-1) are classified as r-I, while the other two (TYC 3431-689-1 and TYC 1716-1548-1) are classified as r-II (see Figure 3.5).

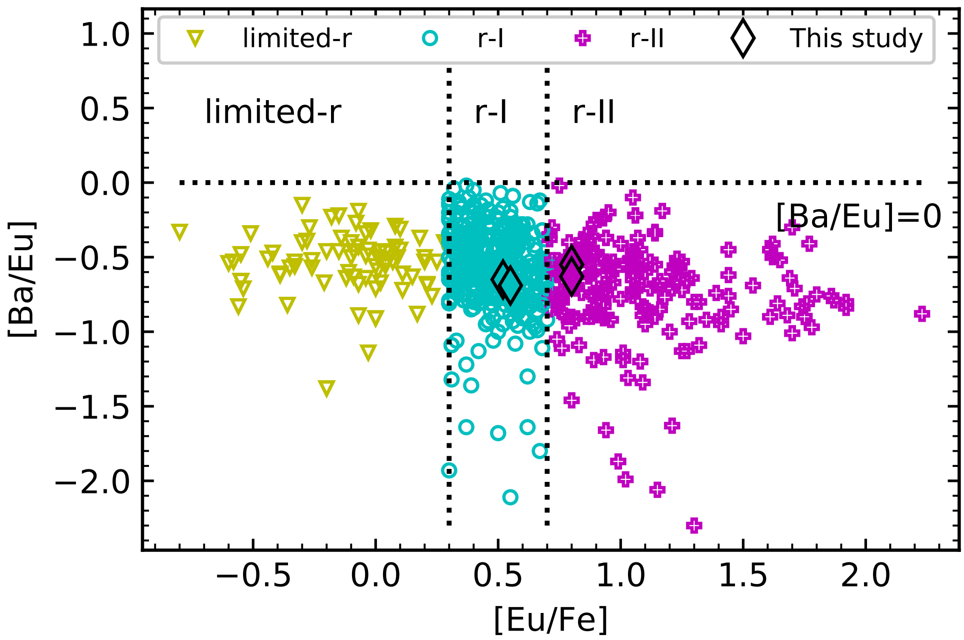

Figure 3.5: Distribution of limited-r (yellow colours), r-I (cyan colours), and r-II (magenta colours) stars in [Ba/Eu] vs [Eu/Fe] plane. The four black diamonds indicate the r-I (cyan) and r-II (magenta) from this study. For data reference, see Saraf et al. (2023).

3.5.2 Evolution of light elements with RPE stars

Figure 3.6 illustrates the light elements up to Zn in our program stars, along with literature data. Our program stars exhibit lower [C/Fe] levels, typical for their evolutionary stage. Some r-II stars reported in the literature (Abohalima & Frebel (2018) show elevated carbon levels ([C/Fe] $> +0.7$), indicative of CEMP-r or CEMP-r/s sub-class stars. We did not include these stars in our study.

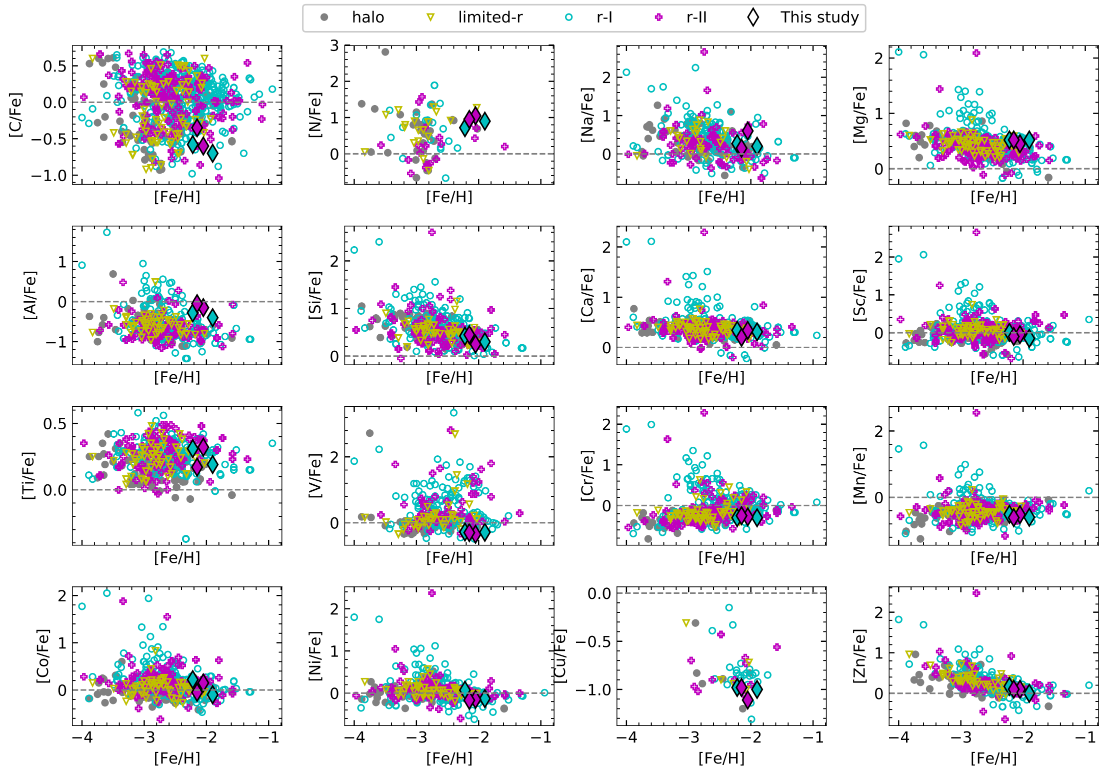

FIGURE 3.6: Light elements abundance evolution limited-r (yellow colour), r-I (cyan colour), and r-II (magenta colour) with metallicity. The four black diamonds indicate the r-I (cyan) and r-II (magenta) from this study. References for the r-process stars are given in the caption of figure 3.5. Normal metal-poor halo stars, indicated with grey filled circles. The grey horizontal lines represent the solar values. For data reference, see Saraf et al. (2023).

Figure 3.7 illustrates that mixed and unmixed stars are distinctly categorized based on their carbon and nitrogen abundances. Approximately two-thirds of the r-II stars are located in the unmixed region, characterized by [N/Fe] $< +0.5$ (Spite et al. 2005; Siqueira Mello et al. 2014). If these C and N abundances originate from the stars birth clouds, lithium should be present in their atmospheres, providing insights into the extent of r-process material mixed with the primordial cloud. Four of our program stars, showing [C/N] ratio of less than -1.0, have likely experienced mixing processes. This is further supported by their $^{12}C/^{13}C$ ratios being less than 10, aligning with the theoretical CN cycle equilibrium values predicted by Caughlan (1965) and Sneden et al. (1986). These ratios are consistent with the positioning of our target stars in Figure 3.7. Similar values of $^{12}C/^{13}C$ have been reported in other stars such as HD 122563 (Lambert & Sneden 1977).

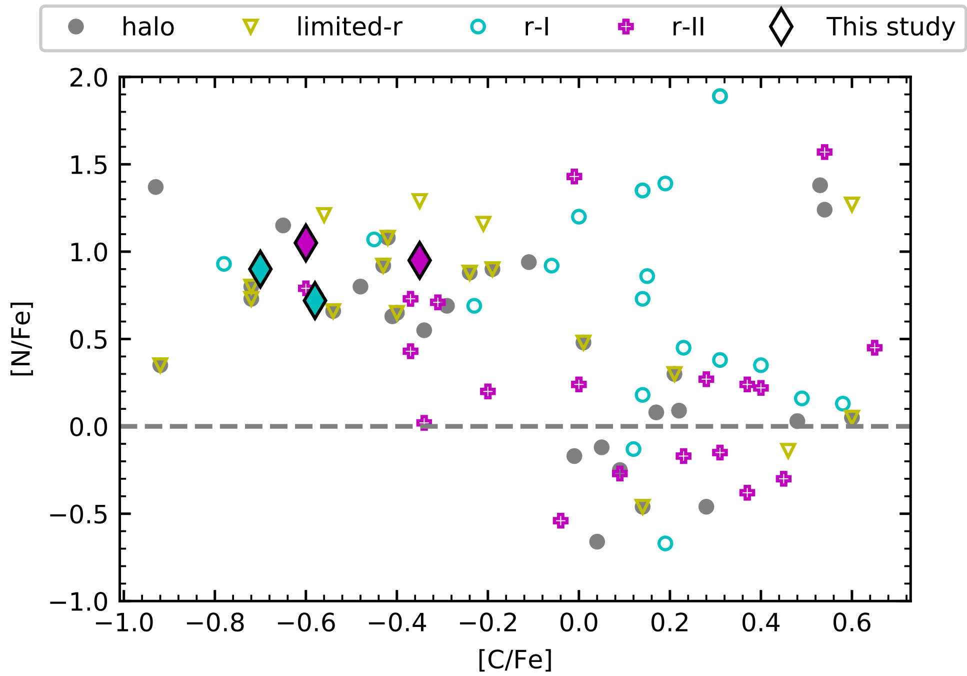

FIGURE 3.7: Relation between the N and C abundances for limited-r (yellow colour), r-I (cyan colour), and r-II (magenta colour). The four black diamonds indicate the r-I (cyan) and r-II (magenta) from this study. References for the RPE stars are given in the caption of Figure 3.5, and references for the normal metal-poor halo stars, indicated with grey filled circles, are listed in the caption of figure 3.6. The grey horizontal line represents the solar value.

The odd-Z elements in our program stars show [Na/Fe] slightly higher than the solar ratio, while [Al/Fe] is slightly sub-solar, consistent with known RPE stars. However, the Na and Al abundances in r-I and r-II exhibit more scatter than normal halo stars. The elevated N abundance alongside Na could suggest a very massive star progenitor for RPE stars. Notably, no Na-Mg anti-correlation is observed.

Metal-poor halo stars typically show a constant enhancement in α-elements ([α/Fe] $\sim$ +0.4) originating from core-collapse supernovae. Our findings reveal [α/Fe] values of approximately +0.35 for TYC 3431-689-1 and HD 263815, +0.43 for TYC 1716-1548-1, and +0.39 for TYC 1191-918-1, aligning well with observed values for metal-poor halo stars (McWilliam 1997).

Figure 3.8 depicts the connection between α-elements and r-process elements; It shows the average α-enhancement ([Mg/Fe] + [Si/Fe] + [Ca/Fe] + [Ti/Fe]) for RPE stars plotted against [Eu/Fe]. The black solid line represents the best fit, with 1σ outliers removed (crosses), while the shaded region denotes the dispersion around the line. Despite a weak, statistically insignificant negative correlation, our program stars align well with the best-fit line.

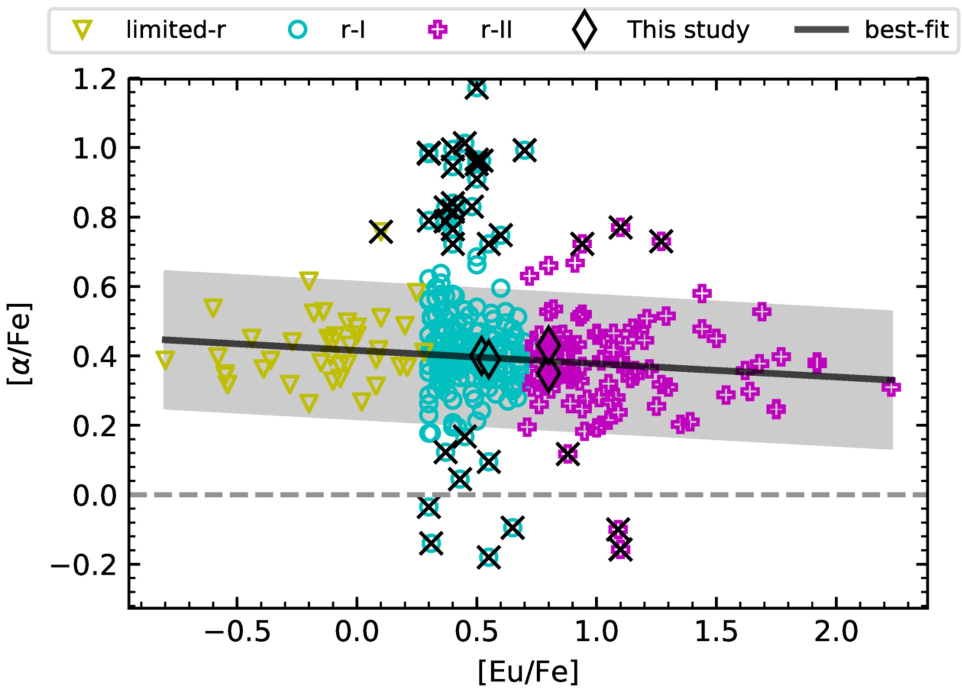

FIGURE 3.8: Alpha-element enhancements in limited-r (yellow colour), r-I (cyan colour), and r-II (magenta colour). The four black diamonds indicate the r-I (cyan) and r-II (magenta) from this study. References for the RPE stars are given in the caption of Figure 3.5. The black line is fitting after removing the 1σ outliers denoted by overlaid crosses. The grey horizontal line represents the solar value.

The iron-peak elements Sc, Co, and Zn demonstrate nearly solar ratios in our program stars, while V, Cr, Mn, and Cu fall below solar levels. Overall, the abundance of iron-peak elements in RPE stars closely resembles that of normal metal-poor halo stars. Although halo stars typically exhibit slightly sub-solar V abundances with minimal dispersion, RPE stars show notably higher dispersions towards super-solar abundances. The incorporation of RPA data from Sakari et al. (2018) and Ezzeddine et al. (2020) leads to increased dispersion in the [V/Fe] ratio, ranging from -0.8 to $+3.3$. However, without this inclusion, the [V/Fe] ratio typically ranges from -0.8 to $+1.0$, in agreement with literature (Sneden et al. 2016; Ou et al. 2020). Additionally, [Zn/Fe] ratio rises towards the metal-poor end for both r-I and r-II compared to normal stars, suggesting a potential extra contribution of Zn from r-process production sites at the metal-poor end.

The [Eu/Zn] ratio in our study closely aligns with that of typical halo stars at lower metallicities and increases as metallicity rises, as shown in Figure 3.9. This indicates that the sites producing r-process elements in the metal-poor regime also generated zinc, whereas r-process progenitors at higher metallicities produced less or no zinc. If Zn and Eu were produced separately at lower metallicities, we would expect higher [Eu/Zn] in RPE stars than normal stars, which we do not see at lower metallicities. But, we are seeing higher [Eu/Zn] with increasing metallicity. This observation aligns with recent theories proposing that hypernovae or massive supernovae were likely responsible for r-process element production in metal-poor environments, with neutron star mergers (NSMs) playing a larger role at higher metallicities (Tarumi et al. 2021; Yong et al. 2021). Four of our program objects, with [Fe/H] from -2.22 to -1.90, show nearly solar [Zn/Fe] ratios. Additionally, the [Eu/Zn] ratio in these stars approaches the upper limit observed in normal halo stars. This suggests that our program stars likely formed from gas primarily enriched by later galactic events like NSMs, with minimal contributions from the early r-process events in the Universe.

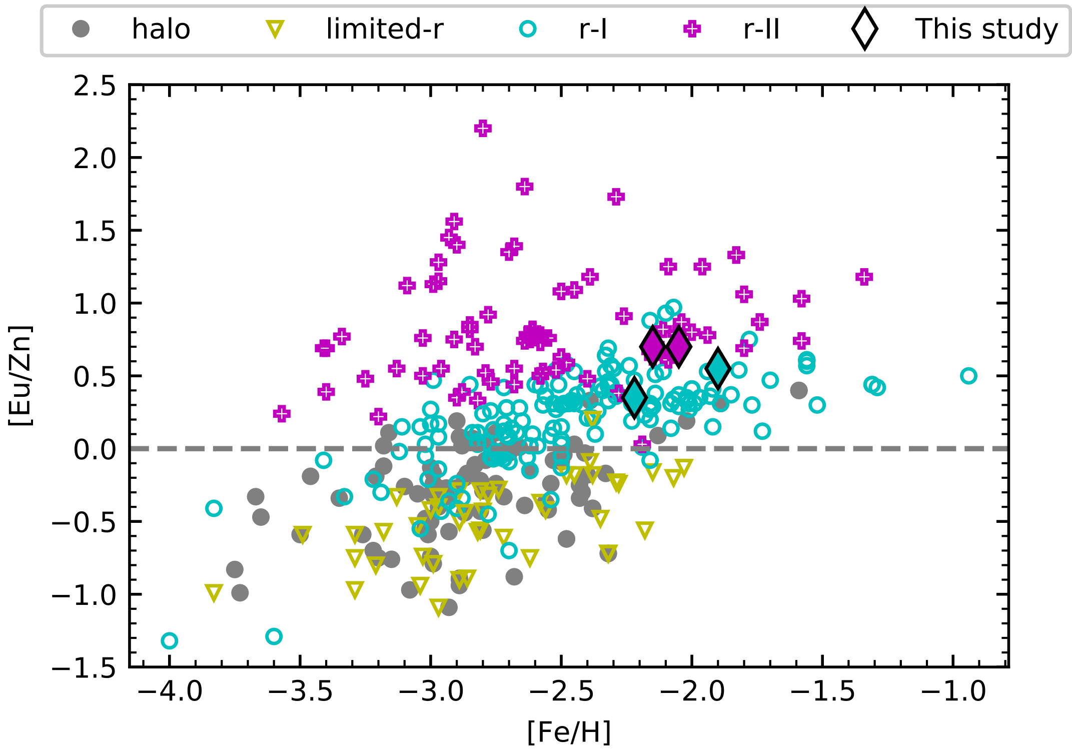

FIGURE 3.9: Evolution of the [Eu/Zn] in limited-r (yellow colour), r-I (cyan colour), and r-II (magenta colour) with metallicity. The four black diamonds indicate the r-I (cyan) and r-II (magenta) from this study. For references, see Figure 3.5, and references for normal metal-poor halo stars, indicated by grey-filled circles, are listed in the caption of Figure 3.6. The grey horizontal lines indicate solar value.

3.5.3 Evolution of Heavy-element Abundance Ratios for RPE Stars

The [Sr/Ba] ratio effectively distinguishes the three sub-classes of RPE stars, as shown in figure 3.10(a). The limited-r stars exhibit the highest [Sr/Ba] ratios and the r-II stars show the lowest [Sr/Ba], whereas the r-I stars fall in between. However, some r-I and r-II stars also show elevated [Sr/Ba] ratios across the same metallicity range as limited-r stars. At lower metallicities, it is generally expected that the majority of Ba originates from r-process events. If Sr were also primarily produced in the same events, we would expect a flat trend of [Sr/Ba] at low metallicity. Nevertheless, the variation in [Sr/Ba] increases as metallicity decreases, as illustrated in figure 3.10(a), suggesting an additional source for Sr production at low metallicities (Travaglio et al. 2004a; Aoki et al. 2013; Spite et al. 2018).

We have also examined the Sr ratio with respect to Eu. The [Sr/Eu] distribution shows a pattern similar to [Sr/Ba], with increased dispersion at lower metallicities (See Figure 3.10(b)). Figure 3.10 (d, e, and f) reveal correlations between [Sr/Fe], [Y/Fe], and [Zr/Fe], with [Eu/Fe], indicating that Sr, Y, and Zr co-produced in the same r-process events with Eu.

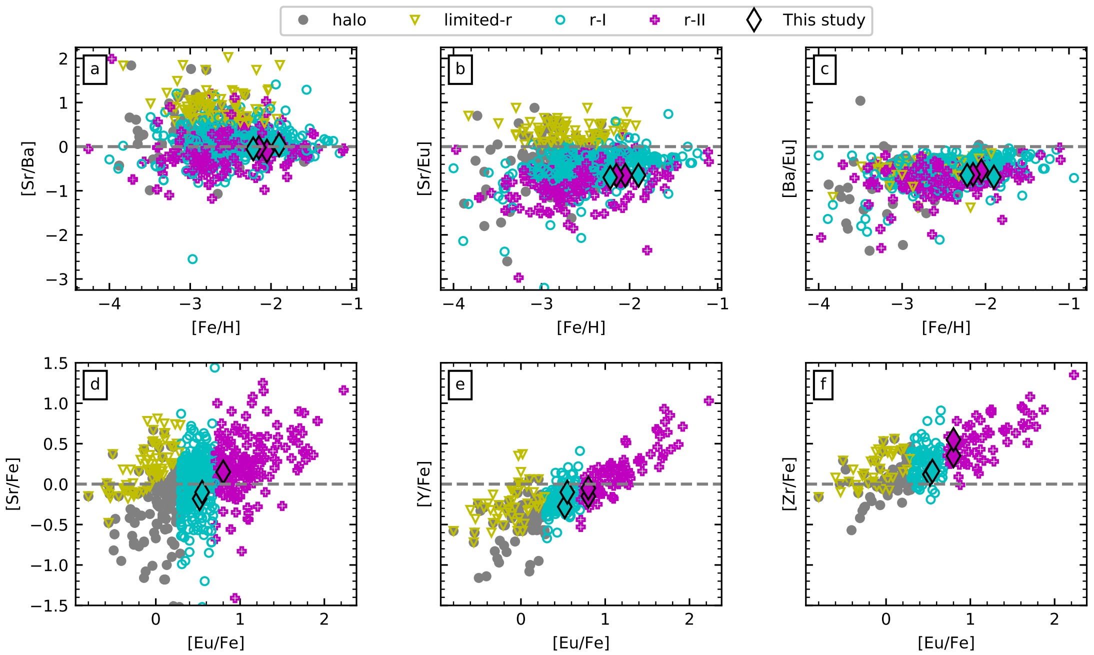

FIGURE 3.10: Evolution of neutron-capture abundance ratios of limited-r (yellow colour), r-I (cyan colour), and r-II (magenta colour) with iron and europium. The four black diamonds indicate the r-I (cyan) and r-II (magenta) from this study. References for the RPE stars are given in the caption of Figure 3.5, and references for normal halo stars are listed in the caption of Figure 3.6.

Figure 3.10(c) illustrates [Ba/Eu] as a function of metallicity. This ratio (excluding a few outliers) displays a small dispersion among r-I, r-II, and limited-r stars, suggesting a similar origin for Ba and Eu in RPE stars. It might be better understood as arising from different levels of dilution of the r-process-element yields from the same source.

Four of our program stars exhibit solar [Sr/Ba] ratios. However, their [Sr/Eu] and [Ba/Eu] ratios are sub-solar, ranging from −0.65 to −0.70 and −0.69 to −0.55, respectively, indicating minimal s-process contamination. The higher [Sr/Ba] ratio compared to [Sr/Eu] and [Ba/Eu] suggests that the ISM where these stars formed was enriched with events producing the first r-process peak elements.

Utilizing the literature sample of RPE stars, we notice that limited-r stars exhibit lower abundances of C, Fe, and Ba compared to r-I and r-II stars (See figure 3.11(a, b, and d)). However, the Sr abundance of limited-r stars spans a similar range as that of r-I and r-II stars. All limited-r objects have metallicities lower than [Fe/H] = −2.0, with only one star, 2MASS J14435196-2106283 from Holmbeck et al. (2020) is found at [Fe/H] = −1.93. Additionally, the [C/H] and [Ba/H] abundance ratios in limited-r stars are consistently smaller than −2.0, with evolution-corrected C abundances falling below [C/H] $<$ −1.7. Most limited-r stars exhibit mixed atmospheres based on their C and N abundances, suggesting RGB mixing or mass transfer from an AGB companion. However, the limited data on C and N abundances do not rule out other potential sources, such as massive-star wind ejecta. Further insights into the origin of limited-r stars can be gained from lithium abundances. These conclusions are drawn from 46 limited-r, 314 r-I, and 128 r-II stars compiled from Gudin et al. (2021). The number of limited-r stars is still not sufficiently large to comment further on their nature.

3.5.4 Evolution and Production of third *r*-process peak

Thorium is exclusively produced through r-process nucleosynthesis. To illustrate how thorium evolves with other light and heavy elements, we present various elemental ratios in Figure 3.12. The [Th/H] ratio shows an increase with the increase in metallicity for both r-I and r-II stars, as depicted in Figure 3.12. At any given metallicity, r-II stars display higher thorium abundances compared to

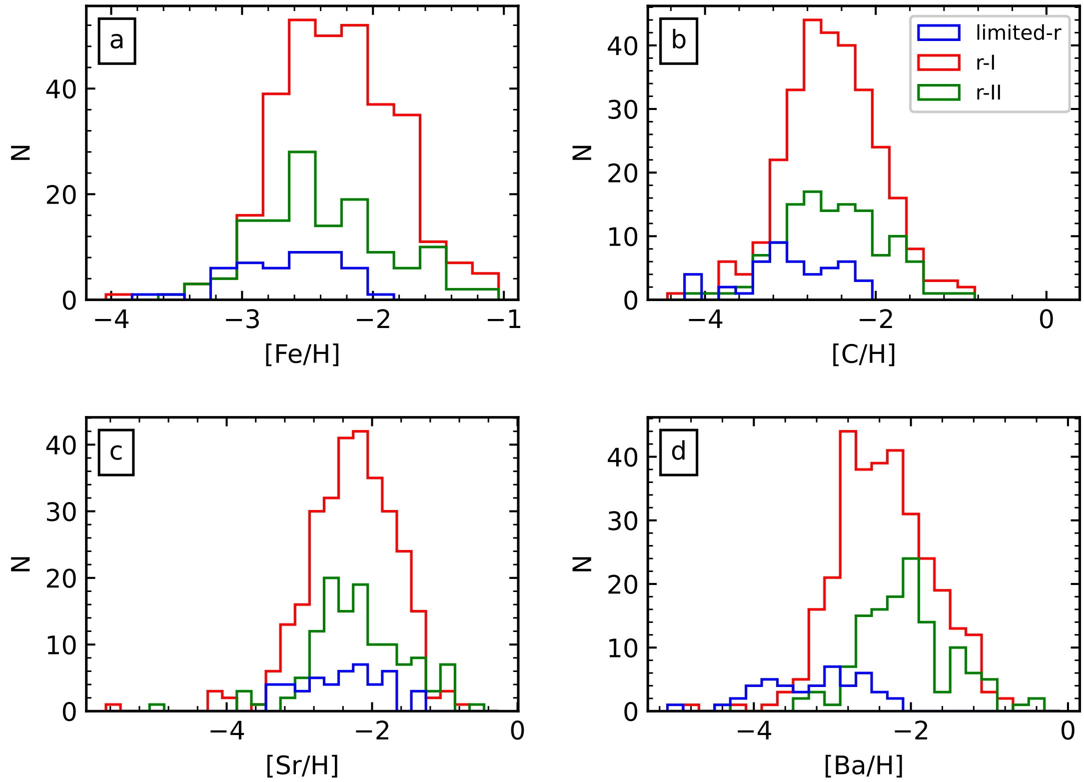

FIGURE 3.11: Comparison of metallicity, C, Sr, and Ba abundance distribution in limited-r (blue color), r-I (red), and r-II (green). References for these objects are given in the caption of Figure 3.5.

r-I stars, which is clear from Figure 3.12(a) and 3.12(b). Unlike [Th/H], the [Th/Fe] ratio decreases with increasing metallicity, even in r-II stars. This could indicate that Fe-peak elements are enriched at a faster rate than the relatively slow radioactive decay of Th.

In Figure 3.12(c), there is an increasing tendency in the [Eu/Th] ratio with [Fe/H]. r-I and r-II exhibit overlapping trends with small scatter. Equal [Eu/Th] ratios in r-I and r-II can be explained with the same production sites for both and more dilution of r-process ejecta in r-I stars.

In Figure 3.12(d), the [Mg/Th] vs. [Fe/H] plot displays interesting distributions for r-I and r-II stars. All r-I stars exhibit higher [Mg/Th] ratios compared to r-II stars. As metallicity increases, [Mg/Th] tends to approach zero, with r-II stars

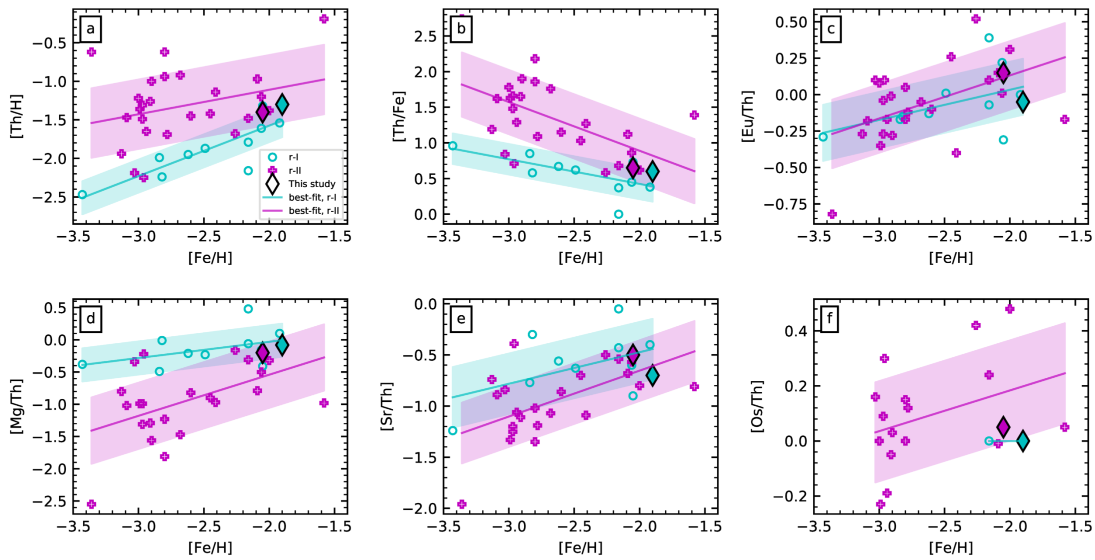

FIGURE 3.12: Evolution of ratios of Th with different elements as a function of metallicity. The r-I are displayed with open cyan circles, and r-II are displayed by magenta crosses. The four black diamonds indicate the r-I (cyan) and r-II (magenta) from this study. The cyan and magenta lines represent fitting to r-I and r-II, respectively. Their corresponding dispersions are shown with the shaded regions. For data reference, see Saraf et al. (2023).

showing a steeper slope than r-I stars. These patterns suggest that differences in the mixing of r-process ejecta in the inherited compositions of r-I and r-II stars may also indicate that r-II stars likely formed earlier than r-I stars. Figure 3.12(e) displays the [Sr/Th] evolution with [Fe/H], showing similar trends for r-I and r-II stars as observed in [Eu/Th], but with larger dispersion. Finally, we have plotted the third-peak element [Os/Th] ratio with metallicity in Figure 3.12(f). For r-II stars, it shows that the [Os/Th] ratio increases with metallicity, similar to the [Eu/Th] ratio. We have only two r-I stars with detectable Os and Th, but their evolutionary trends remain unclear. Future studies involving a larger sample of RPE stars with detected Os and Th should provide deeper insights into their evolution.

Two of our program stars with measured Th abundances reside at higher [Fe/H] values within the sample. Notably, both stars fall within the overlapping region of r-I and r-II trends across all panels of Figure 3.12. The separation of r-I and

r-II sub-classes at the lower-metallicity end seems to disappear as we observe Th evolution with other elements from lighter to heavier elements. Being in the overlapping region and towards higher [Fe/H] values implies that these stars are predominantly enriched by single events, such as NSMs, with little contribution from limited-r events.

3.5.5 The r-process pattern

The abundances of elements produced in the r-process, as a function of their atomic number, exhibit a distinct pattern known as the r-process pattern. This pattern displays three prominent peaks corresponding to atomic numbers $Z \sim 35$ (first peak, probed with Sr, Y, and Zr), $Z \sim 54$ (second peak, probed with Ba and La), and $Z \sim 78$ (third peak, probed with Os and Ir). These peaks arise from three closed neutron shells with neutron numbers 50, 82, and 126, respectively (Sneden et al. 2008; Ji & Frebel 2018b).

Previous works have consistently found that the abundance patterns of metal-poor RPE stars closely resemble the scaled-solar r-process pattern (Sneden et al. 1998; Sneden et al. 2008). This agreement is particularly strong for lanthanides, spanning elements from Ba to Hf. However, lighter r-process elements show some scatter from this pattern, attributed to a different formation mechanism known as the weak r-process or limited-r process. The actinide elements, due to their radioactive nature, also exhibit scatter, with some stars showing excess amounts of Th compared to the scaled-solar r-process pattern, known as actinide-boost stars (Schatz et al. 2002; Mashonkina et al. 2014).

The top panel of Figure 3.13 illustrates the abundance distribution of our program stars relative to their atomic numbers, scaled to the solar r-process Eu. The bottom panel displays their abundances residual. The r-process elemental abundances

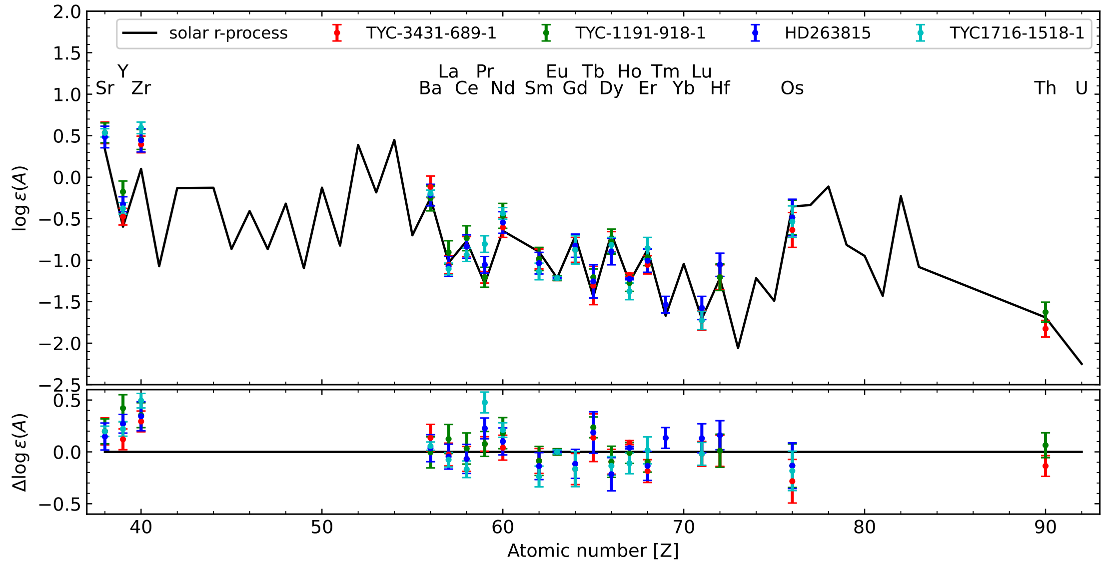

FIGURE 3.13: Top: Black line shows the solar r-process pattern. The elemental abundances of our program stars are scaled to the solar Eu abundance. Bottom: The residual abundances calculated as the difference between scaled stellar abundance and solar abundance. The solar pattern is adopted from Arlandini et al. (1999a)

of our program stars also align with the solar r-process abundances, confirming the main r-process universality pattern (second-peak elements), along with the expected dispersion for the first and third peak elements.

3.5.6 Age estimation

Among the actinide elements, we could estimate the Th abundance for only two of our program stars: TYC 1191-918-1 (r-I star) and TYC 3431-689-1 (r-II star). An upper limit for Th abundance was calculated for HD 263815. Thorium is a radioactive element with a half-life of 14.05 Gyr. The production of Th is only possible in r-process nucleosynthesis (Cowan et al. 1991).

A significant dispersion in the actinide-to-lanthanide abundance ratios has been observed among metal-poor stars (see Holmbeck et al. 2018 and references therein).

Typically, $\log\epsilon$(Th/Eu) serves as an indicator for this ratio. About 30 % of RPE stars exhibit a ratio of 2 to 3 times higher Th/Eu ratio as compared to other RPE stars (Hill et al. 2002a; Mashonkina et al. 2014). These stars, with $\log\epsilon$ (Th/Eu) $> -0.5 \pm 0.15$, classifying them as actinide-boost stars (Holmbeck et al. 2018). Recently, Holmbeck et al. (2019) used $\log\epsilon$(Th/Dy) to categorize stars into different actinide categories.

Actinide-deficient: $\log\epsilon(\mathrm{Th/Dy}) < -1.20$
Actinide-normal: $-1.20 \leq \log\epsilon(\mathrm{Th/Dy}) \leq -0.90$
Actinide-boost: $\log\epsilon(\mathrm{Th/Dy}) > -0.90$

The radioactive nature of Thorium (Th) serves as a chronometer to estimate stellar ages, providing a lower limit on the stellar age based on the time elapsed since its production. The thorium chronometer is based on the universality of the r-process pattern. The Th depletion relative to non-radioactive elements heavier than Barium (Ba), such as Cerium (Ce), Europium (Eu), Dysprosium (Dy), Osmium (Os), Iridium (Ir), etc., are utilized for stellar age calculation. Following relation gives age of the star (Cayrel et al. 2001; Cain et al. 2018; Hansen et al. 2018a):

$$\Delta t = 46.7[\log\epsilon(\mathrm{Th/X})_i - \log\epsilon(\mathrm{Th/X})_f], \tag{3.1}$$

where X is a non-radioactive element above Ba, $\log\epsilon(\mathrm{Th/X})_i$ is the initial abundance ratio when star was born, also known as the production ratio (PR), and $\log\epsilon(\mathrm{Th/X})_f$ is the final abundance ratio, that is now. The error in age is calculated from:

$$\Delta t_{err} = 46.7\sqrt{\sigma^2_{\log\epsilon(\mathrm{Th})} + \sigma^2_{\log\epsilon(\mathrm{X})}}, \tag{3.2}$$

where $\sigma_{\log\epsilon(\mathrm{Th})}$, and $\sigma_{\log\epsilon(\mathrm{X})}$ are the abundance errors of Th and X, respectively. Since the age determination depends only on this abundance ratio, it is necessary to precisely estimate the Th abundance – a small uncertainty of 0.2 dex in log(Th/Eu)

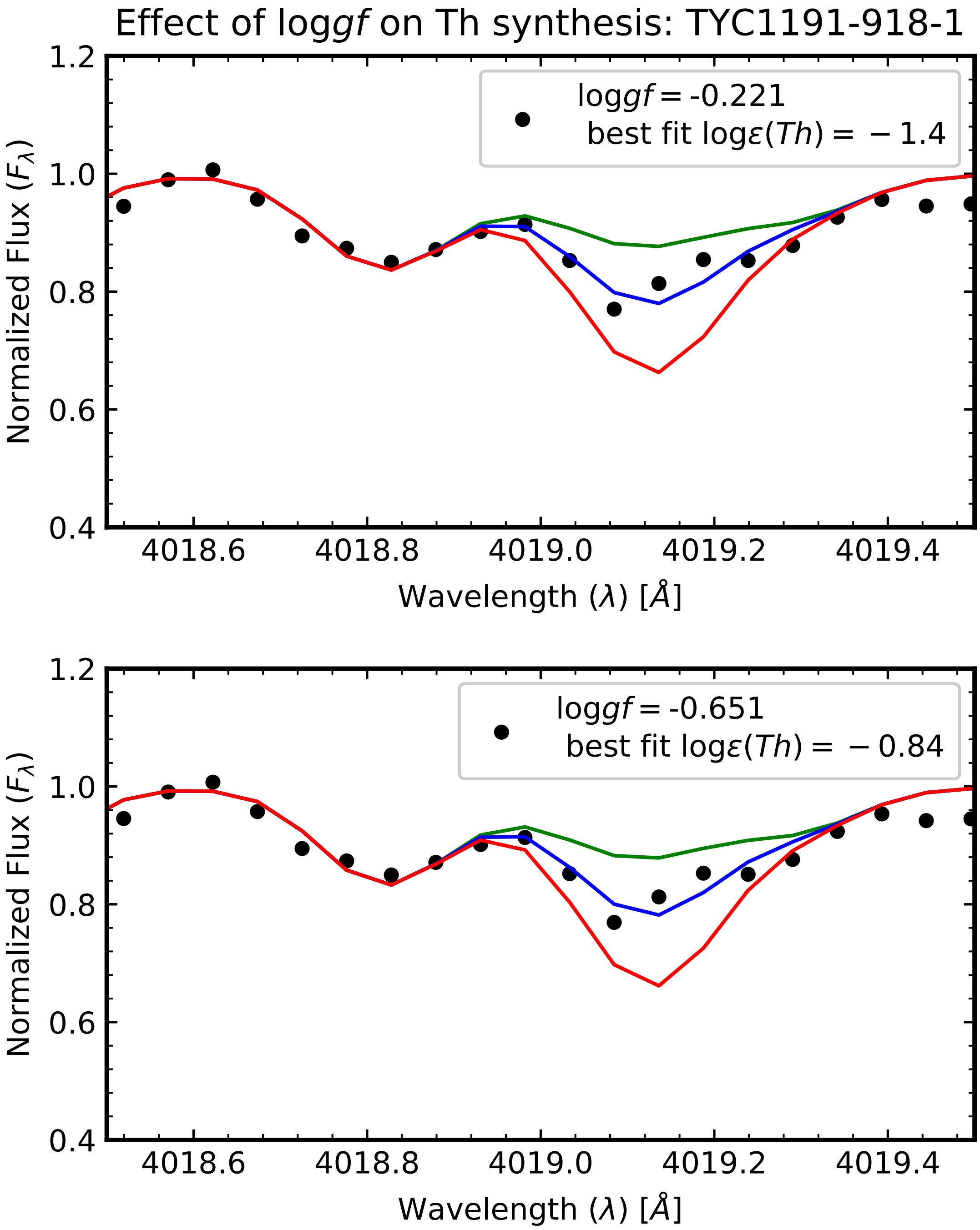

FIGURE 3.14: Th II 4019 Å line synthesis in TYC 1191-918-1 for two different values of $\log gf$, -0.228 and -0.651. The dotted line represents observation and the blue line is the best match model spectrum. The green and red curves show 0.5 dex deviations from the best-fit line.

can produce a 9.3 Gyr error in the age estimate.

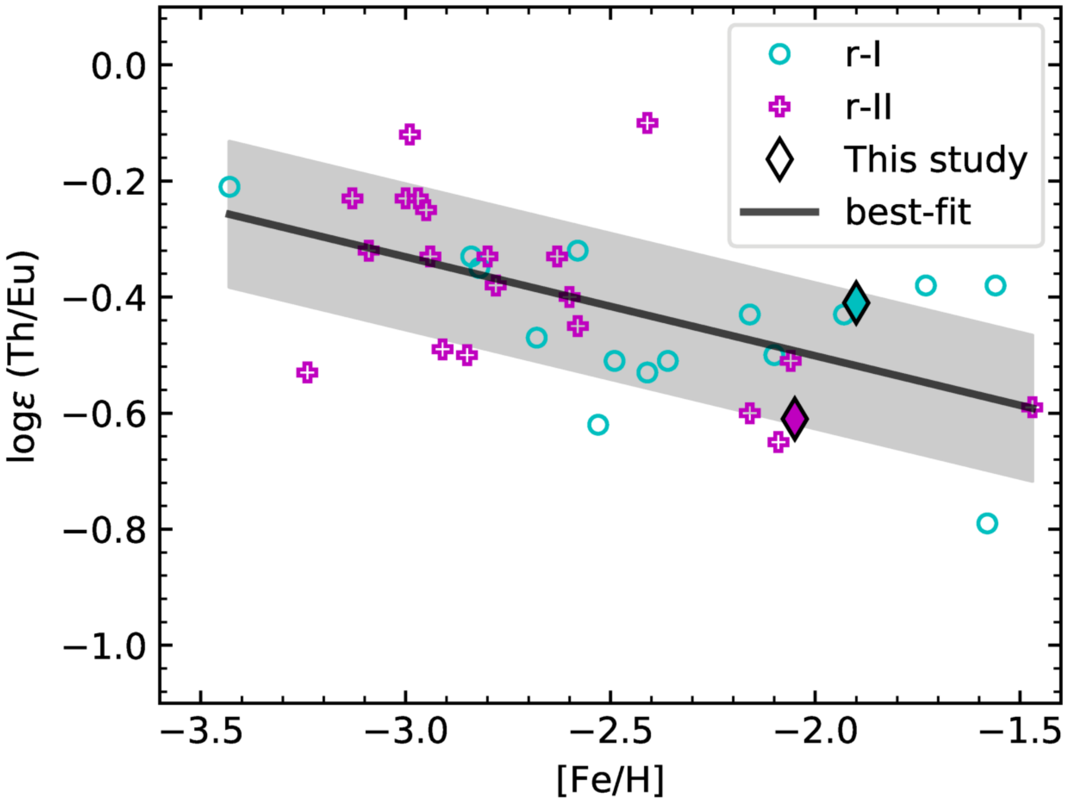

FIGURE 3.15: The $\log\epsilon$ (Th/Eu) evolution with metallicity for RPE stars with measured Th. The r-I are displayed using cyan circles, and the r-II with magenta crosses. The black diamonds indicate the r-I (cyan) and r-II (magenta) from this study. The black line represents the best fit for the data, and the shaded swath is its dispersion. The references for stars with detected Th are given in the caption of Figure 3.12

Even if we carefully consider the effects of the blending in the abundance estimation of Th, the choice of $\log gf$ can significantly affect its abundance determination. In the literature, the value of $\log gf$ for this species is continuously being updated; the current value of $\log gf$ may differ from previously employed values, resulting in different abundance estimates. Figure 3.14 illustrates the spectrum synthesis of the Th II line at 4019 Å in TYC 1191-918-1, using two different $\log gf$ values, -0.228 and -0.651. In this figure, the dots represent the observation, and the blue line indicates the best fit. The green and red lines show dispersion of 0.5 dex. As anticipated, varying $\log gf$ values lead to different Th abundances, which significantly impact the accuracy of age estimates for the star. We use an updated $\log gf$

TABLE 3.12: Age estimation of TYC 3431-689-1.

		TYC 3431-689-1			
Th/X	PR (Schatz et al. 2002)	Age (Gyr)	PR (Hill et al. 2017b)	Age (Gyr)	σ (Gyr)
Th/Ba	–	–	−1.058	30.50	7.67
Th/La	−0.60	7.95	−0.362	19.08	6.95
Th/Ce	−0.79	9.35	−0.724	12.44	7.30
Th/Pr	−0.30	14.96	−0.313	14.36	5.71
Th/Nd	−0.91	14.50	−0.928	13.65	7.30
Th/Sm	−0.61	10.75	−0.796	2.05	7.30
Th/Eu	−0.33	13.09	−0.240	17.3	4.88
Th/Gd	−0.81	6.54	−0.569	17.8	8.43
Th/Dy	−0.89	7.48	−0.827	10.43	7.30
Th/Ho	–	–	−0.071	27.08	4.77
Th/Er	−0.68	4.21	−0.592	8.32	6.95
Th/Hf	−0.20	19.64	−0.036	27.31	8.4
Th/Os	−1.15	1.87	−0.917	12.77	10.88
Median		9.35		14.36	7.30

value of −0.228 for Th abundance estimation and use the resulting abundance for the age calculation of our program stars. The production ratios (PR) of elements used in equation 3.1 are sourced from Schatz et al. (2002) and Hill et al. (2017b). Tables 3.12 and 3.13 list the estimated ages derived from individual species and their median values for Th-detected stars. Using recent PR values from Hill et al. (2017b), the median age of TYC 3431-689-1 is determined to be 14.36 ± 7.3 Gyr, which can be expected for a VMP star. In contrast, the median age of TYC 1191-918-1 is calculated as 9.19 ± 8.98 Gyr, lower than expected, likely due to a higher Th abundance.

Th and U are crucial for estimating the ages of approximately 10 billion-year-old stars. The primary sources of uncertainty in the Th chronometer are its long half-life of 14.05 Gyr and the production ratio of the second and third *r*-process peak elements. The detection of U along with Th would have been of much importance to constrain the ages of our program stars independent from stellar

TABLE 3.13: Age estimation of TYC 1191-918-1.

		TYC 1191-918-1			
Th/X	PR (Schatz et al. 2002)	Age (Gyr)	PR (Hill et al. 2017b)	Age (Gyr)	σ (Gyr)
Th/Ba	–	–	−1.058	14.59	8.98
Th/La	−0.60	5.61	−0.362	16.74	8.62
Th/Ce	−0.79	4.67	−0.724	7.76	8.98
Th/Pr	−0.30	5.61	−0.313	5.00	7.93
Th/Nd	−0.91	11.69	−0.928	10.85	8.98
Th/Sm	−0.61	1.40	−0.796	−7.29	8.62
Th/Eu	−0.33	3.74	−0.240	7.95	5.78
Th/Gd	−0.81	–	−0.569	–	–
Th/Dy	−0.89	−1.87	−0.827	1.07	8.98
Th/Ho	–	–	−0.071	–	–
Th/Er	−0.68	–	−0.592	–	–
Th/Hf	−0.20	10.29	−0.036	17.96	9.35
Th/Os	−1.15	−0.467	−0.917	10.43	11.31
Median		4.67		9.19	8.98

evolution models, and thus the minimum age of the universe, because U has a smaller half-life of 4.5 Gyr, both the elements (Th and U), belongs to same (third) r-process peak, and are only produced in r-process nucleosynthesis (Cayrel et al. 2001; Barbuy et al. 2011).

We have determined the actinide-to-lanthanide abundance ratio for our program stars with detected Th. According to Holmbeck et al. (2018), both stars belong to the actinide-normal category. However, based on the criteria of Holmbeck et al. (2019), TYC 3431-689-1 remains in the actinide-normal class, while TYC 1191-918-1 shifts into the actinide-boost region near the separation boundary. We believe this determination of an actinide boost may be due to the uncertainties in our abundance estimation. TYC 1191-918-1 was previously identified as an actinide-boost star by Bandyopadhyay et al. (2020c), with $\log \epsilon$ (Th/Eu) $= -0.20$. There could be three possible reasons for their higher actinide-to-lanthanide ratio: (1) differences in the adopted stellar parameters, (2) incomplete accounting of the contribution from blended elements, and/or (3) their choice of a lower log gf value.

Figure 3.15 illustrates log ϵ (Th/Eu) with [Fe/H] for our two Th-detected stars, overlaid with the RPE stars from existing literature. Our program stars are denoted by black diamonds, while r-I and r-II are indicated by cyan circles and magenta crosses, respectively. The black solid line indicates the best-fit linear relationship, with the grey region indicating dispersion around this line. From inspection, there is a clear trend of a decreasing actinide-to-lanthanide ratio with increasing metallicity. If we take metallicity as a proxy for age, this implies that older stars are more actinide-rich than younger stars, contrary to the universality of the r-process pattern. According to this paradigm, older stars should be more actinide poor than younger stars. This opposite trend could result from two possibilities for the non-universal production ratio: (1) the late universe is enriched by lanthanides, or (2) the early universe is enriched by actinides. The first possibility appears more likely in terms of the production site(s) of these elements, although the production sites of the actinides are less well understood.

The assumption of a linear trend of the actinide-to-lanthanide production ratio with metallicity may be one of the possible reasons for higher dispersion in this ratio, leading to the actinide-boost phenomenon. Assuming a constant actinide-to-lanthanide production ratio yields negative ages for actinide-boost stars and large uncertainties in the age estimation using this method. If the r-process pattern is truly universal, the production ratio needs to be calibrated for the chemical evolution of the galaxy. And, of course, a much larger sample of RPE stars is needed to provide better constraints on the astrophysical formation sites of such stars.

3.6 Conclusion

In this study, we conducted abundance estimations for four bright ($V < 12$) VMP RPE stars observed with the 10-m class GTC telescope. Due to the excellent high SNR of the spectra in the blue region, we derived abundances for 10 neutron-capture elements not previously reported by (Bandyopadhyay et al. 2020c): Pr, Gd, Tb, Ho, Hf, Er, Tm, Lu, Os, and Th, along with improved estimates for others. Our analysis revealed two r-I and two r-II stars, with Th measured in TYC 1191-918-1 (r-I) and TYC 3431-689-1 (r-II). Additionally, we obtained upper limits for Pb abundances in HD 263815, TYC 3431-689-1, and TYC 1716-1548-1. The elemental abundance patterns of our stars closely resemble the scaled-solar r-process patterns in the main r-process region (Ba to Hf). Notably, we observed [C/N] < -1.0 and ^{12}C/^{13}C< 10, indicating internal mixing of CN-cycle nucleosynthesis products. We also study the elemental-abundance trends among the RPE stars; the main conclusions are listed below.

The RPE stars demonstrate a comparable trend in [α/Fe] and [Fe/H] when contrasted with normal metal-poor halo stars. However, r-II stars display a declining trend in [Eu/Fe], possibly suggesting efficient mixing of the ISM at higher metallicities.

Furthermore, Fe-peak elements generally exhibit flat trends relative to [Eu/Fe], except for Mn, Cr, and Zn. We observed high [Zn/Fe] and low [Eu/Zn] in metal-poor stars, suggesting Zn production via r-process events in the early Galaxy. Four of our program stars, with [Fe/H] ranging from -2.22 to -1.90, show near-solar [Zn/Fe] ratios, implying minimal contribution from r-process sources to Zn abundance at relatively higher metallicities.

The [Sr/Fe], [Y/Fe] and [Zr/Fe] ratio display a linear trend with respect to [Eu/Fe]. This indicates that the site that made Eu is also a significant contributor to Sr, Y and Zr.

The abundance trend in Th and Mg with respect to [Fe/H] indicates that there could be some delay between the formation of r-II stars and r-I stars.

Due to the radioactive properties of thorium, age estimates were derived for TYC 3431-689-1 and TYC 1191-918-1, yielding values of 14.36$\pm$7.3 and 9.19$\pm$8.98 Gyr, respectively. We emphasize the role that production ratios, nuclear physics, and astrophysical sites of the r-process play a role on the uncertainty in age estimation.

We have identified intriguing signatures, yet definitive conclusions necessitate more comprehensive data, including additional stars and abundances, following the footsteps of the RPA. Discovering more RPE stars and analyzing abundances across neutron-capture peaks across a wider metallicity spectrum can elucidate the astrophysical sites of the r-process and their role in the Galaxy's chemical evolution.

Chapter 4

Differential abundance analysis of *r*-process stars using VLT

Abstract

We present a strictly line-by-line differential analysis comparing a moderately RPE star (r-I: HD107752) to an extremely RPE star (r-II: CS31082-0001), to investigate the possible common origin of their heavy element nucleosynthesis with high precision abundances. We utilized high-resolution and high SNR spectra obtained from the UVES spectrograph of the VLT. Focusing only on the lines common to both spectra, we calculated differential abundances for 16 light/Fe-peak elements and 15 neutron-capture elements. We report the abundances of O, Al, Pr, Gd, Dy, Ho, Er, and the detection of Tm in HD107752 for the first time. Our analysis reveals three distinct features in the differential abundance patterns. We observe

nearly equal abundances of light elements up to Zn in both stars, suggesting a common origin for these elements without any noticeable odd-even pattern. Regarding neutron-capture elements, r-I stars exhibit mildly depleted light r-process elements and even more depleted heavier r-process elements, a phenomenon challenging to explain with a single production site for these elements. Notably, a strong correlation between light and main r-process abundances is evident among both r-I and r-II stars, indicating that production sites could be similar in nature.

4.1 Introduction

Despite decades of research, the synthesis and evolution of r-process in the Galaxy is still poorly understood. Several astrophysical sites have been proposed with lacking observational confirmation (see Chapter 1 for more discussion). The accurate determination of elemental abundance patterns in metal-poor stars is crucial for understanding r-process. Traditionally, absolute abundances are employed to investigate stellar chemistry, relying heavily on atomic data for line formation. However, uncertainties associated with atomic data propagate into elemental abundance determinations, persisting even in high-resolution and high SNR spectra (e.g., see elemental errors in Cayrel et al. 2004; Arnone et al. 2005). Nonetheless, the differential abundance analysis technique enhances precision in spectroscopic studies by mitigating errors arising from uncertainties in transition probabilities ($\log gf$) (Bedell et al. 2014; Nissen & Gustafsson 2018).

The technique of differential abundance analysis has a long history in stellar spectroscopy. Its origins trace back to Danziger (1965), who conducted the first-ever differential abundance analysis of HD 116713 and HD 83548 relative to α Boo. Subsequently, numerous researchers have employed this method to achieve high-precision abundance determinations and detect subtle differences in abundance patterns (Sadakane et al. 2003; Ramírez et al. 2019; Nissen & Gustafsson 2018). Notably, Meléndez et al. (2012) utilized this technique to identify HIP 56948 as a potential candidate for hosting an Earth-like system. Differential abundance analysis is commonly utilized in the search for planetary systems, solar-twin stars, and habitable planets, as well as in understanding planet formation processes (Zhao et al. 2002; Paulson et al. 2003; Huang et al. 2005; Meléndez et al. 2009; Liu et al. 2014; Yana Galarza et al. 2016; Jofré et al. 2021). Additionally, Reitermann et al. (1989) extended the application of this technique to globular cluster stars in the Small Magellanic Clouds (SMC) and Large Magellanic Clouds (LMC), revealing under abundances of metals by a factor of three to four in these clusters.

Several investigations have employed the technique of differential abundance analysis to gain insights into metal-poor stars. Recently, O'Malley et al. (2017) conducted differential abundance calculations for metal-poor main-sequence (MS) stars compared to the Sun. Reggiani et al. (2016) were pioneers in utilizing the differential abundance analysis technique for the extremely metal-poor stars G64-12 and G64-37, both of which are CEMP stars (Placco et al. 2016). Over the past decade, there has been growing interest in applying differential analysis to metal-poor globular clusters (GCs). Koch & McWilliam (2011) investigated light elements up to the Fe-peak in the GC NGC 6397 (Roederer & Sneden 2011) and while Yong et al. (2013) explored differential abundances of neutron-capture elements in GCs M92 and NGC 6752, respectively. Additionally, Westin et al. (2000) conducted a detailed analysis of the differential abundance pattern of r-II star HD 115444 relative to the normal metal-poor star HD 122563.

In this investigation, we conducted line-by-line differential analysis of two r-process-rich objects of comparable stellar parameters, one categorized as r-I and other as r-II. This analysis enabled us to determine abundances with errors less than 0.05 dex.

4.2 Sample selection and data acquisition

As a prior work to this study, we initially compiled a dataset comprising all r-process-rich metal-poor stars with [Fe/H] < -1.0, along with their respective atmospheric parameters, sourced from Gudin et al. (2021). This compilation consisted of a total of 519 such stars, gathered from four releases of the RPA data (Hansen et al. 2018b; Sakari et al. 2018; Ezzeddine et al. 2020; Holmbeck et al. 2020), JINAbase (Abohalima & Frebel 2018), and other recent literature. Since the differential abundance analysis method necessitates a well-characterized standard star with closely matching atmospheric parameters to the program star, we conducted a search for suitable candidates within our compiled dataset. BPS CS 31082-0001 (hereafter referred to as CS31082-0001) was chosen as the standard star due to its extensive study and availability of detailed spectroscopic measurements of stellar parameters and abundances. Following the selection of the standard star, we identified HD 107752 (hereafter HD107752) as the program star for our present differential analysis, owing to its closely resembling atmospheric parameters to those of the standard star. Both CS31082-0001 and HD107752 exhibit highly similar stellar atmospheres. Figure 4.1 illustrates the comparison between the standard and program stars in the Eu region.

To minimize errors in the analysis, it is preferable to obtain high-resolution and high SNR spectra of both objects from the same instrument. Considering this, we obtained optical spectra for both stars from the ESO portal *. These observations were conducted with the VLT/UVES (Dekker et al. 2000) facility. CS31082-0001 was observed by R. Cayrel, while HD107752 was observed by CJ Hansen. Table 4.1 lists all basic parameters, such as RA, DEC, V-mag, observation date, observation ID, spectral range, spectral resolution, and heliocentric radial velocity, for the selected stars. Reduced spectra for both stars are available in the ESO archive

*European Southern Observatory (ESO) Science Portal: https://archive.eso.org/scienceportal/home

TABLE 4.1: Basic information of our program stars.

Name	RA	DEC	V-mag	obs date	obs ID	range	S/N	Res	RV (km/s)
CS31082-0001	01:29:31.13	−16:00:45.49	11.64	2003-10-05	072.D-0780	3750-4978	>100	68040	139
CS31082-0001	01:29:31.13	−16:00:45.49	11.64	2001-09-05	165.N-0276	4701-6735	>100	80930	139
HD107752	12:22:52.71	+11:36:25.48	10.07	2020-03-03	0104.D-0059	3281-4516	>100	40970	219
HD107752	12:22:52.71	+11:36:25.48	10.07	2020-03-03	0104.D-0059	4617-6642	>100	42310	219

†. The spectra were normalized using the Image Reduction and Analysis Facility (IRAF) package ‡. Subsequently, we calculate earth-centric radial velocities using an IDL routine, CRSCOR. Additionally, we corrected radial velocities for the Earth's motion to estimate heliocentric radial velocities.

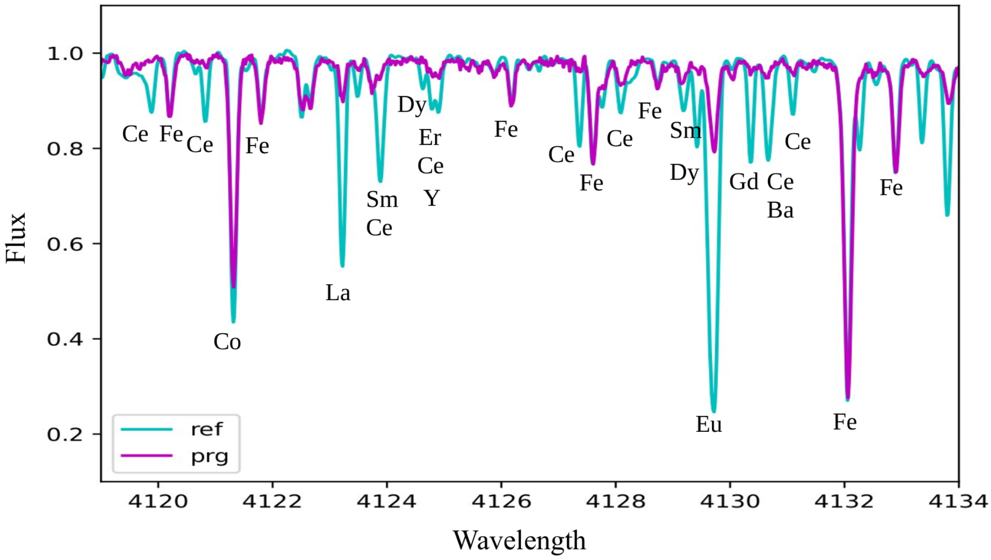

FIGURE 4.1: Comparison of program and reference star spectra in the Eu region.

Next, we degrade the spectral resolution of CS31082-0001 to match the spectral resolution of HD107752. For this purpose, we convolve the spectrum of CS31082-0001 with a Gaussian whose standard deviation varies with wavelength and is given by $\sigma = \sqrt{[(\frac{\lambda}{R_{\rm lr}})^2 - (\frac{\lambda}{R_{\rm hr}})^2]}/2.355$, where $R_{\rm lr}$ and $R_{\rm hr}$ respectively represent spectral resolutions of low-resolution and high-resolution spectra. CS31082-0001 has spectral gaps of 4515-4620 Å & 5595-5765 Å and HD107752 has spectral gaps

†Based on data obtained from the ESO Science Archive Facility with DOI(s): https://doi.org/10.18727/archive/50

‡https://iraf-community.github.io

of 4515-4620 Å & 5595-5670 Å. It leaves us with spectral ranges 3750-4515 Å, 4620-5595 Å and 5765-6642 Å for differential analysis.

4.3 Stellar Parameters

To further proceed, we calculate stellar atmospheric parameters. The stellar atmosphere of a star is characterized by its effective temperature (T_{eff}), surface gravity ($\log g$), metallicity ($[Fe/H]$), and micro-turbulence (ξ). In the following subsections, we will discuss the spectroscopic method for stellar parameter estimation.

4.3.1 Stellar parameters estimation of standard stars

Although there is plenty of literature that provides spectroscopically measured stellar parameters of the standard star CS31082-0001, we performed our own analysis to estimate its stellar parameters. We did not directly adopt the stellar parameters from the literature because we wanted to maintain consistency in the analysis throughout the paper. To move forward after line list preparation, we generate a grid of model stellar atmospheres using ATLAS9 code (Kurucz 1993b; Castelli & Kurucz 2003). We have used TURBOSPECTRUM (Alvarez & Plez 1998; Plez 2012) for abundance calculation of Fe I and Fe II lines which are later used for parameters estimation of stars.

We have used the well-known spectroscopic methodology to derive all four atmospheric parameters. The T_{eff} of the standard object is obtained by forcing zero slope of Fe I abundance vs lower excitation potential (LEP). To estimate the micro-turbulence velocity (ξ), we have forced zero trend of Fe I abundance

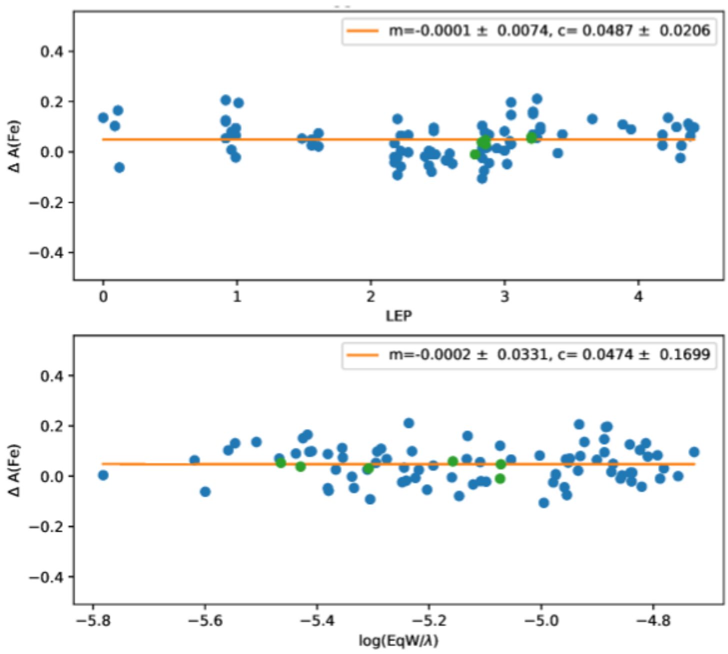

FIGURE 4.2: Stellar parameter estimation of HD107752 using differential abundance analysis with respect to CS31082- 0001

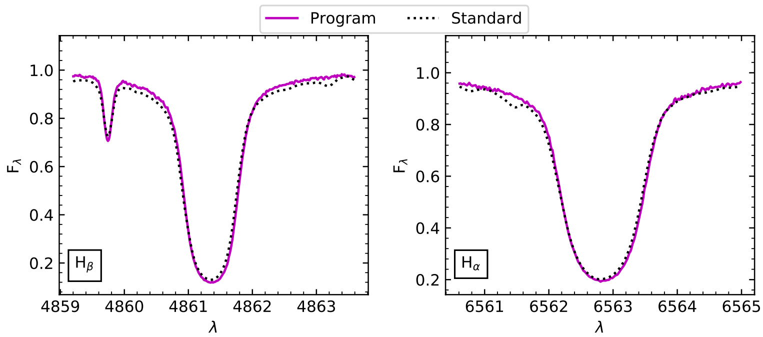

FIGURE 4.3: Comparison of program and reference star spectra in H_β and H_α regions, indicating similarities in the stellar parameters

as a function of reduced EW, $EW_r = \log(EW/\lambda)$. The surface gravity ($\log g$) is calculated assuming ionization equilibrium between neutral and ionized species, i.e., both, Fe I and Fe II provide the same abundance. The metallicity ([Fe/H]) is obtained from the model metallicity satisfying all three conditions simultaneously. Our analysis returns T_{eff} = 4826.00, ξ = 1.80, $\log g$ = 1.55, [Fe/H]= -2.81 for CS31082-0001.

4.3.2 Line-by-line differential stellar parameters of program star

Now, we estimate the stellar parameters of program star HD107752 using a strictly line-by-line differential approach. Thus, we make a line list of Fe I and Fe II features that are measurable in standard and program stars. Since both the stars have nearly similar stellar atmospheres, we used the grid of atmospheric models generated for CS31082-0001 to calculate the abundance of Fe I and Fe II lines. Following Meléndez et al. (2012) and Yong et al. (2013) notation, we define the differential abundance for ith line of element X as,

$$\delta A_i^X = A_i^X(program) - A_i^X(standard) \tag{4.1}$$

The T$_{eff}$ of the program star is estimated assuming excitation equilibrium of Fe I differential abundance,

$$\frac{\partial(\delta A_i^{Fe\ I})}{\partial(LEP)} = 0. \tag{4.2}$$

The micro-turbulence (ξ) is obtained by forcing zero trends of Fe I differential abundance as a function of reduced equivalent width,

$$\frac{\partial(\delta A_i^{Fe\ I})}{\partial(EW_r)} = 0. \tag{4.3}$$

The surface gravity ($\log g$) is obtained assuming ionization balance between neutral and ionized species.

$$\langle\delta A_i^{Fe\ I}\rangle - \langle\delta A_i^{Fe\ II}\rangle = \Delta A^{Fe\ I} - \Delta A^{Fe\ II} = 0, \tag{4.4}$$

where ΔA^X represents the average differential abundance, $\langle\delta A_i^X\rangle$, of element X. The [Fe/H] of the program star is taken from the metallicity of the model atmosphere. Figure 4.2 shows the stellar parameter estimation of HD107752 using the differential technique. Our differential analysis gives T$_{eff}$ = 4926.02, ξ = 1.83,

TABLE 4.2: Stellar parameters of standard and program stars.

T_{eff}	$\log g$	$[Fe/H]$	ξ	Reference
CS31082-0001				
4826.00	1.55	−2.81	1.80	This Work
4876	1.80	−2.81	2.13	Hansen et al. (2018b)
4640	1.25	−3.00	2.25	Frebel et al. (2013)
4846	1.70	−2.82	2.25	Frebel et al. (2013)
4825	1.80	−2.91	1.50	Cayrel et al. (2004)
4866	1.66	−2.75	1.40	Yong et al. (2013)
4650	1.05	−3.03	1.55	Roederer et al. (2014)
4922	1.90	−2.78	1.88	Barklem et al. (2005)
4825	1.50	−2.90	1.80	Hill et al. (2002b)
4925	1.51	−2.81	1.40	Hansen et al. (2013)
HD107752				
4926.02	1.46	−2.77	1.83	This Work
4750	0.80	−2.60	2.70	Luck & Bond (1985)
4700	1.70	−2.69	1.40	Burris et al. (2000)
4826	1.60	−2.78	1.90	Ishigaki et al. (2013)
4649	1.60	−2.78	2.00	Ishigaki et al. (2013)
4826	1.61	−2.77	1.85	Ishigaki et al. (2012)
4370	0.54	−3.16	1.58	Zhang et al. (2009)

$\log g = 1.46$, [Fe/H]$= -2.77$ for HD107752. Table 4.2 represents the comparison of stellar parameters estimation from different literature and this study. Figure 4.3 compares H_β and H_α region of standard and program stars.

4.3.3 Error in stellar parameters

To determine the uncertainty in calculating stellar parameters, we followed the methodology described in Yong et al. (2013). The uncertainty in effective temperature ($\sigma T_{\rm eff}$) was derived from the error in the slope between δAi^X and LEP. We adjusted $T_{\rm eff}$ in our model until the slope matched the error of the original slope (0.0074 in this case). The discrepancy between the original and adjusted $T_{\rm eff}$ provides the error in $T_{\rm eff}$. Similarly, we derived the uncertainty in micro-turbulence ($\sigma\xi$) by altering ξ in the model until the new slope matched the error in the initial slope (0.0331). The difference in micro-turbulence before and after adjustment indicates the error in ξ. For surface gravity ($\sigma \log g$), we modified $\log g$ until the difference $\Delta A^{Fe\ I} - \Delta A^{Fe\ II}$ equaled the total error calculated using the quadrature sum of the errors in $\Delta A^{Fe\ I}$ and $\Delta A^{Fe\ II}$ (i.e ($\sqrt{(\sigma\Delta A^{Fe\ I})^2 + (\sigma\Delta A^{Fe\ II})^2}$)). The uncertainty in metallicity ($\sigma[Fe/H]$) was determined by the standard deviation in $\Delta A^{Fe\ I}$. For our program star, the uncertainties are found to be ($\sigma T_{\rm eff}$, $\sigma\xi$, $\sigma \log g$, $\sigma[Fe/H]$) = (28 K, 0.08 km s^{-1}, 0.017 cgs, 0.09 dex).

4.4 Abundance Analysis

We determine the atmospheric parameters of the standard object using traditional spectroscopic methods and the program object using a line-by-line differential abundance approach. To assess the abundances of other elements, we identified all the element absorption lines present in the spectra. For precise line-by-line differential abundance estimates, we only considered the common lines between the standard and program stars. As mentioned in Section 4.3, we utilized the ATLAS9 atmospheric model with the TURBOSPECTRUM code for abundance measurements. We performed both EW analysis and spectral fitting in this study. The EW analysis was conducted on lines that are clear and unblended, primarily light elements, while spectral synthesis was applied to unclear and blended lines, mainly heavy elements. Blends were accounted for using their distinct lines from other parts of the spectrum. When necessary, hyper-fine splitting was incorporated into the spectral synthesis.

Initially, we calculated the absolute abundances for each identified line in the standard star CS31082-0001 and the program star HD107752. Employing equation (4.1), we conducted a meticulous line-by-line differential analysis of HD107752 relative to CS31082-0001. When multiple lines were available for a particular species, we averaged the differential abundances to represent the overall differential abundance for that species.

4.4.1 Differential abundances of light and Fe-peak elements

We performed the spectral synthesis of a molecular band, CH G-band, near 4313Å wavelength to evaluate the differential abundance of carbon. Due to good SNR and high-resolution spectra, we are able to identify clean and free from blend lines for several light and iron-peak elements. We calculated the EWs of these lines to estimate their elemental abundances in both stars. Then a strictly line-by-line differential abundance analysis is performed for individual feature. Among the light species, we could determine differential abundances of Na, Mg, Al, and Si. In the iron-peak group of elements, we have estimated differential abundances of Ca, Sc, Ti, V, Cr, Mn, Co, Ni, and Zn. The abundances of Na and Al are significantly influenced by the NLTE effect. However, effect gets cancel out due to similar atmospheric parameters.

4.4.2 Differential abundances of neutron-capture elements

For heavy elements, we have used both EW analysis and spectral fitting methods. The equivalent width analysis approach is employed where clean and free-from-blended lines are available. Abundances of blended lines are estimated with spectral synthesis technique. The contribution of blends is measured from clean lines present in the other part of the spectra. Whenever required, we have taken into account the hyperfine transitions from McWilliam (1998). Abundances of lines having hyperfine transitions are always estimated using the spectral synthesis technique. We could measure the abundances of Sr, Y, and Zr among first r-process peak elements. However, we identified Ba, Ce, Pr, Nd, Sm, Eu, Gd, Dy, Er, and Tm from the second r-process peak.

4.4.3 Uncertainties in abundance calculation

The total error in the abundance analysis comprises random and systematic errors. The random error comes particularly from the uncertainty in equivalent width measurement, oscillator strength, and contribution of blends. However, the systematic error appears due to uncertainty in stellar parameter estimation. The sum of all the errors in quadrature returns total uncertainty in the abundance.

$$
\begin{aligned}
\sigma^2_{\log\epsilon} &= \sigma^2_{\rm rand} + \sigma^2_{\rm sys} \\
\sigma^2_{\log\epsilon} &= \sigma^2_{\rm rand} + \left(\frac{\partial \log\epsilon}{\partial T}\right)^2 \sigma^2_T + \left(\frac{\partial \log\epsilon}{\partial \log g}\right)^2 \sigma^2_{\log g} \\
&\quad + \left(\frac{\partial \log\epsilon}{\partial \xi}\right)^2 \sigma^2_\xi + \left(\frac{\partial \log\epsilon}{\partial [Fe/H]}\right)^2 \sigma^2_{[Fe/H]}
\end{aligned}
\tag{4.5}
$$

where $\sigma^2_{\rm rand}$ and $\sigma^2_{\rm sys}$ are the random and systematic errors, respectively. If we use N number of lines to measure the abundance of a species, its random error is defined as $\sigma/\sqrt{N}$. To estimate the partial derivatives of equation (4.5), we

TABLE 4.3: Detailed differential abundances of HD107752 with respect to CS31082-0001.

Element	Species	Atomic No.	N_{lines}	A^X (solar)	*mean_CS*	ΔA^X	Δ[X/Fe]	σ
C	CH-band	6	1	8.39	5.800	0.09	0.05	0.038
O	O I	8	1	8.66	6.670	−0.2	−0.24	0.022
Na	Na I	11	2	6.17	3.664	0.074	0.034	0.069
Mg	Mg I	12	5	7.53	5.281	0.118	0.078	0.056
Al	Al I	13	2	6.37	2.940	−0.1	−0.14	0.054
Si	Si I	14	1	7.51	4.680	0.15	0.11	0.033
Ca	Ca I	20	7	6.31	3.873	0.023	−0.017	0.026
Sc	Sc II	21	4	3.17	0.285	−0.062	−0.102	0.045
Ti	Ti I	22	8	4.9	2.382	0.025	−0.015	0.04
Ti	Ti II	22	12	4.9	2.428	−0.065	−0.105	0.024
V	V II	23	2	4	1.280	−0.045	−0.085	0.052
Cr	Cr I	24	4	5.64	2.565	0.168	0.128	0.037
Cr	Cr II	24	2	5.64	3.122	−0.185	−0.225	0.063
Mn	Mn I	25	4	5.39	2.155	0.005	−0.035	0.041
Fe	Fe I	26	87	7.45	−2.810	0.04	0	0.006
Fe	Fe II	26	8	7.45	−2.810	0.04	0	0.01
Co	Co I	27	1	4.92	2.430	0.05	0.01	0.053
Ni	Ni I	28	4	6.23	3.360	−0.111	−0.151	0.032
Zn	Zn I	30	2	4.6	2.000	−0.065	−0.105	0.021
Sr	Sr II	38	2	2.92	0.745	−0.405	−0.445	0.079
Y	Y II	39	7	2.21	−0.161	−0.616	−0.656	0.03
Zr	Zr II	40	7	2.58	0.551	−0.493	−0.533	0.042
Ba	Ba II	56	4	2.17	0.325	−0.98	−1.02	0.06
La	La II	57	5	1.13	−0.460	−1.12	−1.16	0.045
Ce	Ce II	58	2	1.7	−0.285	−0.825	−0.865	0.034
Pr	Pr II	59	2	0.58	−0.860	−0.855	−0.895	0.075
Nd	Nd II	60	6	1.45	−0.087	−1.068	−1.108	0.028
Sm	Sm II	62	2	1	−0.435	−1.09	−1.13	0.055
Eu	Eu II	63	2	0.52	−0.760	−1.06	−1.1	0.023
Gd	Gd II	64	3	1.11	−0.253	−0.91	−0.95	0.035
Dy	Dy II	66	1	1.14	−0.060	−1.06	−1.1	0.024
Ho	Ho II	67	1	0.51	−1.000	−0.93	−0.97	0.052
Er	Er II	68	1	0.93	−0.320	−1.19	−1.23	0.049
Tm	Tm II	69	1	0	−1.210	−1.03	−1.07	0.047

changed the corresponding stellar parameter by its respective error and calculated the average of $\Delta \log \epsilon / \Delta parameter$.

4.5 Discussion

4.5.1 Abundance pattern of elements up to Zn

In Figure 4.4, we have shown the differential abundances of elements as a function of their atomic numbers. The differential abundance pattern of program star HD107752 with respect to standard star CS31082-0001 shows a small excess of carbon ($\Delta A^{C} = +0.09$) in HD107752 which is nearly comparable to the iron excess ($\Delta A^{Fe} = +0.04$) when we consider their uncertainties. The carbon abundance in the lower atmospheric layer deplete on the giant phase as a result of C to N conversion during CN-cycle (Placco et al. 2014). Thus, carbon of the birth ISM is obtained by correcting the present carbon abundance for the stellar evolution. This correction mainly depends on the metallicity and initial C and N abundances. Using the evolutionary correction from (Placco et al. 2018), both stars show +0.32 dex correction.

Yana Galarza et al. (2021) used the differential pattern of solar-twin to infer the mass of explosive progenitor and birth ISM metallicity. They found a clear odd-even effect in the differential pattern of the light elements, suggesting different progenitors for Sun and solar-twin. Our differential pattern does not show a strong odd-even effect. There is odd-even effect visible for Na, Mg, Al and Si. However, this odd-even pattern is not significant for iron-peak elements.

The $\alpha-$elements and iron-peak elements show more or less constant differential abundances. The mean differences of $\alpha-$elements and iron-peak elements are respectively $+0.05$ dex and -0.01 dex. Given the uncertainty limits, these differential abundances are equivalent to the metallicity difference of two stars. The constant difference in abundance suggests that these elements may have come from

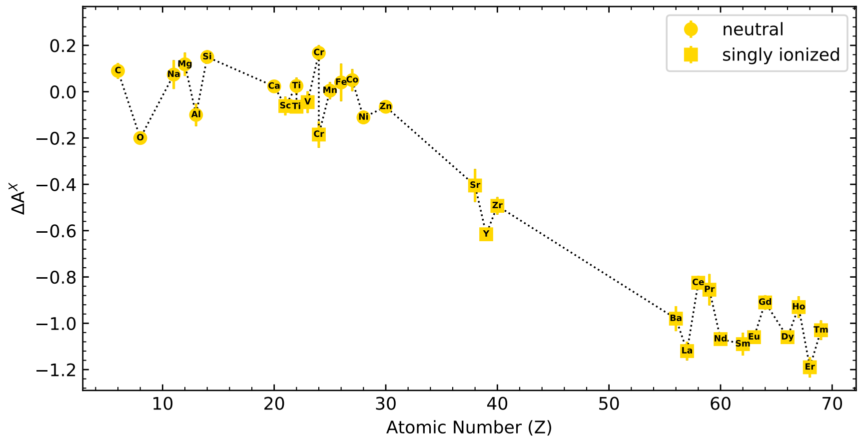

FIGURE 4.4: Differential abundance pattern of r-I star (HD107752) with respect to r-II star (CS31082-0001).

similar nucleosynthesis sites. The primary source of α-elements is core-collapse supernovae (CCSNe) (e.g., see Kobayashi et al. 2006). Since both the objects are very metal-poor, the possible explanation for this constant differential pattern is the ejection of iron-peak elements in energetic CCSNe yield (Andrews et al. 2020). In the early galaxies, CCSNe was the only source for producing iron-peak elements. Type-I supernovae mainly contribute in the late stage of galactic chemical evolution when [Fe/H] > -1 (Kobayashi et al. 2011, 2006; Vincenzo et al. 2018).

4.5.2 Neutron-capture abundance pattern

In this study, program star and standard star are r-process-enhanced: HD107752 is an r-I star, and CS31082-0001 is an r-II star. Therefore, as expected, the differential abundance pattern of HD107752 relative to CS31082-0001 is exhibiting a deficiency of neutron-capture elements in HD107752. However, the differential abundances of Sr, Y, and Zr are larger than the elements from Ba to Tm, which is not expected if r-process elemental synthesis has a single astrophysical site.

Given that both stars are significantly metal-poor with a sub-solar barium-to-europium ratio ($[Ba/Eu] < 0.0$) indicative of minimal to no s-process influence. Therefore, we conclude that the neutron-capture element enrichment in both stars arises solely from r-process nucleosynthesis. Assuming similar astrophysical conditions responsible for their production, we anticipate the differential abundances will be the same for the first and second-peak neutron-capture elements. However, we observed a significant difference between the differential abundances of first and second-peak elements. It indicates more than one astrophysical condition can produce r-process material.

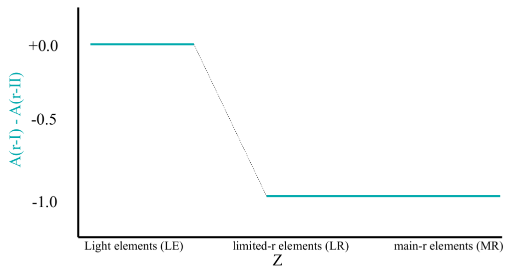

FIGURE 4.5: A schematic diagram illustrating the expected differential abundance pattern of HD107752 relative to CS31082-0001, if the r-process elements are from same kind of progenitor sites

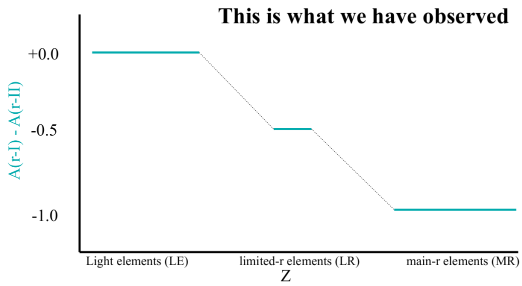

FIGURE 4.6: A schematic diagram explaining the expected differential abundance pattern of HD107752 with respect to CS31082-0001 if the lighter and main r-process elements originate from different types of progenitor sites. This is similar to the observed differential abundance.

Figure 4.5 shows an illustration of a differential pattern if the neutron capture elements were came from the same progenitor type. In this case, the differential abundances of neutron-capture elements are expected to show a plateau. However, the observed abundances are similar to Figure 4.6, showing three plateaus at -0.01, -0.50, and -1.01 dex for the α and Fe-peak elements, lighter r-process elements and the main r-process species respectively. A possible explanation could be pre-enrichment of lighter n-capture elements. However, a production site that can only synthesis the lighter r-process elements without significantly enhancing α and Fe-peak elements is difficult. Hence, we think r-I and r-II have different kinds of progenitors that may operate during similar epochs in the Galaxy history.

4.5.3 Formation scenario of r-I stars

Here, we discuss the various formation mechanisms that explain the formation of r-I stars.

Dilution of Ejecta: The first formation scenario involves the dilution of ejecta. This theory posits that all RPE stars originate from a similar site but with varying degrees of mixing or dilution of the ejecta. As depicted in Figure 4.7, r-II stars are formed in clouds that receive a higher concentration of material from an r-process (RP) event, whereas r-I stars originate from clouds where the material is more diluted, receiving less from the RP event. Under this scenario, the ratio of neutron capture elemental abundances should remain constant. If dilution of ejecta were the primary mechanism for forming r-I stars, then the ratio of neutron capture elements will show constant value with respect to enhancement level, as shown in Figure 4.10.

Pre-enriched ISM: The second formation scenario considers the pre-enrichment of the interstellar medium (ISM) (See Figure 4.8).

This hypothesis suggests that the cloud in which the r-I stars formed was pre enriched in lighter r-process elements (Sr,Y,Zr).

A pre-enriched cloud with high Sr levels can also explain limited-r stars. However, in this scenario, the production site can not add to alpha and iron-peak elements. There are no known sites that can synthesize Sr without

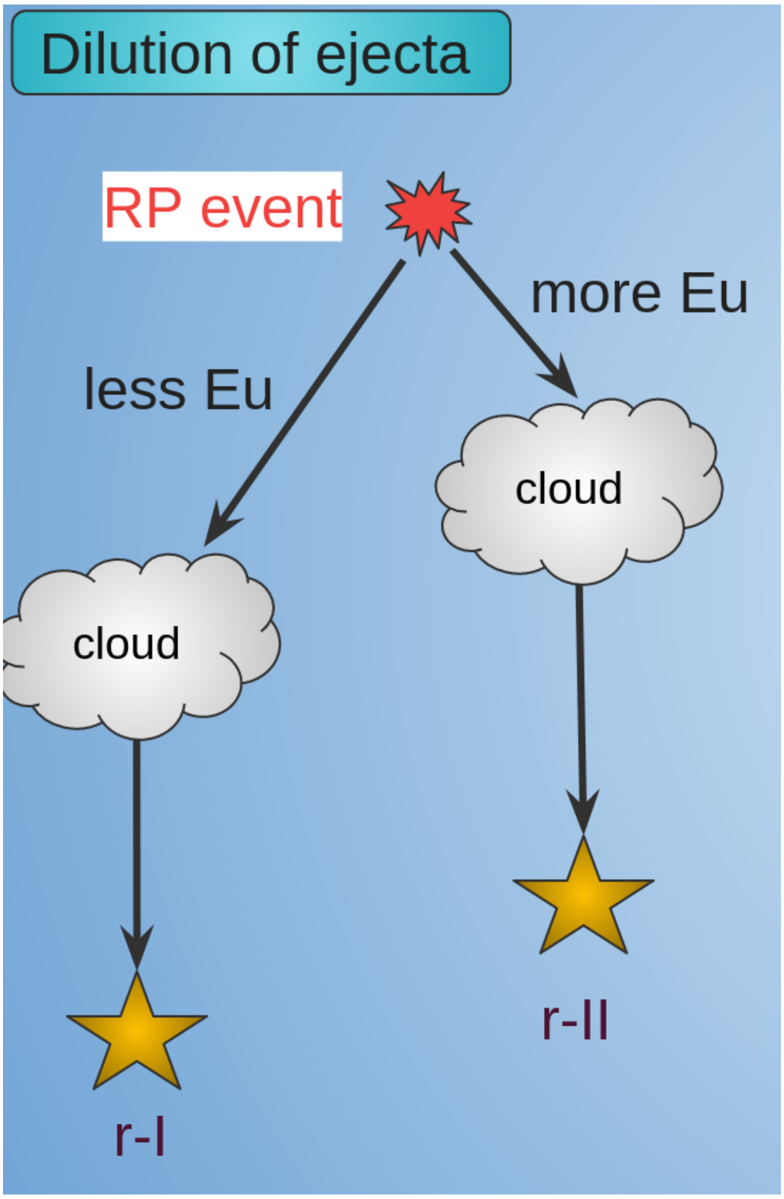

FIGURE 4.7: A schematic diagram to explain the dilution of ejecta.

alpha and Fe elements. Additionally, in this scenario, one would expect a higher number of r-II and limited-r stars than the number of r-I stars. However, r-process-rich stars and r-I stars contribute to the largest numbers. It is also expected that r-II and limited-r stars will be more metal-poor than r-I stars. The current numbers show that r-I and r-II stars have similar metallicity distributions as shown in figure 3.11.

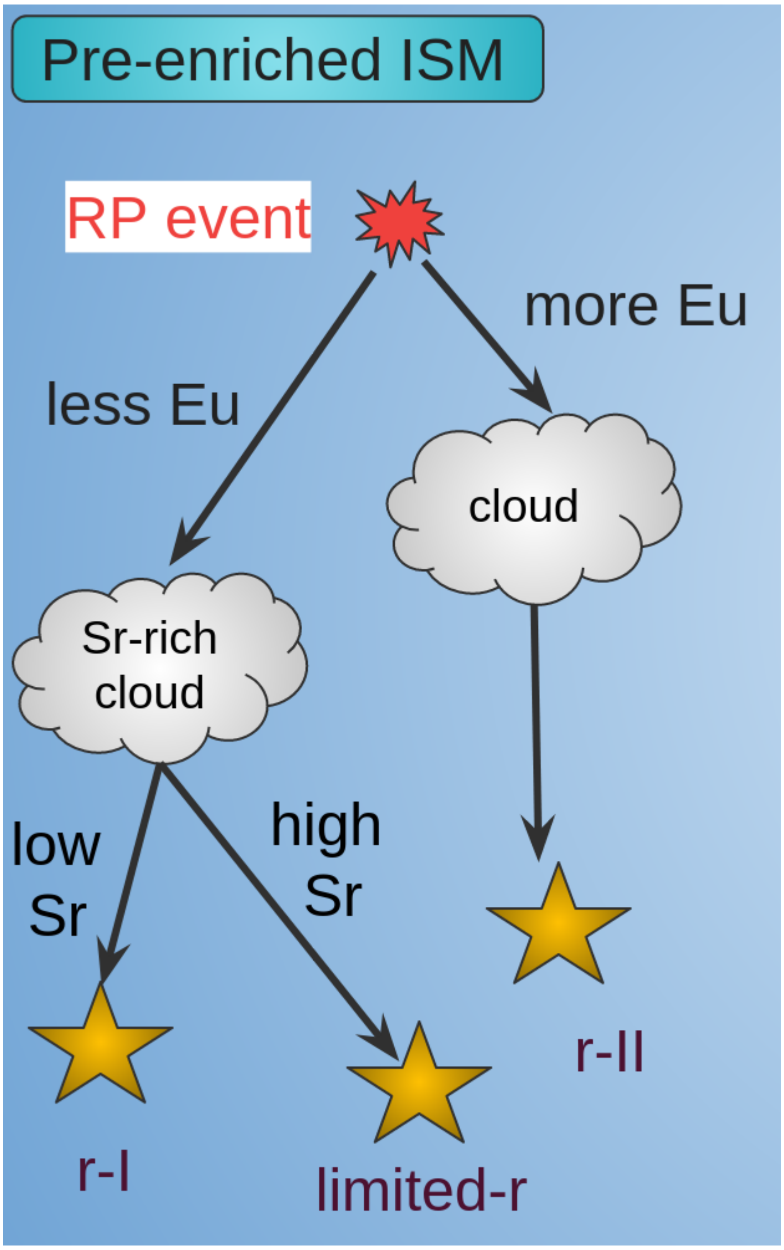

FIGURE 4.8: A scenario to explain the pre-enriched ISM.

Separate sites for r-I and r-II: The third formation scenario proposes separate sites for the production of r-I and r-II stars Figure 4.9.

Support for this idea comes from observations in two dwarf galaxies: Tucana III and Reticulum II. Both of them are ultra faint dwarf galaxies. Their present statistics shows that Tucana III contains only r-I stars and Reticulum II contains only r-II stars, along with stars that are not enhanced in

r-process. Therefore, It is very challenging to explain their r-process enrichment history. Under the dilution and pre-enrichment scenarios, we would expect to find both r-I and r-II in each galaxy. However, the absence of both r-process subclasses in these galaxies leads us to believe that both subclass likely have separate origins. Earlier works suggest that the r-process enhancement in the galaxy depends on the location of the r-process event. If an r-process event occurs near the center of galaxy, it retains a large amount of ejecta. However, if event occurs in the outer part, galaxy receives only small fraction of the ejecta. Thus, it is expected that the r-process event may have occurred in the inner part for Reticulum II and in the outer part for Tucana III (Tarumi et al. 2020). Nonetheless, it is very unlikely to occur an r-process event, like NSM, in the outer part of the galaxy. Additionally, galaxy mass might influence the production of these stars, with more massive galaxies possibly favoring the production of r-I stars and less massive galaxies producing more r-II stars. Tucana III is less massive than Reticulum II and shows the evidences of tidal striping. It was a massive dwarf galaxy in the past when r-process event occurred (probably not in the outer part) and later its outer part has been stripped.

4.5.4 Comparison with Literature

Futher, we explore the entire RPE star samples for the evolution of n-capture elements ratio with europium enhancement. Here, top row of Figure 4.10 displays the evolution of first peak elements alongside Eu, while in the bottom row, we illustrate the evolution of the first peak to Eu ratio. The top row suggests that first peak elements are produced concurrently with Eu. However, the bottom row does not show constant value of [Sr/Eu], [Y/Eu] and [Zr/Eu] with respect to the enrichment, indicating it is not a single site that contribute to these elements. However, it is surprising to note the distinct anti-correlation trend. This may

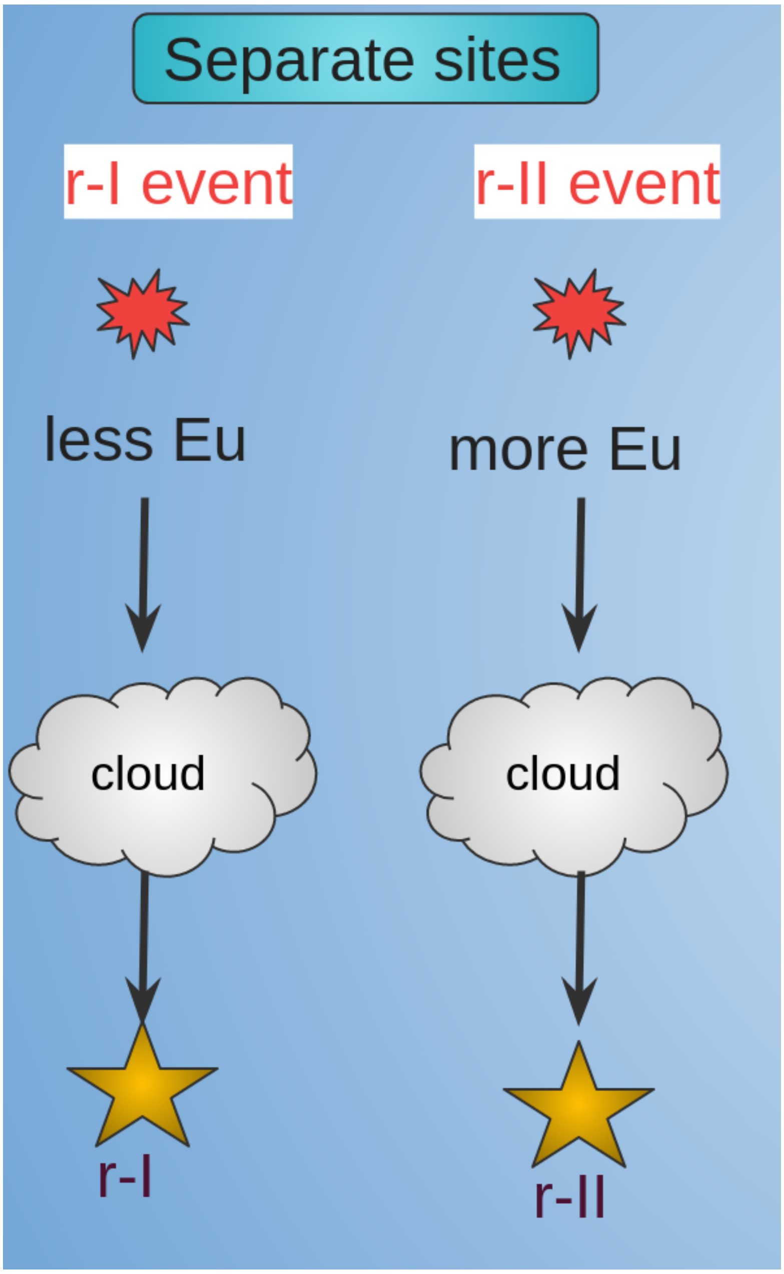

FIGURE 4.9: A separate site scenario to explain the abundance of r-I and r-II.

indicate that the sites producing these elements are related. For example, NS-NS mergers with different levels of disk and jet ejecta may produce this ratio.

Further to search for stars that could have formed from the diluted ejecta of r-II stars, we show in Figure 4.11, a guiding circle for reference. If the dilution of r-process ejecta is responsible for the production of r-I and r-II, we should see stars

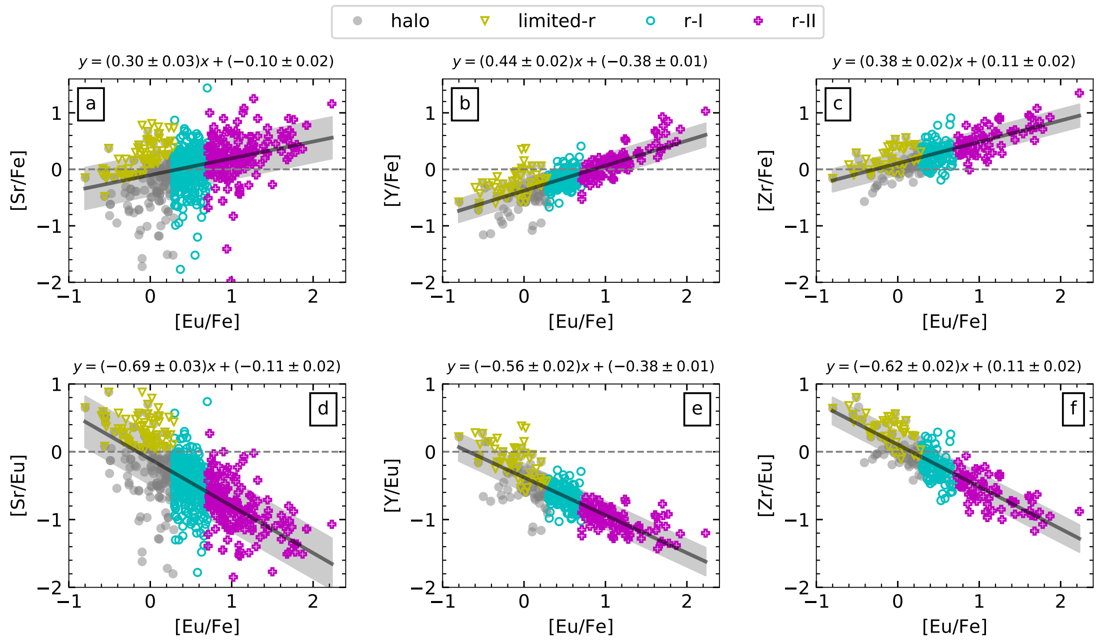

FIGURE 4.10: The evolution of Sr, Y, Zr with r-process enhancement enhancement for limited-r (yellow colours), r-I (cyan colours), and r-II (magenta colours) stars. The black straight line is the fittings to the data, and shaded gray regions display 1σ dispersion. The fitted equations are shown above the respective panels. The gray horizontal lines represent solar values. For reference, see Saraf et al. (2023) and Saraf & Sivarani (2023b).

in the circle. But, we do not have much objects there. It means r-I and r-II may have formed in different events. This fact also supports the case of Tucana III and Reticulum II galaxies where we observe only r-I or r-II. However, this conclusion relies on the present statistics. It may require revision when we have more data available for these galaxies.

Comparison of Observation with NSM simulations: To understand the production of first and second r-process peak elements, we utilise the simulations of NSMs reported in Fujibayashi et al. (2017). To calculate the [Eu/Fe] of the ISM polluted with the NSM ejecta, we assume a dwarf galaxy with gas mass 10^6 solar mass. We consider 75% of this gas is hydrogen. Then, we uniformly mix the NSM ejecta into this gas and calculate the [Eu/Fe] ratio for ISM metallicities ranging from [Fe/H] $= -3.5$ to -1.5 with 0.5 step size.

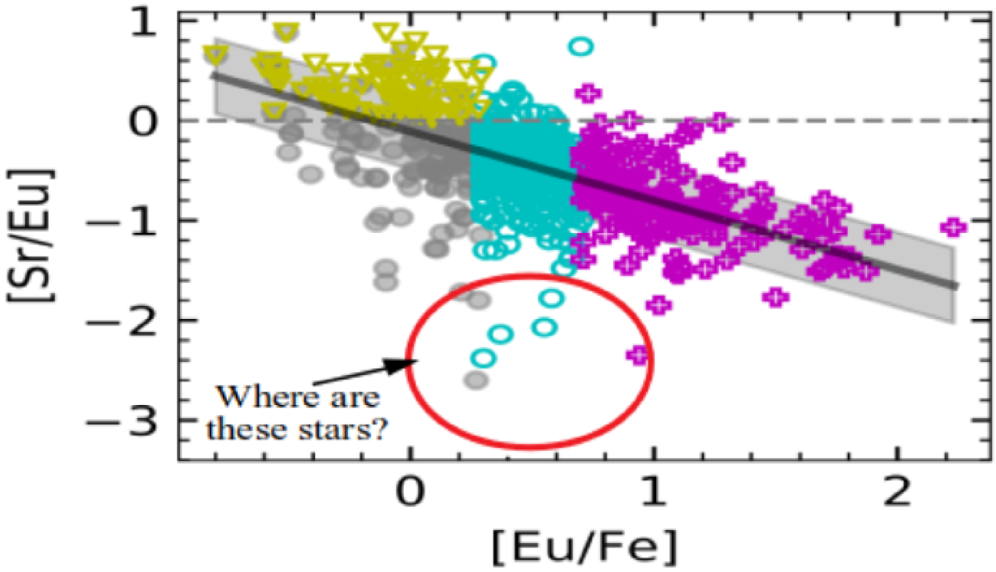

FIGURE 4.11: Evolution of [Sr/Eu] with [Eu/Fe] to infer the separate sites of r-I and r-II. The gray, yellow, cyan, and magenta colors respectively represents normal halo stars, limited-r stars, r-I stars, and r-II stars. The solid black line is the straight line fittings to the data, and shaded gray region displays 1σ dispersion. For reference, see Saraf et al. (2023) and Saraf & Sivarani (2023b).

Figure 4.12 shows the observed data overplotted with model values for five metallicities. The model for metallicity −2.0 reasonably reproduce the trend for r-II stars. However, same model does explain the trends to high values of [Sr/Eu] particularly the r-I and limited-r.

4.5.5 More in the context of universality

We further explored differential abundance of the mean r-I and r-II abundances for large sample of RPE stars, as shown in Figure 4.4. We compiled elemental abundances of r-I and r-II objects from various studies and calculated their mean scaled abundance patterns for [Fe/H] < -2.0 dex. This metallicity threshold was chosen to exclude stars that may include contamination from s-process during the

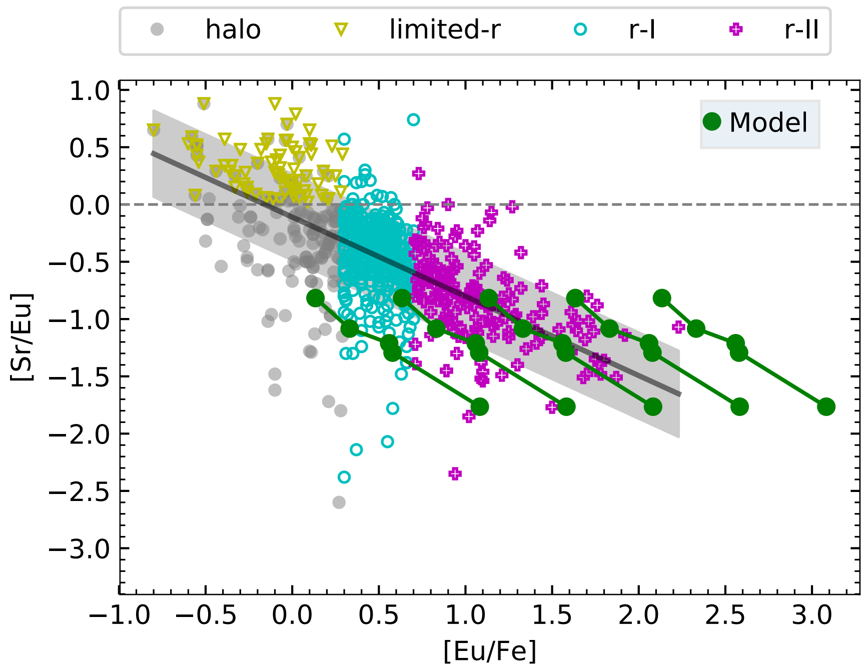

FIGURE 4.12: Evolution of [Sr/Eu] ratio with Eu enhancement in limited-r (yellow colours), r-I (cyan colours), and r-II (magenta colours) stars. The black straight line is fittings to the data, and shaded gray regions display 1σ dispersion. Green color lines show the mixing of NSM ejecta of Fujibayashi et al. (2017) models into different metallicity ISM.

later stages of Galactic chemical enrichment. For calculating the mean abundance pattern, we normalized each star's abundance pattern to A(Eu)= 0 by subtracting the Eu abundance from the respective patterns. This normalization to a consistent A(Eu) value effectively minimizes the scatter in the mean abundance patterns that arises from varying levels of r-process enhancement.

The top panel of Figure 4.13 shows the mean scaled abundance patterns of r-I and r-II stars obtained from literature along with the scaled solar abundance pattern. The mean scaled r-I and r-II patterns, respectively displayed with cyan and magenta colors, are quite well following the scaled solar r-process pattern shown with black curve. It confirms the well known universality of r-process pattern as discussed in earlier studies (e.g., see review Sneden et al. 2008). The mean r-I pattern deviates from solar r-process pattern particularly towards lower atomic number. However, the r-II pattern closely follows solar r-process pattern.

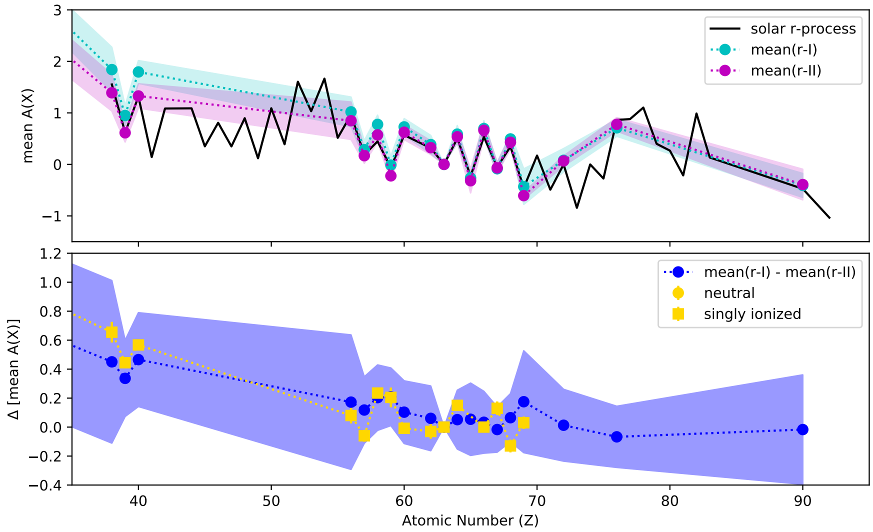

FIGURE 4.13: Top panel compares the mean r-process abundance pattern of r-I stars (cyan color), r-II stars (magenta color), and the Sun (black color). We use stars with $[Fe/H] < -2.0$ For the mean abundance pattern is calculation. Bottom panel compares the mean differential abundance pattern of r-I stars with respect to r-II stars, and the differential abundance pattern of HD107752 (r-I star) with respect to S31082-0001 (r-II star)

The bottom panel of Figure 4.13 shows the differential pattern of mean scaled abundance patterns from literature in blue color, along with the differential abundance pattern from this study in yellow color. The shaded blue color represents one $\sigma = \sqrt{\sigma^2_{r-I} + \sigma^2_{r-II}}$ dispersion. It is evident that the differential abundance pattern of the two stars from this study is showing a good agreement with the differential abundance pattern obtained from the mean r-I and r-II patterns of literature sample. The differential abundances of first peak elements in this study show little excess as compared to the mean differential pattern. It could be due to the range [Eu/Fe] enrichment in the samples.

4.5.6 Orbital kinematics

To further investigate, we calculated orbits of the standard and program stars using the GALA code (Price-Whelan 2017a) in the Milky Way potential (MW

Potential from Bovy 2015a). The GALA is a Python programming-based code for galactic dynamics. It takes RA, DEC, proper motion, radial velocity, and parallax distance as input for orbital parameters calculation. We obtained proper motions, distances from Gaia (Gaia Collaboration et al. 2022), and radial velocities from our measurements to feed in the GALA code. In Figure 4.14, we have shown the orbits of both the stars in Galactocentric coordinates integrated for 5 Gyr back in time with the step-size of 0.1 Myr. The top row panels show the orbit of CS31082-0001 and the bottom row panels display the orbit of HD107752. Axis x, y, and z are respectively positive towards the Galactic center, Galactic rotation, and North Galactic pole from the location of the Sun.

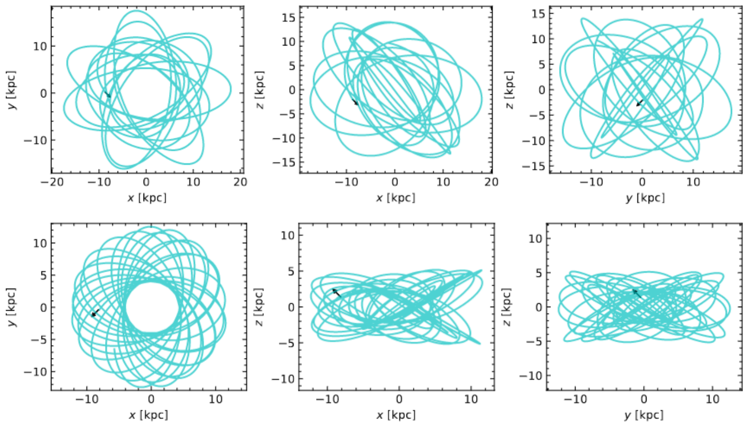

FIGURE 4.14: Orbits of standard and program stars in MW Potential. The black arrow in each panel shows the present location and direction of the star.

From the top row panels of Figure 4.14, it is obvious that CS31082-0001 moves randomly and vertically reaches nearly 14 kpc away from the Galactic mid-plane. It means that CS31082-0001 belongs to the stellar halo of the Galaxy. However, the HD107752 has an ordered orbit and goes a maximum of 5 kpc in the vertical direction from the Galactic mid-plane. It indicates that the HD107752 belongs to the thick disk of the Galaxy. We have listed the orbital parameters of two stars in Table 4.4. Both the stars show negative V and negative l_z indicating they are moving on retrograde orbits (moving opposite to the motion of the Galactic disk).

TABLE 4.4: Orbital parameters of standard and program stars in MW Potential. U, V, and W are velocities towards Galactic center, Galactic rotation and North Galactic pole respectively. The l_x, l_y, and l_z are specific angular momentum compoenents along x, y, z-axis respectively. The r_{peri} is pericenter distance, r_{apo} is apocenter distance, z_{max} is the maximum vertical height, and *ecc* is the eccentricity of the orbit.

Parameter	CS31082-0001	HD107752
U (km s^{-1})	132.21	−122.93
V (km s^{-1})	−400.64	−392.27
W (km s^{-1})	−196.76	120.54
l_z (kpc km s^{-1})	−1535.53	−1342.02
$l_\perp = \sqrt{l_x^2 + l_y^2}$ (kpc km s^{-1})	1947.49	749.04
$r_{peri}(kpc)$	7.97	4.37
$r_{apo}(kpc)$	18.31	12.61
$z_{max}(kpc)$	14.05	5.17
ecc	0.39	0.48

Though both the stars have retrograde orbits, quite similar eccentricities, and stellar parameters, they are very different in terms of pericenter distances, apocenter distances, and maximum vertical heights (see Table 4.4). The retrograde orbits and difference in orbital parameters indicate that HD107752 and CS31082-0001 may have originated in two different stellar systems and later accreted into the Milky Way.

4.6 Summary and conclusions

In this work, we have first time studied the differential abundances of an RPE star HD107752 (subclass *r*-I) with respect to another *r*-process-enhanced star CS31082-0001 (subclass *r*-II). We have done strictly line-by-line abundance estimation of 16 light elements and 15 neutron-capture elements. The accuracy of the abundance determination in this work is less than 0.08 dex. This improved accuracy allows us to constrain the sites of the natal clouds from which these r-process rich stars formed. We noticed three distinct regions in the differential abundance patterns (see Figure 4.4). Light and Fe-peak elements show differential abundances very close to zero suggesting their similar origin in both the stars i.e. core-collapse supernovae. Unequal differential abundances of the first and second r-process peak elements suggest that they are formed in different astrophysical conditions. Simple dilution of r-process yield from a single site such as NSM, collapsar, or MRSNe cannot explain the observed differential abundance pattern.

From our analysis, we concluded that neither the dilution of ejecta nor pre-enriched ISM could adequately explain the sites of r-process elemental production. Instead, we propose that different unique sites could explain the abundances of the two stars and also the mean r-I and r-II star patterns. We also observed a strong correlation among all r-process rich stars regarding the ratio of light to heavy neutron capture elements as a function of r-process enhancement. This indicates that these elements are sourced from distinct astrophysical sites, yet operate on comparable time scales. Furthermore, the two dwarf galaxies, Tucana III and Reticulum II, which host only r-I and r-II type r-process rich stars, provide support for distinct sites for r-I and r-II stars.

In our study, we also compared observational trends of the [Sr/Eu] versus [Eu/Fe] ratios with neutron star merger (NSM) models. Our findings indicate that these models can reasonably explain the trends in [Sr/Eu] versus [Eu/Fe] for r-II stars but they fail to extend the relation further to r-I and limited-r stars. Notably, the model corresponding to a metallicity of -2.5 aligns well with a straight line fit to the observational data, suggesting a partial alignment but also highlighting discrepancies that warrant further investigation.

We also report a clear pattern in the differential abundances of second r-process peak elements in contrast to the universal main r-process pattern as routinely claimed in the studies of RPE stars. The mean differential abundance pattern of previously known r-I and r-II stars with [Fe/H] < -2.0 further supports the significance and reliability of the reported differential pattern in main r-process region. From our kinematic analysis, we found that they may have originated in two different stellar systems and later migrated into the Milky Way. A more detailed differential abundance analysis of a large sample of r-process-enhanced stars can provide us with the key information to understand r-process nucleosynthesis and its production sites.

Appendix

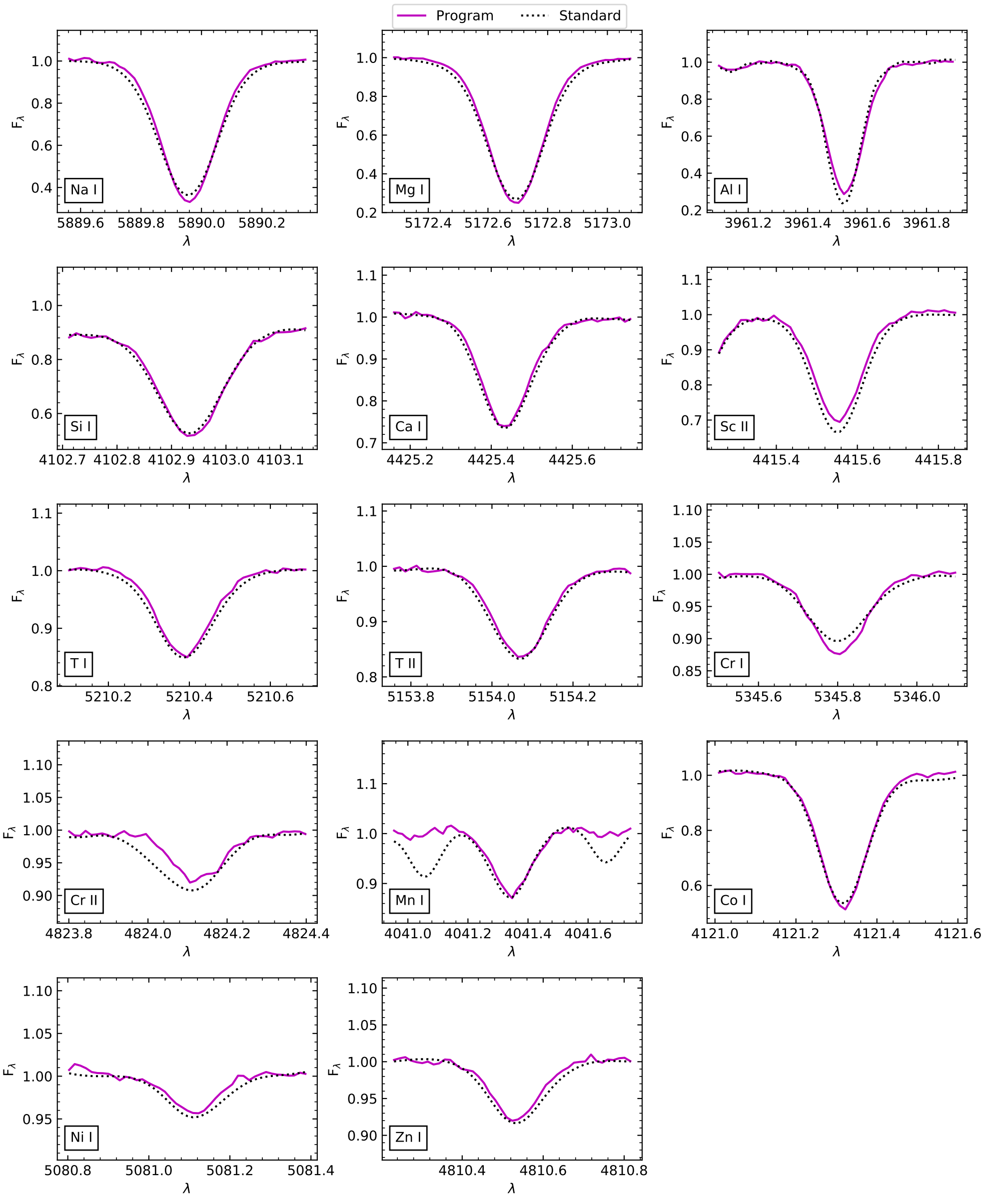

FIGURE 4.15: Comparison of some of the light, alpha, and iron-peak element regions for standard and target stars.

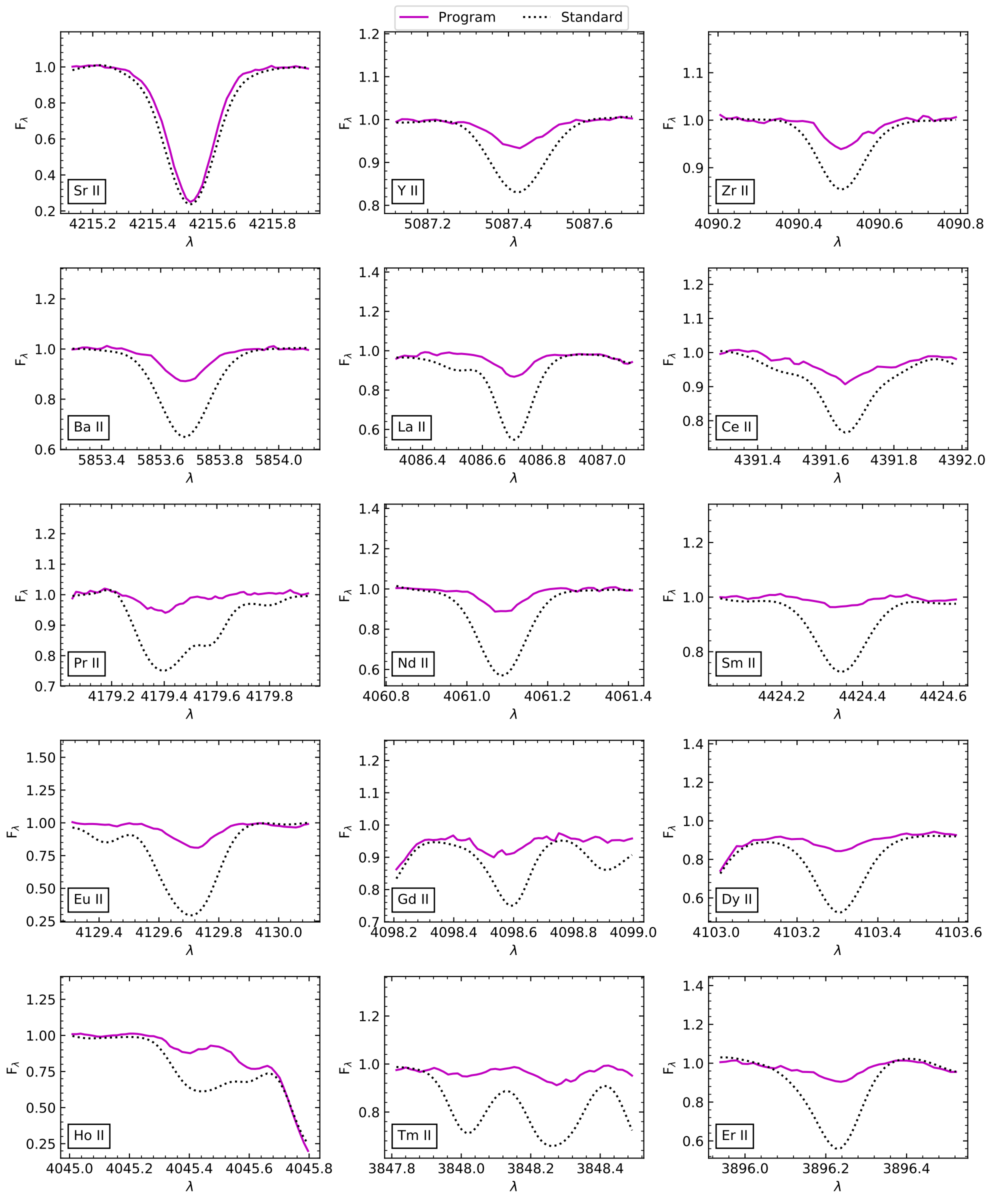

FIGURE 4.16: Comparison of some of the heavy element regions for standard and target stars.

Chapter 5

Kinematics and chemical abundances of different classes of RPE stars

Abstract

The elemental abundance trends of metal poor RPE stars showed that more than one r-process sites are needed to explain the abundance trends. Even with the clear evidence of NSM producing r-process rich ejecta, the timescale of its operation late in the Galaxy possess a problem. In our investigation, we focus on the kinematics of RPE stars to shed light on their enrichment across different Galactic components and timescales. We analyze the orbital parameters of a large sample of 448 metal-poor RPE stars ([Fe/H] < -1.0) and categorize them into

bulge, disk, and halo components using a physically motivated definition of Galactic components based on apocenter distance (r_a) and maximum absolute vertical height (z_{max}) of their orbits. Our analysis reveals that the Toomre diagram may not effectively segregate stars into disk and halo components, particularly when they exhibit highly eccentric and/or retrograde orbits. Contrary to previous assumptions, both disk and halo components exhibit a similar fraction of RPE stars. Notably, the majority of the most probably accreted stars originate from the halo, with three-quarters of the stars located in a mixed-zone. The inner disk, inner halo and outer halo stars show similar abundance trends of n-capture elements.

5.1 Introduction

The study of RPE (r-process-enhanced) stars offers crucial insights into the astrophysical conditions where the r-process occurs. The comprehensive study of the RPE stars involves spectroscopy and kinematics approaches. In spectroscopy, we perform complete abundance analysis of the stellar spectra and look for peculiar signatures in abundance pattern of elements to infer astrophysical conditions during their formation (Sneden et al. 2003). On the other hand, in kinematics, we calculate orbital parameters of the stars in the MW and look for grouping in the energy-action phase space to reveal their birthplace (Gudin et al. 2021; Shank et al. 2022, 2023).

In literature, numerous works have aimed to connect the kinematics and chemical characteristics of stars, with the goal of unveiling the chemical enrichment history of the Milky Way. Navarro et al. (2011) distinguished between thin and thick disk components by examining α, Fe, and the r-process element Eu. In the [(α + Eu)/Fe]−[Fe/H] plane, thin disk and thick disk stars show noticeable separation along the $[(\alpha + \mathrm{Eu})/\mathrm{Fe}] = 0.2$ line. Roederer et al. (2018) investigated orbits of 35 RPE objects of r-II class and noted that all exhibited halo-like kinematics.

Using a sizeable sample of nearly 1500 metal-poor objects, (Limberg et al. 2022) identified 38 Dynamically Tagged Groups (DTGs) in 4D energy-action space. Several of these groups were previously known streams or substructures. Various RPE stars show similar dynamics to some DTGs indicating the possible origin of RPE stars in dwarf galaxies. Similar DTGs are reported in Shank et al. (2022, 2023) for significantly large sample of metal-poor stars and their association with known Galactic substructures is discussed.

Gudin et al. (2021) identified 30 DTGs among RPE metal-poor stars. Although these groups were solely identified based on kinematics, they exhibited similar chemical signatures, indicating a shared chemical evolution history. Subsequently, Shank et al. (2023) performed a similar study on a large RPE objects sample, identifying 36 DTGs, including previously known groups. These collective findings suggest that RPE stars may have originated from external systems that were later disrupted and merged into the MW.

Both spectroscopy and kinematics play crucial roles in investigating the location(s) of r-process nucleosynthesis. In this work, we will combine the spectroscopic and kinematic information of RPE stars to investigate the environmental conditions where the r-process occurred and how it enriched the Galaxy with heavy elements. Previous research has primarily focused on dynamically tagged groups (DTGs) of stars and their correlation with RPE stars. Our objective is to categorize RPE stars into distinct galactic components (bulge, disk, and halo) based on orbital structure and analyze their unique chemical characteristics.

5.2 The sample

5.2.1 The sample selection

We have complied data RPE stars from different sources (see Chapter 3 for references.) In addition to C, Fe, Ba, Eu, we have also compiled abundance data for other elements available in the literature. Elements with upper limit abundance estimations have been excluded from our sample. For this study, we have adopted the updated definition of r-process subclasses outlined in Holmbeck et al. (2020) and have only considered carbon-normal stars with ([C/Fe] $\leq$ 0.7). This criterion resulted in a selection of 284 r-I, 120 r-II, and 44 limited-r stars. Parallax, proper motion, and radial velocity data for these objects were obtained from the Gaia EDR3 and Gaia DR3 (Gaia Collaboration et al. 2021b, 2023).

5.2.2 Orbit calculation

We performed back orbit integration for all r-process stars within the Milky Way Potential using the *gala* code (Bovy 2015b; Price-Whelan 2017c). The *gala* is a Python-based galactic dynamics code that primarily utilizes Astropy for astronomical units and coordinate systems. It takes the object's RA, DEC, parallax, proper motion, and radial velocity as input to compute its trajectory within the chosen potential. The code outputs various orbital parameters, including position, velocity, energy, angular momentum, eccentricity, apocenter distance, and pericenter distance. In this study, we calculated orbital trajectories for 5 Gyr into the past with a step size of 0.1 million years. Additionally, we verified our results using a smaller step size of 0.001 million years. The choice of 5 Gyr integration time for orbital trajectories does not affect our results. We verified the orbital parameters with higher integration time for different types of orbits and good convergence at 5 Gyr.

5.2.3 Galactic bulge, disk, and halo

The Milky Way comprises distinct morphological components: the bulge, disk, and stellar halo (or simply halo) (see chapter 1). It is very difficult to associate the stars to these morphological components of the Galaxy. The present location of the star in the MW is deceiving when it comes to the separation of three components. A star which is presently in the disk region may not be part of the disk. It could be part of the bulge or halo and is presently passing through the disk. Thus, we adopted a physically motivated definition of Galactic components based on the orbital parameters in the MW: apocenter distance (r_a) and maximum absolute vertical height (z_{max}). We used the following definitions for different galactic components (Goodwin et al. 1998; Bland-Hawthorn & Gerhard 2016; Zoccali & Valenti 2016):

– Bulge: $r_a \leq 3$ kpc and $|z_{max}| \leq 3$ kpc

– Inner disk: 3 kpc $< r_a \leq 15$ kpc and $|z_{max}| \leq 3$ kpc

– Outer disk: $r_a > 15$ kpc and $|z_{max}| \leq 3$ kpc

– Inner halo: 3 kpc $< r_a \leq 15$ kpc and $|z_{max}| > 3$ kpc

– Outer halo: $r_a > 15$ kpc and $|z_{max}| > 3$ kpc

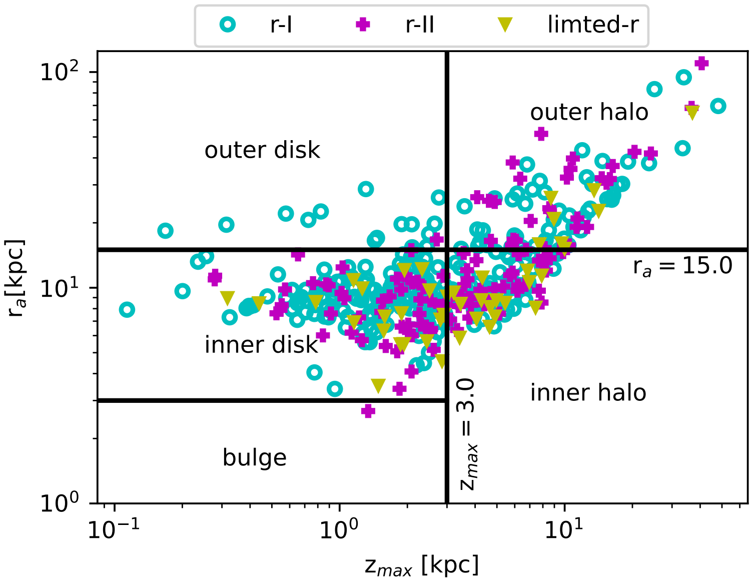

FIGURE 5.1: Bulge, disk, and halo classification: The apocenter distance (r_a) as a function of maximum vertical height (z_{max}) of the stellar orbits. For better visibility, we have set the axes scale to log-scale. The vertical black line at $z_{max} = 3$ kpc and horizontal black lines at $r_a = 3$ kpc and $r_a = 15$ kpc separate RPE stars into five different Galactic components namely, bulge, inner disk, inner halo, outer disk, and outer halo. Open cyan circles show *r*-I, *r*-II are displayed by magenta crosses, and limited-*r* stars are displayed with yellow down triangles.

5.3 Results

5.3.1 Orbit based association of RPE stars to Galactic components

Initially, we measured the average apocenter distance (r_a) and the average maximum absolute vertical height (z_{max}) of stellar orbits over a 5-billion-year period to classify stars associated with the bulge, disk, and halo components. In Figure 5.1, we illustrate the relationship between r_a and z_{max} to categorize RPE stars into distinct Galactic components, as per the definitions provided in Section 5.2.3. The Figure delineates five rectangular regions corresponding to bulge, inner disk, inner halo, outer disk, and outer halo stars. The three subclasses of RPE stars are denoted by open cyan circles (r-I), magenta crosses (r-II), and yellow down triangles (limited-r).

By employing orbit-based classification of Galactic components, we identified 143 r-I, 47 r-II, and 19 limited-r within the inner disk, constituting approximately $\sim$ 48% of all stars. In the outer disk, we found 15 r-I and 1 r-II, contributing to approximately $\sim$ 4%. No limited-r is observed in the outer disk. The inner halo exhibited 71 r-I, 34 r-II, and 16 limited-r stars, making up roughly $\sim$ 28%. The outer halo contained 49 r-I, 31 r-II, and 8 limited-r, contributing to the remaining approximately $\sim$ 20%. Only one star was detected in the bulge region, identified as an r-II type RPE star. An example of a disk and halo star is illustrated in Figure 5.2.

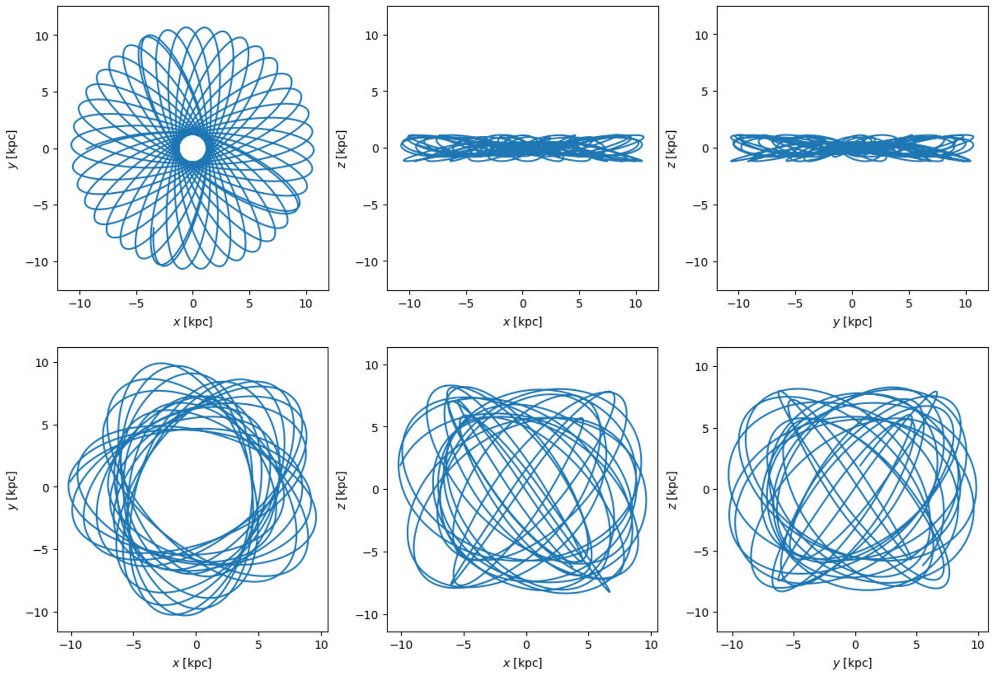

FIGURE 5.2: Example orbits of two stars in the Milky Way potential (MW Potential). The top panel shows the star orbiting in disk plane and bottom panel shows the star orbiting in the stellar halo.

5.3.2 Galactic components in Toomre diagram

The Toomre diagram, which plots velocities in the plane perpendicular to the Galactic disk against velocities in the Galactic plane, is commonly utilized to distinguish between disk and halo stars. This diagram relies on present-day velocities (U, V, W) in the MW, where U represents velocity in the Galactic center direction, V denotes the azimuthal velocity along Galactic rotation, and W indicates the velocity in the North Galactic Pole direction. For the Toomre diagram, we calculated the present-day velocities of the sample, taking into account the Sun's velocity from Coşkunoğlu et al. (2011) i.e., ($U_\odot$, $V_\odot$, $W_\odot$) = (8.5, 13.4, 6.5) km s^{-1} with respect to the LSR.

In Figure 5.3, we illustrate the Toomre diagram for our sample. The x-axis represents azimuthal velocity ($V\phi$ = V), while the y-axis denotes transverse velocity (Vt = $\sqrt{U^2 + W^2}$) of the stars. The diagram displays the distribution of different r-process subclasses. The red color semi-circle commonly serves as the boundary between disk and halo stars: those within the semi-circle are associated with the disk, while those outside are associated with the halo. According to this definition, the majority of RPE stars belong to the halo. A vertical line at V=0 segregates prograde (V $>$ 0: moving in the Galactic rotation direction) and retrograde (V $<$ 0 : moving opposite to the Galactic rotation) stars. Our analysis reveals approximately $\sim$ 56% prograde orbits (150 r-I, 66 r-II, and 30 limited-r) and approximately $\sim$ 44% retrograde orbits (129 r-I, 48 r-II, and 13 limited-r) among all r-process stars. Our orbital parameter-based definition of Galactic components reveals that the Toomre diagram does not effectively distinguish between disk and halo components. While the majority of halo stars lie outside the red semi-circle, a significant number of disk stars also fall beyond this boundary (See Figure 5.4).

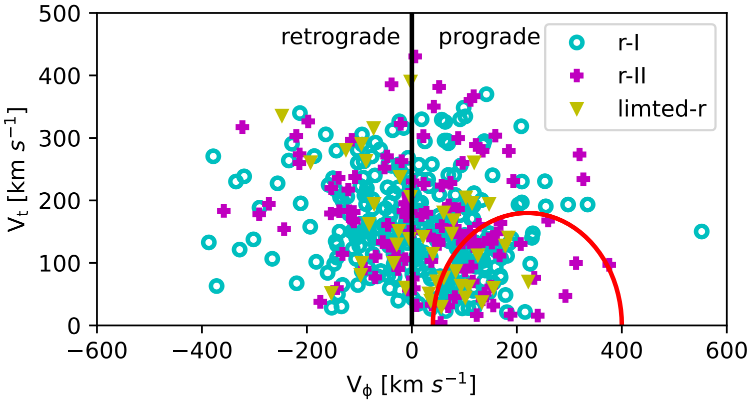

FIGURE 5.3: Toomre diagram for RPE stars, where the large red circle with a radius of 180 km/s around LSR is used to separate the disk stars from halo stars. The black vertical line separates the stars on retrograde and prograde motions. Open cyan circles show r-I stars , r-II stars are represented by magenta crosses, and limited-r stars are displayed with yellow down triangles.

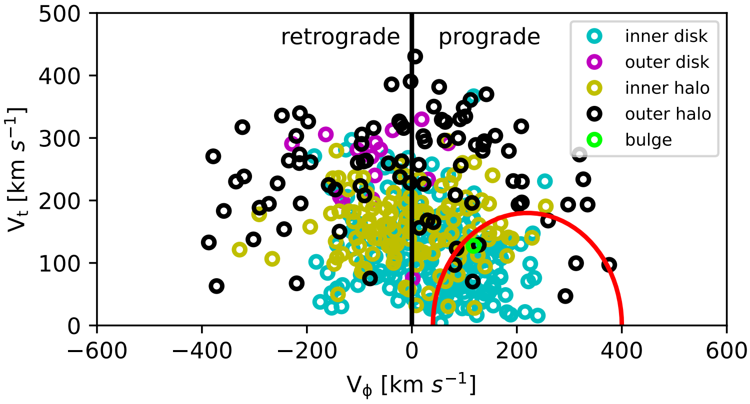

FIGURE 5.4: Same as Figure 5.3 for RPE stars categorized as in Section 5.2.3.

To investigate this discrepancy further, we plot orbital eccentricity as a function of azimuthal velocity in Figure 5.5. Orbital eccentricity, defined as $e = (r_a - r_p)/(r_a + r_p)$, where r_a represents the apocenter distance and r_p indicates the pericenter distance of the orbit, quantifies the orbit's shape, ranging from 0 for a circular orbit to 1 for a radial orbit. Figure 5.5 illustrates that a significant proportion of disk stars exhibit retrograde orbits ($V_\phi < 0$). Also, if we see the eccentricity of prograde orbits, it shows a clear decreasing trend with increasing azimuthal velocity. Highly eccentric orbits (with eccentricity close to 1) possess higher radial velocity components, resulting in high transverse velocities. Both

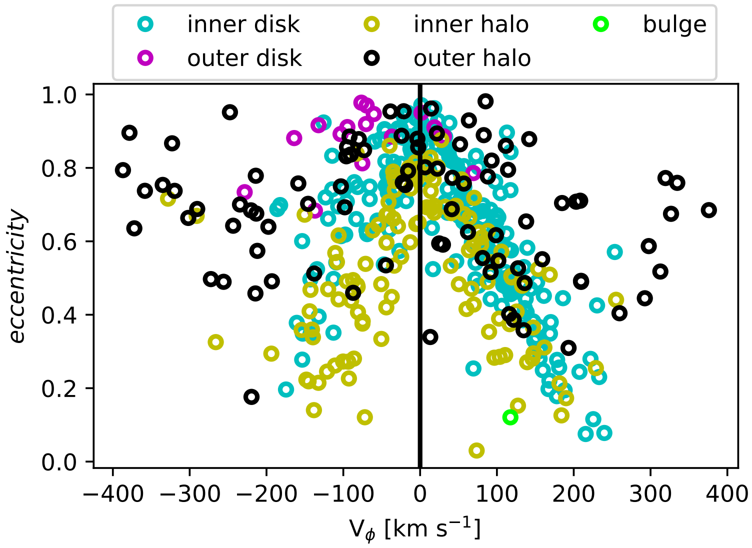

FIGURE 5.5: Orbital eccentricity of r-process-enhanced stars as a function of azimuthal velocity. Stars are color-coded with different galactic components as defined in Section 5.2.3. Colors of different Galactic components are shown in the legend at the top of the figure.

retrograde motion and eccentric orbits move star outside the disk–halo separating semi-circle. It confirms that the Toomre diagram does not provide a good diagnostic to separate disk and halo stars when the orbit are highly radial and/or retrograde. Thus, we use the orbital parameter based classification for the stars to associate them with the Galactic components.

5.3.3 In-situ and ex-situ origin of RPE stars

RPE stars have been observed not only within the Milky Way but also in nearby dwarf satellite galaxies such as Carina, Draco, Fornax, Ursa Minor (UMi), and Sculptor. The recent discovery of highly RPE stars in ultrafaint dwarf galaxy Reticulum II (Ret II) received most attention. There were seven r-II stars in nine studied stars (Ji et al. 2016). The existence of RPE stars in both Milky Way halo and the satellite galaxies suggests that these stars may have originated in external systems that were subsequently disrupted and accreted into the MW (Ji et al. 2016; Roederer et al. 2018). Additionally, Brauer et al. (2019) proposed that approximately half of the r-II observed in the Galaxy may have originated in now-destroyed dwarf galaxies.

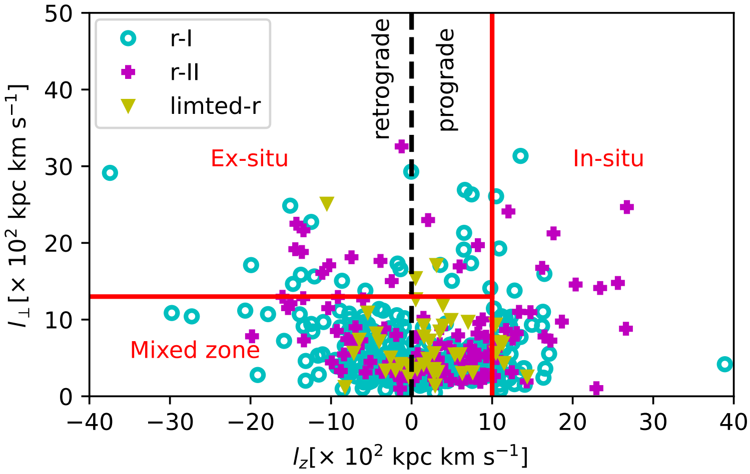

FIGURE 5.6: This is the specific angular momentum diagram for RPE stars, where the black dotted line delineates retrograde and prograde objects. The vertical red line at $l_z = 1000$ kpc km s^{-1}, and horizontal red line at $l_\perp = 1300$ kpc km s^{-1} separate in-situ, ex-situ and mixed stars. Open cyan circles show r-I stars, r-II are marked by magenta crosses, and limited-r stars are displayed with yellow down triangles.

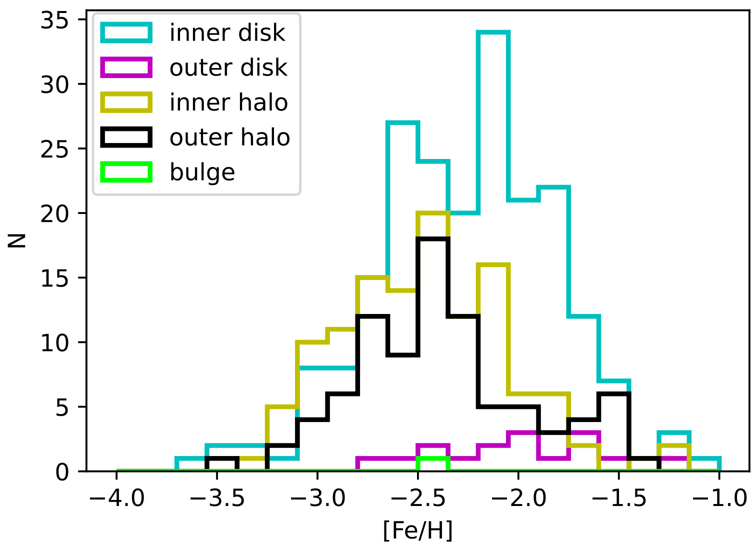

FIGURE 5.7: Metallicity ([Fe/H]) distribution of RPE stars in different Galactic components.

To explore the formation history of RPE stars, distinguishing between in-situ (formed within the Galaxy) and ex-situ (accreted from other stellar systems) origins, we plotted the total specific angular momentum in the disk plane ($l_\perp = \sqrt{l_x^2 + l_y^2}$) against specific angular momentum perpendicular to the disk plane (l_z). The average specific angular momenta over a 5-billion-year orbit are presented in Figure 5.6. Using the definitions of Di Matteo et al. (2020), we classified stars into in-situ, ex-situ, and mixed-zone origins. Objects with $l_z > 1000$ kpc km s^{-1} are in-situ, those with $l_z < 1000$ kpc km s^{-1} and $l_\perp > 1300$ kpc km s^{-1} are considered ex-situ. Stars with $l_z < 1000$ kpc km s^{-1} and $l_\perp < 1300$ kpc km s^{-1} are categorized as belonging to the mixed-zone, as they could have formed either in-situ or ex-situ. Our analysis showed that approximately $\sim 17\%$ (46 r-I, 23 r-II, and 6 limited-r) of RPE stars are formed in-situ, around $\sim 9\%$ (21 r-I, 13 r-II, and 3 limited-r) are formed ex-situ, and roughly $\sim 74\%$ (212 r-I, 78 r-II, and 34 limited-r) are situated in the mixed-zone.

It is evident that about 3/4 fraction of RPE stars are in mixed-zone. An individual r-process subclass also roughly shows a 3/4 fraction in mixed-zone. Based on our classification of Galactic components (for brevity, figure is not shown here), we found that all the ex-situ stars belong to the halo region. On the other hand, all the outer disk stars lie in mixed zone. This is because all the outer disk stars are on highly radial orbits as can be seen in Figure 5.5.

5.3.4 R-process enrichment of Galactic components

As a first step to understand the chemical evolution of RPE stars in different Galactic components, we calculate the number distribution of RPE stars relative to their metallicity. Figure 5.7 illustrates the metallicity histogram of RPE stars sampled from the bulge, inner disk, inner halo, outer disk, and outer halo. Notably, the inner disk displays a bimodal distribution in metallicity, with peaks occurring around [Fe/H]=−2.5 and −2.1 dex. RPE stars in the outer disk are predominantly situated toward the higher end of the metallicity spectrum. The mean [Fe/H] of outer disk coincides the second peak ([Fe/H]=−2.1) of inner disk distribution. However, the peaks of inner and outer halos coincide with the first peak ([Fe/H]=−2.5) of inner disk distribution. There is also a little signature of bi-modality in inner halo coinciding with the second peak ([Fe/H]=−2.1) of inner disk RPE stars. The bimodal metallicity distribution of inner disk and inner halo could be related to different formation mechanisms.

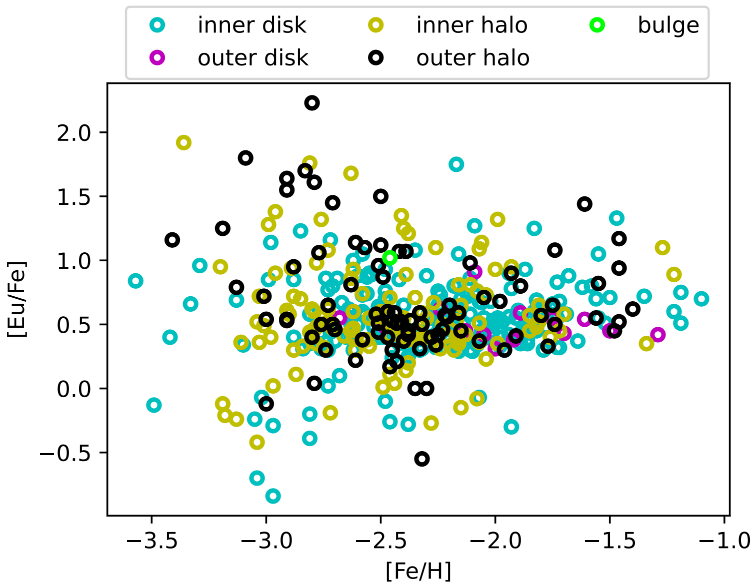

FIGURE 5.8: The [Eu/Fe] evolution in RPE stars metallicity for various Galactic components categorized in this work.

In Figure 5.8, the plot displays the [Eu/Fe] with [Fe/H] for RPE objects in different Galactic components. It is clear that inner disk, inner halo and outer halo exhibit similar abundance distributions with metallicity. All these components show large scatter at low metallicity except the outer disk stars. The stars in outer disk region show nearly constant [Eu/Fe] abundance. Limited-*r* stars are generally close to the inner disk and halo. Similar distribution is observed for Ba abundance as well.

We have also calculated the [Eu/Fe] distribution in different Galactic components as a function of their apocenter distances and shown in Figure 5.9. RPE stars

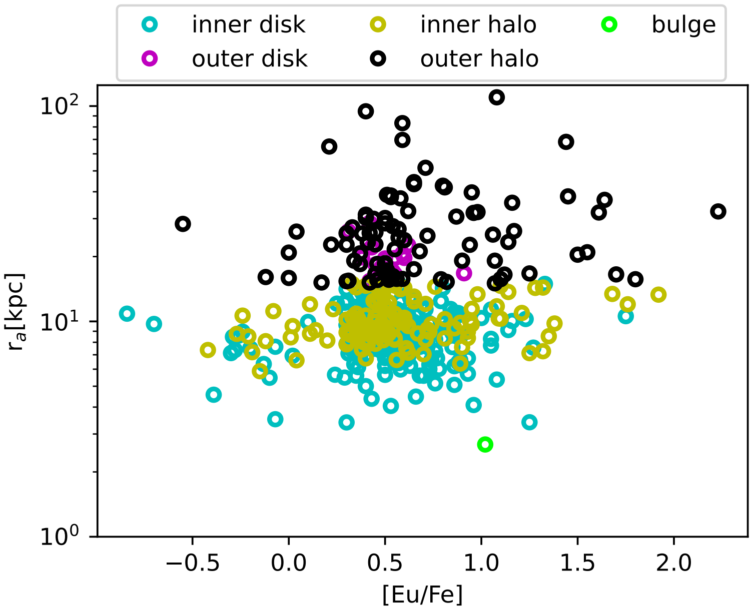

FIGURE 5.9: Apocenter distance of RPE stars with metallicity for Galactic components categorized in this work.

in inner disk, inner halo and outer halo show range of Eu abundance. However, outer disk stars are clustering in smaller region. In Figure 5.5, we found outer disk stars are on highly eccentric orbits and majority of them is on retrograde motion. It indicates that RPE stars in outer disk may have born in single event/ environment. The above conclusions are tentative given the small number of stars in each of the categories.

5.4 Conclusions

We have assembled a dataset comprising 448 metal-poor RPE stars from existing literature for kinematic analysis. This dataset consists of 44 limited-r, 284 r-I, and 120 r-II stars. We perform back orbit integration over a period of $\sim$ 5 Gyr, and computed their orbital parameters. By considering the pericenter distance and maximum vertical height of their orbits, we categorized these objects into the bulge, inner disk, inner halo, outer disk, and outer halo. Below, we present our findings based on this analysis.

- Our classification of RPE stars based on orbital parameters yielded 1 star in the bulge, 209 in the inner disk, 121 in the inner halo, 16 in the outer disk, and 88 in the outer halo. Consequently, our classification demonstrates a nearly equal distribution of RPE stars between the disk (inner + outer $\approx$ 52%) and the halo (inner + outer $\approx$ 48%).

- We have demonstrated that the classification of disk and halo stars based on the Toomre diagram is inadequate for highly eccentric and/or retrograde orbits. We recommend to use physically motivated orbital parameter based definitions for separating bulge, disk, and halo stars.

- Using specific angular momenta of the orbits, we found that all the most probably accreted (exsitu) RPE stars belong to the halo region. However, approximately three-quarters of RPE stars are located in the mixed zone. This majority in mixed zone complicates the understanding of in-situ and ex-situ origin.

- RPE stars located in the outer disk region exhibit clustering within the [Eu/Fe]$-r_a$ plane. These stars follow highly eccentric orbits, predominantly displaying retrograde motion. This suggests that they may have come from the same event of heavy element synthesis.

- The elemental trends of n-capture elements for the inner disk, inner halo, and outer halo stars do not exhibit significant differences. Limited-r stars tend to be closer to the inner disk and halo relative to r-I and r-II.

- Our study relies on a relatively limited dataset of RPE objects. A thorough examination of r-process enrichment necessitates a larger sample of RPE objects with intricate kinematics. The continued endeavors of RPA in uncovering additional RPE stars will offer a thorough understanding of their origin in the Galaxy.

Chapter 6

Probing the origin of *r*-process elements in CEMP-*r/s*, and assessing the classification of *r*-process rich stars using clustering algorithms.

Abstract

One of the objectives of this chapter is to explore the origin of r-process elements in CEMP-r/s stars. Despite having high europium abundances similar to r-II stars, the CEMP-r/s stars show significant carbon and s-process abundances. Using archival data from ESO-UVES and KECK-HIRES, we investigate the abundance

of the third r-process peak elements, such as thorium and osmium in CEMP-r/s stars to understand the conditions of r-process production and constrain the astrophysical sites. We also revisit the classification of r-I, r-II, and CEMP-r/s stars using the Gaussian Mixture Model (GMM) clustering. The study reveals that r-I and r-II belong to two distinct classes; in addition, some stars classified as r-I stars based on the low europium enhancements have abundance ratios similar to those of r-II stars. Hence, they might have formed from a much diluted ejecta of r-process material compared to r-II stars. We refer to this new class as the "diluted r-II class." We also find that CEMP-r/s stars and RPE stars represent two distinct classes of objects. These findings indicate that future studies incorporating additional elements and similar methodologies could lead to a more precise classification based on elemental ratios, reflecting the underlying physical processes.

6.1 Introduction

For decades, astronomers have been exploring RPE metal-deficient stars in the MW and its satellite to identify the sites of r-process. One significant group within these is the CEMP stars (Beers & Christlieb 2005a; Lee et al. 2013; Skúladóttir et al. 2015), which are often enhanced in r-process and/or in s-process. CEMP stars enriched with only the r-process are called CEMP-r, whereas CEMP stars with r- and s-process excess are known as CEMP-r/s. There are about two dozen CEMP-r/s objects that does not match typical s-process or r-process patterns, indicating an unclear origin. Despite various modeling efforts, explaining the abundances of CEMP-r/s has been challenging (Cohen et al. 2003; Jonsell et al. 2006; Abate et al. 2016). Multiple mechanisms have been proposed for explaining the r-process enhancement in CEMP-r/s. One scenario suggests that after the primary star in binary system undergoes the AGB stage, it go through type 1.5 supernova outburst (Zijlstra 2004; Wanajo et al. 2006). Another theory posits that the r-process enhancement occurs through an accretion-driven collapse of primary star, which then enriches the secondary object in the system (Cohen et al. 2003; Qian & Wasserburg 2003). Additionally, some studies propose that the triple system involving massive star could be responsible for the r-process enrichment of the secondary (Cohen et al. 2003). Another theory suggests that the ISM where CEMP-r/s are formed was already polluted with r-process event ejecta (Bisterzo et al. 2011). CEMP-r/s objects exhibit significant europium excess ([Eu/Fe] > 1.0), similar to r-II subclass. If the origins of europium is from the similar astrophysical sites, then it is likely that the r-process abundance patterns will be similar. In this study, we use the archival high-resolution spectroscopic data to estimate the third r-process peak elements in CEMP-r/s. Currently, there is only one CEMP-r/s object reported in (Gull et al. 2018), which shows a mix of r- and s-process material also enhancement in thorium. Furthermore, in this chapter, we intend to refine the classification of RPE stars by considering a broader range of elements beyond just Europium. The chapter is organised as follows: Following the introduction, we present the analysis of CEMP-r/s objects compiled from the archive data to derive osmium and thorium abundance. In the later part, we discuss the machine learning clustering techniques used to define the classification criteria for r-I, r-II and CEMP-r/s stars.

6.2 Osmium and Thorium abundance in CEMP-r/s

Osmium and thorium are part of the third n-capture peak. The abundance of these elements are sensitivity to neutron density and only a few astrophysical environments can synthesis these elements. For this study, we reviewed the literature to identify known CEMP-r/s objects, specifically from Hampel et al. (2019). We

TABLE 6.1: Basic information for the program stars.

Star name	RA	DEC	V mag	SNR	Resolution	Telescope
HD 209621	22:04:25.14	$+21:03:08.99$	8.86	74.87	65030	UVES(VLT)
HD 187861	19:56:26.94	$-65:22:08.01$	9.18	26.22	71050	UVES(VLT)
CS 22948-027	21:37:45.76	$-39:27:22.31$	12.66	26.55	115000	UVES(VLT)
CS29497-034	00:41:39.81	$-26:18:54.46$	12.22	38.90	58640	UVES(VLT)
HD 224959	00:02:08.02	$-02:49:12.23$	9.6	37.36	71050	UVES(VLT)
HE 1405-0822	14:07:42.97	$-08:36:14.38$	14.09	15.80	21800	UVES(VLT)
HE 0243-3044	02:45:16.44	$-30:32:02.11$	16.10	14.36	49620	UVES(VLT)
CS 22183-015	01:00:53.023	$-02:28:19.95$	13.73	34.31	40970	UVES(VLT)
LP 625-44	16:43:14.037	$-01:55:30.41$	11.68	33.0	47700	HiRES(KECK)
CS 31062-050	00:30:31.06	$-12:05:10.87$	13.05	33.0	47800	HiRES(KECK)
BS 17436-058	13:36:46.03	$+45:03:08.64$	13.80	33.0	47700	HiRES(KECK)
HE 0336+0113	03:38:52.90	$+01:23:07.77$	14.96	17.00	35800	HiRES(KECK)
CS 31062-012	00:44:03.56	$-13:55:26.26$	12.15	63.57	40970	UVES(VLT)
HE 0338-3945	03:39:55.006	$-39:35:42.90$	15.33	27.80	36840	UVES(VLT)
CS 22898-027	21:05:45.09	$-18:36:57.50$	12.76	45.87	58640	UVES(VLT)
BS 16080-175	16:51:08.80	$+57:12:27.76$	14.40	24.00	47700	HiRES(KECK)
HE 0143-0441	01:45:37.91	$-04:26:43.24$	16.38	6.00	35850	HiRES(KECK)
HE 2148-1247	21:51:17.909	$-12:33:41.55$	14.79	12.00	47800	HiRES(KECK)
CS 22887-048	22:46:44.62	$-11:08:42.41$	12.87	33.13	58640	UVES(VLT)
CS 29497-030	00:40:47.93	$-24:07:34.18$	12.65	73.58	40970	UVES(VLT)

focused on the strong lines of Os and Th towards the blue region of the spectrum, next, we searched the high-resolution archival data. We found seven spectra from HIRES of Keck Observatory and thirteen from UVES of Very Large Telescope (VLT). These spectra span the spectral resolution between 21000 and 115000. The details about the telescopes and spectrographs are provided in Chapter 2. Table 6.1 shows the basic information of our target stars obtained of this study. For further analysis, we normalize the spectra to unity and correct for radial velocity

6.2.1 Synthesis of Thorium and Osmium

Thorium has a blended line at 4019 Å in the optical region, which is used to confirm its presence in the spectra. Thorium is a pure r-process element because its

TABLE 6.2: Estimated Thorium and Osmium abundances of CEMP-r/s stars.

Star name	$T_{\rm eff}$ (K)	$\log g$	[Fe/H]	ξ (km/s)	A(Os)$_{\rm syn}$	A(Th)$_{\rm syn}$	[Os/Fe]	[Th/Fe]
HD 209621	4500	2.0	−1.94	2.00	-	-	-	-
HD 187861	4600	1.7	−2.36	1.70	−0.15	< -3.0	-	-
CS 22948-027	4800	1.8	−2.47	1.50	< 0.1	< -2.5	-	-
CS29497-034	4800	1.8	−2.90	1.50	−0.3	< -3.0	-	-
HD 224959	5050	2.1	−2.42	2.00	0.75	< -3.0	-	-
HE 1405-0822	5220	1.7	−2.4	1.88	< -0.1	< -2.5	-	-
HE 0243-3044	5400	3.2	−2.58	0.9	< -0.1	< -2.5	-	-
CS 22183-015	4650	1.1	−1.90	1.45	< -0.1	-	-	-
LP 625-44	5500	2.8	−2.70	1.60	< -0.1	< -3.0	-	-
CS 31062-050	5500	2.7	−2.40	1.88	< -0.1	< -3.0	-	-
BS 17436-058	5690	2.7	−1.80	2.70	< -0.1	< -3.0	-	-
HE 0336+0113	5700	3.5	−2.80	1.60	< -0.1	< -3.0	-	-
CS 31062-012	6099	4.2	−2.80	1.30	< -0.1	< -3.0	-	-
HE 0338-3945	6160	4.13	−2.42	1.13	< -0.1	< -3.0	-	-
CS 22898-027	6250	3.7	−2.25	1.40	< -0.1	< -3.0	-	-
BS 16080-175	6240	3.7	−1.90	1.05	< -0.1	< -3.0	-	-
HE 0143-0441	6240	3.7	−2.38	1.60	< -0.1	< -3.0	-	-
HE 2148-1247	6380	3.9	−2.40	1.70	-	−3.0	-	-
CS 22887-048	6500	3.35	−1.70	2.05	< -0.1	< -3.0	-	-
CS 29497-030	6650	3.50	−2.70	2.00	< -0.1	< -3.0	-	-

production can only occur through r-process nucleosynthesis. In synthesizing thorium in the spectra, we carefully addressed all potential line blends. Specifically, the 4019 Å Th II feature comes with ^{13}CH and other species with non-negligible contribution. We adopt the stellar parameters and elemental composition in Th region from (Hampel et al. 2019) and the reference therein for CEMP-r/s objects in this study. Additionally, we considered the ^{12}C/^{13}C ratio when synthesizing the thorium lines. We do not detect thorium in any of twenty stars studied. We have only provided the upper limits of thorium detection in Table 6.2.

Osmium is also an important element found in the third peak of r-process pattern. It shows two main spectral lines at 4420 and 4260 Å in the optical range. We focused on estimating the strength of the Osmium line at 4260 Å. The contributions of other lines while synthesizing osmium is taken from (Hampel et al. 2019) and the reference therein. Among the twenty stars studied, we detected Osmium in

2 stars and provided upper limits for its detection in the others. We detected Osmium in two stars namely HD 224959 and HD 187861 with $\log\epsilon(\mathrm{Os}) = 0.75$ and $\log\epsilon(\mathrm{Os}) = -0.15$ respectively. The former star is an osmium-rich star with a high Osmium detection of $\log\epsilon(\mathrm{Os}) = 0.75$, making highly Os-rich object known. The estimation of thorium and osmium in twenty stars is given in Table 6.2. The spectral synthesis for two stars with Osmium detection is shown below in Figure 6.1.

6.3 Classification of RPE stars

Before discussing the application of GMM for classifying RPE stars, we will briefly discuss the current classification criteria used in the literature. Beers & Christlieb (2005a) have originally suggested a threshold for distinguishing r-I and r-II stars at [Eu/Fe] > 1.0. However, Holmbeck et al. (2020) refined this classification method by using a data-driven approach to categorize these stars based on their europium-to-iron ratios. They analyzed a total of 471 stars (including limited-r) using the k-means partitioning technique, which is similar to k-means and works by minimizing the distance between cluster members to identify central values. Holmbeck et al. (2020) considered scenarios with both two and three clusters. They set a boundary at [Eu/Fe] $= +0.4 \pm 0.2$ between r-I and r-II stars using two clusters. When they allowed for three clusters then the criteria for r-I and r-II class was found to be at [Eu/Fe] $= +0.3 \pm 0.1$ and $+0.7 \pm 0.2$ respectively. These boundaries allowed for a more detailed classification between r-I and r-II stars. Better classification of r-process rich stars, considering abundance ratios and absolute abundance of multiple elements, is very useful, as it could relate to stellar evolution timescale and astrophysical environments. Hence, the frequency of these class of stars will help to infer the chemical enrichment history. For example, among the Milky Way satellites, Ret II shows only r-II stars and Tuc III shows only r-I stars, possibly

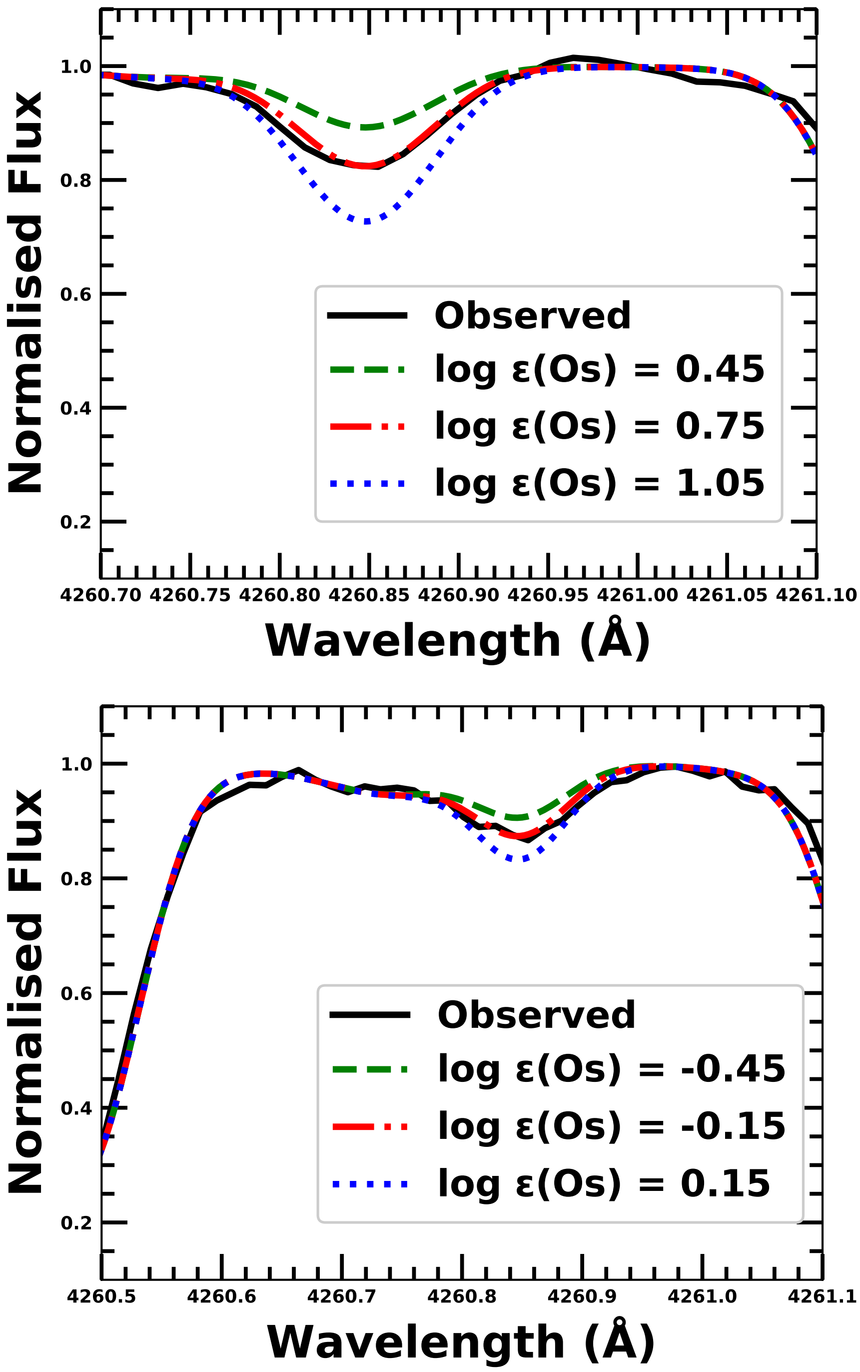

FIGURE 6.1: Top: Osmium synthesis in HD 224959. Bottom: Osmium synthesis in HD 187861. Red curves show best fit to the observed black color curves. Blue and green curves represent synthesis with a 0.3 dex difference.

hinting separate progenitors for r-I and r-II class of objects (also see Chapter 4). In previous classifications, the focus was solely on the element Eu to distinguish RPE stars. In the current study, we have broadened the approach by incorporating multiple elements to classify these stars more comprehensively using a clustering algorithms called Gaussian Mixture Model (GMM, McLachlan et al. 2019). This method allows for a robust and comprehensive understanding of the r-process enhancement, potentially leading to more accurate and insightful categorizations of stellar populations.

6.4 Machine learning Algorithms

To explore the similarities and distinctions between r-process and CEMP-r/s objects, and to revisit the classification scheme of RPE stars, we utilized a machine learning algorithm known as the Gaussian Mixture Model (GMM).

6.4.1 Gaussian Mixture Model

The Gaussian Mixture Model (GMM) is a clustering algorithm that identifies and separates clusters in data by fitting multiple Gaussian distributions to it. Each Gaussian corresponds to a different cluster and is defined by its mean and variance, which capture the center and spread of the cluster, respectively. In practice, GMM estimates these parameters such that each point in the dataset is associated with a Gaussian based on how likely it is to belong to that distribution.

For instance, in a one-dimensional dataset (see top panel of Figure 6.2) with overlapping data points, GMM can discern and separate the clusters by fitting two Gaussians, each aligning with the peak of the data distribution. This enables the model to clearly identify two distinct groups where the data points overlap. The same principle applies to two-dimensional datasets (see bottom panel of Figure 6.2), where GMM effectively separates overlapping clusters by fitting each

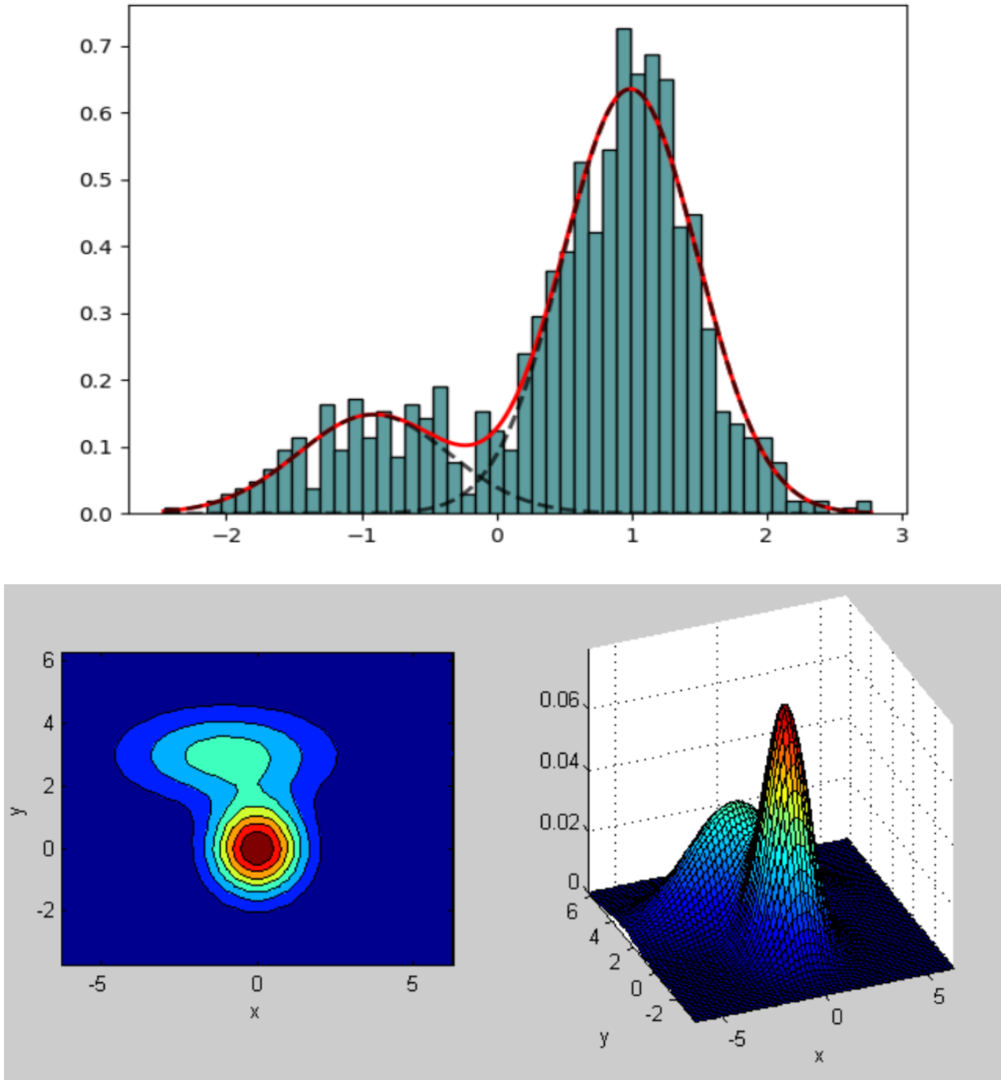

FIGURE 6.2: Examples of Gaussian Mixture Model (GMM) for cluster identification. Top: GMM application for one dimensional dataset. Bottom: GMM application for two dimensional dataset.

with its own Gaussian, thus revealing the underlying structure of the data even when clusters are not visibly distinct. This probabilistic approach allows GMM to handle complex and subtle data distributions effectively.

6.5 Results

6.5.1 Revisiting *r*-I and *r*-II classes using GMM

First, in contrast to the earlier clustering analysis in one dimensional [Eu/Fe] plane, we performed GMM clustering on all the RPE stars in five dimensional plane of Fe, C, Sr, Ba, and Eu abundances. We allowed GMM to fit 1 to 10 clusters with minimum number of stars 10 in each clusters. Then we choose the statistically significant number of clusters using Bayesian information criterion (BIC). The model which returns minimum value of BIC is considered the best model. Our analysis results in three clusters in the RPE objects as displayed trough four projection in Figure 6.3. It shows three groups G1, G2, G3 identified in our GMM analysis in various projected planes.

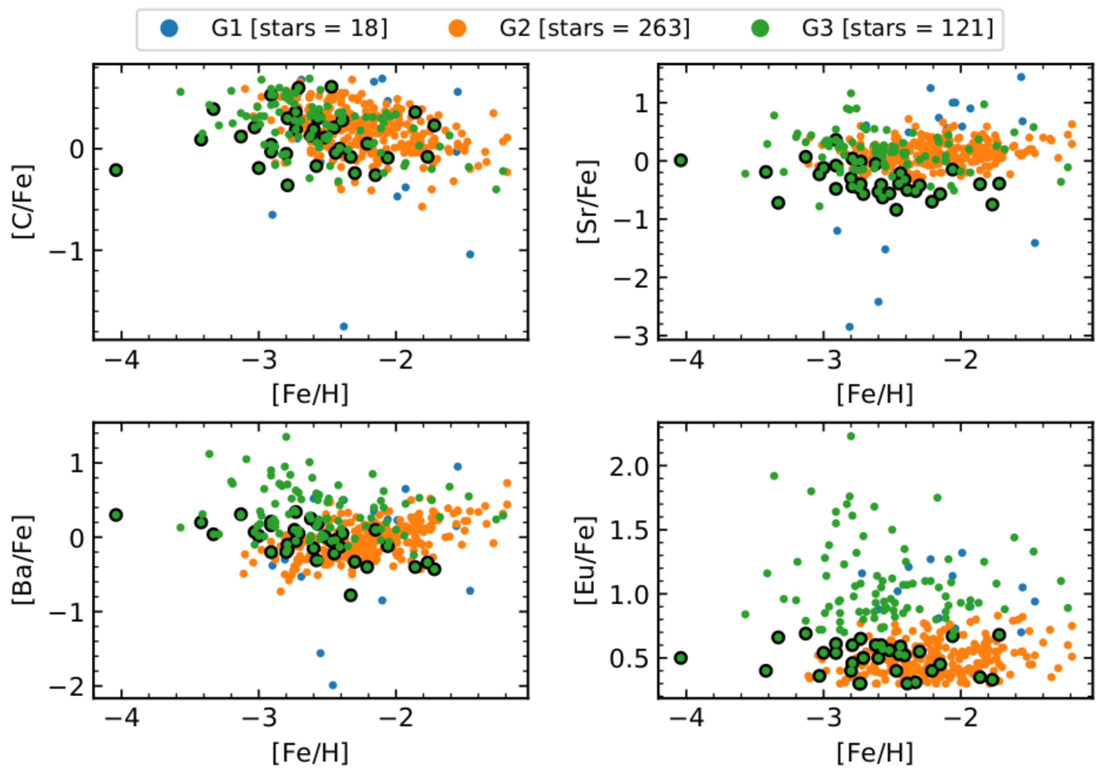

FIGURE 6.3: Classification of r-I and r-II objects using Gaussian Mixture Model in five dimensional plane of shown elements.

This analysis identifies two big groups G2 and G3. It appears that majority of G2 stars represent r-I and G3 stars represent r-II. In terms of fractional composition, group G1 contains 32% r-I and 68% r-II; group G2 contains 92% r-I and 8% r-II; and group G3 contains 29% r-I and 71 % r-II. It indicates that the r-I stars makes a clear group in five dimensional space, but r-II does not clearly separate out in this five dimensional space. Some of the G3 stars (29%) overlap with G2 stars. We have encircled in black those G3 stars that fall in the r-I region. Further inspection reveals that G3 stars overlapping with G2 stars are low in strontium, barium, and europium.

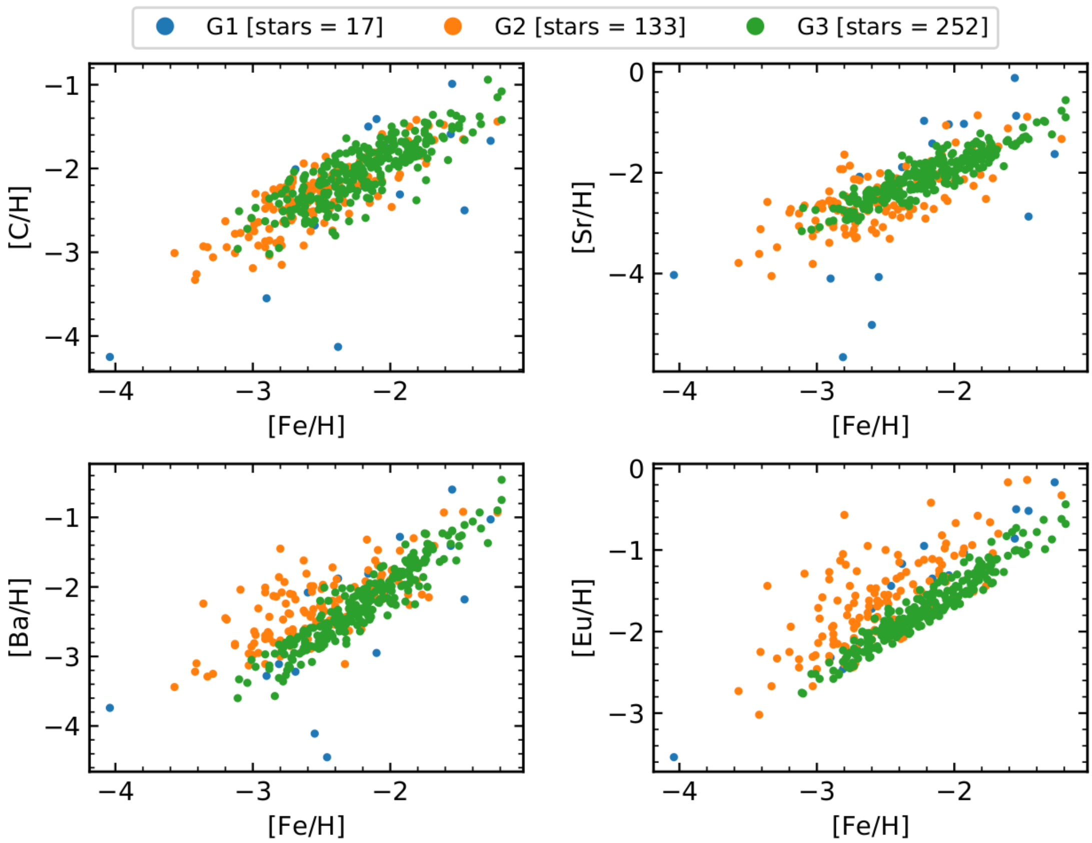

FIGURE 6.4: Categorization of r-I and r-II objects using Gaussian Mixture Model in five dimensional plane of shown elements.

We performed similar GMM analysis in five dimensional space, but for abundances relative to hydrogen. Again the clustering analysis identify three clusters as can be seen in Figure 6.4. Here, group G1 has 41% r-I and 59% r-II; group G2 contains

28% r-I and 69% r-II; and group G3 comprises of 91% r-I and 7% r-II. It indicates robustness of groups identification in two different planes.

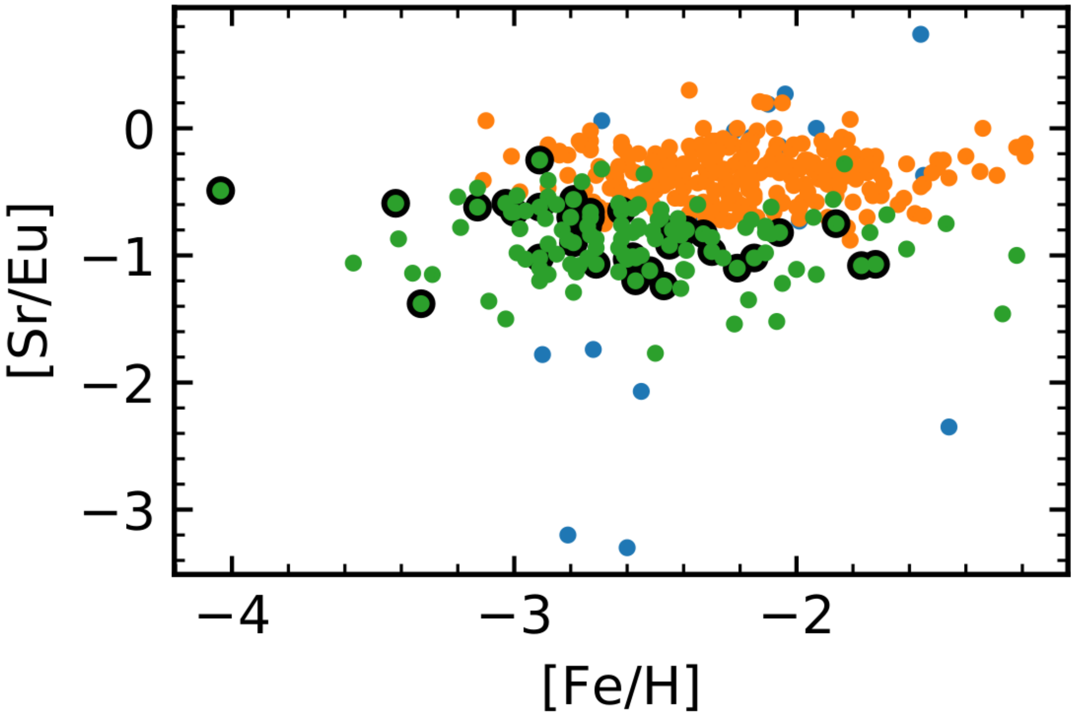

FIGURE 6.5: The same groups from Figure 6.3 in [Sr/Eu]−[Fe/H] plane.

Next, we examined the identity of group G3 stars encircled in black color in Figure 6.3, which overlap with r-I stars in group G2. For this we plot [Sr/Eu] with metallicity as displayed in Figure 6.5. All these stars now separate from the r-I stars of group G2 and show a low [Sr/Eu] ratio similar to that of r-II stars. Their low [Eu/Fe] similar to r-I stars, low [Sr/Eu] similar to r-II stars, and their presence in group G3 where the majority are r-II, suggest that they are born in the ISM mixed with diluted r-process ejecta from r-II like progenitor. Probably, group G3 forms a pristine set of stars which have similar r-process progenitors. We believe this approach provides a more effective way for accurate classifications based on ratios that reflect the underlying physical processes, rather than relying on arbitrary cutoffs.

6.5.2 Are CEMP-r/s and RPE stars the same?

For exploring the connection between CEMP-r/s and RPE objects, we perform GMM clustering analysis on our sample of RPE stars from Section 6.5.1 and on a sample of CEMP-r/s stars. As in Section 6.5.1, we performed GMM in five dimensional plane with varying number of clusters from 1 to 10, and finally choose the model which returns minimum BIC value. Our GMM analysis resulted in four groups G1, G2, G3, and G4 as shown in the four projection of Figure 6.6. The black asterisk represents the CEMP-r/s object which have reported Th detection (Gull et al. 2018).

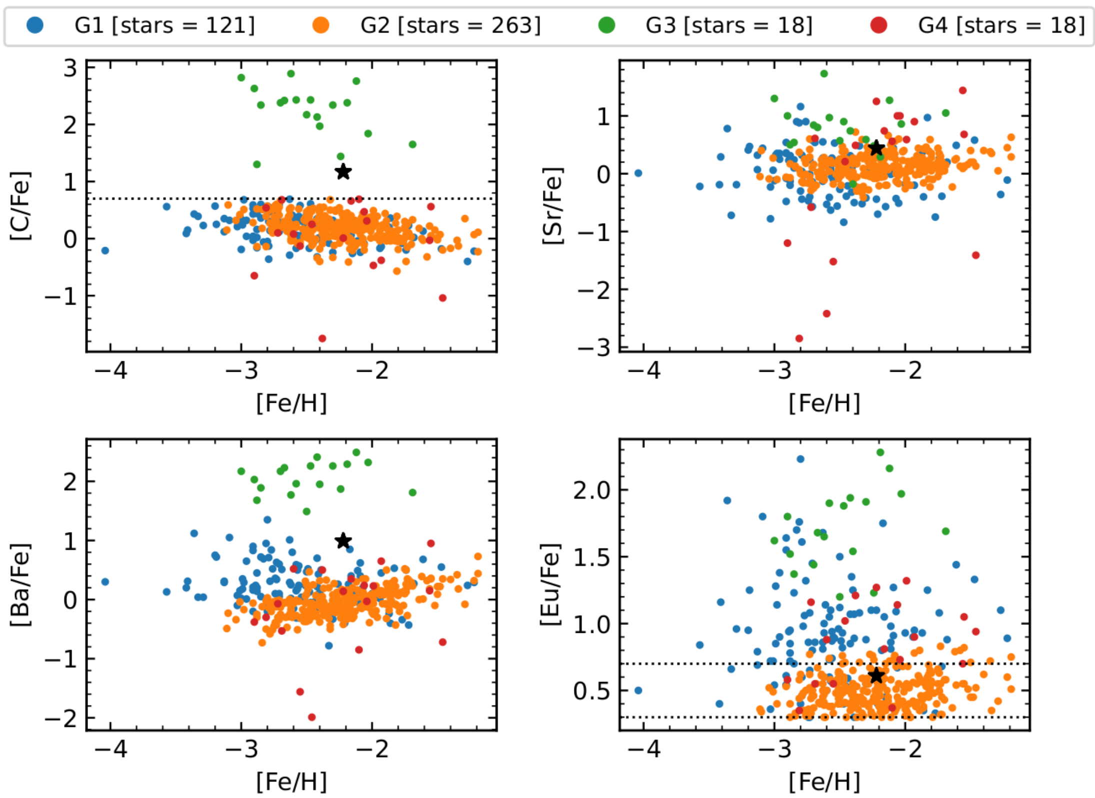

FIGURE 6.6: Grouping of r-I, r-II, CEMP-r/s objects using Gaussian Mixture Model in five dimensional plane of shown elements.

The groups G1, G2, and G4 identified in this analysis are similar to those identified in Section 6.5.1. The extra group G3 is new group which particularly includes all the CEMP-r/s stars. The group G1 includes 27% r-I and 73% r-II; group G2 has 92% r-I and 8% r-II; group G3 is entirely CEMP-r/s at 100%; and group G4 has 42% r-I and 58% r-II. The group G3 (group of CEMP-r/s stars) show clear demarcation based on their carbon and barium content, indicating that CEMP-r/s stars form a separate class, distinct from r-I and r-II.

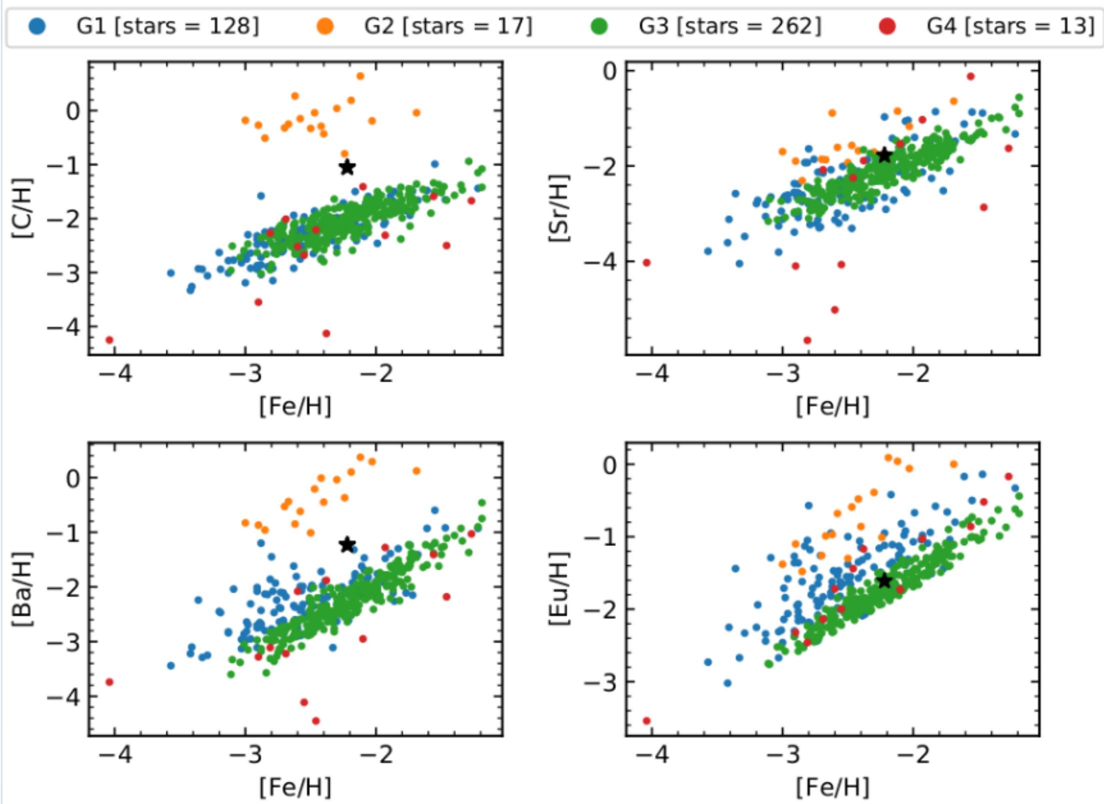

FIGURE 6.7: Grouping of r-I, r-II, CEMP-r/s objects using GMM in the [X/H] vs [Fe/H] plane.

Further, we perform GMM clustering in five dimensional space taking abundance relative to hydrogen. Again we found four clusters as can be seen in Figure 6.7. Here, group G1 has 22% r-I, 74% r-II, and 1% CEMP-r/s; group G2 is entirely CEMP-r/s at 100%; group G3 consists of 91% r-I and 7% r-II; and group G4 includes 54% r-I and 46% r-II. These findings highlight the clear divisions between these groups, emphasizing the unique characteristics of CEMP-r/s stars compared to other types.

The black asterisk shown in Figure 6.6 and Figure 6.7 represents the only CEMP-r/s stars with Th detection. In Section 6.2.1, we used high-resolution and high

SNR spectra of twenty CEMP-r/s stars and measure Th. Nonetheless, we could not identify any significant Th feature, except upper limits for a few stars. Although these objects are highly r-process enriched, similar to r-II stars, the lack of Th detection challenges their r-process enrichment. The CEMP-r/s star reported by Gull et al. (2018) may set a dividing line for Th detection and C enhancement. A further investigation of CEMP-r/s stars near [C/Fe]≈1 will provide more information about the relationship between C enhancement and Th detection, and possibly the origin of r-process in these stars.

6.6 Conclusions

We carried out spectrum synthesis of Os and Th lines in CEMP-r/s stars. Additionally, for the first time, we employed machine learning clustering algorithms to classify RPE stars into different groups using six parameters: abundances of C, Fe, Sr, Ba, and Eu.

In our sample of 20 CEMP-r/s objects, we detected Os in two of them. We did not find any significant signature of Th in these stars, except for upper limits in a few objects. The absence of Th detection in these highly RPE stars challenges our understanding of their r-process enrichment.

Our clustering analysis showed two major groups in RPE stars. One group includes majority of r-I stars while the other group includes both r-I and r-II stars. Further analysis revealed that the existence of r-I stars with r-II stars indicates that these r-I stars are likely enriched with the diluted ejecta from a similar progenitor that enriched the r-II stars.

When including CEMP-r/s stars in the clustering analysis, they form a separate group, leaving other groups nearly undisturbed. The only Th-detected CEMP-r/s star from Gull et al. (2018) appears at the boundary of these groups, leaving scope for further investigation at the boundary region to understand the r-process richness in CEMP-r/s stars.

Our machine learning based classification scheme using multiple parameters will be beneficial in better reflecting the actual physical processes of r-process enhancement. A larger sample of RPE objects in the future will further constrain these clustering analyses.

Chapter 7

New metal-poor stars from HESP-GOMPA survey-II: stellar parameters, abundances and kinematics

Abstract

Bright stars with very low metal content ($V < 12$, $[Fe/H] < -2.0$) offer valuable opportunities to study early star formation and chemical enrichment processes across various galactic components. We analyzed the abundances of light and n-capture elements in 33 newly discovered bright, metal-poor stars as a part of the HESP-GOMPA (Hanle Echelle SPectrograph – Galactic survey Of Metal Poor stArs) survey. These stars were initially identified from low-resolution LAMOST

spectra and selected through automated spectrum synthesis. Most of these stars have metallicities ranging from −3.2 to −1.5, a critical range where the abundance patterns of key elements change significantly, indicating major milestones in the galaxy evolution and the operation of new nucleosynthesis sites. This metallicity range is also overlaps with the formation of the majority of stars in the thick disk and inner halo of our galaxy. From the survey, we identified several stars enriched with r-process elements, CEMP stars, and EMP stars. We compare elemental abundances of these stars with halo stars to understand the characteristics of their massive star ancestors. Detailed analysis of elemental abundances, and kinematics provides insights into their chemical and dynamical origins. Many of these bright stars, with their detailed abundance data, could serve as benchmarks for future surveys of metal-poor stars.

7.1 Introduction

The study of MP stars, known as "near-field cosmology," has advanced greatly over the past seventy years, starting with early discoveries highlighted by Chamberlain & Aller (1951). Significant progress came through large-scale spectroscopic surveys, like the HK survey (Beers et al. 1985, 1992) and the Hamburg/ESO Survey (Christlieb 2003), which greatly expanded the catalog. Recent spectroscopic survey projects such as SDSS, SEGUE, APOGEE, RAVE, LAMOST, GALAH (Fulbright et al. 2010; Ivezić et al. 2012; Zhao et al. 2012; Aoki et al. 2013; García Pérez et al. 2013; Anders et al. 2014; De Silva et al. 2015; Li et al. 2015) have further boosted our understanding, increasing the sample of MP stars from hundreds to thousands. Future surveys like WEAVE (Dalton et al. 2014), 4MOST (de Jong et al. 2019), and SDSS V's Milky Way Mapper (Kollmeier et al. 2017) aim to expand spectroscopic data to millions of stars. However, detailed studies of high-resolution spectroscopy and kinematic separation are still limited. The

SAGA database reveals only about 1000 objects below −3.0 metallicity, about 200 below −3.5 metallicity, and about 50 below −4.0 metallicity due to the challenges of obtaining high-quality spectra and precise astrometric data, especially for faint stars (For instant, see Figure 7.1). Still, there are several candidate bright metal-poor stars that lack detailed abundances, offering opportunities for high resolution follow-up, particularly using 2-m class small telescope facilities, e.g., HCT in India.

Though the objects below metallicity of −3.0 are the best candidates to probe early nucleosynthesis, there number decreases sharply for a statistical study as we move towards much lower metallicities. On the other hand, metallicity interval $-3.0 < [Fe/H] < -2.0$ is an interesting window where we have significant candidate bright metal-poor stars for statistical analysis of the nucleosynthesis process acting during transition period of Type II to Type I supernovae, the major source of metal enrichment. Certain supernova events such as pair instability supernovae, known for their significant iron production, are expected to increase ISM metal content up to $[Fe/H] \sim -2$ (Salvadori et al. 2019), hence probing these metallicities will be important to study rare events of the early Galaxy. This is where we take advantage of our HESP-GOMPA survey which particularly focus on the bright metal-poor stars selected from various large scale low/medium-resolution surveys for high-resolution follow-up to provide their detailed chemical composition.

This chapter explores a detailed analysis of 33 newly identified metal-poor stars through the HESP-GOMPA survey II. Following is the outline of this chapter: Section 7.1 provides an introduction to metal-poor stars, and highlights various previous metal-poor star surveys and scope for further investigation. Section 7.2 outlines the methodology of the high-resolution observations, data preparation, and the calculation of radial velocities for the stars. Sections 7.3 and 7.4 present the estimation of stellar atmospheric parameters and detail our abundance measurement. Section 7.5 discuss the analysis of abundance, highlights peculiarities of the objects, and offers a discussion of our findings, where as section 7.6 describes

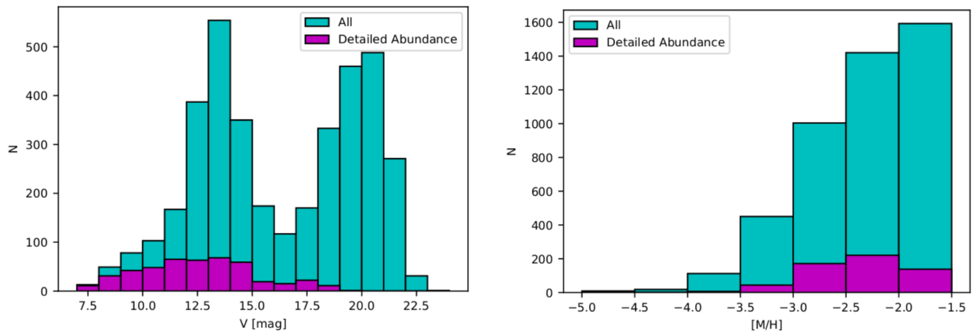

FIGURE 7.1: Left: Vmag distribution of the SAGA database. The cyan bars represent all the metal-poor stars, while the magenta bars represent stars with accurate abundances of alpha, iron peak, and neutron capture elements. Right: Metallicity distribution of the same stars from the SAGA database. It is evident that only around 10% of the sample has detailed abundances, leaving 90% without detailed abundance measurements.

about the kinematical behaviour of the stars followed by a concise conclusion in Section 7.7.

7.2 Sample Selection, data preparation and radial velocity estimation

In the initial HESP-GOMPA survey, high-resolution spectroscopic follow-up was conducted on metal-poor stars selected from the SDSS-MARVELS survey. Some of the results were presented in (Bandyopadhyay et al. 2018, 2020b,d, 2022, 2024; Saraf & Sivarani 2024, 2023a; Saraf et al. 2024). In the phase-II, the MP stars ([Fe/H] < -2.0) were obtained from the LAMOST catalogue and further automated spectral fitting of the LAMOST low resolution spectra. Details are presented in Chapter 2. The observations span about 1.5 years starting from early 2022 over 1.5 years. Standard data processing is carried out. This involved converting raw spectra into calibrated science spectra, transitioning from pixel-based to wavelength-based data, and performing continuum normalization using an IRAF package. Table 7.1 presents details of the observed targets, including star names,

TABLE 7.1: Basic observational information for our program stars.

Star name	RA	DEC	SNR	Exposure time (sec)	V mag	Date of observation
UCAC4 488-001423	00:59:27.84	07:31:11.34	54.27	2400*3	12.02	2022-12-14
TYC 1795-438-1	03:05:35.74	28:34:22.70	63.15	2400*3	11.96	2022-10-24
TYC 665-522-1	03:57:37.94	12:45:51.07	59.62	2400*3	10.92	2022-10-24
TYC 1939-202-1	08:09:00.32	28:50:08.40	44.51	2400*3	11.57	2022-12-13
TYC 195-1636-1	08:12:09.95	00:28:46.90	58.77	2400*3	11.84	2022-12-13
TYC 23-815-1	01:12:28.01	04:21:02.29	44.74	2400*3	11.8	2022-09-29
TYC 2985-737-1	08:50:38.88	41:43:48.85	37.21	2400*3	11.93	2022-02-19
TYC 1404-1448-1	09:04:59.41	18:34:59.08	47.86	2400*3	11.33	2022-04-06
TYC 1406-971-1	09:32:56.49	18:23:09.48	65.10	2400*3	11.04	2022-04-06
TYC 243-502-1	09:58:31.09	06:29:12.79	47.76	2400*3	11.79	2023-01-27
TYC 3443-1105-1	10:49:47.47	46:00:41.81	64.01	2400*3	11.37	2022-04-06
LP 491-46	11:00:36.34	11:27:49.12	46.16	2400*3	11.22	2023-01-27
TYC 1436-366-1	11:01:49.39	20:31:25.90	61.95	2400*3	11.51	2022-03-13
TYC 2533-1475-1	12:36:03.30	34:24:39.55	54.53	2400*3	11.32	2022-03-13
TYC 1465-1148-1	13:31:49.67	21:00:00.51	49.93	2400*3	11.24	2022-03-13
TYC 1192-20-1	00:55:27.49	18:57:57.17	46.36	2400*3	10.77	2022-09-29
TYC 2014-552-1	14:22:22.76	28:41:37.38	77.36	2400*3	11.42	2023-05-22
TYC 3474-142-1	14:59:10.00	46:41:29.20	65.57	2400*3	10.86	2022-05-19
TYC 1501-1445-1	15:48:59.48	21:13:28.44	49.92	2400*3	10.55	2023-05-24
TYC 1760-1284-1	01:57:41.77	26:01:17.26	35.76	2400*3	12.25	2022-12-14
TYC 2601-637-1	16:51:41.83	37:07:55.78	43.96	2400*3	11.72	2023-05-23
TYC 975-2188-1	16:51:43.98	08:54:16.74	49.47	2400*3	11.76	2023-05-22
TYC 1576-1703-1	18:21:10.51	19:14:42.45	80.05	2400*3	11.7	2022-07-05
TYC 3534-57-1	18:29:18.10	48:52:38.90	54.04	2400*3	11.9	2022-09-28
TYC 1653-657-1	21:09:58.02	17:25:43.98	52.53	2400*3	10.69	2022-07-05
TYC 1170-642-1	23:45:05.83	09:19:19.77	50.71	2400*3	12.1	2022-12-14
TYC 1988-1110-1	12:04:59.84	28:23:29.15	53.88	2400*3	11.3	2022-03-13
UCAC4 430-119026	22:12:54.60	-04:08:59.35	54.23	2400*3	11.66	2022-10-24
TYC 1120-1253-1	21:40:11.96	08:29:22.46	58.22	2400*3	11.68	2022-09-29
TYC 224-475-1	08:48:17.00	07:00:41.27	78.55	2400*3	11.03	2022-12-14
TYC 1741-618-1	00:38:59.67	27:25:51.69	46.87	2400*3	11.73	2022-09-28
TYC 267-308-1	11:22:30.05	03:59:40.28	52.31	2400*3	10.85	2023-01-28
TYC 279-1113-1	11:58:52.14	05:31:59.10	50.11	2400*3	11.58	2023-01-28

right ascension (RA), declination (DEC), SNR at 5000 Å, exposure, V-band magnitudes and date of observation.

The spectra are corrected for radial velocity (RV) by cross-correlating observed spectra with templates spectra of similar stellar parameters using the IDL routine CRSCOR. The continuum-normalized spectra are shifted to account for the RV using the IRAF task DOPCOR. RV measurements, adjusted for the Earth's motion around the Sun and we report the heliocentric RVs. Table 7.2 lists the

TABLE 7.2: RV of our program stars.

Star name	Geocentric (km/s)	Heliocentric (km/s) [This study]	GAIA DR3
UCAC4 488-001423	−98.75	−126.16±0.24	−126.02±0.04
TYC 1795-438-1	−48.25	−38.21±0.23	−36.52±1.12
TYC 665-522-1	−91.9	−77.86±0.33	−78.69±0.39
TYC 1939-202-1	−30.65	−13.13±0.28	−10.76±0.71
TYC 195-1636-1	+170.1	+189.62±0.33	+189.73±0.31
TYC 23-815-1	−57.5	−51.76±0.29	-
TYC 2985-737-1	−124.7	−137.22±0.51	−137.76±1.28
TYC 1404-1448-1	+208.1	+181.76±0.34	+181.91±0.16
TYC 1406-971-1	+178.1	+153.57±0.22	+154.23±0.79
TYC 243-502-1	+165	+176.43±0.30	+176.17±1.73
TYC 3443-1105-1	+150.5	+131.54±0.26	+131.73±1.28
LP 491-46	+49	+66.3±0.24	-
TYC 1436-366-1	+98.5	+91.44±0.43	+89.28±0.055
TYC 2533-1475-1	+248.8	+248.7±0.26	+250.94±0.70
TYC 1465-1148-1	−129.15	−120.29±0.39	-
TYC 1192-20-1	+11.3	+17.69±0.20	+24.23±2.72
TYC 2014-552-1	−44.6	−58.65±0.24	−56.09±0.84
TYC 3474-142-1	+31.4	+21.78±0.25	+20.02±0.05
TYC 1501-1445-1	−27.7	−33.12±0.37	−32.83±4.36
TYC 1760-1284-1	−173.5	−194.55±0.57	−192.3±1.91
TYC 2601-637-1	−10.9	−10.41±0.31	−10.2±0.49
TYC 975-2188-1	−245.5	−241.13±0.24	−241.79±1.00
TYC 1576-1703-1	−146.9	−149.34±0.48	−149.83±1.65
TYC 3534-57-1	+0.5	−8.38±0.25	−8.08±2.24
TYC 1653-657-1	−258.75	−241.94±0.26	−241.44±0.34
TYC 1170-642-1	−154.35	−183.68±0.23	−184.63±0.66
TYC 1988-1110-1	+33	+31.22±0.38	+46.8±6.08
UCAC4 430-119026	−245.7	−270.91±0.24	−270.25±0.32
TYC 1120-1253-1	−338.9	−355.53±0.37	−354.68±1.46
TYC 224-475-1	+157.9	+180.54±0.27	+180.89±0.34
TYC 1741-618-1	−107	−100.5±0.30	−97.56±2.07
TYC 267-308-1	+365.4	+385.36±0.24	+387.51±0.60
TYC 279-1113-1	+23.25	+46.12±0.38	+45.96±1.07

geocentric RVs, heliocentric RVs, and comparison to GAIA. Recent Gaia DR3 values correspond well with these calculations, except for two stars: TYC 1192-20-1 and TYC 1988-1110-1, which show differences of 6.54 and 15.58 km/sec, respectively. Of these, TYC 1988-1110-1 is confirmed as a spectroscopic binary (Gaia Collaboration 2018). The RV measurement of TYC 1192-20-1 suggests it may likely be a binary or multi-star system, prompting plans for periodic radial velocity monitoring in the future.

7.3 Stellar parameter Estimation

We utilized both photometric and spectroscopic measurements to estimate the stellar parameters ($T_{\rm eff}$, $\log g$, ξ, and [Fe/H]) of our program stars. The detailed methodology for estimating these stellar parameters is outlined in Chapter 2. Table 7.3 and Table 7.4 show the estimated temperatures and surface gravities for all of our program stars, obtained through various techniques. The detailed discussion on estimating temperatures and surface gravities using various methods can be found in chapter 2. For the consistency check, we place our program stars on the evolutionary tracks ranging from 8-12 Gyr in age. Figure 7.2 shows the CMD of our program stars. All the stars, except two, are evolved and falling on giant branch. Two stars, TYC 1576-1703-1 and TYC 3534-57-1, are in the sub-giant phase. Our estimated surface gravities show decreasing difference with Gaia DR2 as $\log g$ increases, which is consistent with previous findings (e.g., see, Ezzeddine et al. 2020).

For further analysis, we have restricted ourselves to the stellar parameters in Table 7.5 obtained using the spectroscopic method, i.e., $T_{\rm eff}$ from excitation equilibrium, $\log g$ from ionization balance, micro-turbulence from zero trend of Fe I with normalized EW, and metallicity from the mean Fe I abundance.

7.4 Abundance Calculation

We utilized the ATLAS9 atmospheric model (Kurucz 1993a; Castelli & Kurucz 2003) in a one-dimensional LTE framework to get the abundances of many elements in our stars. For line synthesis, we employed the most recent version of the TURBOSPECTRUM code (Turbospectrum2019) (Alvarez & Plez 1998; Plez 2012). Our methodology involved a combination of EW analysis and spectrum

TABLE 7.3: Estimates of temperatures of our program stars using different methods.

Star name	Temp (FeI and Fe II)	Hα	V-K	J-H	J-K	SED	GAIA DR2	GAIA DR3
UCAC4 488-001423	4858	4858	5103	4936	4855	5500	-	-
TYC 1795-438-1	4653	4703	4803	4625	4722	3750	5115.67	6099.2
TYC 665-522-1	4901	4851	5161	5136	5244	-	4889	-
TYC 1939-202-1	5042	4942	5094	4720	4752	-	4953.37	-
TYC 195-1636-1	4829	4929	4898	4947	4934	-	5163.1	6157.7
TYC 23-815-1	5023	5073	5301	5157	5083	-	5327	-
TYC 2985-737-1	4857	4957	5163	4904	4880	-	5234.16	5400.4
TYC 1404-1448-1	4851	4801	4711	4524	4543	-	4803.2	-
TYC 1406-971-1	4763	4763	4928	4856	4789	-	5072.94	6005
TYC 243-502-1	5050	5050	5039	4967	4855	-	5662.71	6116.8
TYC 3443-1105-1	4805	4855	4993	4796	4802	-	5068.58	-
LP 491-46	5517	5617	5803	5711	5556	-	5935.95	-
TYC 1436-366-1	5560	5610	5300	5543	5201	-	5694	6257.8
TYC 2533-1475-1	4898	4798	4814	4857	4820	4250	5214.46	-
TYC 1465-1148-1	4942	4892	5118	4751	4841	-	5119.35	-
TYC 1192-20-1	4734	4884	5345	4747	4775	-	5321	-
TYC 2014-552-1	5154	5104	5342	5212	5185	-	5438.67	-
TYC 3474-142-1	5087	5178	5334	5133	5176	3750	5580.5	6172.5
TYC 1501-1445-1	5292	5192	5291	5056	4967	-	5377.25	-
TYC 1760-1284-1	5578	5628	5327	5599	5549	-	5339	5728.8
TYC 2601-637-1	5113	4963	4968	4986	4967	-	5411	6099.1
TYC 975-2188-1	5168	5068	5428	4993	4887	-	5052.08	-
TYC 1576-1703-1	6241	6575	-	-	-	4250	6282	-
TYC 3534-57-1	6425	6325	6203	-	-	-	6709.67	6480.7
TYC 1653-657-1	4660	4710	4911	4695	4775	5500	4952.01	5356.5
TYC 1170-642-1	4934	4934	5003	4936	4994	-	4901.91	-
TYC 1988-1110-1	4518	4568	4597	-	-	-	4919.25	-
UCAC4 430-119026	4500	4600	4723	4520	4616	-	5070.75	5982.7
TYC 1120-1253-1	5215	5115	5605	5052	5067	-	5335.1	-
TYC 224-475-1	4941	4991	5001	5193	5009	-	5365	-
TYC 1741-618-1	4826	4776	4789	4819	5013	-	5087.88	-
TYC 267-308-1	4540	4690	4828	4600	4622	-	4930.33	-
TYC 279-1113-1	5539	5589	5512	5577	5657	-	5864.67	-

synthesis techniques for elemental abundance calculation. For more detail see chapter 2.

TABLE 7.4: Estimates of surface gravities of stars in this study using different methods.

Star name	$\log g$ (Fe I and Fe II)	Mg triplet	GAIA DR3	GAIA DR2 (using luminosity)
UCAC4 488-001423	1.97	1.77	-	2.67
TYC 1795-438-1	1.25	1.25	2.66	1.81
TYC 665-522-1	2.1	2.43	4.26	2.87
TYC 1939-202-1	2.02	1.82	-	2.24
TYC 195-1636-1	1.91	1.89	3.09	2.57
TYC 23-815-1	1.66	1.76	-	2.9
TYC 2985-737-1	1.35	1.53	2.28	2.12
TYC 1404-1448-1	1.93	2.03	-	1.61
TYC 1406-971-1	1.32	1.32	2.59	-
TYC 243-502-1	2.15	2.25	3.11	2.55
TYC 3443-1105-1	1.65	1.75	-	1.91
LP 491-46	3.01	3.01	-	-
TYC 1436-366-1	3.41	3.11	3.31	3.07
TYC 2533-1475-1	1.72	1.92	-	1.99
TYC 1465-1148-1	2.04	2.04	-	1.99
TYC 1192-20-1	1.4	1.6	-	2.6
TYC 2014-552-1	2.26	2.26	-	2.48
TYC 3474-142-1	2.03	2	3.57	3.16
TYC 1501-1445-1	2.52	2.62	-	3.01
TYC 1760-1284-1	2.99	3.09	2.64	2.74
TYC 2601-637-1	2.64	2.54	3.38	3.08
TYC 975-2188-1	2.9	3.1	-	2.66
TYC 1576-1703-1	3.65	3.9	-	3.63
TYC 3534-57-1	3.91	3.52	4.21	-
TYC 1653-657-1	1.29	1.49	2.43	1.84
TYC 1170-642-1	1.91	1.81	-	2.51
TYC 1988-1110-1	1.01	1.21	-	-
UCAC4 430-119026	1.01	1.01	2.45	-
TYC 1120-1253-1	2.8	2.5	-	2.78
TYC 224-475-1	2	1.9	-	2.93
TYC 1741-618-1	1.64	1.64	-	2.69
TYC 267-308-1	1.06	0.96	-	1.51
TYC 279-1113-1	2.79	2.79	-	3.71

Table 7.5: Final adopted stellar parameters for our program stars.

Star name	$T_{\rm eff}$ (K)	$\log g$	[Fe/H]	ξ (km/s)
UCAC4 488-001423	4858	1.97	−2.08	1.3
TYC 1795-438-1	4653	1.25	−2.55	1.3
TYC 665-522-1	4901	2.1	−2.43	1.28
TYC 1939-202-1	5042	2.02	−2.39	2.4
TYC 195-1636-1	4829	1.91	−2.44	1.8
TYC 23-815-1	5023	1.66	−2.5	1.3
TYC 2985-737-1	4857	1.35	−2.37	2.91
TYC 1404-1448-1	4851	1.93	−2.33	1.77
TYC 1406-971-1	4763	1.32	−2.23	1.41
TYC 243-502-1	5050	2.15	−2.1	2.36
TYC 3443-1105-1	4805	1.65	−2.54	1.05
LP 491-46	5517	3.01	−2.13	1.48
TYC 1436-366-1	5560	3.41	−2.49	1.02
TYC 2533-1475-1	4898	1.72	−2.65	1.01
TYC 1465-1148-1	4942	2.04	−2.76	1.05
TYC 1192-20-1	4734	1.4	−2.44	1.22
TYC 2014-552-1	5154	2.26	−2.43	0.85
TYC 3474-142-1	5087	2.03	−2.45	1.58
TYC 1501-1445-1	5292	2.52	−2.21	1.36
TYC 1760-1284-1	5578	2.99	−1.97	2.89
TYC 2601-637-1	5113	2.64	−2.46	0.8
TYC 975-2188-1	5168	2.9	−2.4	0.8
TYC 1576-1703-1	6241	3.65	−2.18	1.27
TYC 3534-57-1	6425	3.91	−1.76	2.02
TYC 1653-657-1	4660	1.29	−2.77	1.23
TYC 1170-642-1	4934	1.91	−2.37	2.19
TYC 1988-1110-1	4518	1.01	−3.11	1.04
UCAC4 430-119026	4500	1.01	−2.41	1.27
TYC 1120-1253-1	5215	2.8	−2.15	1.38
TYC 224-475-1	4941	2.00	−2.33	1.31
TYC 1741-618-1	4826	1.64	−2.57	1.28
TYC 267-308-1	4540	1.06	−2.34	1.74
TYC 279-1113-1	5539	2.79	−1.82	2.65

7.4.1 Light, alpha and iron-peak elements

We determined the abundances of light elements including C, Na I, Mg I, Ca I, Sc II, Ti I, Ti II, Cr I, Cr II, Mn I, Co I, Ni I, and Zn I across all the stars. It is relevant to note that not all stars may contain every element listed here.

Carbon abundances were determined through spectral fitting centered around the

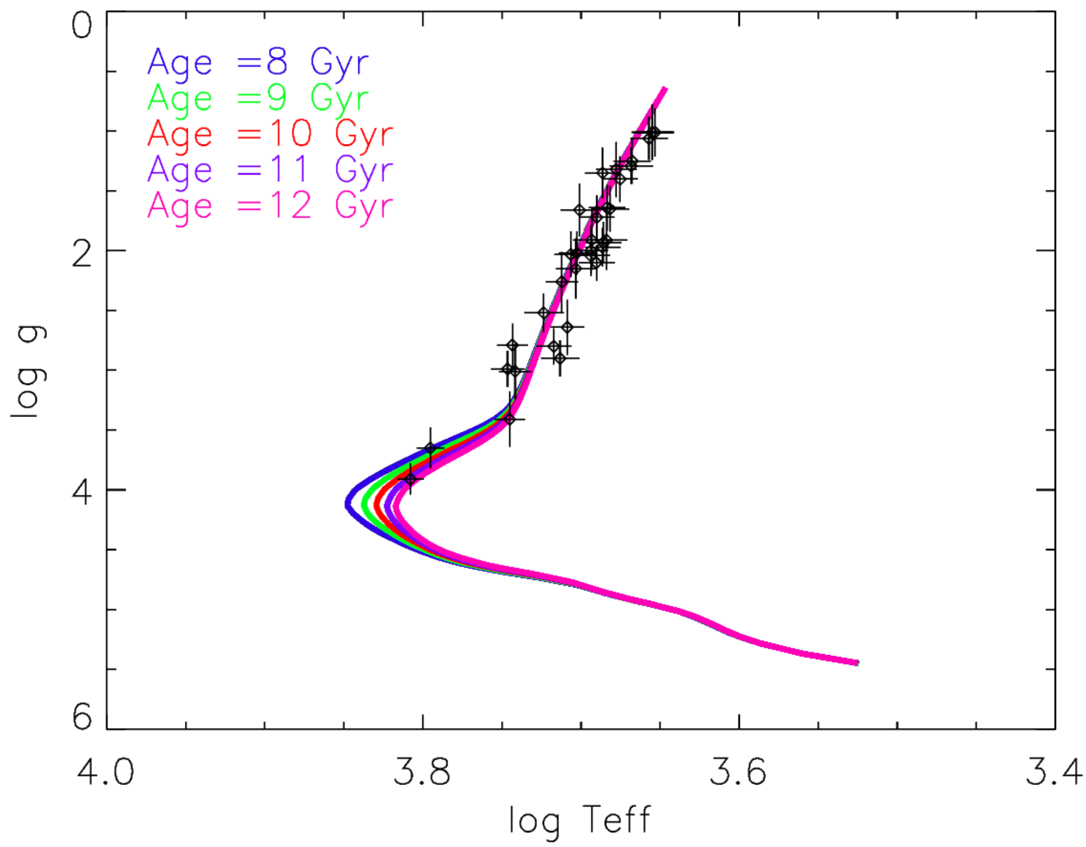

FIGURE 7.2: Surface gravity ($\log g$) versus effective temperature ($\log T_{\rm eff}$) for our program stars. The black diamonds show the locations of the program stars along with the measurement uncertainties. Different color curves shows isochrones ranging 8 to 12 Gyr in age.

CH G band near 4313 Å. These abundances were corrected for the star's current evolutionary stage and are detailed in Table 7.6. Notably, some stars exhibit enhanced carbon levels, which are discussed in the subsequent section. For illustration, the synthesis of carbon band is shown in Figure 7.3.

Na, the odd-Z element was estimated using the D1 and D2 lines located at 5890 Å and 5896 Å, respectively. NLTE corrections for Na were applied to refine these values (Andrievsky et al. 2007), which are incorporated into the final results. Among the α-elements, Mg and Ca were studied in these stars. While multiple spectral lines for Mg and Ca were available, only those free from contamination were used to derive their abundances. Si lines were detectable in some stars but

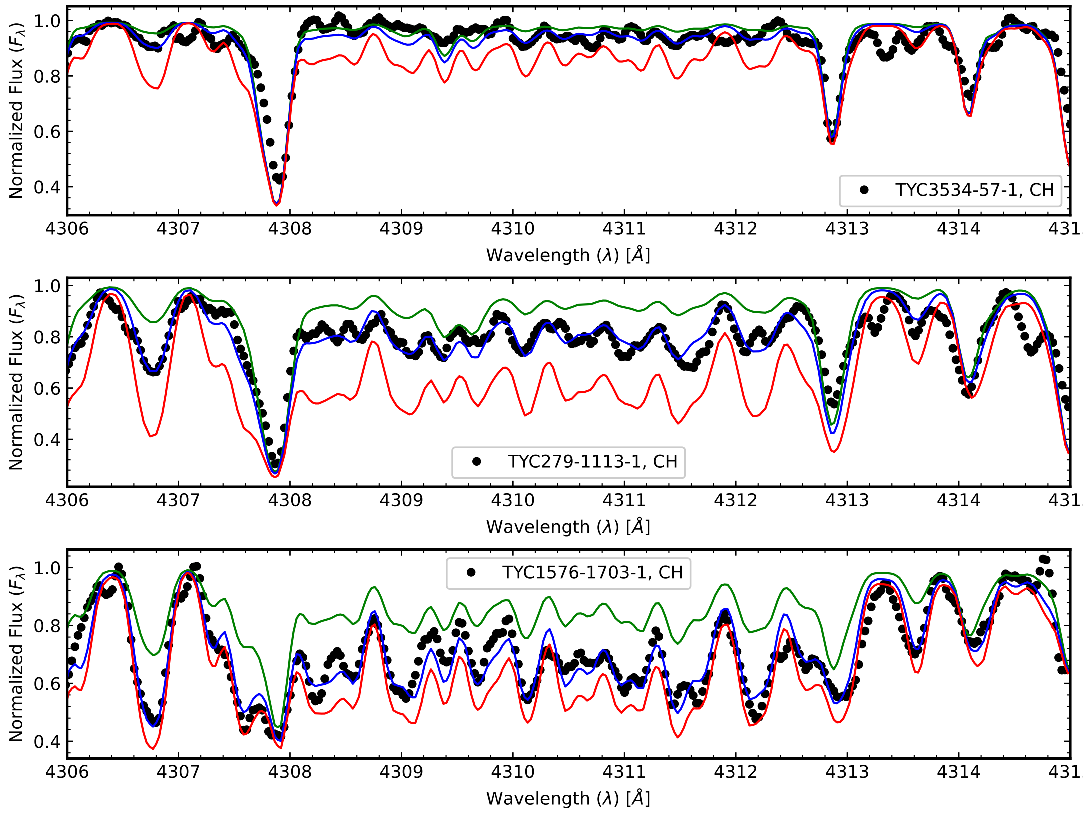

FIGURE 7.3: Synthesis of carbon band for three CEMP stars. Blue color shows the best fit to the observed points shown in black. Green and red colors represent 0.5 dex scatter from the best fit curve.

too weak in others to derive meaningful abundances.

For the Fe-peak elements (Cr, Co, Mn, Ni, Zn), a combination of EW analysis and spectral synthesis was employed. Hyperfine splitting effects were considered where necessary. Iron (Fe I and Fe II) abundances were calculated using the equivalent-width method during the stellar parameter estimation process. The abundance of Co was also estimated for certain stars based on the availability of uncontaminated spectral lines in the spectra.

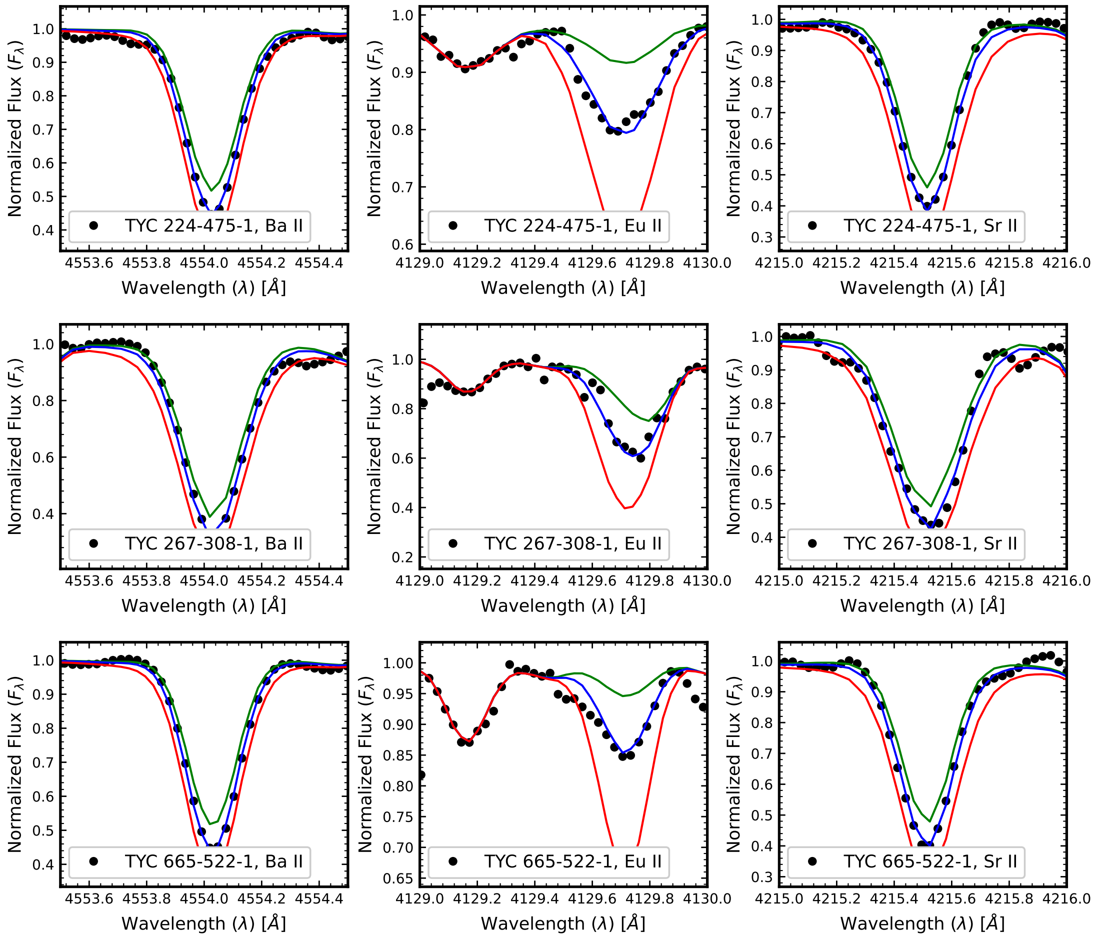

FIGURE 7.4: Synthesis of Ba, Eu, and Sr lines in TYC 224-475-1, TYC 267-308-1, and TYC 665-522-1. Black dots are observed spectra and blue curves are best fit. Green and red colors represent 0.5 dex scatter from the best fit curve.

7.4.2 Neutron-capture elements

Neutron capture elements such as Sr, Ba, and Eu were measurable in all stars. Sr abundances were derived using 4077 Å and 4215 Å Sr II resonance lines. For Ba, lines at 4554 Å, 4934 Å, 5853 Å, 6142 Å, and 6496 Å were utilized. The NLTE effect on the 4554 Å line was corrected following Short & Hauschildt (2006b), accounting for up to a dex of +0.14 at [Fe/H] = −4.0. The line at 4934 Å is contaminated with an Fe I line whose $\log gf$ is not well-constrained (Gallagher et al. 2012; Hansen et al. 2018c). The abundance of Eu primarily relied on lines at 4129 Å and 4205 Å. Spectral synthesis methods were used to determine the

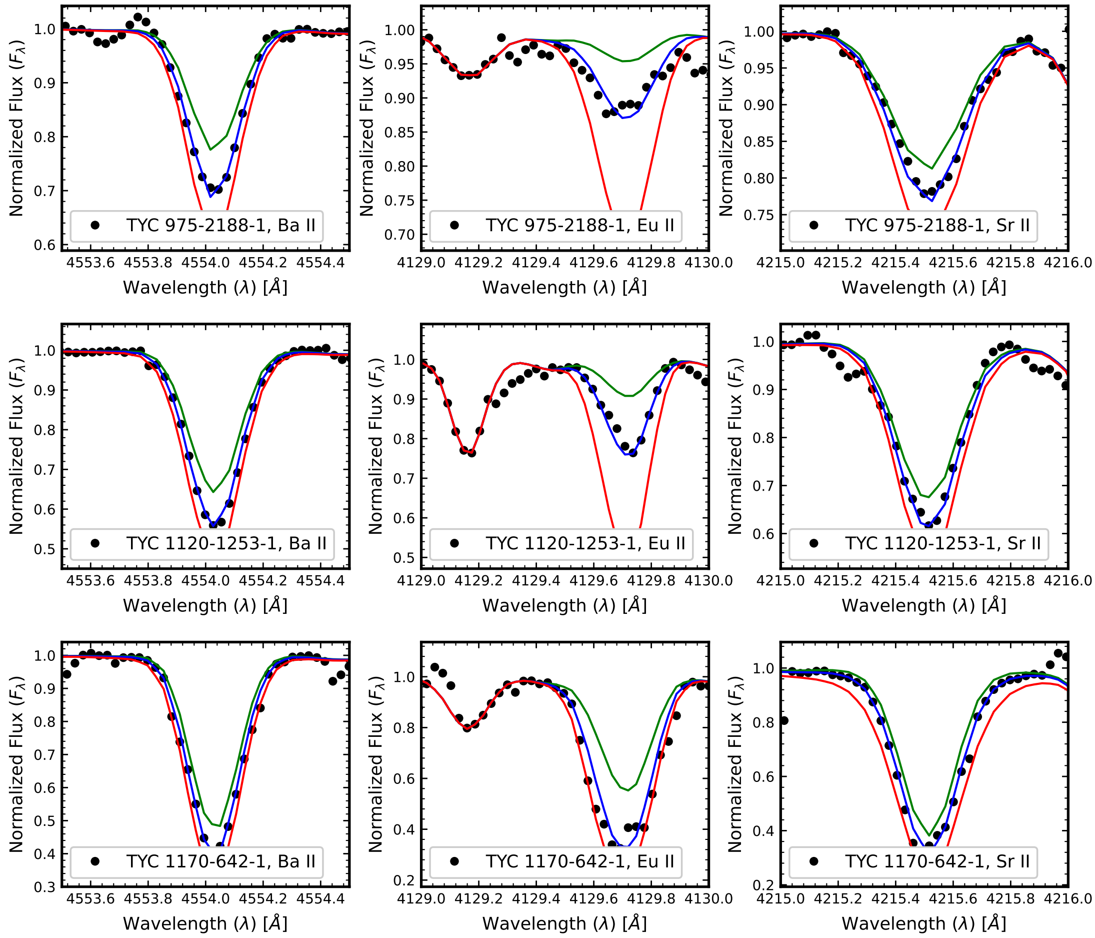

FIGURE 7.5: Synthesis of Ba, Eu, and Sr lines in TYC 975-2188-1, TYC 1120-1253-1, and TYC 1170-642-1. Black dots are observed spectra and blue curves are best fit. Green and red colors represent 0.5 dex scatter from the best fit curve.

abundances, ensuring that hyperfine transitions were appropriately considered. In Figure 7.4, 7.5, 7.6, 7.7 show the synthesis of Ba, Eu, and Sr lines in some of our program stars. The chemical abundances of our program stars are listed in Table C.1, C.2, C.3, C.4, C.5, C.6, C.7, C.8, C.9, C.10, C.11, C.12, C.13, C.14, C.15, C.16, C.17, C.18, C.19, C.20, C.21, C.22, C.23, C.24, C.25, C.26, C.27, C.28, C.29, C.30, C.31, C.32, C.33.

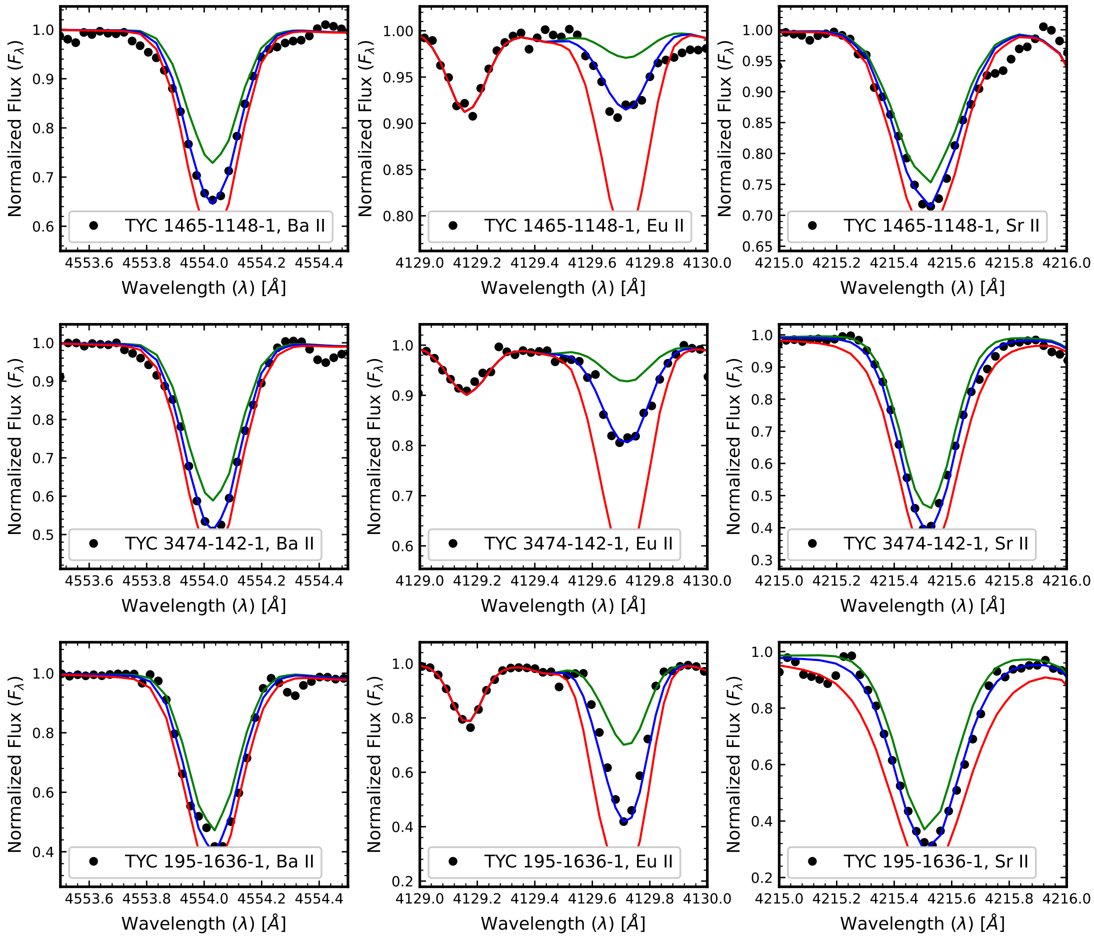

FIGURE 7.6: Synthesis of Ba, Eu, and Sr lines in TYC 1465-1148-1, TYC 3474-142-1, and TYC 195-1636-1. Black dots are observed spectra and blue curves are best fit. Green and red colors represent 0.5 dex scatter from the best fit curve.

7.5 Results and Discussion

7.5.1 C to Zn abundance variation

In Figure 7.8, we show the variations in light elements up to Zn as a function of metallicity for our program stars (magenta asterisk), overlaid with halo stars from the literature (grey circles; Abohalima & Frebel 2018; Suda et al. 2008). Our program stars cover a wide metallicity range from −3.2 to −1.8, which represents region just before the transition from Type-II to Type-I supernovae as major

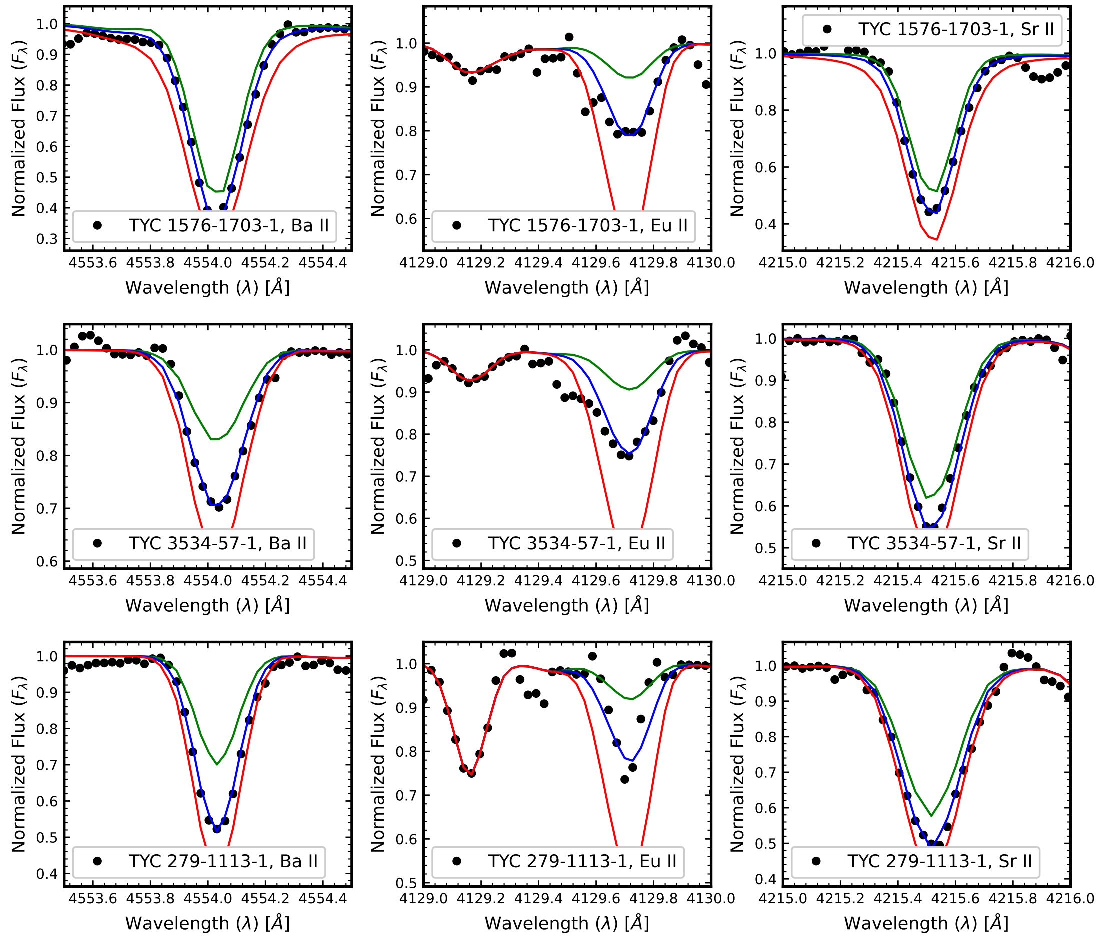

FIGURE 7.7: Synthesis of Ba, Eu, and Sr lines in TYC 1576-1703-1, TYC 3534-57-1, and TYC 279-1113-1. Black dots are observed spectra and blue curves are best fit. Green and red colors represent 0.5 dex scatter from the best fit curve.

metal pollutants. They include stars spanning [C/Fe] values from −1.0 to +1.0. A limited number of stars exhibiting [C/Fe] > +0.7 are categorized as CEMP stars. Notably, one CEMP star stands out with exceptionally high [C/Fe] of 1.98 (see Section 7.5.4).

Among the odd-Z elements, we were able to detect only sodium abundances using the D1 and D2 lines. Our program stars span a large range of [Na/Fe] values from sub-solar to super-solar levels, consistent with halo stars in the literature.

We determined the abundances of α-elements Mg, Si, Ca, and Ti, and the results

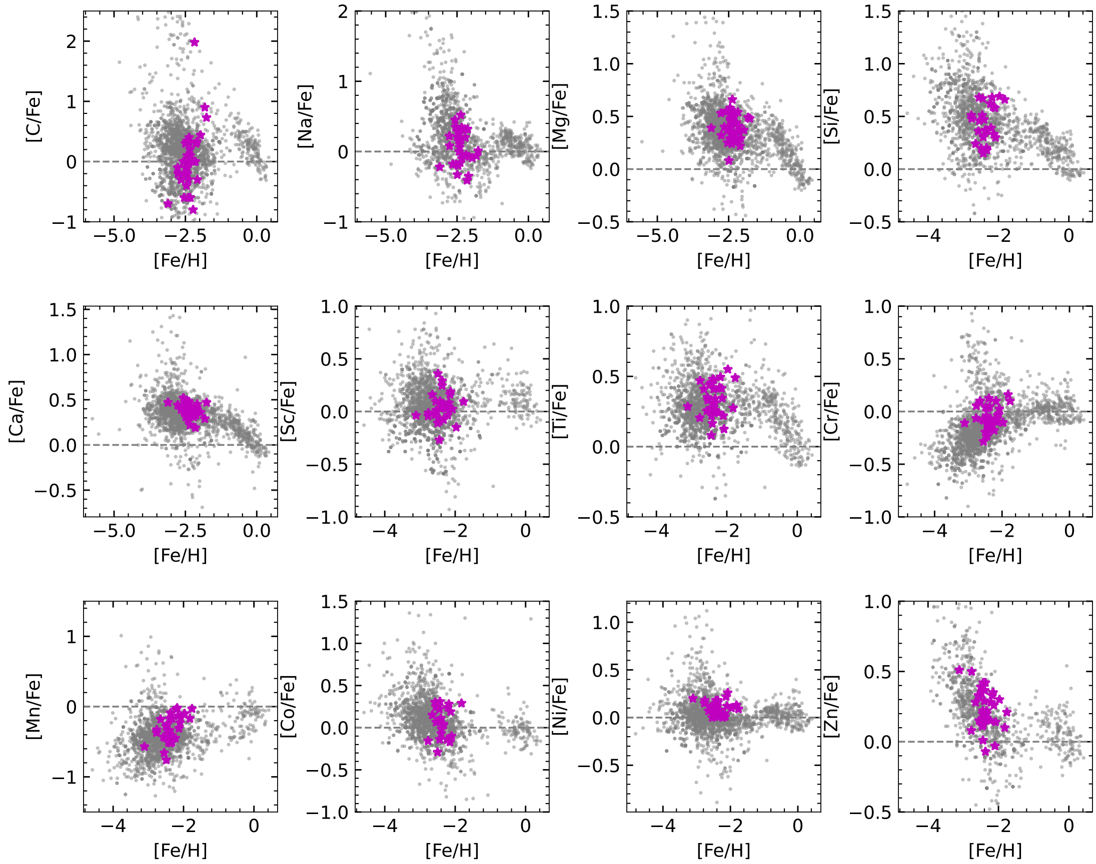

FIGURE 7.8: Evolution of light, alpha, and iron-peak elements with metallicity ([Fe/H]). The magenta color asterisk are from this study and grey circles are from literature (Abohalima & Frebel 2018; Suda et al. 2008).

are detailed in tables (See Appendix C.1 to C.33). Halo stars typically demonstrate a near constant enhancement in α-elements ([α/Fe] $\sim +0.4$). This enrichment is primarily attributed to the contribution from CCSN. Most of our program stars exhibit consistency with halo stars, with the exception of TYC 1436-366-1, which shows a slight deficiency in magnesium ([Mg/Fe] $= +0.08$) and calcium ([Ca/Fe] $= +0.31$) compared to the typical trends observed.

Moving to the estimation of abundance for Fe-peak elements such as Sc, Cr, Mn, Co, Ni, and Zn, we find that the ratios of these elements generally align with those reported in the literature. Our program stars span a broad range of abundances from sub-solar to super-solar levels, with the notable abundances of [Mn/Fe] and [Ni/Fe] values, which respectively displays sub-solar and super-solar values across our sample.

The [Co/Fe] and [Zn/Fe] ratios show increasing trends towards low metallicities, consistent with findings in the literature (Ezzeddine et al. 2019), while [Mn/Fe] and [Cr/Fe] abundances decrease under similar conditions. This comprehensive analysis underscores the diverse elemental compositions observed among our program stars and highlights their agreement with established trends in metal-poor star populations.

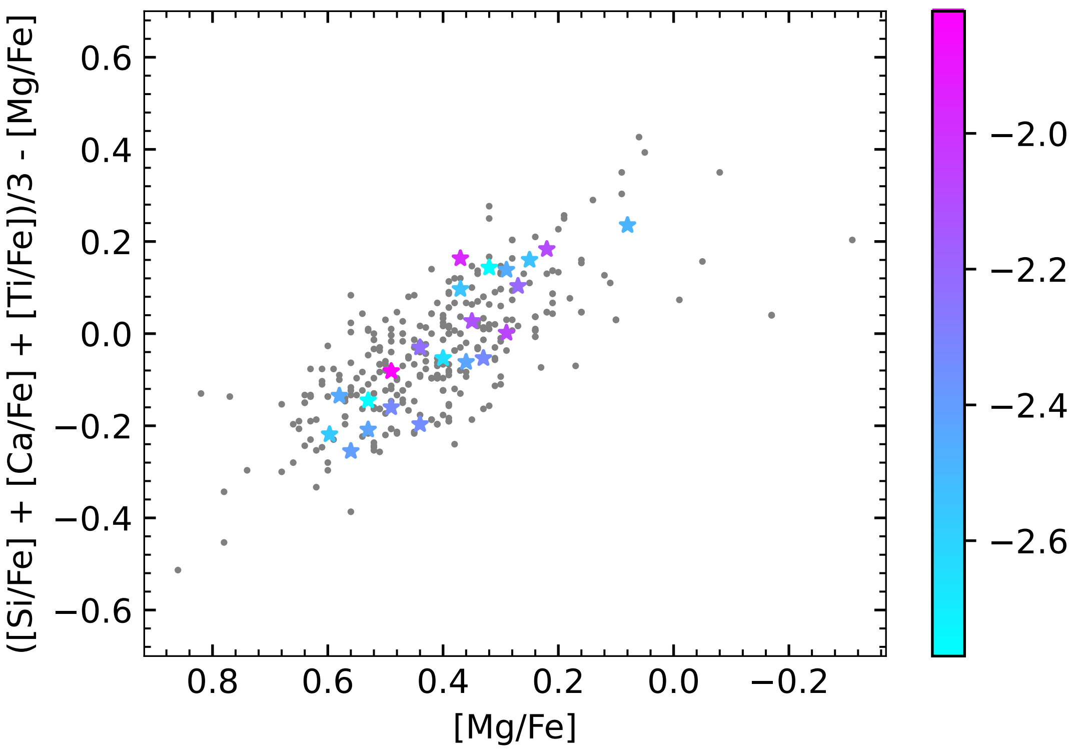

FIGURE 7.9: Evolution of ([Si/Fe] + [Ca/Fe] + [Ti/Fe])/3 − [Mg/Fe] as a function of [Mg/Fe]. Objects from this study are shown with asterisk symbols and color coded with their respective metallicities. The grey filled circles represent sample from literature (Abohalima & Frebel 2018; Suda et al. 2008). We find a clear enhancement of Si, Ca and Ti in Mg poor stars.

The α-elements are key indicators of the early enrichment of interstellar gas and subsequent star formation in the universe. At lowest metallicities, they provide valuable insights into their origins and the nucleosynthesis processes responsible for their production. Magnesium (Mg) are primarily produced through hydrostatic burning in the cores of massive stars during their evolution. On the other hand, Silicon (Si), Calcium (Ca), and Titanium (Ti) are predominantly produced through explosive nucleosynthesis inside stars with slightly lower masses, particularly during supernova explosions. These events are responsible for dispersing the α-elements into the surrounding interstellar medium, enriching it for future generations of stars.

Studying the relative abundances of these α-elements at the lowest metallicities allow us to disentangle the contributions from different nucleosynthesis processes. At low metallicities, where the influence of stellar enrichment processes is less diluted by subsequent generations of star formation, we can observe more clearly the imprint left by massive stars through hydrostatic burning versus lower mass stars through explosive nucleosynthesis. This is clarified in Figure 7.9. As you move towards decreasing [Mg/Fe], the value of ([Si/Fe] + [Ca/Fe] + [Ti/Fe])/3 − [Mg/Fe] increases. This suggests that in regions where [Mg/Fe] is lower, the enhancement of silicon, calcium, and titanium relative to iron is more pronounced compared to the enhancement of magnesium.

7.5.2 Heavy element variation

In our study, we measured strontium (Sr), barium (Ba), and europium (Eu) abundances for the majority of our program stars. Europium is primarily produced through the r-process, which occurs in explosive astrophysical events such as NSM or certain types of supernovae. However, strontium and barium are produced in both r-, and s-process. The s-process typically occurs in lower mass stars during their AGB phase. To understand their evolution, we have plotted these heavy element with metallicity in Figure 7.10. On average, we find [Sr/Fe] $= -0.1$ and [Ba/Fe] $= -0.16$. Additionally, europium (Eu) abundances have been determined for several stars, with an average [Eu/Fe] = 0.27 with some of the stars showing enhanced in europium that is discussed in next section. The low [Sr/Fe] in some of our stars indicates that strontium was produced differently compared to iron, reflecting an inhomogeneous protogalaxy with varying contributions from different nucleosynthetic processes (McWilliam et al. 1995) and the reference there in.

We have detected significant enrichment in n-capture elements in one specific star, TYC 1576-1703-1. This star exhibits large enhancements in barium (Ba), strontium (Sr), and europium (Eu), alongside elevated levels of carbon. The noticeable dispersion in [Sr/Ba], with a mean value around 0.1, complicates linking these elements to specific progenitor events during star formation. This variability implies diverse enrichment histories or contributions from different nucleosynthesis processes across our sample. The observed low [Sr/Ba] ratios anticipated at [Fe/H] $>$ -3.0 mark the onset of substantial *s*-process contributions in the Galaxy, where barium (Ba) is primarily produced.

To investigate the evolution of n-capture elements, we plotted [Sr/H] + [Ba/H] as a function of [Eu/H] (see Figure 7.11). It is clear from the figure that stars enriched in europium (likely from *r*-process events) also tend to show higher abundances of strontium and barium. This correlation indicates that the synthesis of Sr and Ba may be associated to the same events that produce europium, such as neutron star mergers. The total content of (Sr+Ba) increases with increase in Eu indicating similar evolutionary scenario for these elements at low metallicities.

7.5.3 New *r*-Process Stars and Their Origins

Conventionally C, Fe, Sr, Ba, and Eu abundances serve as key indicators for categorizing metal-poor stars based on their respective enhancement levels. Specifically, Sr, Ba, and Eu abundances play crucial roles in determining the predominant

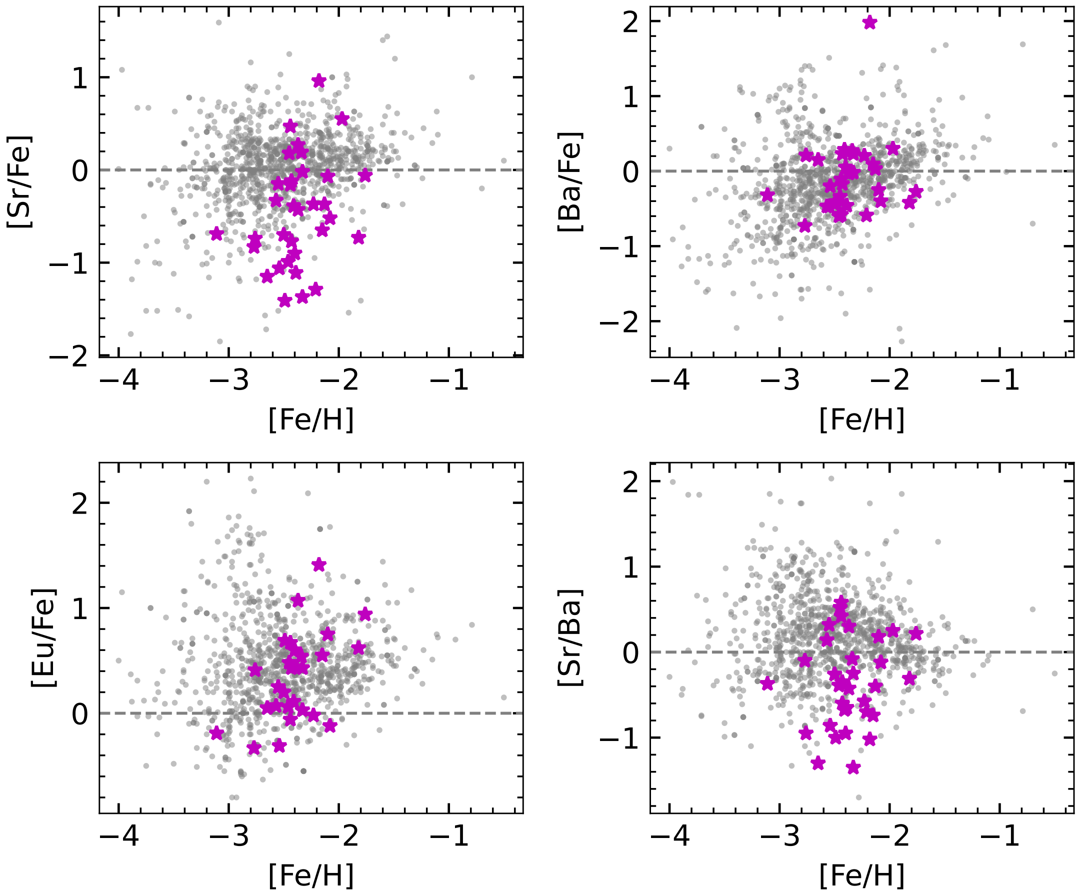

FIGURE 7.10: Evolution of heavy elements Sr, Ba and Eu with metallicity. Magenta color asterisks show stars from this study and grey circles represent objects compiled from literature (Abohalima & Frebel 2018; Suda et al. 2008). Horizontal dashed lines depict reference for solar abundances.

source of r-process and in quantifying various segments of the r-process pattern. The discrimination of n-capture s- and r-processes is provided by measuring the Ba and Eu abundances (Frebel 2018c). For instance, a [Ba/Eu] ratio lower than the Solar value ([Ba/Eu] < 0) suggests dominance of the r-process, whereas a higher [Ba/Eu] ratio indicates prevalence of the s-process. The abundance of Europium serves as a indicator for classifying RPE stars.

Initially, we derived abundances of C, Sr, Ba, and Eu for our stars to classify them as r-I, r-II, limited-r, CEMP-s, CEMP-r, or non-r-process-enhanced stars. Since our star selection process favored those without carbon enhancement, we initially

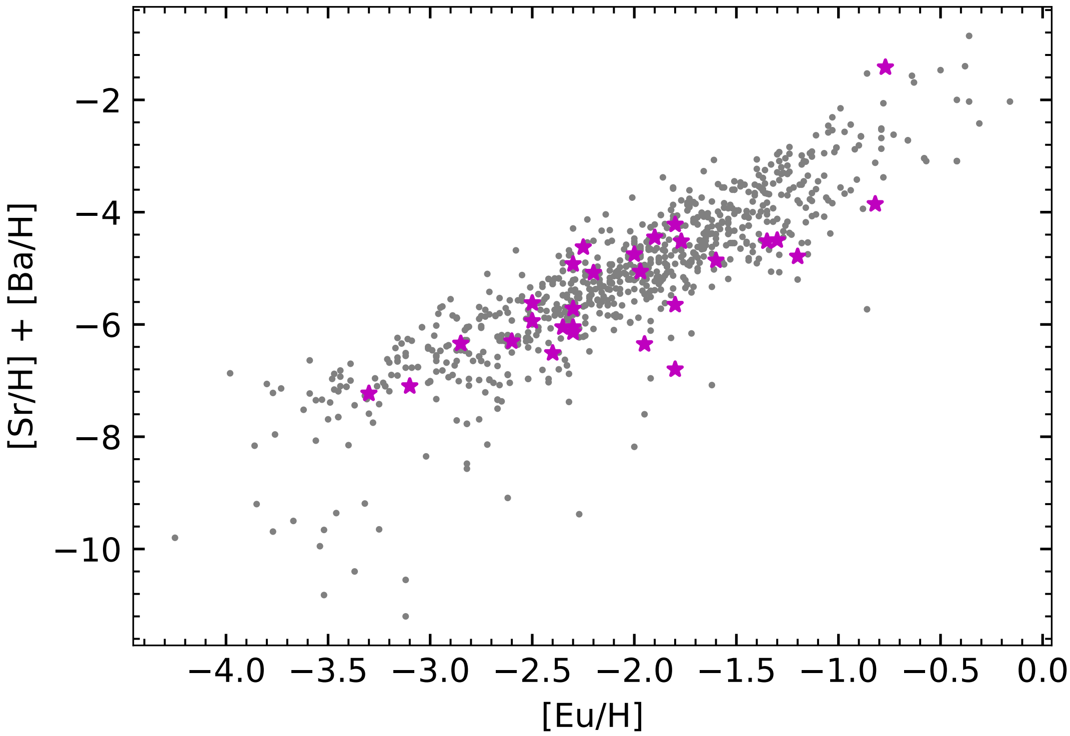

FIGURE 7.11: Evolution of [Sr/H]+[Ba/H] as a function of [Eu/H]. Magenta color asterisks show stars from this study and grey circles represent objects compiled from literature (Abohalima & Frebel 2018; Suda et al. 2008).

anticipated a limited presence of CEMP-*s* or CEMP-*r* stars, however we found 3 CEMP stars. A comprehensive analysis of heavy element abundances of the present sample of stars will be detailed in future publications.

Considering the selection criteria of abundance outlined in Table 1.1 of chapter 1, we identify one *r*-II and seven *r*-I stars among 33 stars observed, based on the recent classification by Holmbeck et al. (2020) used in this study. Figure 7.12 illustrates the positions of our stars in the [Ba/Eu] vs [Eu/Fe] plane.

[Mg/Eu] vs [Fe/H] shown in Figure 7.13 for our program stars is superimposed with data from halo stars sourced from existing literature, based on [Eu/Fe]. The figure suggests the existence of distinct pathways for the production of Mg and Eu, re-iterating that they are produced in different astrophysical sites.

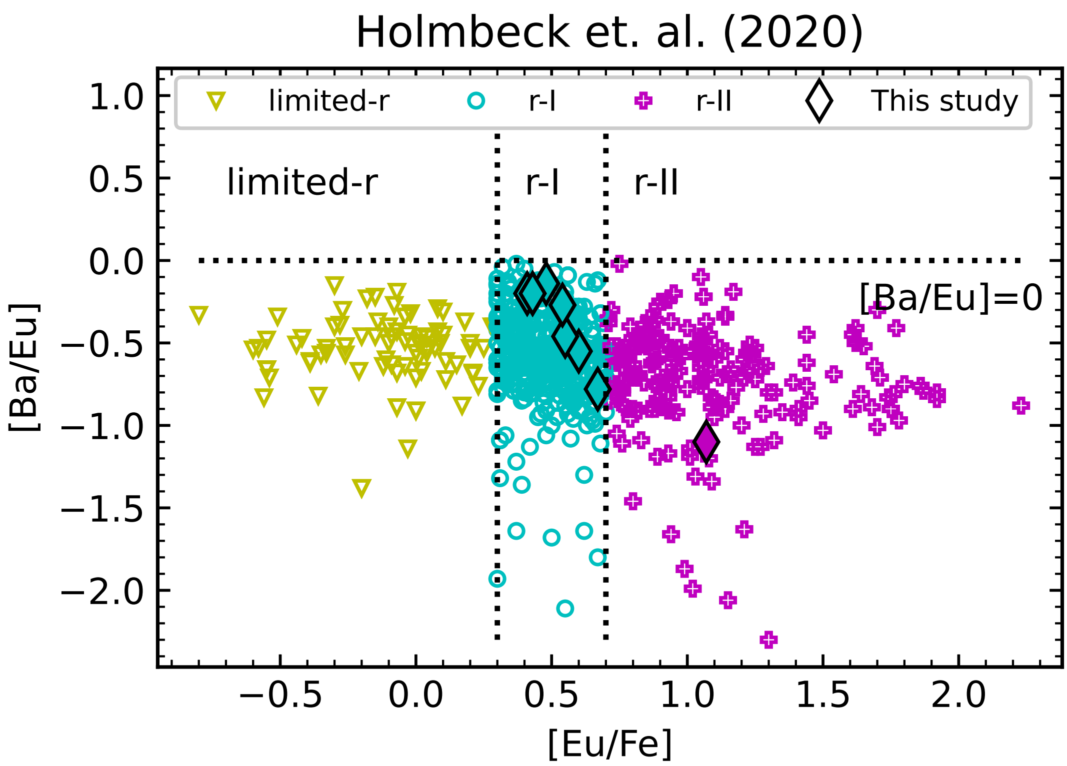

FIGURE 7.12: Distribution of limited-r (yellow colours), r-I (cyan colours), and r-II (magenta colours) stars in [Ba/Eu] vs [Eu/Fe] plane. The diamond symbols show objects from this study. See Saraf et al. (2023) for literature reference of compiled sample.

TABLE 7.6: Dilution of carbon corrected according to Placco et al. (2014), and r-process classification of our program stars from Holmbeck et al. (2020).

Star name	[Fe/H]	$[C/Fe]_{LTE}$	$\Delta[C/Fe]^{a}_{cor}$	$[C/Fe]_{cor}$	[Sr/Fe]	[Ba/Fe]	[Eu/Fe]	[Ba/Eu]	[Sr/Ba]	Class
TYC 665-522-1	−2.43	−0.10	+0.01	−0.09	−0.12	+0.23	+0.43	−0.20	−0.35	r-I
TYC 1465-1148-1	−2.76	−0.20	+0.03	−0.17	−0.74	+0.21	+0.41	−0.20	−0.95	r-I
TYC 3474-142-1	−2.45	+0.34	+0.05	+0.39	+0.18	−0.34	+0.48	−0.82	+0.52	r-I
TYC 975-2188-1	−2.40	−0.3	+0.01	−0.29	−0.9	+0.05	+0.60	−0.55	−0.95	r-I
TYC 1120-1253-1	−2.15	+0.0	+0.01	+0.01	−0.65	+0.09	+0.55	−0.46	−0.74	r-I
TYC 224-475-1	−2.33	+0.1	+0.05	+0.15	−0.02	+0.23	+0.43	−0.20	−0.25	r-I
TYC 267-308-1	−2.34	+0.19	+0.58	+0.77	+0.19	+0.27	+0.54	−0.27	−0.08	r-I
TYC 195-1636-1	−2.44	+0.1	+0.13	+0.23	+0.47	−0.11	+0.67	−0.78	+0.58	r-I
TYC 1170-642-1	−2.37	+0.4	+0.14	+0.54	+0.27	−0.03	+1.07	−1.1	+0.3	r-II
TYC 1576-1703-1	−2.18	+1.98	+0.0	+1.98	+0.96	+1.98	+1.41	+0.57	−1.02	CEMP-r/s
TYC 3534-57-1	−1.76	+0.73	+0.0	+0.73	−0.06	−0.275	+0.94	−1.21	+0.215	CEMP-r
TYC 279-1113-1	−1.82	+0.89	+0.02	+0.91	−0.73	−0.42	+0.62	−1.04	−0.31	CEMP-r

[a] https://vplacco.pythonanywhere.com/.

Of the 11 RPE stars, one (TYC 1170-642-1) that is highly enriched in r-process elements (r-II) exhibits thick disc kinematics. Among the 8 moderately enhanced stars (r-I), 2 display thin disc kinematics (TYC 195-1636-1 and TYC 665-522-1), 4 display thick disc kinematics (TYC 224-475-1, TYC 975-2188-1, TYC 3474-142-1,

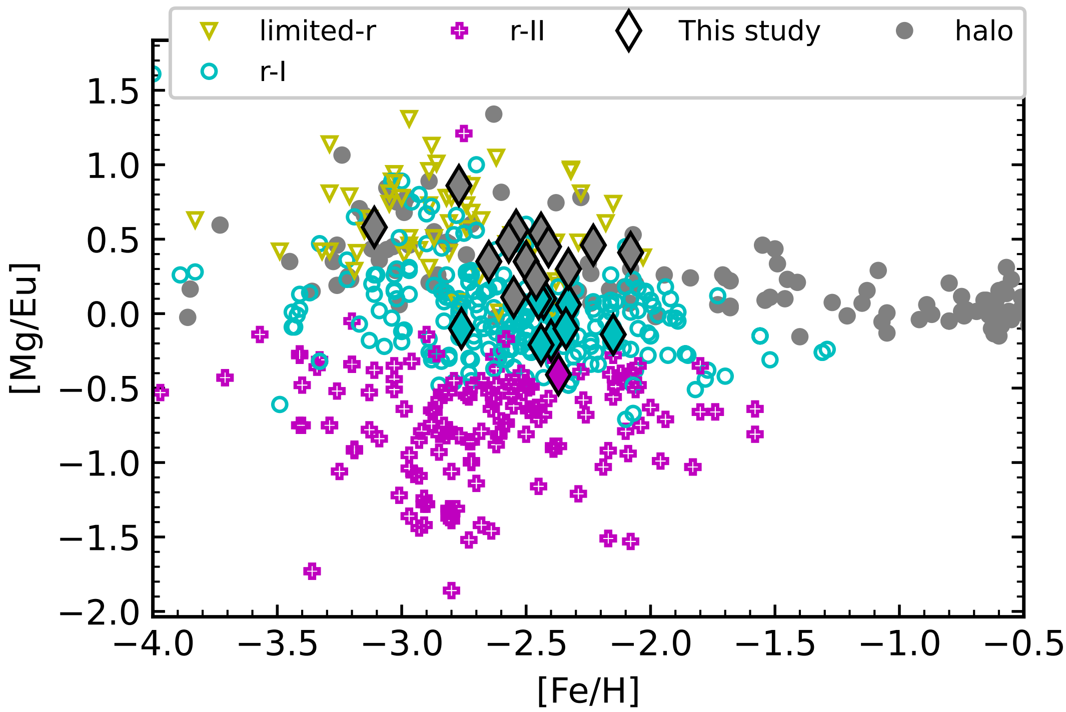

FIGURE 7.13: Evolution of the [Mg/Eu] in limited-r (yellow colour), r-I (cyan colour), and r-II (magenta colour) with metallicity. The diamonds show objects from this study. Grey symbols show normal halo stars. See Saraf et al. (2023) for literature reference of compiled sample.

and TYC 1465-1148-1), and 2 show halo kinematics (TYC 267-308-1 and TYC 1120-1253-1).

7.5.4 Yoon diagram and new cemp stars

The Yoon-Beers diagram, as discussed in various studies (Spite et al. 2013; Bonifacio et al. 2015), reveals distinct bands in the A(C) vs. [Fe/H] plane that classify CEMP stars. The upper band centering around A(C)$\sim$8.0 predominantly includes CEMP-s and/or CEMP-r/s stars, whereas the lower band centering around A(C)$\sim$6.3 consists primarily of CEMP-no stars. Hansen et al. (2016) noted that many binary stars align closely with the upper band. Yoon et al. (2016) expanded this understanding by identifying three main groups in the Yoon-Beers diagram,

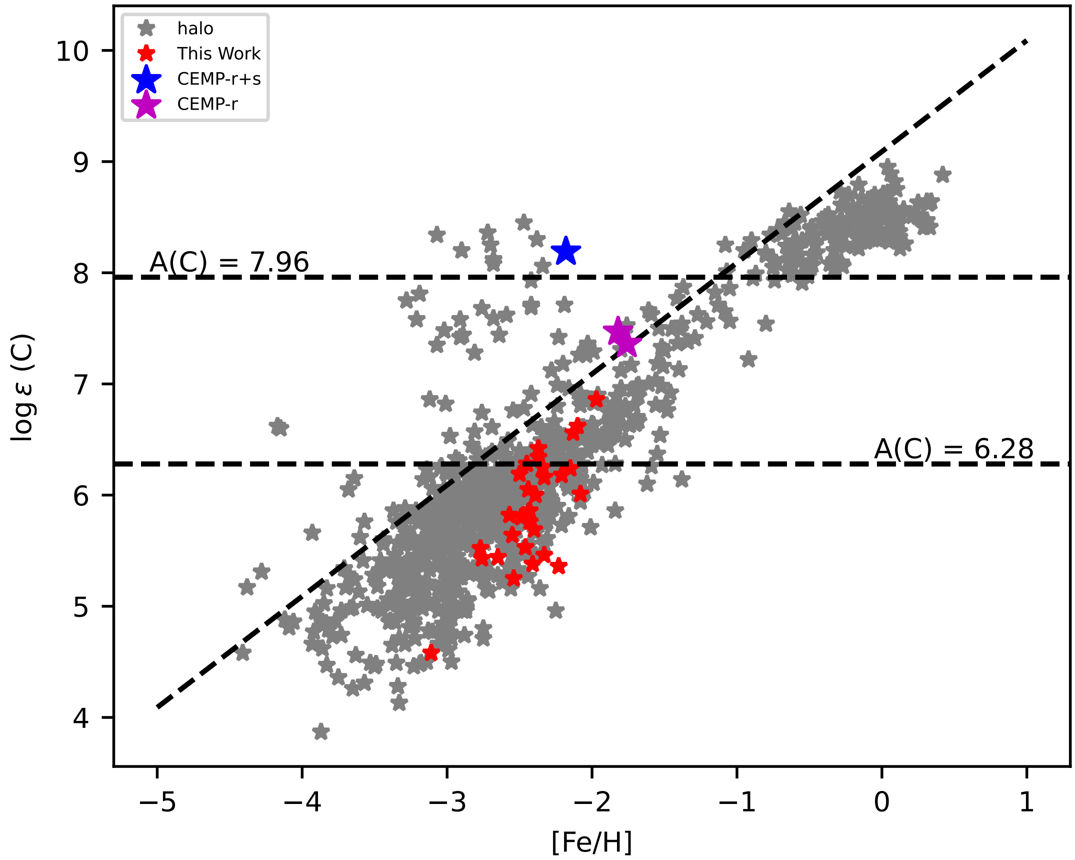

FIGURE 7.14: Yoon-Beers diagram for our sample stars. Grey asterisks represent samples from literature (Abohalima & Frebel 2018; Suda et al. 2008), red asterisks are carbon normal stars from this study, magenta asterisks are CEMP-r, and blue asterisk is CEMP-r/s. The slant line separates normal and carbon enhanced stars at [C/Fe]=0.7, whereas horizontal lines represent centers of Group I and Group III from Yoon et al. (2016) at A(C)∼8.0 and A(C)∼6.3 respectively.

proposing a separation at A(C) = 7.1 to distinguish Group I CEMP-s stars above this level and Group II and III CEMP-no stars below it. Numerous investigations have demonstrated that the metallicity of CEMP-s and CEMP-r/s stars is typically between −3 to −1 (Yoon et al. (2016) and references therein).

In our analysis, we found one CEMP-r/s star, namely TYC 1576-1703-1, and two CEMP-r star with carbon abundances of 8.19, 7.36, and 7.47, respectively. Figure 7.14 shows the position of stars on Yoon-Beers diagram. In this figure, the slant line separates normal and carbon enhanced stars at [C/Fe]=0.7, whereas

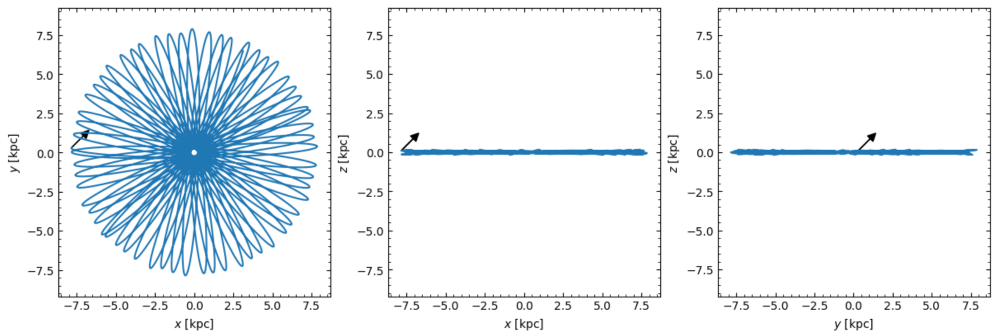

FIGURE 7.15: CEMP-r/s star showing thin disc kinematics in three different orbital plane x, y and z.

horizontal lines represents centers of Group I and Group III following Yoon et al. (2016) at A(C)$\sim$8.0 and A(C)$\sim$6.3 respectively. Three of our CEMP stars identified in this study are falling in Group I. CEMP-r/s is very carbon rich, but CEMP-r are near the boundary of CEMP definition.

Of the two CEMP-r stars, TYC 3534-57-1 exhibits thick disc kinematics, while TYC 279-1113-1 exhibits thin disc kinematics. The star that is enhanced in carbon and enriched in both s- and r-process elements, such as Ba and Eu, shows thin disc kinematics. The Figure 7.15 illustrates the orbits of CEMP-r/s stars that display thin disc kinematics.

7.6 Kinematic analysis

7.6.1 r_a vs z_{max}: association to Galactic components

Different components of the Galaxy show different kinematic characteristics. For example, disk stars rotate in the Galactic plane, whereas halo stars move randomly around Galactic center. Thus, kinematics information help in understanding their place in Galaxy. To investigate where our program stars belong in the Galaxy, we

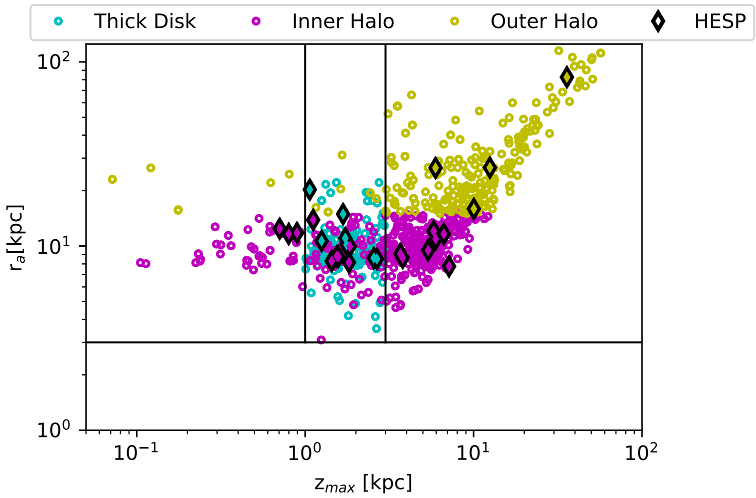

FIGURE 7.16: Apocenter distance (r_a) vs maximum vertical height (z_{max}). Stars from this study are shown with black diamonds and literature sample is shown with open circles. Thick disk, inner halo and outer halo are respectively represented with cyan, magenta, and yellow colors. The literature sample is obtained from Gudin et al. (2021).

calculate orbital parameters of our program stars using GALA code (Price-Whelan 2017b) utilizing GAIA parallaxes and proper motions (Gaia Collaboration et al. 2022) along with our radial velocities. For this purpose, we back integrate the orbits for 5 Gyr in MW Potential available in GALA code.

As discussed in Chapter 5, apocenter distance (r_a) and maximum vertical height (z_{max}) of the stellar orbit precisely separate stars into different Galactic components. In Figure 7.16, we plot r_a as a function of z_{max} for our program stars shown with black diamonds along with other stars from literature. Following the definitions from Chapter 5, we color code stars into thick disk, inner halo, and outer halo with cyan, magenta, and yellow colors respectively. We found 7 thick stars, 16 inner halo stars, and 4 outer halo stars. Rest 6 stars belong to thin disk. In later, we will be focusing on thick disk, inner halo, and outer halo components.

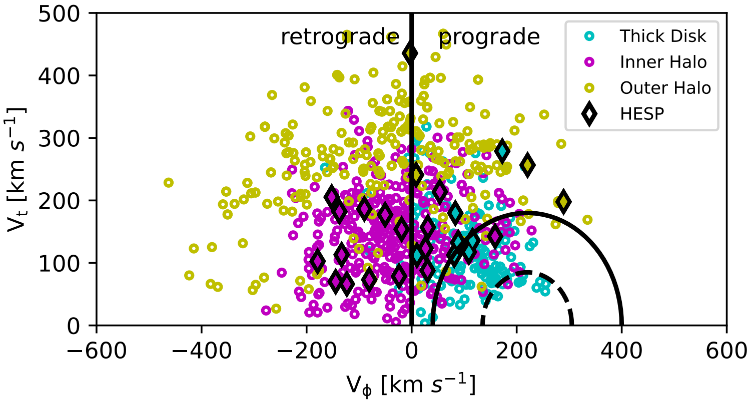

FIGURE 7.17: Toomre diagram for our program stars shown with black diamonds. The open circles represents objects collected from literature. All the objects are color coded with cyan, magenta, and yellow colors to respectively indicate thick disk, inner halo, and outer halo stars are categorized in Section–7.6.1. The solid and dotted semicircles respectively enclose thick disk and thin disk stars. The vertical line separates retrograde and prograde stars. The literature sample is obtained from Gudin et al. (2021).

7.6.2 Toomre diagram

Toomre diagram provide a simple diagnostic to separate disk and halo stars just using present-day velocity information of the stars. Toomre diagram places stars on the azimuth velocity (V_ϕ) and transverse velocity (V_t) plane as shown in Figure 7.17. Here, open circles represents objects collected from literature, and black diamonds display stars from this study. All the objects are color coded with cyan, magenta, and yellow to respectively represent thick disk, inner halo, and outer halo stars as categorized in Section–7.6.1. The solid and dotted semicircles respectively enclose thick disk and thin disk stars according to the Toomre diagram. The vertical $V_\phi = 0$ line separates prograde and retrograde stars. We found that out of thick disk, and halo stars reported in this study, 15 stars exhibit prograde motion, while 12 stars exhibit retrograde motion.

As we can see from Figure 7.17, Toomre diagram does a great deal in separating disk and halo stars. However, we can also see that some objects which are classified as disk are falling in the halo region. Vice-versa, some objects which are classified as halo are falling in the disk region. The main region for this discrepancy is the nature of the orbit. For detail, we refer the reader to Chapter 5. The disk stars which have highly elliptical orbit tends to show high transverse velocity compared to azimuth velocity putting them outside the semicircle. On the other hand, the halo stars which are currently moving along disk rotation tend to show higher azimuthal velocity compared to transverse velocity, placing them inside the semicircle, though, being associated with halo, they would be on different orbit during their evolution in past/future. According to Toomre diagram, from our sample, 4 disk stars fall into halo region, and 1 halo stars fall into disk region. It makes a significant exchange of stars in different components when studying already small sample of chemically peculiar stars. Our analysis emphasize on using orbital parameter based definition when studying stars in different galactic components.

7.6.3 Di Matteo diagram

Di Matteo diagram is similar to Toomre diagram. Instead of separating disk and halo components, it separates in-situ and ex-situ formed stars. It places stars on specific angular momentum l_z and $l_\perp = \sqrt{l_x^2 + l_y^2}$ plane, where l_x, l_y, and l_z are the components of specific angular momentum along x, y, and z directions. The in-situ formed stars are expected to move along galactic rotation and show high l_z. In contrast, low l_z and high $l_\perp$ are anticipated for ex-situ formed stars. In Figure 7.18, we plot Di Matteo diagram for our program stars and sample collected from literature. Stars from this study are shown with black diamonds and literature stars are displayed with open circles. All the objects are color-coded with cyan, magenta, and yellow to respectively represent thick dick, inner and outer halo Galactic components. Here in-situ, ex-situ, and mixed zone regions are marked with maroon boxes. Similar to Toomre diagram, $l_z = 0$ vertical line separates retrograde and prograde stars.

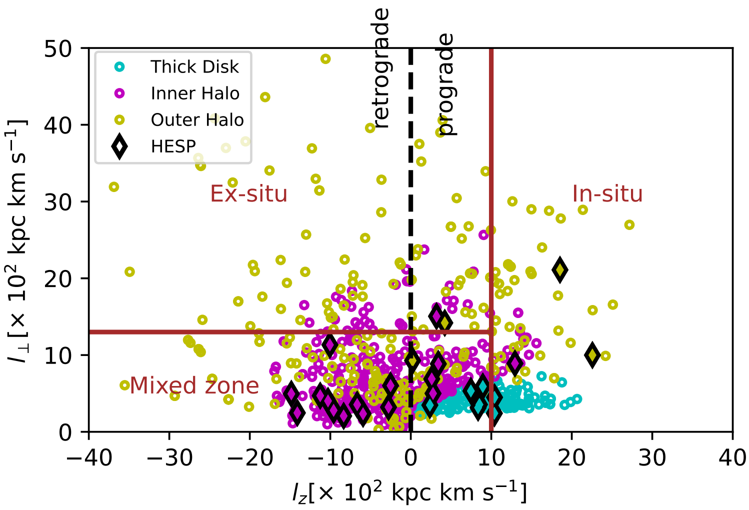

FIGURE 7.18: Place of our program stars (black diamonds) on Di Matteo diagram. Open circles represents sample compiled from literature. Our orbital parameter based thick disk, inner halo, and outer halo components are respectively shown cyan, magenta, and yellow colors. The maroon lines divide the image into in-situ, ex-situ, and mixed zone regions of star formation. The black vertical line at $l_z = 0$ separates prograde and retrograde components of the Galaxy. The literature sample is obtained from Gudin et al. (2021).

We found that out of our thick disk and halo objects presented in this study, 5 stars are falling into in-situ region, 2 stars are falling in ex-situ region, and rest 20 stars are in the mixed zone. When we look from Galactic components' perspective, 2 thick disk, 1 inner halo and 2 outer halo stars are formed in-situ. Similarly, 1 inner halo and 1 outer halo stars are formed ex-situ. Remaining majority of our sample is in the mixed zone consistent with the literature data. Rest of the stars which we do not discuss in this section belongs to thin disk on the Galaxy.

7.6.4 Metallicity Distribution of Stars in Galactic Components

Further, we plot the distribution of metallicity of thick disk, inner, and outer halo components in Figure 7.19 to investigate their assembly history. It includes literature sample and metal-poor stars from our HESP-GOMPA survey. This disk

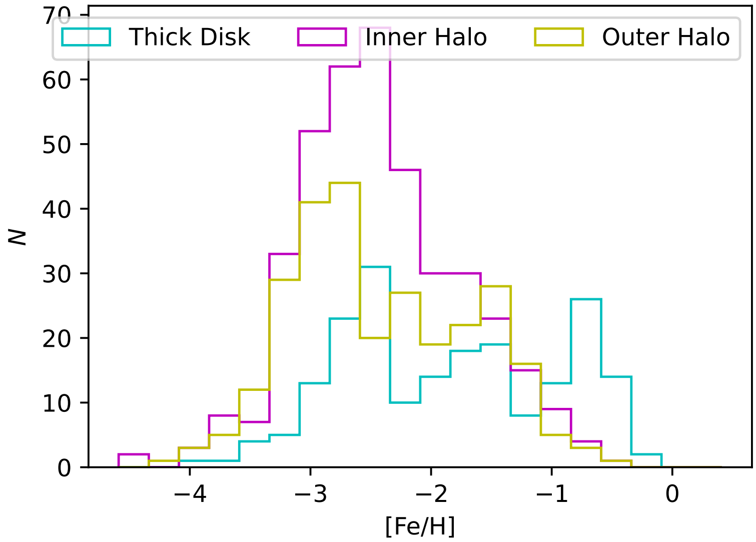

FIGURE 7.19: Metallicity distribution of thick disc, inner halo and outer halo components for the complete sample (literature + HESP GOMPA survey). Cyan histogram shows thick disk stars, magenta histogram displays inner halo stars, and yellow histogram shows outer halo stars.

stars show three peaks near metallicities −2.6, −1.5 and −0.7. The peak near −0.7 metallicity is possibly thin disk component which have been heated during the evolution of the Milky Way. The peak in the thick disk distribution near metallicity −1.5 coincides with the peak in the outer halo suggesting continuous mixing of thick disk and outer halo components. Some of the thick disk stars are likely reaching higher vertical heights and mixing with the outer halo, complicating their separation using solely orbital information. Orbital information accompanied with stellar metallicity could be better tool to finely separated different Galactic components. Additionally, all three components show distinct peaks near −2.6 metallicity. It suggests that these three components assembled very soon in the history of Milky Way formation. Given our limited sample size it is difficult to infer any significant delay between their assembly. Some works suggests inner halo assembled earlier than the thick disk of the Milky Way (Xiang & Rix 2022). A large sample size will allow us to distinctly find the peak separation of three components near −2.6 metallicity to further comment on their assembly period.

7.7 Conclusions

In this chapter, we report the identification of 33 new MP stars from our ongoing HESP-GOMPA survey and the detailed spectroscopic abundance analysis. We found 30 stars with metallicities in the range $-3.0 \leq$ [Fe/H] < -2.0, 2 stars with $-1.5 \leq$ [Fe/H] < -2.0, and notably, one EMP star with [Fe/H] $= -3.11$.

Among these stars, two stars were identified as spectroscopic binary candidates. One of these binaries has been previously confirmed in the literature, while the other is selected for follow-up radial velocity monitoring in the near future. We have determined the 1D LTE atmospheric stellar parameters for our sample. Additionally, we derived abundances for various elemental groups such as light elements (including carbon), α-, Fe-peak, and n-capture elements where appropriate spectral lines were available. We have only measured the abundances of Barium (Ba), Europium (Eu), and Strontium (Sr) among the neutron capture elements, which are crucial for categorizing metal-poor stars into various sub-groups. In the near future, we plan to conduct a thorough analysis of other heavy elemental abundances in these stars.

Out of the 33 stars studied, our analysis identified 8 new r-I stars and 1 new r-II star using Eu, Ba, and Sr abundances. Notably, all r-process stars consistently exhibit low ratios of [Ba/Eu] (< -0.5), characteristic of pure r-process enhancement. Furthermore, we identified 2 CEMP-r stars and 1 CEMP-r/s star. We have also compared the abundance ratios of n-capture and other elements with existing literature values, including those from the RPA-samples, to contextualize our findings.

Additionally, we analyse the kinematics of our program stars and compared with compiled sample from literature. Using our orbit based classification of Galactic components, we found 7 thick disk, 16 inner halo, 4 outer halo, and rest 6 thin disk stars.

We further investigate 27 thick disk and halo stars by placing them on Toomre and Di Matteo diagrams. We found 15 of them are moving on prograde orbits and 12 on retrograde. In our limited sample of 27 stars, 4 disk stars fall into halo region, and 1 halo stars fall into disk region defined by Toomre diagram.

Chapter 8

Thesis Conclusions and Future work

8.1 Thesis conclusion

The thesis focuses on high-resolution spectroscopy and kinematics of various low metallicity stars within the extremely metal-poor range, particularly targeting RPE stars. We start outlining basics of the MW, galaxy formation models, stellar nucleosynthesis, and proposed sites of heavy elements synthesis in Chapter 1. Then, we discuss the methods and tools used to accomplish this thesis work in Chapter 2.

In Chapter 3, we report complete abundance analysis of four RPE stars using 10-m GTC. Thanks to the excellent SNR of our observed stars, we have identified third r-process peak elements like Os and Th in two of them. Utilizing Thorium, we have estimated the ages of these stars. There appears to be a metallicity-dependent production ratio for Thorium and possibly for other neutron capture elements as well. Interestingly, the elemental abundance trends among alpha and iron peak elements alongside neutron capture elements do not distinctly differentiate between different astrophysical sites. While most Fe-peak elements show flat trends with respect to [Eu/Fe], exceptions include Mn, Cr, and Zn. The [Sr/Fe] ratio displays a relatively flat trend and significant scatter with [Eu/Fe], whereas [Y/Fe] and [Zr/Fe] exhibit sharper trends and less scatter relative to [Eu/Fe]. This suggests that the source responsible for Eu production also contributes significantly to Y and Zr, as opposed to Sr. Additionally, the abundance trends in Th and Mg with [Fe/H] hint at a potential delay between the formation of r-II and r-I stars.

Comparison of abundance trends of r-I and r-II stars and a plausible explanation for r-process enrichment using precise differential abundance analysis is provided in Chapter 4. Their nearly identical abundances of light elements up to Zn suggest a common origin in the early Universe, likely from core-collapse supernovae (CC-SNe). However, the unequal differential abundance for first and second r-process peak elements imply distinct formation sites. Notably, we observed a distinct pattern in the differential abundances of second r-process peak elements, challenging the commonly assumed universal main r-process pattern in studies of RPE stars. The enrichment of both light and heavy elements in RPE stars cannot be solely explained by a single event with dilution and pre-enrichment. Instead, the presence of two similar sites operating at similar metallicities appears to be a plausible explanation for r-process enrichment. While NSM models with different mass ratios may account for r-I and r-II classifications, they need refinement to accurately produce the full range of observed trends from r-I to limited-r stars.

Chapter 5 discusses the kinematic analysis of all the RPE stars compiled from literature. For the first time, we conducted orbital-based kinematic analysis of about 448 RPE stars to associate them with Galactic bulge, disk and halo components.

We discuss the significance of using orbit based association of stars to Galactic components by comparing Toomre diagram based classification. From the analysis, we found that, while limited-r stars concentrated in the inner regions, there does not seem to be any particular preferred location in the Galaxy for r-I and r-II stars.

Chapter 6 focuses on the r-process enrichment in CEMP stars using clustering techniques on CEMP-r/s and RPE stars. The abundance analysis of 20 CEMP-r/s stars does not show any signature of Th detection even these objects are highly RPE with [Eu/Fe] > 1.0. CEMP-r/s and RPE stars exhibit distinct class of objects from our clustering analysis. While r-I and r-II stars do not neatly divide into two distinct groups, there exists an intermediate category, possibly comprising diluted or mixed stars of r-II progenitors, which is falling in the r-I category. By incorporating more elements and employing similar investigative methods in the future, we can enhance classification based on different elemental ratios, providing insight into the underlying physical processes rather than relying on arbitrary cutoff points.

In Chapter 7, we have undertaken abundance analyses of both light and neutron-capture elements for 33 bright metal-poor stars recently identified through our HESP-GOMPA survey. These stars predominantly fall within the metallicity range of -3.2 to -1.5, a critical span where significant shifts in abundance trends of crucial elements occur, marking key milestones in galactic evolution or the emergence of novel nucleosynthesis mechanisms. This chapter unveils numerous RPE stars, CEMP stars, and EMP stars. It also conducts comparative analyses with halo stars to glean insights into the characteristics of their progenitor massive stars. We have also studies the kinematics of these stars. The examination of these bright metal-poor stars, with their detailed abundance profiles along with kinematics, could serve as benchmark stars for future surveys targeting metal-poor stars, offering the potential to derive abundances for a wide array of elements.

8.2 Future work

- In the near future, our aim is to conduct a thorough analysis of the abundance of all stars observed using the 2-meter Himalayan Chandra Telescope with the HESP spectrograph mentioned in Chapter 7. We have identified several stars showing enhancement in the r-process as well as some stars showing enhancement in carbon. Further exploration into their complete r-process abundance patterns and their peculiarity will be detailed in an upcoming publication.

- We have plan to revisit key elemental abundances of the different classes of peculiar stars using the Gaia stellar parameters which will provide precise stellar abundances using differential abundance methods which also can provide insights into the small differences in the abundance ratios. It will also provide a more robust measure of dispersion in the abundance ratios of the different classes of objects and different metallicities.

- The abundance levels of some key n-capture elements, such as Sr and Ba, are essential for understanding GCE. To achieve this, we have constructed a grid of Sr abundances ranging from 2.92 to 0.08 in 0.5 spacing, and Ba abundances ranging from 2.17 to -2.83 in 0.5 spacing for metallicities ranging from 0.0 to -2.5. This grid allows us to estimate Sr and Ba abundances for a substantial sample of stars from the LAMOST catalogue, specifically selecting nearly 1.5 million spectra of cool stars with a SNR greater than 10 in the g band. The main purpose of this study is to estimate consistent abundances of n-capture elements across a large stellar sample. In the future, we plan to use supervised machine learning algorithms using LAMOST spectra with abundances calculated in GALAH, and then utilize these trained algorithms to estimate abundances for unknown samples. An example of such analysis is shown in Figure 8.1, and 8.2.

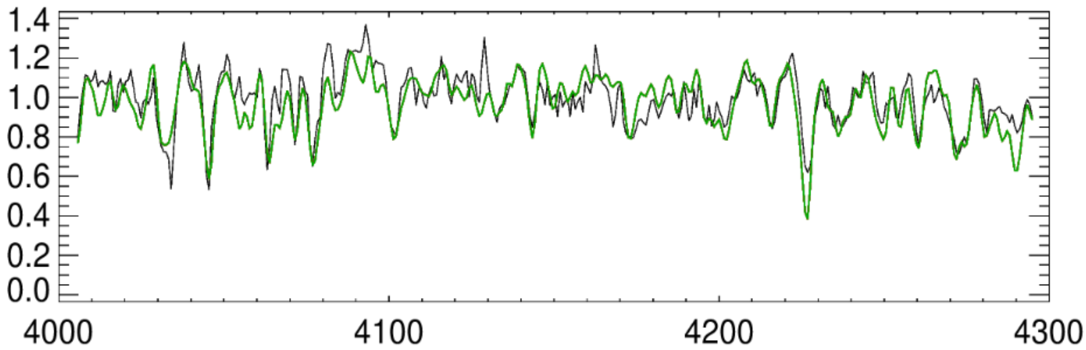

FIGURE 8.1: Figure illustrating the synthesis of the strontium region in a LAMOST spectrum within a 300 Å spectral range.

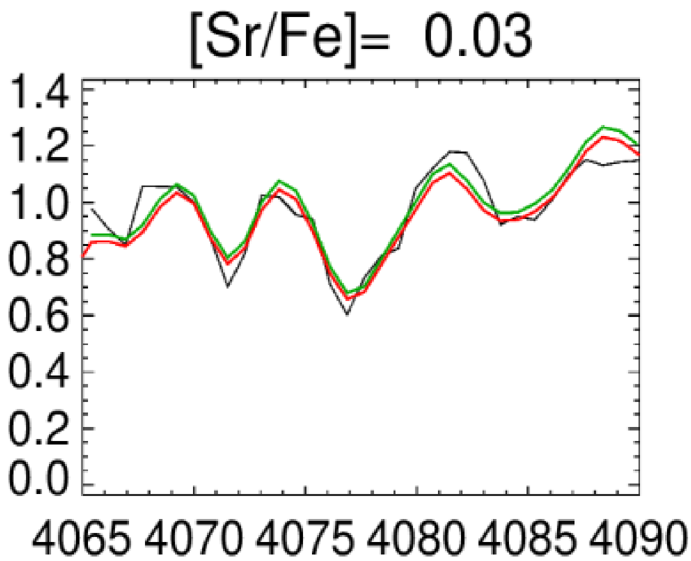

FIGURE 8.2: Synthesis of the Sr line in LAMOST spectra at 4077 Å.

Bibliography

Abate C., Pols O. R., Izzard R. G., Mohamed S. S., de Mink S. E., 2013, *Astron. Astrophys.*, 552, A26

Abate C., Stancliffe R. J., Liu Z.-W., 2016, *Astron. Astrophys.*, 587, A50

Abbott B. P., et al., 2017, Physical Review Letters, 119, 161101

Abohalima A., Frebel A., 2018, *Astrophys. J. Suppl.*, 238, 36

Allende Prieto C., 2021, Nature Astronomy, 5, 105

Alonso A., Arribas S., Martínez-Roger C., 1999, *Astron. Astrophys. Suppl.*, 140, 261

Alpher R. A., Bethe H., Gamow G., 1948, Phys. Rev., 73, 803

Alvarez R., Plez B., 1998, *Astron. Astrophys.*, 330, 1109

Anders F., et al., 2014, *Astron. Astrophys.*, 564, A115

Andrews S., Fryer C., Even W., Jones S., Pignatari M., 2020, *Astrophys. J.*, 890, 35

Andrievsky S. M., Spite M., Korotin S. A., Spite F., Bonifacio P., Cayrel R., Hill V., François P., 2007, *Astron. Astrophys.*, 464, 1081

Aoki W., Suda T., Boyd R. N., Kajino T., Famiano M. A., 2013, *Astrophys. J. Lett.*, 766, L13

Arcavi I., et al., 2017, *Nature*, 551, 64

Arcones A., Janka H. T., Scheck L., 2007, *Astron. Astrophys.*, 467, 1227

Arlandini C., Käppeler F., Wisshak K., Gallino R., Lugaro M., Busso M., Straniero O., 1999a, *Astrophys. J.*, 525, 886

Arlandini C., Käppeler F., Wisshak K., Gallino R., Lugaro M., Busso M., Straniero O., 1999b, *Astrophys. J.*, 525, 886

Arnone E., Ryan S. G., Argast D., Norris J. E., Beers T. C., 2005, *Astron. Astrophys.*, 430, 507

Asplund M., Grevesse N., Sauval A. J., Scott P., 2009, *Ann. Rev. Astron. Astrophys.*, 47, 481

Bandyopadhyay A., Sivarani T., Susmitha A., Beers T. C., Giridhar S., Surya A., Masseron T., 2018, *Astrophys. J.*, 859, 114

Bandyopadhyay A., Thirupathi S., Beers T. C., Susmitha A., 2020a, *Mon. Not. Roy. Astron. Soc.*, 494, 36

Bandyopadhyay A., Thirupathi S., Beers T. C., Susmitha A., 2020b, *Mon. Not. Roy. Astron. Soc.*, 494, 36

Bandyopadhyay A., Sivarani T., Beers T. C., 2020c, *Astrophys. J.*, 899, 22

Bandyopadhyay A., Sivarani T., Beers T. C., 2020d, *Astrophys. J.*, 899, 22

Bandyopadhyay A., Sivarani T., Beers T. C., Susmitha A., Nayak P. K., Pandey J. C., 2022, *Astrophys. J.*, 937, 52

Bandyopadhyay A., Beers T. C., Ezzeddine R., Sivarani T., Nayak P. K., Pandey J. C., Saraf P., Susmitha A., 2024, *Mon. Not. Roy. Astron. Soc.*, 529, 2191

Banerjee P., Qian Y.-Z., Heger A., 2018, *Astrophys. J.*, 865, 120

Banerjee P., Wu M.-R., Yuan Z., 2020, *Astrophys. J. Lett.*, 902, L34

Barbuy B., et al., 2011, *Astron. Astrophys.*, 534, A60

Barklem P. S., O'Mara B. J., 2001, Journal of Physics B Atomic Molecular Physics, 34, 4785

Barklem P. S., et al., 2005, *Astron. Astrophys.*, 439, 129

Battaglia G., North P., Jablonka P., Shetrone M., Minniti D., Díaz M., Starkenburg E., Savoy M., 2017, *Astron. Astrophys.*, 608, A145

Baumueller D., Gehren T., 1997, *Astron. Astrophys.*, 325, 1088

Bayo A., Rodrigo C., Barrado Y Navascués D., Solano E., Gutiérrez R., Morales-Calderón M., Allard F., 2008, *Astron. Astrophys.*, 492, 277

Bedell M., Meléndez J., Bean J. L., Ramírez I., Leite P., Asplund M., 2014, *Astrophys. J.*, 795, 23

Beers T. C., Christlieb N., 2005a, *Ann. Rev. Astron. Astrophys.*, 43, 531

Beers T. C., Christlieb N., 2005b, *Ann. Rev. Astron. Astrophys.*, 43, 531

Beers T. C., Preston G. W., Shectman S. A., 1985, *Astron. J.*, 90, 2089

Beers T. C., Preston G. W., Shectman S. A., 1992, *Astron. J.*, 103, 1987

Bell E. F., 2008, *Astrophys. J.*, 682, 355

Bensby T., Zenn A. R., Oey M. S., Feltzing S., 2007, *Astrophys. J. Lett.*, 663, L13

Bensby T., et al., 2011, *Astron. Astrophys.*, 533, A134

Bensby T., et al., 2013, *Astron. Astrophys.*, 549, A147

Bergemann M., Hansen C. J., Bautista M., Ruchti G., 2012, *Astron. Astrophys.*, 546, A90

Bethe H. A., 1990, Reviews of Modern Physics, 62, 801

Biémont É., et al., 2011, *Mon. Not. Roy. Astron. Soc.*, 414, 3350

Binney J., Tremaine S., 2008, Galactic Dynamics: Second Edition

Binney J., Jiang I.-G., Dutta S., 1998, *Mon. Not. Roy. Astron. Soc.*, 297, 1237

Bisterzo S., Gallino R., Straniero O., Cristallo S., Käppeler F., 2011, *Mon. Not. Roy. Astron. Soc.*, 418, 284

Bland-Hawthorn J., Gerhard O., 2016, *Ann. Rev. Astron. Astrophys.*, 54, 529

Bonifacio P., et al., 2015, *Astron. Astrophys.*, 579, A28

Bord D. J., Cowley C. R., Mirijanian D., 1997, in American Astronomical Society Meeting Abstracts #190. p. 04.01

Bovard L., Martin D., Guercilena F., Arcones A., Rezzolla L., Korobkin O., 2017, Physical Review D, 96, 124005

Bovy J., 2015a, *Astrophys. J. Suppl.*, 216, 29

Bovy J., 2015b, *Astrophys. J. Suppl.*, 216, 29

Bowen I. S., 1947, *Pub. Astron. Soc. Pac.*, 59, 253

Brauer K., Ji A. P., Frebel A., Dooley G. A., Gómez F. A., O'Shea B. W., 2019, *Astrophys. J.*, 871, 247

Bressan A., Marigo P., Girardi L., Salasnich B., Dal Cero C., Rubele S., Nanni A., 2012, *Mon. Not. Roy. Astron. Soc.*, 427, 127

Burbidge E. M., Burbidge G. R., Fowler W. A., Hoyle F., 1957, Reviews of Modern Physics, 29, 547

Burris D. L., Pilachowski C. A., Armandroff T. E., Sneden C., Cowan J. J., Roe H., 2000, *Astrophys. J.*, 544, 302

Busso M., Gallino R., Wasserburg G. J., 1999, *Ann. Rev. Astron. Astrophys.*, 37, 239

Cain M., et al., 2018, *Astrophys. J.*, 864, 43

Cain M., et al., 2020, *Astrophys. J.*, 898, 40

Cameron A. G. W., 1957, *Pub. Astron. Soc. Pac.*, 69, 201

Campbell S. W., Lattanzio J. C., 2008, *Astron. Astrophys.*, 490, 769

Campbell S. W., Lugaro M., Karakas A. I., 2010, *Astron. Astrophys.*, 522, L6

Cardon B. L., Smith P. L., Scalo J. M., Testerman L., Whaling W., 1982, *Astrophys. J.*, 260, 395

Carollo D., et al., 2007, *Nature*, 450, 1020

Carollo D., et al., 2010, *Astrophys. J.*, 712, 692

Castelli F., Kurucz R. L., 2003, in Piskunov N., Weiss W. W., Gray D. F., eds, Proceedings of the International Astronomical Union Vol. 210, Modelling of Stellar Atmospheres. p. A20 (arXiv:astro-ph/0405087)

Caughlan G. R., 1965, *Astrophys. J.*, 141, 688

Cayrel R., 1988, in Cayrel de Strobel G., Spite M., eds, Proceedings of the International Astronomical Union Vol. 132, The Impact of Very High S/N Spectroscopy on Stellar Physics. p. 345

Cayrel R., et al., 2001, *Nature*, 409, 691

Cayrel R., et al., 2004, *Astron. Astrophys.*, 416, 1117

Chamberlain J. W., Aller L. H., 1951, *Astrophys. J.*, 114, 52

Cheng J. Y., et al., 2012, *Astrophys. J.*, 752, 51

Chornock R., et al., 2017, *Astrophys. J. Lett.*, 848, L19

Christlieb N., 2003, Reviews in Modern Astronomy, 16, 191

Clarkson W., et al., 2008, *Astrophys. J.*, 684, 1110

Clarkson O., Herwig F., Pignatari M., 2018, *Mon. Not. Roy. Astron. Soc.*, 474, L37

Coşkunoğlu B., et al., 2011, *Mon. Not. Roy. Astron. Soc.*, 412, 1237

Cohen J. G., Christlieb N., Qian Y. Z., Wasserburg G. J., 2003, *Astrophys. J.*, 588, 1082

Côté B., Denissenkov P., Herwig F., Ruiter A. J., Ritter C., Pignatari M., Belczynski K., 2018, *Astrophys. J.*, 854, 105

Cowan J. J., Rose W. K., 1977, *Astrophys. J.*, 212, 149

Cowan J. J., Thielemann F.-K., Truran J. W., 1991, Physics Reports, 208, 267

Cowan J. J., Sneden C., Lawler J. E., Aprahamian A., Wiescher M., Langanke K., Martínez-Pinedo G., Thielemann F.-K., 2021, Reviews of Modern Physics, 93, 015002

Cristallo S., Piersanti L., Straniero O., Gallino R., Domínguez I., Käppeler F., 2009, *Publications of the Astronomical Society of Australia*, 26, 139

Cui W. Y., Sivarani T., Christlieb N., 2013, *Astron. Astrophys.*, 558, A36

Dalton G., et al., 2014, in Ramsay S. K., McLean I. S., Takami H., eds, Society of Photo-Optical Instrumentation Engineers (SPIE) Conference Series Vol. 9147, Ground-based and Airborne Instrumentation for Astronomy V. p. 91470L (`arXiv:1412.0843`), doi:10.1117/12.2055132

Danziger I. J., 1965, *Mon. Not. Roy. Astron. Soc.*, 131, 51

Dardelet L., et al., 2014, in XIII Nuclei in the Cosmos (NIC XIII). p. 145, doi:10.22323/1.204.0145

De Silva G. M., et al., 2015, *Mon. Not. Roy. Astron. Soc.*, 449, 2604

Dekker H., D'Odorico S., Kaufer A., Delabre B., Kotzlowski H., 2000, in Iye M., Moorwood A. F., eds, Society of Photo-Optical Instrumentation Engineers (SPIE) Conference Series Vol. 4008, Optical and IR Telescope Instrumentation and Detectors. pp 534–545, doi:10.1117/12.395512

Den Hartog E. A., Lawler J. E., Sobeck J. S., Sneden C., Cowan J. J., 2011, *Astrophys. J. Suppl.*, 194, 35

Denissenkov P. A., Herwig F., Battino U., Ritter C., Pignatari M., Jones S., Paxton B., 2017, *Astrophys. J. Lett.*, 834, L10

Denissenkov P. A., Herwig F., Woodward P., Andrassy R., Pignatari M., Jones S., 2019, *Mon. Not. Roy. Astron. Soc.*, 488, 4258

Di Matteo P., Spite M., Haywood M., Bonifacio P., Gómez A., Spite F., Caffau E., 2020, *Astron. Astrophys.*, 636, A115

Dodelson S., Schmidt F., 2020, Modern Cosmology, doi:10.1016/C2017-0-01943-2.

Doherty C. L., Gil-Pons P., Siess L., Lattanzio J. C., Lau H. H. B., 2015, *Mon. Not. Roy. Astron. Soc.*, 446, 2599

Drout M. R., et al., 2017, Science, 358, 1570

Duncan R. C., Shapiro S. L., Wasserman I., 1986, *Astrophys. J.*, 309, 141

Eggen O. J., Lynden-Bell D., Sandage A. R., 1962, *Astrophys. J.*, 136, 748

Eichler D., Livio M., Piran T., Schramm D. N., 1989, *Nature*, 340, 126

Eichler M., et al., 2015, *Astrophys. J.*, 808, 30

Ezzeddine R., et al., 2019, *Astrophys. J.*, 876, 97

Ezzeddine R., et al., 2020, *Astrophys. J.*, 898, 150

Frebel A., 2018a, Annual Review of Nuclear and Particle Science, 68, 237

Frebel A., 2018b, Annual Review of Nuclear and Particle Science, 68, 237

Frebel A., 2018c, Annual Review of Nuclear and Particle Science, 68, 237

Frebel A., Norris J. E., 2015a, *Ann. Rev. Astron. Astrophys.*, 53, 631

Frebel A., Norris J. E., 2015b, *Ann. Rev. Astron. Astrophys.*, 53, 631

Frebel A., et al., 2005, *Nature*, 434, 871

Frebel A., Casey A. R., Jacobson H. R., Yu Q., 2013, *Astrophys. J.*, 769, 57

Frebel A., Yu Q., Jacobson H. R., 2016, in Journal of Physics Conference Series. p. 012051, doi:10.1088/1742-6596/665/1/012051

Freeman K., Bland-Hawthorn J., 2002, *Ann. Rev. Astron. Astrophys.*, 40, 487

Fuhrmann K., 1998, *Astron. Astrophys.*, 338, 161

Fujibayashi S., Sekiguchi Y., Kiuchi K., Shibata M., 2017, *Astrophys. J.*, 846, 114

Fujimoto S.-i., Nishimura N., Hashimoto M.-a., 2008a, *Astrophys. J.*, 680, 1350

Fujimoto S.-i., Nishimura N., Hashimoto M.-a., 2008b, *Astrophys. J.*, 680, 1350

Fulbright J. P., McWilliam A., Rich R. M., 2006, *Astrophys. J.*, 636, 821

Fulbright J. P., et al., 2010, *Astrophys. J. Lett.*, 724, L104

Gaia Collaboration 2018, VizieR Online Data Catalog: Gaia DR2 (Gaia Collaboration, 2018), VizieR On-line Data Catalog: I/345. Originally published in: 2018A&A...616A...1G; doi:10.5270/esa-ycs, doi:10.26093/cds/vizier.1345

Gaia Collaboration 2022, VizieR Online Data Catalog, p. I/355

Gaia Collaboration et al., 2021a, *Astron. Astrophys.*, 649, A1

Gaia Collaboration et al., 2021b, *Astron. Astrophys.*, 649, A1

Gaia Collaboration et al., 2022, arXiv e-prints, p. arXiv:2208.00211

Gaia Collaboration et al., 2023, *Astron. Astrophys.*, 674, A1

Gallagher A. J., Ryan S. G., Hosford A., García Pérez A. E., Aoki W., Honda S., 2012, *Astron. Astrophys.*, 538, A118

Gallino R., Arlandini C., Busso M., Lugaro M., Travaglio C., Straniero O., Chieffi A., Limongi M., 1998, *Astrophys. J.*, 497, 388

García Pérez A. E., et al., 2013, *Astrophys. J. Lett.*, 767, L9

Garstang R. H., 2000, *Memorie della Societa Astronomica Italiana*, 71, 83

Ge J., et al., 2015, in American Astronomical Society Meeting Abstracts #225. p. 409.03

Gehren T., Liang Y. C., Shi J. R., Zhang H. W., Zhao G., 2004, *Astron. Astrophys.*, 413, 1045

Gilmore G., Reid N., 1983, *Mon. Not. Roy. Astron. Soc.*, 202, 1025

Goodwin S. P., Gribbin J., Hendry M. A., 1998, The Observatory, 118, 201

Goriely S., Bauswein A., Janka H.-T., 2011, *Astrophys. J. Lett.*, 738, L32

Gudin D., et al., 2021, *Astrophys. J.*, 908, 79

Gull M., et al., 2018, *Astrophys. J.*, 862, 174

Hampel M., Stancliffe R. J., Lugaro M., Meyer B. S., 2016, *Astrophys. J.*, 831, 171

Hampel M., Karakas A. I., Stancliffe R. J., Meyer B. S., Lugaro M., 2019, *Astrophys. J.*, 887, 11

Hansen C. J., Bergemann M., Cescutti G., François P., Arcones A., Karakas A. I., Lind K., Chiappini C., 2013, *Astron. Astrophys.*, 551, A57

Hansen T. T., Andersen J., Nordström B., Beers T. C., Placco V. M., Yoon J., Buchhave L. A., 2016, *Astron. Astrophys.*, 586, A160

Hansen T. T., et al., 2017, *Astrophys. J.*, 838, 44

Hansen C. J., El-Souri M., Monaco L., Villanova S., Bonifacio P., Caffau E., Sbordone L., 2018a, *Astrophys. J.*, 855, 83

Hansen T. T., et al., 2018b, *Astrophys. J.*, 858, 92

Hansen T. T., et al., 2018c, *Astrophys. J.*, 858, 92

Heiter U., et al., 2015, *Physica Scripta*, 90, 054010

Helmi A., Babusiaux C., Koppelman H. H., Massari D., Veljanoski J., Brown A. G. A., 2018, *Nature*, 563, 85

Herwig F., Pignatari M., Woodward P. R., Porter D. H., Rockefeller G., Fryer C. L., Bennett M., Hirschi R., 2011, *Astrophys. J.*, 727, 89

Hill V., et al., 2002a, *Astron. Astrophys.*, 387, 560

Hill V., et al., 2002b, *Astron. Astrophys.*, 387, 560

Hill V., Christlieb N., Beers T. C., Barklem P. S., Kratz K. L., Nordström B., Pfeiffer B., Farouqi K., 2017a, *Astron. Astrophys.*, 607, A91

Hill V., Christlieb N., Beers T. C., Barklem P. S., Kratz K. L., Nordström B., Pfeiffer B., Farouqi K., 2017b, *Astron. Astrophys.*, 607, A91

Hirai Y., Ishimaru Y., Saitoh T. R., Fujii M. S., Hidaka J., Kajino T., 2015, *Astrophys. J.*, 814, 41

Hirai Y., Beers T. C., Chiba M., Aoki W., Shank D., Saitoh T. R., Okamoto T., Makino J., 2022, *Mon. Not. Roy. Astron. Soc.*, 517, 4856

Holmbeck E. M., et al., 2018, The Astrophysical Journal, 859, L24

Holmbeck E. M., Frebel A., McLaughlin G. C., Mumpower M. R., Sprouse T. M., Surman R., 2019, The Astrophysical Journal, 881, 5

Holmbeck E. M., et al., 2020, *Astrophys. J. Suppl.*, 249, 30

Huang C., Zhao G., Zhang H. W., Chen Y. Q., 2005, *Mon. Not. Roy. Astron. Soc.*, 363, 71

Ishigaki M. N., Chiba M., Aoki W., 2012, *Astrophys. J.*, 753, 64

Ishigaki M. N., Aoki W., Chiba M., 2013, *Astrophys. J.*, 771, 67

Ivezić Ž., Beers T. C., Jurić M., 2012, *Ann. Rev. Astron. Astrophys.*, 50, 251

Janiuk A., 2019, *Astrophys. J.*, 882, 163

Ji A. P., Frebel A., 2018a, *Astrophys. J.*, 856, 138

Ji A. P., Frebel A., 2018b, The Astrophysical Journal, 856, 138

Ji A. P., Frebel A., Simon J. D., Chiti A., 2016, *Astrophys. J.*, 830, 93

Ji A. P., et al., 2022, arXiv e-prints, p. arXiv:2207.03499

Jofré P., Weiss A., 2011, *Astron. Astrophys.*, 533, A59

Jofré E., et al., 2021, *Astron. J.*, 162, 291

Jones S., Hirschi R., Nomoto K., 2014, *Astrophys. J.*, 797, 83

Jones S., Ritter C., Herwig F., Fryer C., Pignatari M., Bertolli M. G., Paxton B., 2016, *Mon. Not. Roy. Astron. Soc.*, 455, 3848

Jonsell K., Barklem P. S., Gustafsson B., Christlieb N., Hill V., Beers T. C., Holmberg J., 2006, *Astron. Astrophys.*, 451, 651

Jurić M., et al., 2008, *Astrophys. J.*, 673, 864

Karakas A. I., 2010, *Mon. Not. Roy. Astron. Soc.*, 403, 1413

Karakas A. I., Lattanzio J. C., 2014, *Publications of the Astronomical Society of Australia*, 31, e030

Kasen D., Bildsten L., 2010, *Astrophys. J.*, 717, 245

Keller S. C., et al., 2014, *Nature*, 506, 463

Kitaura F. S., Janka H. T., Hillebrandt W., 2006, *Astron. Astrophys.*, 450, 345

Kobayashi C., Umeda H., Nomoto K., Tominaga N., Ohkubo T., 2006, *Astrophys. J.*, 653, 1145

Kobayashi C., Karakas A. I., Umeda H., 2011, *Mon. Not. Roy. Astron. Soc.*, 414, 3231

Koch A., McWilliam A., 2011, *Astron. J.*, 142, 63

Kollmeier J. A., et al., 2017, arXiv e-prints, p. arXiv:1711.03234

Kunder A., et al., 2012, *Astron. J.*, 143, 57

Kupka F., Piskunov N., Ryabchikova T. A., Stempels H. C., Weiss W. W., 1999, *Astron. Astrophys. Suppl.*, 138, 119

Kurucz R. L., 1993a, Robert L. Kurucz, `http://kurucz.harvard.edu/`

Kurucz R., 1993b, ATLAS9 Stellar Atmosphere Programs and 2 km/s grid. Kurucz CD-ROM No. 13. Cambridge, 13

Lambert D. L., Sneden C., 1977, *Astrophys. J.*, 215, 597

Lattimer J. M., Schramm D. N., 1974a, *Astrophys. J. Lett.*, 192, L145

Lattimer J. M., Schramm D. N., 1974b, *Astrophys. J. Lett.*, 192, L145

Lattimer J. M., Schramm D. N., 1976, *Astrophys. J.*, 210, 549

Lawler J. E., Wickliffe M. E., Cowley C. R., Sneden C., 2001a, *Astrophys. J. Suppl.*, 137, 341

Lawler J. E., Bonvallet G., Sneden C., 2001b, *Astrophys. J.*, 556, 452

Lawler J. E., Wickliffe M. E., den Hartog E. A., Sneden C., 2001c, *Astrophys. J.*, 563, 1075

Lawler J. E., Sneden C., Cowan J. J., 2004, *Astrophys. J.*, 604, 850

Lawler J. E., Den Hartog E. A., Labby Z. E., Sneden C., Cowan J. J., Ivans I. I., 2006, arXiv e-prints, pp astro–ph/0611036

Lawler J. E., Sneden C., Cowan J. J., Wyart J. F., Ivans I. I., Sobeck J. S., Stockett M. H., Den Hartog E. A., 2008, *Astrophys. J. Suppl.*, 178, 71

Lawler J. E., Wood M. P., Den Hartog E. A., Feigenson T., Sneden C., Cowan J. J., 2014, *Astrophys. J. Suppl.*, 215, 20

Lawler J. E., Hala Sneden C., Nave G., Wood M. P., Cowan J. J., 2019, *Astrophys. J. Suppl.*, 241, 21

Lee Y. S., et al., 2013, *Astron. J.*, 146, 132

Li H.-N., Aoki W., Honda S., Zhao G., Christlieb N., Suda T., 2015, Research in Astronomy and Astrophysics, 15, 1264

Limberg G., Souza S. O., Pérez-Villegas A., Rossi S., Perottoni H. D., Santucci R. M., 2022, *Astrophys. J.*, 935, 109

Liu F., Asplund M., Ramirez I., Yong D., Melendez J., 2014, *Mon. Not. Roy. Astron. Soc.*, 442, L51

Ljung G., Nilsson H., Asplund M., Johansson S., 2006, *Astron. Astrophys.*, 456, 1181

Luck R. E., Bond H. E., 1985, *Astrophys. J.*, 292, 559

Lugaro M., Doherty C. L., Karakas A. I., Maddison S. T., Liffman K., García-Hernández D. A., Siess L., Lattanzio J. C., 2012, Meteoritics & Planetary Science, 47, 1998

Madriz Aguilar J. E., Zamarripa J., Peraza A., Licea J. A., 2017, Physics of the Dark Universe, 18, 11

Malcheva G., Blagoev K., Mayo R., Ortiz M., Xu H. L., Svanberg S., Quinet P., Biémont E., 2006, *Mon. Not. Roy. Astron. Soc.*, 367, 754

Maoz D., 2016, Astrophysics in a Nutshell. Second Edition

Marek A., Dimmelmeier H., Janka H. T., Müller E., Buras R., 2006, *Astron. Astrophys.*, 445, 273

Marigo P., Bressan A., Nanni A., Girardi L., Pumo M. L., 2013, *Mon. Not. Roy. Astron. Soc.*, 434, 488

Marshall J. L., et al., 2019, *Astrophys. J.*, 882, 177

Mashonkina L., Christlieb N., Eriksson K., 2014, *Astron. Astrophys.*, 569, A43

Masseron T., et al., 2014, *Astron. Astrophys.*, 571, A47

Matsuno T., Aoki W., Beers T. C., Lee Y. S., Honda S., 2017, *Astron. J.*, 154, 52

McLachlan G. J., Lee S. X., Rathnayake S. I., 2019, Annual Review of Statistics and Its Application, 6, 355

McWilliam A., 1997, *Ann. Rev. Astron. Astrophys.*, 35, 503

McWilliam A., 1998, *Astron. J.*, 115, 1640

McWilliam A., Preston G. W., Sneden C., Searle L., 1995, *Astron. J.*, 109, 2757

Meléndez J., et al., 2008, *Astron. Astrophys.*, 484, L21

Meléndez J., Asplund M., Gustafsson B., Yong D., 2009, *Astrophys. J. Lett.*, 704, L66

Meléndez J., et al., 2012, *Astron. Astrophys.*, 543, A29

Mendoza C., Eissner W., LeDourneuf M., Zeippen C. J., 1995, Journal of Physics B Atomic Molecular Physics, 28, 3485

Metzger B. D., 2017, arXiv e-prints, p. arXiv:1710.05931

Meyer B. S., 1989, *Astrophys. J.*, 343, 254

Minniti D., Zoccali M., 2008, in Bureau M., Athanassoula E., Barbuy B., eds, International Astronomical Union series Vol. 245, Formation and Evolution of Galaxy Bulges. pp 323–332 (`arXiv:0710.3104`), doi:10.1017/S1743921308018048

Mirizzi A., Tamborra I., Janka H. T., Saviano N., Scholberg K., Bollig R., Hüdepohl L., Chakraborty S., 2016, Nuovo Cimento Rivista Serie, 39, 1

Mishenina T., et al., 2017, *Mon. Not. Roy. Astron. Soc.*, 469, 4378

Molina R. E., Giridhar S., Pereira C. B., Arellano Ferro A., Muneer S., 2014a, Revista Mexicana de Astronomía y Astrofísica, 50, 293

Molina R. E., Giridhar S., Pereira C. B., Arellano Ferro A., Muneer S., 2014b, Revista Mexicana de Astronomía y Astrofísica, 50, 293

Navarro J. F., Abadi M. G., Venn K. A., Freeman K. C., Anguiano B., 2011, *Mon. Not. Roy. Astron. Soc.*, 412, 1203

Nicholl M., Guillochon J., Berger E., 2017, *Astrophys. J.*, 850, 55

Nilsson H., Zhang Z. G., Lundberg H., Johansson S., Nordström B., 2002, *Astron. Astrophys.*, 382, 368

Nissen P. E., Gustafsson B., 2018, *Astron. Astrophys. Rev.*, 26, 6

Nitz D. E., Kunau A. E., Wilson K. L., Lentz L. R., 1999, *Astrophys. J. Suppl.*, 122, 557

Nordström B., et al., 2004, *Astron. Astrophys.*, 418, 989

O'Malley E. M., McWilliam A., Chaboyer B., Thompson I., 2017, *Astrophys. J.*, 838, 90

Obergaulinger M., Just O., Aloy M. A., 2018, Journal of Physics G Nuclear Physics, 45, 084001

Ono M., Hashimoto M., Fujimoto S., Kotake K., Yamada S., 2012, Progress of Theoretical Physics, 128, 741

Ou X., Roederer I. U., Sneden C., Cowan J. J., Lawler J. E., Shectman S. A., Thompson I. B., 2020, *Astrophys. J.*, 900, 106

Palmeri P., Quinet P., Wyart J. F., Biémont E., 2000, *Physica Scripta*, 61, 323

Paulson D. B., Sneden C., Cochran W. D., 2003, *Astron. J.*, 125, 3185

Placco V. M., Frebel A., Beers T. C., Stancliffe R. J., 2014, *Astrophys. J.*, 797, 21

Placco V. M., Beers T. C., Reggiani H., Meléndez J., 2016, *Astrophys. J. Lett.*, 829, L24

Placco V. M., et al., 2018, *Astron. J.*, 155, 256

Plez B., 2012, Turbospectrum: Code for spectral synthesis (ascl:1205.004)

Plez B., Cohen J. G., 2005, *Astron. Astrophys.*, 434, 1117

Price-Whelan A. M., 2017a, The Journal of Open Source Software, 2, 388

Price-Whelan A. M., 2017b, The Journal of Open Source Software, 2, 388

Price-Whelan A. M., 2017c, The Journal of Open Source Software, 2

Qian Y. Z., Wasserburg G. J., 2003, *Astrophys. J.*, 588, 1099

Qian Y. Z., Woosley S. E., 1996, *Astrophys. J.*, 471, 331

Quinet P., Palmeri P., Biémont É., Jorissen A., van Eck S., Svanberg S., Xu H. L., Plez B., 2006, *Astron. Astrophys.*, 448, 1207

Ralchenko Y., Kramida A., Gillaspy J. D., Reader J., Fischer C. F., 2014, Determination of atomic data pertinent to the Fusion Energy Science Program, doi:10.2172/1149577, `https://www.osti.gov/biblio/1149577`

Ramírez I., Khanal S., Lichon S. J., Chanamé J., Endl M., Meléndez J., Lambert D. L., 2019, *Mon. Not. Roy. Astron. Soc.*, 490, 2448

Reddy B. E., Lambert D. L., 2008, *Mon. Not. Roy. Astron. Soc.*, 391, 95

Reddy B. E., Lambert D. L., Allende Prieto C., 2006, *Mon. Not. Roy. Astron. Soc.*, 367, 1329

Reddy A. B. S., Giridhar S., Lambert D. L., 2012, *Mon. Not. Roy. Astron. Soc.*, 419, 1350

Reggiani H., Meléndez J., Yong D., Ramírez I., Asplund M., 2016, *Astron. Astrophys.*, 586, A67

Reitermann A., Stahl O., Wolf B., Baschek B., 1989, *Astrophys. Space Sci.*, 156, 113

Roederer I. U., Lawler J. E., 2012, *Astrophys. J.*, 750, 76

Roederer I. U., Sneden C., 2011, *Astron. J.*, 142, 22

Roederer I. U., et al., 2012, *Astrophys. J. Suppl.*, 203, 27

Roederer I. U., Preston G. W., Thompson I. B., Shectman S. A., Sneden C., 2014, *Astrophys. J.*, 784, 158

Roederer I. U., et al., 2016a, *Astron. J.*, 151, 82

Roederer I. U., Karakas A. I., Pignatari M., Herwig F., 2016b, *Astrophys. J.*, 821, 37

Roederer I. U., Sakari C. M., Placco V. M., Beers T. C., Ezzeddine R., Frebel A., Hansen T. T., 2018, *Astrophys. J.*, 865, 129

Rosswog S., Korobkin O., Arcones A., Thielemann F. K., Piran T., 2014, *Mon. Not. Roy. Astron. Soc.*, 439, 744

Ruphy S., Robin A. C., Epchtein N., Copet E., Bertin E., Fouque P., Guglielmo F., 1996, *Astron. Astrophys.*, 313, L21

Ryabchikova T. A., Savanov I. S., Hatzes A. P., Weiss W. W., Handler G., 2000, *Astron. Astrophys.*, 357, 981

Sadakane K., Ohkubo M., Honda S., 2003, *Pub. Astron. Soc. Japan*, 55, 1005

Sakari C. M., et al., 2018, *Astrophys. J.*, 868, 110

Salvadori S., Bonifacio P., Caffau E., Korotin S., Andreevsky S., Spite M., Skúladóttir Á., 2019, *Mon. Not. Roy. Astron. Soc.*, 487, 4261

Saraf P., Sivarani T., 2023a, in Metal Production and Distribution in a Hierarchical Universe - II. p. 22, doi:10.5281/zenodo.10200367

Saraf P., Sivarani T., 2023b, arXiv e-prints, p. arXiv:2308.05097

Saraf P., Sivarani T., 2024, in 42nd meeting of the Astronomical Society of India (ASI). p. P161

Saraf P., Allende Prieto C., Sivarani T., Bandyopadhyay A., Beers T. C., Susmitha A., 2023, *Mon. Not. Roy. Astron. Soc.*, 524, 5607

Saraf P., Sivarani T., Bandyopadhyay A., 2024, in European Physical Journal Web of Conferences. p. 02009, doi:10.1051/epjconf/202429702009

Schatz H., Toenjes R., Pfeiffer B., Beers T. C., Cowan J. J., Hill V., Kratz K.-L., 2002, *Astrophys. J.*, 579, 626

Schramm D. N., 1973, *Astrophys. J.*, 185, 293

Shank D., et al., 2022, *Astrophys. J.*, 926, 26

Shank D., et al., 2023, *Astrophys. J.*, 943, 23

Shappee B. J., et al., 2017, Science, 358, 1574

Shi J. R., Gehren T., Butler K., Mashonkina L. I., Zhao G., 2008, *Astron. Astrophys.*, 486, 303

Short C. I., Hauschildt P. H., 2006a, *Astrophys. J.*, 641, 494

Short C. I., Hauschildt P. H., 2006b, *Astrophys. J.*, 641, 494

Siegel D. M., Metzger B. D., 2017, Physical Review Letters, 119, 231102

Siegel D. M., Barnes J., Metzger B. D., 2019, *Nature*, 569, 241

Siqueira Mello C., et al., 2014, *Astron. Astrophys.*, 565, A93

Siqueira-Mello C., Andrievsky S. M., Barbuy B., Spite M., Spite F., Korotin S. A., 2015, *Astron. Astrophys.*, 584, A86

Skúladóttir Á., Tolstoy E., Salvadori S., Hill V., Pettini M., Shetrone M. D., Starkenburg E., 2015, *Astron. Astrophys.*, 574, A129

Sneden C., Pilachowski C. A., Vandenberg D. A., 1986, *Astrophys. J.*, 311, 826

Sneden C., Cowan J. J., Burris D. L., Truran J. W., 1998, The Astrophysical Journal, 496, 235

Sneden C., Cowan J. J., Ivans I. I., Fuller G. M., Burles S., Beers T. C., Lawler J. E., 2000a, *Astrophys. J. Lett.*, 533, L139

Sneden C., Johnson J., Kraft R. P., Smith G. H., Cowan J. J., Bolte M. S., 2000b, *Astrophys. J. Lett.*, 536, L85

Sneden C., et al., 2003, *Astrophys. J.*, 591, 936

Sneden C., Cowan J. J., Gallino R., 2008, *Ann. Rev. Astron. Astrophys.*, 46, 241

Sneden C., Lawler J. E., Cowan J. J., Ivans I. I., Den Hartog E. A., 2009a, *Astrophys. J. Suppl.*, 182, 80

Sneden C., Lawler J. E., Cowan J. J., Ivans I. I., Den Hartog E. A., 2009b, *Astrophys. J. Suppl.*, 182, 80

Sneden C., Lawler J. E., Cowan J. J., Ivans I. I., Den Hartog E. A., 2009c, *Astrophys. J. Suppl.*, 182, 80

Sneden C., Lucatello S., Ram R. S., Brooke J. S. A., Bernath P., 2014, *Astrophys. J. Suppl.*, 214, 26

Sneden C., Cowan J. J., Kobayashi C., Pignatari M., Lawler J. E., Den Hartog E. A., Wood M. P., 2016, *Astrophys. J.*, 817, 53

Sofue Y., Honma M., Omodaka T., 2009, *Pub. Astron. Soc. Japan*, 61, 227

Solà J., Gómez-Valent A., 2015, International Journal of Modern Physics D, 24, 1541003

Soubiran C., Bienaymé O., Siebert A., 2003, *Astron. Astrophys.*, 398, 141

Sousa S. G., Santos N. C., Israelian G., Mayor M., Monteiro M. J. P. F. G., 2007, *Astron. Astrophys.*, 469, 783

Spite M., et al., 2005, *Astron. Astrophys.*, 430, 655

Spite M., Caffau E., Bonifacio P., Spite F., Ludwig H. G., Plez B., Christlieb N., 2013, *Astron. Astrophys.*, 552, A107

Spite F., Spite M., Barbuy B., Bonifacio P., Caffau E., François P., 2018, *Astron. Astrophys.*, 611, A30

Stancliffe R. J., Dearborn D. S. P., Lattanzio J. C., Heap S. A., Campbell S. W., 2011, *Astrophys. J.*, 742, 121

Suda T., et al., 2008, *Pub. Astron. Soc. Japan*, 60, 1159

Sumiyoshi K., Terasawa M., Mathews G. J., Kajino T., Yamada S., Suzuki H., 2001, *Astrophys. J.*, 562, 880

Symbalisty E., Schramm D. N., 1982, Astrophysical Letters, 22, 143

Symbalisty E. M. D., Schramm D. N., Wilson J. R., 1985, *Astrophys. J. Lett.*, 291, L11

Tabernero H. M., et al., 2020, *Mon. Not. Roy. Astron. Soc.*, 498, 4222

Takahashi K., Witti J., Janka H. T., 1994, *Astron. Astrophys.*, 286, 857

Takeda Y., et al., 2002, *Pub. Astron. Soc. Japan*, 54, 765

Tanaka M., et al., 2017, *Pub. Astron. Soc. Japan*, 69, 102

Tanvir N. R., et al., 2017, *Astrophys. J. Lett.*, 848, L27

Tarumi Y., Yoshida N., Inoue S., 2020, *Mon. Not. Roy. Astron. Soc.*, 494, 120

Tarumi Y., Hotokezaka K., Beniamini P., 2021, *Astrophys. J. Lett.*, 913, L30

Thielemann F. K., Eichler M., Panov I. V., Wehmeyer B., 2017, Annual Review of Nuclear and Particle Science, 67, 253

Travaglio C., Gallino R., Arnone E., Cowan J., Jordan F., Sneden C., 2004a, *Astrophys. J.*, 601, 864

Travaglio C., Gallino R., Arnone E., Cowan J., Jordan F., Sneden C., 2004b, *Astrophys. J.*, 601, 864

Vejar G., Schuler S. C., Stassun K. G., 2021, *Astrophys. J.*, 919, 100

Villar V. A., et al., 2017a, *Astrophys. J. Lett.*, 851, L21

Villar V. A., et al., 2017b, *Astrophys. J. Lett.*, 851, L21

Vincenzo F., Kobayashi C., Taylor P., 2018, *Mon. Not. Roy. Astron. Soc.*, 480, L38

Wanajo S., Kajino T., Mathews G. J., Otsuki K., 2001, *Astrophys. J.*, 554, 578

Wanajo S., Tamamura M., Itoh N., Nomoto K., Ishimaru Y., Beers T. C., Nozawa S., 2003, *Astrophys. J.*, 593, 968

Wanajo S., Nomoto K., Iwamoto N., Ishimaru Y., Beers T. C., 2006, *Astrophys. J.*, 636, 842

Wanajo S., Nomoto K., Janka H. T., Kitaura F. S., Müller B., 2009, *Astrophys. J.*, 695, 208

Wanajo S., Janka H.-T., Müller B., 2011, *Astrophys. J. Lett.*, 726, L15

Wanajo S., Müller B., Janka H.-T., Heger A., 2018, *Astrophys. J.*, 852, 40

Watson D., et al., 2019, *Nature*, 574, 497

Wehmeyer B., Pignatari M., Thielemann F. K., 2015, *Mon. Not. Roy. Astron. Soc.*, 452, 1970

Westin J., Sneden C., Gustafsson B., Cowan J. J., 2000, *Astrophys. J.*, 530, 783

Wheeler J. C., Cowan J. J., Hillebrandt W., 1998, *Astrophys. J. Lett.*, 493, L101

Winteler C., Käppeli R., Perego A., Arcones A., Vasset N., Nishimura N., Liebendörfer M., Thielemann F. K., 2012, *Astrophys. J. Lett.*, 750, L22

Wood M. P., Lawler J. E., Den Hartog E. A., Sneden C., Cowan J. J., 2014, *Astrophys. J. Suppl.*, 214, 18

Woosley S. E., 1993a, *Astrophys. J.*, 405, 273

Woosley S. E., 1993b, *Astrophys. J.*, 405, 273

Wu M.-R., Fernández R., Martínez-Pinedo G., Metzger B. D., 2016, *Mon. Not. Roy. Astron. Soc.*, 463, 2323

Wyse R. F. G., Gilmore G., Norris J. E., Wilkinson M. I., Kleyna J. T., Koch A., Evans N. W., Grebel E. K., 2006, *Astrophys. J. Lett.*, 639, L13

Xiang M., Rix H.-W., 2022, *Nature*, 603, 599

Yana Galarza J., Meléndez J., Ramírez I., Yong D., Karakas A. I., Asplund M., Liu F., 2016, *Astron. Astrophys.*, 589, A17

Yana Galarza J., Meléndez J., Karakas A. I., Asplund M., Lorenzo-Oliveira D., 2021, *Mon. Not. Roy. Astron. Soc.*, 502, L104

Yong D., et al., 2013, *Astrophys. J.*, 762, 26

Yong D., et al., 2014, *Mon. Not. Roy. Astron. Soc.*, 441, 3396

Yong D., et al., 2021, *Nature*, 595, 223

Yoon J., et al., 2016, *Astrophys. J.*, 833, 20

Zepeda J., Rasmussen K. C., Beers T. C., Placco V. M., Huang Y., Depagne É., 2022, *Astrophys. J.*, 927, 13

Zhang Z. G., Svanberg S., Jiang Z., Palmeri P., Quinet P., Quinet P., Biémont E., Biémont E., 2001, *Physica Scripta*, 63, 122

Zhang L., Ishigaki M., Aoki W., Zhao G., Chiba M., 2009, *Astrophys. J.*, 706, 1095

Zhao G., Chen Y. Q., Qiu H. M., Li Z. W., 2002, *Astron. J.*, 124, 2224

Zhao G., Zhao Y.-H., Chu Y.-Q., Jing Y.-P., Deng L.-C., 2012, Research in Astronomy and Astrophysics, 12, 723

Zijlstra A. A., 2004, *Mon. Not. Roy. Astron. Soc.*, 348, L23

Zoccali M., Valenti E., 2016, *Publications of the Astronomical Society of Australia*, 33, e025

Zoccali M., et al., 2003, *Astron. Astrophys.*, 399, 931

Şahin T., Lambert D. L., 2009, *Mon. Not. Roy. Astron. Soc.*, 398, 1730

de Jong R. S., et al., 2019, The Messenger, 175, 3

Appendix

A Fe-I and Fe-II lines information

Table A.1 provides a complete Fe I and Fe II line list for all the program stars. It includes the elemental ionization, wavelength, lower excitation potential (LEP), and $\log gf$. References of the $\log gf$ values for these lines are written below the Table A.1.

Table A.1: Information about the Fe line list.

Element	wavelength (Å)	EP (eV)	$\log gf$
Fe I	4107.488	2.831	−0.879
Fe I	4170.902	3.017	−1.086
Fe I	4174.913	0.915	−2.969
Fe I	4175.636	2.845	−0.827
Fe I	4182.383	3.017	−1.18
Fe I	4206.697	0.052	−3.96
Fe I	4216.22	2.453	−5.376
Fe I	4225.454	3.417	−0.51
Fe I	4233.603	2.482	−0.604
Fe I	4433.219	3.654	−0.7
Fe I	4433.782	3.602	−1.267
Fe I	4442.339	2.198	−1.255
Fe I	4447.717	2.223	−1.342
Fe I	4494.563	2.198	−1.136
Fe I	4517.525	3.071	−1.858
Fe I	4602.001	1.608	−3.154
Fe I	4602.941	1.485	−2.209
Fe I	4625.045	3.241	−1.34
Fe I	4632.912	1.608	−2.913
Fe I	4710.283	3.018	−1.612
Fe I	4733.592	1.485	−2.988
Fe I	4736.773	3.211	−0.752
Fe I	4871.318	2.865	−0.363
Fe I	4872.138	2.882	−0.567
Fe I	4890.755	2.875	−0.394
Fe I	4891.492	2.851	−0.112
Fe I	4903.31	2.882	−0.926
Fe I	4924.77	2.279	−2.241

Fe I	4939.687	0.859	−3.34
Fe I	4946.388	3.368	−1.17
Fe I	4982.524	4.103	0.144
Fe I	4994.13	0.915	−3.08
Fe I	5001.864	3.881	0.01
Fe I	5002.793	3.396	−1.58
Fe I	5014.943	3.943	−0.303
Fe I	5027.12	4.154	−0.559
Fe I	5039.252	3.368	−1.573
Fe I	5044.211	2.851	−2.038
Fe I	5049.82	2.279	−1.355
Fe I	5051.635	0.915	−2.795
Fe I	5060.079	0	−5.46
Fe I	5068.766	2.94	−1.042
Fe I	5079.74	0.99	−3.22
Fe I	5083.339	0.958	−2.958
Fe I	5090.774	4.256	−0.4
Fe I	5125.117	4.22	−0.14
Fe I	5127.359	0.915	−3.307
Fe I	5133.689	4.178	0.14
Fe I	5150.84	0.99	−3.003
Fe I	5162.273	4.178	0.02
Fe I	5166.282	0	−4.195
Fe I	5171.596	1.485	−1.793
Fe I	5191.455	3.038	−0.551
Fe I	5192.344	2.998	−0.421
Fe I	5194.942	1.557	−2.09
Fe I	5198.711	2.223	−2.135
Fe I	5202.336	2.176	−1.838
Fe I	5215.181	3.266	−0.871

Fe I	5216.274	1.608	−2.15
Fe I	5217.389	3.211	−1.07
Fe I	5225.526	0.11	−4.789
Fe I	5232.94	2.94	−0.058
Fe I	5247.05	0.087	−4.946
Fe I	5250.209	0.121	−4.938
Fe I	5250.646	2.198	−2.181
Fe I	5254.97	4.294	−4.035
Fe I	5263.306	3.266	−0.879
Fe I	5266.555	2.998	−0.386
Fe I	5281.79	3.038	−0.834
Fe I	5283.621	3.241	−0.432
Fe I	5322.041	2.279	−2.803
Fe I	5324.179	3.211	−0.103
Fe I	5332.9	1.557	−2.777
Fe I	5339.929	3.266	−0.647
Fe I	5367.467	4.415	0.443
Fe I	5369.962	4.371	0.536
Fe I	5383.369	4.312	0.645
Fe I	5389.479	4.415	−0.41
Fe I	5393.168	3.241	−0.715
Fe I	5397.128	0.915	−1.993
Fe I	5400.502	4.371	−0.16
Fe I	5415.199	4.386	0.642
Fe I	5445.042	4.386	−0.02
Fe I	5497.516	1.011	−2.849
Fe I	5501.465	0.958	−3.047
Fe I	5506.779	0.99	−2.797
Fe I	5572.842	3.396	−0.275
Fe I	5576.089	3.43	−1

Fe I	5586.822	3.695	−5.961
Fe I	5624.542	3.417	−0.755
Fe I	5762.992	4.209	−0.45
Fe I	5956.694	0.859	−4.605
Fe I	6065.482	2.608	−1.53
Fe I	6136.615	2.453	−1.4
Fe I	6137.692	2.588	−1.403
Fe I	6213.43	2.223	−2.482
Fe I	6230.723	2.559	−1.281
Fe I	6232.641	3.654	−1.223
Fe I	6246.319	3.602	−0.733
Fe I	6252.555	2.404	−1.687
Fe I	6265.134	2.176	−2.55
Fe I	6318.018	2.453	−2.338
Fe I	6393.601	2.433	−1.432
Fe I	6411.649	3.654	−0.595
Fe I	6421.351	2.279	−2.027
Fe I	6430.846	2.176	−2.006
Fe I	6592.914	2.727	−1.473
Fe I	6593.87	2.433	−2.422
Fe I	6663.442	2.424	−2.479
Fe I	6677.987	2.692	−1.418
Fe II	4233.172	2.583	−1.9
Fe II	4416.83	2.778	−2.41
Fe II	4489.183	2.828	−2.97
Fe II	4491.405	2.856	−2.7
Fe II	4508.288	2.856	−2.25
Fe II	4515.339	2.844	−2.45
Fe II	4520.224	2.807	−2.6
Fe II	4541.524	2.856	−2.79

Fe II	4582.835	2.844	−3.09
Fe II	4583.837	2.807	−1.86
Fe II	4620.521	2.828	−3.24
Fe II	4666.797	7.94	−3.798
Fe II	5197.568	10.398	−2.116
Fe II	5276.002	3.199	−1.94
Fe II	5362.869	3.199	−2.739
Fe II	6247.57	5.956	−4.011
Fe II	6456.383	3.903	−2.1

References for $\log gf$ values for Fe I and Fe II lines: Kupka et al. (1999) [VALD], Ralchenko et al. (2014) [NIST], Kurucz Linelist [http://kurucz.harvard.edu/linelists.html].

B Other Lines List

In table Table B.1, we have listed a complete line list for elements other than Fe I and Fe II. The values of the lower excitation potential (LEP), and the $\log gf$ values listed in this table are adopted from the recent literature. Again, a checkmark represents the presence of a line in the spectra.

TABLE B.1: Information about the line list.

Element	wavelength (Å)	EP (eV)	$\log gf$	Reference
Na I	5889.951	0.000	0.117	(1)
Na I	5895.924	0.000	−0.184	(1)
Mg I	5711.088	4.346	−1.833	(2)
Mg I	5528.405	4.346	−0.620	(2)
Mg I	5183.604	2.712	−0.180	(2)

Mg I	5172.684	2.712	−0.402	(2)
Mg I	4702.991	4.346	−0.666	(2)
Mg I	4571.096	0.000	−5.691	(2)
Mg I	4167.271	4.346	−1.004	(2)
Al I	3944.0	0.000	−0.640	(3)
Al I	3961.520	0.010	−0.340	(3)
Si I	4102.936	1.909	−3.140	(4)
Si I	6155.134	5.619	−0.400	(4)
Ca I	6493.781	2.521	−0.109	(5)
Ca I	6449.808	2.521	−1.015	(5)
Ca I	6439.075	2.526	0.394	(5)
Ca I	6102.723	1.879	−0.862	(5)
Ca I	5601.277	2.526	−0.552	(5)
Ca I	5588.749	2.526	0.313	(5)
Ca I	5590.114	2.521	−0.596	(5)
Ca I	5594.462	2.523	0.051	(5)
Ca I	5598.480	2.521	−0.134	(5)
Ca I	4578.551	2.521	−0.170	(5)
Ca I	4425.437	1.879	−0.286	(5)
Sc I*	4023.677	0.021	–	(6)
Sc II*	6245.637	1.507	–	(6)
Sc II*	5526.790	1.768	–	(6)
Sc II*	5239.813	1.455	–	(6)
Sc II*	5031.021	1.357	–	(6)
Sc II*	4670.407	1.357	–	(6)
Sc II*	4431.352	0.605	–	(6)
Sc II*	4324.996	0.595	–	(6)
Sc II*	4354.598	0.605	–	(6)
Sc II*	4415.557	0.595	–	(6)
Sc II*	4246.822	0.315	–	(6)

Sc II*	5641.001	1.500	–	(6)
Sc II*	5657.896	1.507	–	(6)
Sc II*	5657.896	1.507	–	(6)
Ti I	5336.848	1.582	−1.630	(7)
Ti I	5210.385	0.048	−0.884	(7)
Ti I	5193.881	2.345	−0.942	(7)
Ti I	5173.743	0.000	−1.118	(7)
Ti I	5036.464	1.443	0.130	(7)
Ti I	5038.397	1.430	0.013	(7)
Ti I	5040.613	0.826	−1.787	(7)
Ti I	5016.161	0.848	−0.574	(7)
Ti I	5020.026	0.836	−0.414	(7)
Ti I	5022.868	0.826	−0.434	(7)
Ti I	5024.844	0.818	−0.602	(7)
Ti I	4999.503	0.826	0.250	(7)
Ti I	4981.731	0.848	0.504	(7)
Ti I	4656.469	0.000	−1.345	(7)
Ti I	4617.269	1.749	0.389	(7)
Ti I	4623.097	1.739	0.110	(7)
Ti I	4534.776	0.836	0.280	(7)
Ti I	4533.241	0.848	0.476	(7)
Ti I	4512.734	0.836	−0.480	(7)
Ti I	4441.439	3.186	−1.792	(7)
Ti II	6491.561	2.061	−1.793	(7)
Ti II	5418.751	1.582	−2.110	(7)
Ti II	5490.690	1.566	−2.650	(7)
Ti II	5381.015	1.566	−1.970	(7)
Ti II	5211.536	2.590	−1.356	(7)
Ti II	5185.913	1.893	−1.370	(7)
Ti II	5188.680	1.582	−1.050	(7)

Ti II	5154.070	1.566	−1.920	(7)
Ti II	5129.152	1.892	−1.300	(7)
Ti II	5013.677	1.582	−1.990	(7)
Ti II	4911.193	3.124	−0.650	(7)
Ti II	4865.612	1.116	−2.810	(7)
Ti II	4805.085	2.061	−0.960	(7)
Ti II	4763.881	1.221	−2.360	(7)
Ti II	4779.985	2.048	−1.370	(7)
Ti II	4589.985	1.237	−1.620	(7)
Ti II	4568.314	1.224	−2.650	(7)
Ti II	4563.761	1.221	−0.790	(7)
Ti II	4544.028	1.243	−2.530	(7)
Ti II	4529.474	1.572	−1.650	(7)
Ti II	4493.513	1.080	−2.830	(7)
Ti II	4501.270	1.116	−0.760	(7)
Ti II	4443.801	1.080	−0.700	(7)
Ti II	4444.558	1.116	−2.210	(7)
Ti II	4411.074	3.095	−0.670	(7)
Ti II	4411.925	1.224	−2.550	(7)
Ti II	4394.051	1.221	−1.770	(7)
Ti II	4395.850	1.243	−1.970	(7)
V I*	4406.633	0.301	–	(8)
V I	4390.099	2.616	−1.504	(8)
V I*	4379.230	0.301	–	(8)
V I*	4111.774	0.301	–	(8)
V I*	4099.812	2.211	–	(8)
V II	4023.378	1.805	−0.689	(8)
V II	4036.777	1.476	−1.594	(8)
V II	4183.428	2.050	−1.112	(8)
Cr I	4646.148	1.030	−0.700	(9)

Cr I	4651.282	0.983	−1.460	(9)
Cr I	4652.152	1.004	−1.030	(9)
Cr I	4626.174	0.968	−1.320	(9)
Cr I	4616.120	0.983	−1.190	(9)
Cr I	5409.772	1.030	−0.720	(9)
Cr I	5345.801	1.004	−0.980	(9)
Cr I	5348.312	1.004	−1.290	(9)
Cr I	5296.691	0.983	−1.400	(9)
Cr I	5298.277	0.983	−1.150	(9)
Cr I	4591.457	3.422	−1.888	(9)
Cr I	4545.945	0.941	−1.370	(9)
Cr I	4254.332	0.000	−0.114	(9)
Cr II	4824.127	3.871	−0.970	(9)
Cr II	4634.070	4.072	−0.990	(9)
Cr II	4618.803	4.074	−0.840	(9)
Cr II	4588.199	4.071	−0.627	(9)
Cr II	4558.650	4.073	−0.449	(9)
Mn I*	4823.524	2.319	–	(10)
Mn I*	4783.427	2.298	–	(10)
Mn I*	4766.418	2.920	–	(10)
Mn I*	4754.042	2.282	–	(10)
Mn I*	4034.483	0.000	–	(10)
Mn I*	4033.062	0.000	–	(10)
Mn I*	4235.295	2.888	–	(10)
Mn I*	4041.355	2.114	–	(10)
Co I	4020.828	3.665	−0.961	(11)
Co I	4110.530	1.049	−1.080	(11)
Co I	4121.311	0.923	−0.320	(11)
Ni I	6643.629	1.676	−2.300	(12)
Ni I	6108.107	1.676	−2.450	(12)

Ni I	5155.762	3.898	0.011	(12)
Ni I	5115.389	3.834	−0.110	(12)
Ni I	5099.927	3.679	−0.100	(12)
Ni I	5080.528	3.655	0.330	(12)
Ni I	5081.107	3.847	0.300	(12)
Ni I	5035.357	3.635	0.290	(12)
Ni I	5017.568	3.539	−0.020	(12)
Ni I	4904.407	3.542	−0.170	(12)
Ni I	4866.262	3.539	−0.210	(12)
Ni I	4714.408	3.380	0.260	(12)
Ni I	4715.757	3.543	−0.320	(12)
Cu I*	5105.537	–	–	(13)
Zn I	4722.153	4.030	−0.338	(14)
Zn I	4810.528	4.078	−0.137	(14)
Sr II	4077.709	0.000	0.167	(15)
Sr II	4215.519	0.000	−0.145	(15)
Y II	4124.907	0.409	−1.500	(16)
Y II	4682.324	0.409	−1.510	(16)
Y II	4854.863	0.992	−0.11	(16)
Y II	4883.684	1.084	0.265	(16)
Y II	5087.416	1.084	−0.170	(16)
Y II	5123.211	0.992	−1.219	(16)
Y II	5200.406	0.992	−0.570	(16)
Y II	5662.925	1.944	0.38	(16)
Zr II	4029.684	0.713	−0.78	(17)
Zr II	4050.316	0.713	−1.000	(17)
Zr II	4090.535	0.758	−1.009	(17)
Zr II	4161.213	0.713	−0.59	(17)
Zr II	4150.986	0.802	−0.992	(17)
Zr II	4208.977	0.713	−0.460	(17)

Zr II	4211.907	0.527	−1.083	(17)
Zr II	4317.299	0.713	−1.450	(17)
Ba II	6496.897	0.604	−0.377	(18)
Ba II*	5853.700	–	–	(18)
Ba II*	6141.713	–	–	(18)
Ba II*	4554.033	–	–	(18)
Ba II*	4934.077	–	–	(18)
La II*	4333.753	–	–	(19)
La II*	4086.709	–	–	(19)
La II*	4123.218	–	–	(19)
La II	4921.776	0.244	−0.45	(19)
La II*	4322.503	–	–	(19)
Ce II	4186.594	0.864	0.74	(20)
Ce II	4562.359	0.478	0.23	(20)
Ce II	4486.909	0.295	−0.090	(20)
Ce II	4628.161	0.516	0.220	(20)
Pr II*	4143.11	–	–	(21)
Pr II*	4179.39	–	–	(21)
Nd II	4061.080	0.471	0.347	(22)
Nd II	4109.448	0.321	0.184	(22)
Nd II*	4232.374	–	–	(22)
Nd II	4135.321	0.631	−0.400	(22)
Nd II	4327.932	0.559	−0.430	(22)
Nd II	4338.690	0.742	−0.290	(22)
Nd II*	4358.161	–	–	(22)
Nd II	4825.478	0.182	−0.776	(22)
Sm II*	4424.337	–	–	(23)
Sm II	4434.318	0.378	−0.204	(23)
Sm II*	4467.341	–	–	(23)
Eu II*	4129.801	–	–	(24)

Eu II*	4205.05	–	–	(24)
Gd II	3850.97	0.000	−0.094	(25)
Gd II	4037.33	0.662	−0.020	(25)
Gd II	4085.6	0.731	−0.07	(25)
Gd II	4098.61	0.819	0.312	(25)
Tb II	3976.84	0.000	0.08	(26)
Dy II	4103.306	0.103	−0.390	(27)
Dy II	4111.343	0.000	−0.850	(27)
Dy II	4449.704	0.000	−1.030	(27)
Ho II	4045.44	0.000	−0.05	(28)
Ho II	4152.58	0.079	−0.930	(28)
Er II	3830.48	0.000	−0.22	(29)
Er II	3896.23	0.055	−0.12	(29)
Tm II	3848.02	0.000	−0.140	(30)
Lu II	5476.69	1.760	−0.276	(31)
Hf II	3918.09	0.452	−1.14	(32)
Hf II	4093.15	0.452	−1.15	(32)
Os I	4260.85	0.000	−1.440	(33)
Os I	4420.47	0.000	−1.20	(33)
Pb I*	4057.8	–	–	(34)
Th II	4019.12	0.000	−0.228	(35)

References for $\log gf$: (1) Sneden et al. (2014), (2) Sneden et al. (2014); Yong et al. (2014); Heiter et al. (2015), (3) Mendoza et al. (1995), (4) Shi et al. (2008), (5) Ryabchikova et al. (2000), (6) Lawler et al. (2019), (7) Kupka et al. (1999)[VALD]; Ralchenko et al. (2014)[NIST] (8) Lawler et al. (2014); Wood et al. (2014), (9) Kupka et al. (1999)[VALD]; Ralchenko et al. (2014)[NIST], (10) Den Hartog et al. (2011), (11) Nitz et al. (1999); Cardon et al. (1982), (12) Siqueira-Mello et al. (2015); Vejar et al. (2021) (13) Kurucz Linelist [http://kurucz.harvard.edu/linelists.html],

(14) Takeda et al. (2002), (15) Mishenina et al. (2017), (16) Biémont et al. (2011) , (17) Ljung et al. (2006); Malcheva et al. (2006), (18) (McWilliam 1998; Cui et al. 2013) , (19) Lawler et al. (2001b) , (20) Palmeri et al. (2000); Zhang et al. (2001), (21) Sneden et al. (2009a), (22) Kupka et al. (1999)[VALD] , (23) Kupka et al. (1999)[VALD] , (24) Lawler et al. (2001c), (25) Kupka et al. (1999)[VALD] , (26) Lawler et al. (2001a), (27) Sneden et al. (2009b), (28) Lawler et al. (2004), (29) Lawler et al. (2008), (30) Sneden et al. (2009c), (31) Bord et al. (1997), (32) Lawler et al. (2006), (33) Quinet et al. (2006), (34) Roederer & Lawler (2012), (35) Nilsson et al. (2002).

Note: * with the name of element represents hyperfine splitting.

C Elemental abundances of objects presented in Chapter 7

Table C.1: Detailed abundance determination for UCAC4 488-001423.

Element	species	atomic no.	N-lines	Solar	$A(X)_{syn}$	[X/H]	[X/Fe]	σ
C	CH	6	1	8.39	6.01	−2.38	−0.3	0.23
Na	Na I	11	2	6.17	4.02	−2.15	−0.07	0.09
Mg	Mg I	12	5	7.53	5.74	−1.79	0.29	0.16
Si	Si I	14	1	7.51	5.73	−1.78	0.3	0.07
Ca	Ca I	20	9	6.31	4.68	−1.63	0.45	0.12
Sc	Sc II	21	8	3.17	1.04	−2.12	−0.045	0.10
Ti	Ti I	22	10	4.90	2.85	−2.05	0.03	0.14
Ti	Ti II	22	15	4.90	3.04	−1.86	0.22	0.19
Cr	Cr I	24	7	5.64	3.25	−2.39	−0.31	0.18
Cr	Cr II	24	3	5.64	3.92	−1.72	0.36	0.02
Mn	Mn I	25	4	5.39	3.15	−2.24	−0.16	0.19
Ni	Ni I	28	7	6.23	4.41	−1.82	0.26	0.16
Zn	Zn I	30	2	4.60	2.66	−1.94	0.14	0.17
Sr	Sr II	38	2	2.92	0.32	−2.6	−0.52	0.13
Ba	Ba II	56	5	2.17	−0.31	−2.48	−0.4	0.13
Eu	Eu II	63	2	0.52	−1.68	−2.2	−0.12	0.03

Table C.2: Detailed abundance determination for TYC 1795-438-1.

Element	species	atomic no.	N-lines	Solar	$A(X)_{syn}$	[X/H]	[X/Fe]	σ
C	CH	6	1	8.39	5.64	−2.75	−0.2	0.23
Na	Na I	11	2	6.17	3.97	−2.2	0.36	0.07
Mg	Mg I	12	5	7.53	5.35	−2.18	0.37	0.18
Si	Si I	14	1	7.51	5.64	−1.87	0.68	0.11
Ca	Ca I	20	6	6.31	4.13	−2.18	0.37	0.16
Sc	Sc II	21	4	3.17	0.567	−2.60	−0.052	0.10
Ti	Ti I	22	5	4.90	2.66	−2.24	0.31	0.19
Ti	Ti II	22	10	4.90	2.74	−2.16	0.39	0.17
Cr	Cr I	24	5	5.64	2.74	−2.9	−0.35	0.13
Cr	Cr II	24	3	5.64	2.87	−2.77	−0.22	0.09
Mn	Mn I	25	3	5.39	2.18	−3.20	−0.65	0.08
Co	Co I	27	2	4.92	2.62	−2.30	0.25	0.1
Ni	Ni I	28	10	6.23	3.80	−2.43	0.12	0.07
Zn	Zn I	30	2	4.60	2.2	−2.40	0.15	0.11
Sr	Sr II	38	2	2.92	0.22	−2.7	−0.15	0.12
Ba	Ba II	56	5	2.17	−0.85	−3.02	−0.47	0.15
Eu	Eu II	63	1	0.52	−1.78	−2.3	0.25	0.08

TABLE C.3: Detailed abundance determination for TYC 665-522-1.

Element	species	atomic no.	N-lines	Solar	$A(X)_{syn}$	[X/H]	[X/Fe]	σ
C	CH	6	1	8.39	5.86	−2.53	−0.1	0.20
Na	Na I	11	2	6.17	3.99	−2.18	0.25	0.11
Mg	Mg I	12	7	7.53	5.63	−1.9	0.53	0.14
Si	Si I	14	2	7.51	5.38	−2.12	0.305	0.13
Ca	Ca I	20	9	6.31	4.32	−1.99	0.44	0.12
Sc	Sc II	21	5	3.17	0.838	−2.33	0.098	0.10
Ti	Ti I	22	7	4.90	2.61	−2.29	0.14	0.12
Ti	Ti II	22	7	4.90	2.77	−2.13	0.3	0.09
Cr	Cr I	24	5	5.64	2.87	−2.77	−0.34	0.09
Cr	Cr II	24	2	5.64	3.32	−2.32	0.11	0.11
Mn	Mn I	25	3	5.39	2.61	−2.78	−0.35	0.1
Co	Co I	27	3	4.92	2.80	−2.12	0.31	0.09
Ni	Ni I	28	3	6.23	3.9	−2.33	0.1	0.07
Zn	Zn I	30	2	4.60	2.29	−2.31	0.12	0.15
Sr	Sr II	38	2	2.92	0.37	−2.55	−0.12	0.07
Ba	Ba II	56	5	2.17	−0.03	−2.2	0.23	0.16
Eu	Eu II	63	2	0.52	−1.48	−2.0	0.43	0.10

TABLE C.4: Detailed abundance determination for TYC 1939-202-1.

Element	species	atomic no.	N-lines	Solar	$A(X)_{syn}$	[X/H]	[X/Fe]	σ
C	CH	6	1	8.39	6.00	−2.39	0.00	0.18
Na	Na I	11	2	6.17	3.62	−2.55	−0.16	0.04
Mg	Mg I	12	6	7.53	5.38	−2.15	0.24	0.13
Ca	Ca I	20	7	6.31	4.27	−2.04	0.35	0.10
Sc	Sc II	21	3	3.17	0.83	−2.34	0.05	0.09
Ti	Ti I	22	5	4.90	2.76	−2.14	0.25	0.13
Ti	Ti II	22	8	4.90	2.79	−2.11	0.28	0.14
Cr	Cr I	24	4	5.64	3.33	−2.31	0.08	0.03
Cr	Cr II	24	1	5.64	3.42	−2.22	0.17	0.12
Mn	Mn I	25	3	5.39	2.82	−2.56	−0.17	0.09
Co	Co I	27	2	4.92	2.51	−2.40	−0.015	0.14
Ni	Ni I	28	4	6.23	3.96	−2.27	0.12	0.15
Zn	Zn I	30	2	4.60	2.57	−2.03	0.36	0.05
Sr	Sr II	38	2	2.92	−0.58	−3.50	−1.11	0.08
Ba	Ba II	56	5	2.17	−0.68	−2.85	−0.46	0.10

Table C.5: Detailed abundance determination for TYC 195-1636-1.

Element	species	atomic no.	N-lines	Solar	$A(X)_{syn}$	[X/H]	[X/Fe]	σ
C	CH	6	1	8.39	6.05	−2.34	0.1	0.23
Na	Na I	11	2	6.17	3.89	−2.28	0.16	0.14
Mg	Mg I	12	4	7.53	5.55	−1.98	0.46	0.13
Ca	Ca I	20	7	6.31	4.23	−2.08	0.36	0.12
Sc	Sc II	21	5	3.17	0.63	−2.53	−0.09	0.09
Ti	Ti I	22	8	4.90	2.89	−2.01	0.43	0.19
Ti	Ti II	22	9	4.90	2.94	−1.96	0.48	0.17
Cr	Cr I	24	5	5.64	2.92	−2.72	−0.28	0.19
Cr	Cr II	24	2	5.64	3.01	−2.63	−0.19	0.09
Mn	Mn I	25	8	5.39	2.53	−2.86	−0.42	0.11
Co	Co I	27	3	4.92	2.34	−2.58	−0.14	0.04
Ni	Ni I	28	-	6.23	3.84	−2.39	0.05	0.03
Zn	Zn I	30	2	4.60	2.17	−2.43	0.01	0.1
Sr	Sr II	38	2	2.92	0.95	−1.97	0.47	0.13
Ba	Ba II	56	5	2.17	−0.38	−2.55	−0.11	0.13
Eu	Eu II	63	2	0.52	−1.25	−1.77	0.67	0.03

Table C.6: Detailed abundance determination for TYC 23-815-1.

Element	species	atomic no.	N-lines	Solar	$A(X)_{syn}$	[X/H]	[X/Fe]	σ
C	CH	6	1	8.39	6.19	−2.2	0.3	0.23
Na	Na I	11	2	6.17	3.88	−2.29	0.21	0.11
Mg	Mg I	12	6	7.53	5.58	−1.95	0.55	0.12
Ca	Ca I	20	4	6.31	4.28	−2.03	0.47	0.14
Sc	Sc II	21	5	3.17	0.56	−2.61	−0.11	0.11
Ti	Ti I	22	4	4.90	2.62	−2.28	0.22	0.12
Ti	Ti II	22	10	4.90	2.7	−2.2	0.30	0.17
Cr	Cr I	24	4	5.64	2.95	−2.69	−0.19	0.11
Cr	Cr II	24	2	5.64	2.94	−2.7	−0.2	0.09
Mn	Mn I	25	4	5.39	2.61	−2.78	−0.28	0.09
Co	Co I	27	2	4.92	2.13	−2.78	−0.28	0.12
Ni	Ni I	28	3	6.23	3.84	−2.39	0.109	0.07
Zn	Zn I	30	2	4.60	2.49	−2.11	0.39	0.11
Sr	Sr II	38	2	2.92	−0.28	−3.20	−0.70	0.10
Ba	Ba II	56	5	2.17	−0.77	−2.94	−0.44	0.09
Eu	Eu II	63	2	0.52	−1.78	−2.30	0.2	0.10

Table C.7: Detailed abundance determination for TYC 2985-737-1.

Element	species	atomic no.	N-lines	Solar	$A(X)_{syn}$	[X/H]	[X/Fe]	σ
C	CH	6	1	8.39	6.34	−2.05	0.1	0.2
Na	Na I	11	2	6.17	4.32	−1.85	0.52	0.08
Mg	Mg I	12	4	7.53	5.44	−2.09	0.28	0.11
Si	Si I	14	2	7.51	5.51	−1.99	0.37	0.12
Ca	Ca I	20	5	6.31	4.42	−1.89	0.48	0.12
Sc	Sc II	21	5	3.17	0.66	−2.51	−0.14	0.10
Ti	Ti I	22	9	4.90	3.09	−1.81	0.56	0.14
Ti	Ti II	22	8	4.90	2.92	−1.98	0.39	0.14
Cr	Cr I	24	4	5.64	3.13	−2.51	−0.14	0.17
Cr	Cr II	24	4	5.64	3.17	−2.47	−0.1	0.19
Mn	Mn I	25	3	5.39	2.5	−2.89	−0.52	0.19
Ni	Ni I	28	3	6.23	4.02	−2.21	0.16	0.07
Zn	Zn I	30	2	4.60	2.16	−2.44	−0.07	0.08
Sr	Sr II	38	2	2.92	0.12	−2.8	−0.43	0.14
Ba	Ba II	56	5	2.17	−0.205	−2.37	-0.005	0.05

Table C.8: Detailed abundance determination for TYC 1404-1448-1.

Element	species	atomic no.	N-lines	Solar	$A(X)_{syn}$	[X/H]	[X/Fe]	σ
C	CH	6	1	8.39	5.46	−2.93	−0.6	0.24
Na	Na I	11	2	6.17	3.74	−2.43	−0.1	0.09
Mg	Mg I	12	5	7.53	5.53	−2.00	0.33	0.13
Si	Si I	14	2	7.51	5.36	−2.15	0.18	0.19
Ca	Ca I	20	9	6.31	4.29	−2.02	0.31	0.16
Sc	Sc II	21	7	3.17	1.08	−2.09	0.24	0.07
Ti	Ti I	22	8	4.90	2.75	−2.15	0.18	0.18
Ti	Ti II	22	9	4.90	3.07	−1.83	0.5	0.04
Cr	Cr I	24	7	5.64	3.21	−2.43	−0.1	0.11
Cr	Cr II	24	3	5.64	3.22	−2.42	−0.09	0.17
Mn	Mn I	25	5	5.39	2.55	−2.84	−0.51	0.09
Co	Co I	27	2	4.92	2.62	−2.30	0.03	0.17
Ni	Ni I	28	6	6.23	3.91	−2.32	0.01	0.11
Zn	Zn I	30	2	4.60	2.43	−2.17	0.16	0.07
Sr	Sr II	38	2	2.92	−0.78	−3.7	−1.37	0.11
Ba	Ba II	56	5	2.17	−0.18	−2.35	−0.02	0.13
Eu	Eu II	63	2	0.52	−1.78	−2.3	0.03	0.2

Table C.9: Detailed abundance determination for TYC 1406-971-1.

Element	species	atomic no.	N-lines	Solar	$A(X)_{syn}$	[X/H]	[X/Fe]	σ
C	CH	6	1	8.39	5.36	−3.03	−0.8	0.2
Na	Na I	11	2	6.17	4.26	−1.91	0.32	0.07
Mg	Mg I	12	6	7.53	5.74	−1.79	0.44	0.14
Si	Si I	14	2	7.51	5.90	−1.61	0.62	0.16
Ca	Ca I	20	11	6.31	4.45	−1.86	0.37	0.15
Sc	Sc II	21	9	3.17	1.11	−2.06	0.17	0.13
Ti	Ti I	22	11	4.90	2.84	−2.06	0.17	0.10
Ti	Ti II	22	15	4.90	2.98	−1.92	0.31	0.18
Cr	Cr I	24	8	5.64	3.11	−2.53	−0.3	0.06
Cr	Cr II	24	3	5.64	3.35	−2.29	−0.06	0.04
Mn	Mn I	25	4	5.39	2.71	−2.68	−0.45	0.10
Co	Co I	27	2	4.92	2.55	−2.37	−0.14	0.05
Ni	Ni I	28	11	6.23	4.00	−2.23	0.00	0.18
Zn	Zn I	30	2	4.60	2.52	−2.08	0.15	0.08
Sr	Sr II	38	2	2.92	0.32	−2.6	−0.37	0.1
Ba	Ba II	56	5	2.17	0.145	−2.02	0.205	0.07
Eu	Eu II	63	2	0.52	−1.73	−2.25	−0.02	0.17

Table C.10: Detailed abundance determination for TYC 243-502-1.

Element	species	atomic no.	N-lines	Solar	$A(X)_{syn}$	[X/H]	[X/Fe]	σ
C	CH	6	1	8.39	6.62	−1.77	0.33	0.16
Na	Na I	11	2	6.17	3.72	−2.45	−0.35	0.25
Mg	Mg I	12	5	7.53	5.65	−1.88	0.22	0.18
Si	Si I	14	2	7.51	5.99	−1.52	0.58	0.08
Ca	Ca I	20	8	6.31	4.62	−1.69	0.41	0.17
Sc	Sc II	21	7	3.17	1.04	−2.12	−0.03	0.13
Ti	Ti I	22	6	4.90	3.02	−1.88	0.22	0.12
Ti	Ti II	22	6	4.90	3.02	−1.88	0.22	0.19
Cr	Cr I	24	5	5.64	3.57	−2.07	0.03	0.18
Cr	Cr II	24	2	5.64	3.46	−2.18	−0.08	0.05
Mn	Mn I	25	4	5.39	3.06	−2.33	−0.23	0.19
Co	Co I	27	2	4.92	2.72	−2.2	−0.1	0.24
Ni	Ni I	28	6	6.23	4.25	−1.98	0.12	0.18
Zn	Zn I	30	2	4.60	2.47	−2.13	−0.029	0.10
Sr	Sr II	38	2	2.92	0.75	−2.17	−0.07	0.05
Ba	Ba II	56	5	2.17	−0.18	−2.35	−0.25	0.1

TABLE C.11: Detailed abundance determination for TYC 3443-1105-1.

Element	species	atomic no.	N-lines	Solar	$A(X)_{syn}$	[X/H]	[X/Fe]	σ
C	CH	6	1	8.39	5.25	−3.14	−0.6	0.23
Na	Na I	11	2	6.17	3.45	−2.72	−0.18	0.16
Mg	Mg I	12	6	7.53	5.24	−2.29	0.25	0.17
Si	Si I	14	2	7.51	5.43	−2.08	0.46	0.13
Ca	Ca I	20	14	6.31	4.21	−2.1	0.44	0.12
Sc	Sc II	21	5	3.17	0.85	−2.32	0.22	0.10
Ti	Ti I	22	11	4.90	2.67	−2.23	0.31	0.12
Ti	Ti II	22	22	4.90	2.71	−2.19	0.35	0.18
Cr	Cr I	24	6	5.64	2.93	−2.71	−0.17	0.12
Cr	Cr II	24	3	5.64	3.1	−2.54	0.00	0.13
Mn	Mn I	25	5	5.39	2.41	−2.97	−0.43	0.19
Co	Co I	27	2	4.92	2.44	−2.47	0.065	0.24
Ni	Ni I	28	7	6.23	3.69	−2.54	0.00	0.15
Zn	Zn I	30	2	4.60	2.38	−2.22	0.32	0.13
Sr	Sr II	38	2	2.92	−0.68	−3.6	−1.06	0.13
Ba	Ba II	56	5	2.17	−0.57	−2.74	−0.2	0.13
Eu	Eu II	63	2	0.52	−2.33	−2.85	−0.31	0.03

TABLE C.12: Detailed abundance determination for LP 491-46.

Element	species	atomic no.	N-lines	Solar	$A(X)_{syn}$	[X/H]	[X/Fe]	σ
C	CH	6	1	8.39	6.56	−1.83	0.3	0.25
Na	Na I	11	2	6.17	4.36	−1.81	0.32	0.01
Mg	Mg I	12	5	7.53	5.75	−1.78	0.35	0.08
Si	Si I	14	2	7.51	5.71	−1.8	0.33	0.13
Ca	Ca I	20	5	6.31	4.51	−1.80	0.33	0.12
Sc	Sc II	21	4	3.17	1.22	−1.94	0.187	0.10
Ti	Ti I	22	5	4.90	3.08	−1.82	0.31	0.18
Ti	Ti II	22	3	4.90	3.15	−1.75	0.38	0.13
Cr	Cr I	24	3	5.64	3.25	−2.39	−0.26	0.11
Cr	Cr II	24	2	5.64	3.7	−1.94	0.19	0.07
Mn	Mn I	25	3	5.39	2.95	−2.44	−0.31	0.19
Co	Co I	27	2	4.92	2.98	−1.94	0.19	0.24
Ni	Ni I	28	4	6.23	4.32	−1.91	0.22	0.11
Zn	Zn I	30	2	4.60	2.73	−1.87	0.26	0.08
Sr	Sr II	38	2	2.92	0.42	−2.5	−0.37	0.09
Ba	Ba II	56	5	2.17	0.07	−2.10	0.03	0.08

Table C.13: Detailed abundance determination for TYC 1436-366-1.

Element	species	atomic no.	N-lines	Solar	$A(X)_{syn}$	[X/H]	[X/Fe]	σ
C	CH	6	1	8.39	5.8	−2.59	−0.1	0.18
Na	Na I	11	2	6.17	3.35	−2.82	−0.33	0.08
Mg	Mg I	12	7	7.53	5.12	−2.41	0.08	0.17
Si	Si I	14	2	7.51	5.21	−2.29	0.196	0.10
Ca	Ca I	20	5	6.31	4.13	−2.18	0.31	0.15
Sc	Sc II	21	3	3.17	0.70	−2.47	0.02	0.09
Ti	Ti I	22	4	4.90	2.68	−2.22	0.27	0.07
Ti	Ti II	22	7	4.90	3.02	−1.88	0.61	0.18
Cr	Cr I	24	4	5.64	3.19	−2.45	0.04	0.14
Cr	Cr II	24	2	5.64	3.19	−2.45	0.04	-
Mn	Mn I	25	3	5.39	2.14	−3.24	−0.75	0.09
Co	Co I	27	3	4.92	2.68	−2.23	0.25	0.12
Ni	Ni I	28	5	6.23	3.87	−2.36	0.13	0.11
Zn	Zn I	30	2	4.60	2.46	−2.13	0.35	0.08
Sr	Sr II	38	2	2.92	−0.98	−3.9	−1.41	0.10
Ba	Ba II	56	5	2.17	−0.73	−2.9	−0.41	0.15

Table C.14: Detailed abundance determination for TYC 2533-1475-1.

Element	species	atomic no.	N-lines	Solar	$A(X)_{syn}$	[X/H]	[X/Fe]	σ
C	CH	6	1	8.39	5.44	−2.95	−0.3	0.21
Na	Na I	11	2	6.17	3.34	−2.83	−0.18	0.08
Mg	Mg I	12	6	7.53	5.28	−2.25	0.4	0.18
Si	Si I	14	2	7.51	5.10	−2.41	0.24	0.16
Ca	Ca I	20	9	6.31	4.05	−2.26	0.39	0.23
Sc	Sc II	21	7	3.17	0.57	−2.60	0.05	0.09
Ti	Ti I	22	9	4.90	2.56	−2.34	0.31	0.13
Ti	Ti II	22	11	4.90	2.76	−2.14	0.51	0.18
Cr	Cr I	24	4	5.64	3.00	−2.64	0.01	0.09
Cr	Cr II	24	3	5.64	3.18	−2.46	0.19	0.03
Mn	Mn I	25	3	5.39	2.56	−2.83	−0.18	0.11
Co	Co I	27	3	4.92	2.42	−2.49	0.15	0.07
Ni	Ni I	28	7	6.23	3.65	−2.58	0.07	0.20
Zn	Zn I	30	2	4.60	2.23	−2.37	0.28	0.03
Sr	Sr II	38	2	2.92	−0.88	−3.8	−1.15	0.11
Ba	Ba II	56	5	2.17	−0.33	−2.50	0.15	0.08
Eu	Eu II	63	2	0.52	−2.08	−2.6	0.05	0.09

TABLE C.15: Detailed abundance determination for TYC 1465-1148-1.

Element	species	atomic no.	N-lines	Solar	$A(X)_{syn}$	[X/H]	[X/Fe]	σ
C	CH	6	1	8.39	5.43	-2.96	-0.2	0.21
Na	Na I	11	2	6.17	3.49	-2.68	0.08	0.06
Mg	Mg I	12	7	7.53	5.09	-2.44	0.32	0.19
Si	Si I	14	2	7.51	5.23	-2.28	0.48	0.16
Ca	Ca I	20	11	6.31	3.99	-2.32	0.44	0.16
Sc	Sc II	21	5	3.17	0.618	-2.55	0.20	0.10
Ti	Ti I	22	3	4.90	2.59	-2.31	0.45	0.10
Ti	Ti II	22	6	4.90	2.63	-2.27	0.49	0.07
Cr	Cr I	24	5	5.64	2.88	-2.76	0.00	0.17
Cr	Cr II	24	-	5.64	2.99	-2.65	0.11	-
Mn	Mn I	25	8	5.39	2.30	-3.09	-0.33	0.19
Ni	Ni I	28	3	6.23	3.65	-2.58	0.18	0.07
Zn	Zn I	30	2	4.60	2.34	-2.26	0.5	0.19
Sr	Sr II	38	2	2.92	-0.58	-3.5	-0.74	0.06
Ba	Ba II	56	5	2.17	-0.38	-2.55	0.21	0.11
Eu	Eu II	63	2	0.52	-1.83	-2.35	0.41	0.1

TABLE C.16: Detailed abundance determination for TYC 1192-20-1.

Element	species	atomic no.	N-lines	Solar	$A(X)_{syn}$	[X/H]	[X/Fe]	σ
C	CH	6	1	8.39	5.85	-2.54	-0.1	0.21
Na	Na I	11	2	6.17	3.88	-2.28	0.159	0.25
Mg	Mg I	12	7	7.53	5.57	-1.96	0.48	0.19
Ca	Ca I	20	8	6.31	4.30	-2.01	0.43	0.19
Sc	Sc II	21	5	3.17	0.598	-2.57	-0.132	0.12
Ti	Ti I	22	6	4.90	2.53	-2.37	0.07	0.08
Ti	Ti II	22	10	4.90	2.55	-2.35	0.09	0.10
Cr	Cr I	24	10	5.64	2.81	-2.83	-0.39	0.13
Cr	Cr II	24	2	5.64	3.20	-2.44	0.00	0.16
Mn	Mn I	25	3	5.39	2.51	-2.88	-0.44	0.17
Co	Co I	27	2	4.92	2.55	-2.36	0.077	0.09
Ni	Ni I	28	8	6.23	3.86	-2.37	0.069	0.18
Zn	Zn I	30	2	4.60	2.38	-2.22	0.22	0.08
Sr	Sr II	38	2	2.92	0.32	-2.60	-0.16	0.09
Ba	Ba II	56	5	2.17	-0.85	-3.02	-0.58	0.13
Eu	Eu II	63	2	0.52	-1.98	-2.5	-0.06	0.03

Table C.17: Detailed abundance determination for TYC 2014-552-1.

Element	species	atomic no.	N-lines	Solar	$A(X)_{syn}$	[X/H]	[X/Fe]	σ
C	CH	6	1	8.39	5.76	−2.63	−0.20	0.25
Na	Na I	11	2	6.17	3.74	−2.43	0.00	0.07
Mg	Mg I	12	7	7.53	5.46	−2.07	0.36	0.19
Si	Si I	14	2	7.51	5.23	−2.28	0.15	0.14
Ca	Ca I	20	8	6.31	4.35	−1.96	0.47	0.12
Sc	Sc II	21	9	3.17	0.69	−2.48	−0.05	0.08
Ti	Ti I	22	5	4.90	2.63	−2.27	0.16	0.09
Ti	Ti II	22	7	4.90	2.86	−2.04	0.39	0.14
Cr	Cr I	24	5	5.64	3.08	−2.56	−0.13	0.03
Cr	Cr II	24	2	5.64	3.40	−2.24	0.19	0.02
Mn	Mn I	25	5	5.39	2.45	−2.94	−0.51	0.19
Ni	Ni I	28	5	6.23	3.98	−2.25	0.18	0.20
Zn	Zn I	30	2	4.60	2.59	−2.01	0.42	0.12
Sr	Sr II	38	2	2.92	−0.28	−3.20	−0.77	0.1
Ba	Ba II	56	5	2.17	−0.43	−2.60	−0.17	0.12

Table C.18: Detailed abundance determination for TYC 3474-142-1.

Element	species	atomic no.	N-lines	Solar	$A(X)_{syn}$	[X/H]	[X/Fe]	σ
C	CH	6	1	8.39	6.28	−2.11	0.34	0.24
Na	Na I	11	2	6.17	4.00	−2.17	0.28	0.05
Mg	Mg I	12	4	7.53	5.66	−1.87	0.58	0.06
Si	Si I	14	1	7.51	5.73	−1.78	0.67	0.13
Ca	Ca I	20	10	6.31	4.26	−2.05	0.40	0.16
Sc	Sc II	21	3	3.17	0.54	−2.63	−0.18	0.12
Ti	Ti I	22	8	4.90	2.75	−2.15	0.3	0.11
Ti	Ti II	22	15	4.90	2.68	−2.22	0.23	0.20
Cr	Cr I	24	5	5.64	2.97	−2.67	−0.22	0.11
Cr	Cr II	24	2	5.64	3.2	−2.44	0.01	0.18
Mn	Mn I	25	4	5.39	2.50	−2.88	−0.43	0.11
Co	Co I	27	2	4.92	2.69	−2.23	0.22	0.05
Ni	Ni I	28	5	6.23	3.90	−2.33	0.12	0.11
Zn	Zn I	30	2	4.60	2.35	−2.25	0.20	0.08
Sr	Sr II	38	2	2.92	0.65	−2.27	0.18	0.11
Ba	Ba II	56	5	2.17	−0.62	−2.79	−0.34	0.07
Eu	Eu II	63	2	0.52	−1.45	−1.97	0.48	0.04

Table C.19: Detailed abundance determination for TYC 1501-1445-1.

Element	species	atomic no.	N-lines	Solar	$A(X)_{syn}$	[X/H]	[X/Fe]	σ
C	CH	6	1	8.39	6.18	−2.21	0.00	0.22
Na	Na I	11	2	6.17	4.16	−2.01	0.2	0.19
Mg	Mg I	12	5	7.53	5.59	−1.94	0.27	0.14
Si	Si I	14	2	7.51	5.69	−1.82	0.39	0.13
Ca	Ca I	20	8	6.31	4.41	−1.9	0.31	0.15
Sc	Sc II	21	9	3.17	0.902	−2.26	−0.057	0.08
Ti	Ti I	22	5	4.90	3.01	−1.89	0.32	0.12
Ti	Ti II	22	9	4.90	3.21	−1.69	0.52	0.05
Cr	Cr I	24	5	5.64	3.09	−2.55	−0.34	0.19
Cr	Cr II	24	2	5.64	3.61	−2.03	0.18	0.08
Mn	Mn I	25	3	5.39	3.14	−2.25	−0.04	0.11
Co	Co I	27	2	4.92	2.95	−1.97	0.24	0.07
Ni	Ni I	28	4	6.23	4.04	−2.19	0.02	0.08
Zn	Zn I	30	2	4.60	2.67	−1.93	0.28	0.04
Sr	Sr II	38	2	2.92	−0.58	−3.5	−1.29	0.1
Ba	Ba II	56	5	2.17	−0.63	−2.8	−0.59	0.13

Table C.20: Detailed abundance determination for TYC 1760-1284-1.

Element	species	atomic no.	N-lines	Solar	$A(X)_{syn}$	[X/H]	[X/Fe]	σ
C	CH	6	1	8.39	6.86	−1.53	0.44	0.23
Na	Na I	11	2	6.17	4.11	−2.06	−0.09	0.12
Mg	Mg I	12	5	7.53	5.93	−1.6	0.37	0.14
Si	Si I	14	1	7.51	6.23	−1.28	0.69	0.11
Ca	Ca I	20	6	6.31	4.7	−1.61	0.36	0.17
Sc	Sc II	21	4	3.17	1.1	−2.07	−0.10	0.10
Ti	Ti I	22	6	4.90	3.48	−1.42	0.55	0.06
Ti	Ti II	22	4	4.90	3.48	−1.42	0.55	0.19
Cr	Cr I	24	4	5.64	3.65	−1.99	−0.02	0.11
Cr	Cr II	24	1	5.64	3.48	−2.16	−0.19	0.08
Mn	Mn I	25	3	5.39	3.32	−2.06	−0.09	0.09
Ni	Ni I	28	3	6.23	4.36	−1.87	0.1	0.12
Zn	Zn I	30	2	4.60	2.93	−1.67	0.3	0.13
Sr	Sr II	38	2	2.92	1.5	−1.42	0.55	0.06
Ba	Ba II	56	5	2.17	0.5	−1.67	0.3	0.1

TABLE C.21: Detailed abundance determination for TYC 2601-637-1.

Element	species	atomic no.	N-lines	Solar	$A(X)_{syn}$	[X/H]	[X/Fe]	σ
C	CH	6	1	8.39	5.53	−2.86	−0.4	0.2
Na	Na I	11	2	6.17	3.51	−2.66	−0.2	0.15
Mg	Mg I	12	5	7.53	5.36	−2.17	0.29	0.09
Si	Si I	14	2	7.51	5.56	−1.95	0.51	0.13
Ca	Ca I	20	8	6.31	4.18	−2.13	0.33	0.17
Sc	Sc II	21	3	3.17	0.42	−2.75	−0.29	0.011
Ti	Ti I	22	8	4.90	2.68	−2.22	0.24	0.19
Ti	Ti II	22	8	4.90	3.09	−1.81	0.65	0.12
Cr	Cr I	24	4	5.64	2.9	−2.74	−0.28	0.09
Cr	Cr II	24	2	5.64	3.38	−2.26	0.2	0.12
Mn	Mn I	25	8	5.39	2.67	−2.71	−0.258	0.09
Ni	Ni I	28	5	6.23	3.78	−2.45	0.01	0.13
Zn	Zn I	30	2	4.60	2.25	−2.35	0.11	0.08
Sr	Sr II	38	2	2.92	−0.53	−3.45	−0.99	0.07
Ba	Ba II	56	5	2.17	−0.89	−3.06	−0.6	0.1
Eu	Eu II	63	2	0.52	−1.88	−2.4	0.06	0.12

TABLE C.22: Detailed abundance determination for TYC 975-2188-1.

Element	species	atomic no.	N-lines	Solar	$A(X)_{syn}$	[X/H]	[X/Fe]	σ
C	CH	6	1	8.39	5.69	−2.7	−0.3	0.24
Na	Na I	11	2	6.17	3.88	−2.29	0.11	0.12
Mg	Mg I	12	4	7.53	5.55	−1.98	0.42	0.13
Ca	Ca I	20	9	6.31	4.37	−1.94	0.46	0.16
Sc	Sc II	21	5	3.17	1.01	−2.15	0.24	0.10
Ti	Ti I	22	11	4.90	2.95	−1.95	0.45	0.14
Ti	Ti II	22	18	4.90	3.01	−1.89	0.51	0.05
Cr	Cr I	24	7	5.64	3.12	−2.52	−0.12	0.13
Cr	Cr II	24	3	5.64	3.15	−2.49	−0.09	0.09
Mn	Mn I	25	4	5.39	2.65	−2.74	−0.34	0.09
Co	Co I	27	2	4.92	2.45	−2.47	−0.07	0.12
Ni	Ni I	28	4	6.23	3.96	−2.27	0.13	0.16
Zn	Zn I	30	2	4.60	2.49	−2.11	0.29	0.09
Sr	Sr II	38	2	2.92	−0.38	−3.3	−0.9	0.11
Ba	Ba II	56	5	2.17	−0.18	−2.35	0.05	0.06
Eu	Eu II	63	2	0.52	−1.28	−1.8	0.6	0.12

TABLE C.23: Detailed abundance determination for TYC 1576-1703-1.

Element	species	atomic no.	N-lines	Solar	$A(X)_{syn}$	[X/H]	[X/Fe]	σ
C	CH	6	1	8.39	8.19	−0.2	1.98	0.21
Na	Na I	11	2	6.17	3.94	−2.23	−0.05	0.06
Mg	Mg I	12	5	7.53	5.89	−1.64	0.54	0.12
Si	Si I	14	1	7.51	6.01	−1.5	0.68	0.09
Ca	Ca I	20	7	6.31	4.55	−1.76	0.42	0.14
Sc	Sc II	21	9	3.17	1.34	−1.83	0.35	0.10
Ti	Ti I	22	3	4.90	3.28	−1.62	0.56	0.06
Ti	Ti II	22	5	4.90	3.15	−1.75	0.43	0.06
Cr	Cr I	24	5	5.64	3.57	−2.07	0.11	0.14
Cr	Cr II	24	4	5.64	3.55	−2.09	0.09	0.16
Mn	Mn I	25	3	5.39	3.19	−2.19	−0.01	0.08
Co	Co I	27	3	4.92	3.02	−1.9	0.28	0.14
Ni	Ni I	28	4	6.23	4.09	−2.14	0.04	0.09
Zn	Zn I	30	2	4.60	2.75	−1.85	0.33	0.05
Sr	Sr II	38	2	2.92	1.7	−1.22	0.96	0.05
Ba	Ba II	56	5	2.17	1.97	−0.2	1.98	0.1
Eu	Eu II	63	2	0.52	−0.25	−0.77	1.41	0.08

TABLE C.24: Detailed abundance determination for TYC 3534-57-1.

Element	species	atomic no.	N-lines	Solar	$A(X)_{syn}$	[X/H]	[X/Fe]	σ
C	CH	6	1	8.39	7.36	−1.03	0.73	0.25
Na	Na I	11	2	6.17	4.42	−1.75	0.01	0.18
Mg	Mg I	12	6	7.53	6.25	−1.28	0.48	0.12
Ca	Ca I	20	9	6.31	5.02	−1.29	0.47	0.19
Sc	Sc II	21	4	3.17	1.6	−1.57	0.19	0.13
Ti	Ti I	22	5	4.90	3.66	−1.24	0.52	0.15
Ti	Ti II	22	11	4.90	3.6	−1.3	0.46	0.15
Cr	Cr I	24	5	5.64	4.08	−1.56	0.2	0.14
Cr	Cr II	24	3	5.64	3.88	−1.76	0.0	0.08
Mn	Mn I	25	3	5.39	3.6	−1.79	−0.03	0.1
Ni	Ni I	28	5	6.23	4.56	−1.67	0.09	0.12
Zn	Zn I	30	2	4.60	3.05	−1.55	0.21	0.03
Sr	Sr II	38	2	2.92	1.1	−1.82	−0.06	0.09
Ba	Ba II	56	5	2.17	0.135	−2.03	−0.275	0.07
Eu	Eu II	63	2	0.52	−0.3	−0.82	0.94	0.1

TABLE C.25: Detailed abundance determination for TYC 1653-657-1.

Element	species	atomic no.	N-lines	Solar	$A(X)_{syn}$	[X/H]	[X/Fe]	σ
C	CH	6	1	8.39	5.52	−2.87	−0.1	0.2
Na	Na I	11	2	6.17	3.62	−2.55	0.22	0.05
Mg	Mg I	12	6	7.53	5.29	−2.24	0.53	0.19
Si	Si I	14	2	7.51	5.25	−2.26	0.51	0.11
Ca	Ca I	20	11	6.31	3.98	−2.33	0.44	0.17
Sc	Sc II	21	6	3.17	0.52	−2.64	0.12	0.06
Ti	Ti I	22	6	4.90	2.25	−2.65	0.12	0.06
Ti	Ti II	22	13	4.90	2.42	−2.48	0.29	0.18
Cr	Cr I	24	6	5.64	2.71	−2.93	−0.16	0.11
Cr	Cr II	24	1	5.64	2.90	−2.74	0.03	0.06
Mn	Mn I	25	5	5.39	2.25	−3.13	−0.36	0.08
Co	Co I	27	3	4.92	1.99	−2.92	−0.156	0.1
Ni	Ni I	28	5	6.23	3.61	−2.62	0.15	0.04
Zn	Zn I	30	2	4.60	1.91	−2.69	0.08	0.10
Sr	Sr II	38	2	2.92	−0.68	−3.6	−0.83	0.11
Ba	Ba II	56	5	2.17	−1.33	−3.5	−0.73	0.09
Eu	Eu II	63	2	0.52	−2.58	−3.1	−0.33	0.1

TABLE C.26: Detailed abundance determination for TYC 1170-642-1.

Element	species	atomic no.	N-lines	Solar	$A(X)_{syn}$	[X/H]	[X/Fe]	σ
C	CH	6	1	8.39	6.42	−1.97	0.4	0.23
Na	Na I	11	2	6.17	4.12	−2.05	0.32	0.14
Mg	Mg I	12	6	7.53	5.82	−1.71	0.66	0.11
Ca	Ca I	20	5	6.31	4.25	−2.06	0.31	0.18
Sc	Sc II	21	7	3.17	1.09	−2.07	0.292	0.10
Ti	Ti I	22	5	4.90	2.91	−1.99	0.38	0.13
Ti	Ti II	22	7	4.90	2.97	−1.93	0.44	0.17
Cr	Cr I	24	8	5.64	3.22	−2.42	−0.05	0.12
Cr	Cr II	24	2	5.64	3.41	−2.23	0.14	0.05
Mn	Mn I	25	2	5.39	2.93	−2.46	−0.09	0.05
Ni	Ni I	28	5	6.23	4.04	−2.19	0.18	0.13
Zn	Zn I	30	2	4.60	2.65	−1.95	0.42	0.05
Sr	Sr II	38	2	2.92	0.82	−2.1	0.27	0.08
Ba	Ba II	56	5	2.17	−0.23	−2.4	−0.03	0.1
Eu	Eu II	63	2	0.52	−0.88	−1.4	0.97	0.09

Table C.27: Detailed abundance determination for TYC 1988-1110-1.

Element	species	atomic no.	N-lines	Solar	$A(X)_{syn}$	[X/H]	[X/Fe]	σ
C	CH	6	1	8.39	4.58	−3.81	−0.7	0.22
Na	Na I	11	2	6.17	2.84	−3.33	−0.22	0.08
Mg	Mg I	12	6	7.53	4.81	−2.72	0.39	0.13
Si	Si I	14	1	7.51	3.7	−3.81	−0.7	0.09
Ca	Ca I	10	10	6.31	3.67	−2.64	0.47	0.18
Sc	Sc II	21	7	3.17	0.24	−2.92	0.18	0.10
Ti	Ti I	22	6	4.90	1.96	−2.94	0.17	0.10
Ti	Ti II	22	8	4.90	2.19	−2.71	0.4	0.06
Cr	Cr I	24	5	5.64	2.24	−3.4	−0.29	0.07
Cr	Cr II	24	3	5.64	2.6	−3.04	0.07	0.1
Mn	Mn I	25	8	5.39	1.71	−3.68	−0.57	0.12
Ni	Ni I	28	6	6.23	3.32	−2.91	0.2	0.17
Zn	Zn I	30	2	4.60	2.00	−2.60	0.51	0.08
Sr	Sr II	38	2	2.92	−0.88	−3.8	−0.69	0.13
Ba	Ba II	56	3	2.17	−1.26	−3.43	−0.32	0.11
Eu	Eu II	63	2	0.52	−2.78	−3.3	−0.19	0.09

Table C.28: Detailed abundance determination for UCAC4 430-119026.

Element	species	atomic no.	N-lines	Solar	$A(X)_{syn}$	[X/H]	[X/Fe]	σ
C	CH	6	1	8.39	5.38	−3.01	−0.60	0.26
Na	Na I	11	2	6.17	3.82	−2.35	0.06	0.08
Mg	Mg I	12	6	7.53	5.68	−1.85	0.56	0.19
Si	Si I	14	2	7.51	5.57	−1.94	0.47	0.17
Ca	Ca I	20	8	6.31	4.18	−2.13	0.28	0.12
Sc	Sc II	21	11	3.17	0.76	−2.41	0.00	0.10
Ti	Ti I	22	11	4.90	2.5	−2.40	0.01	0.11
Ti	Ti II	22	17	4.90	2.81	−2.09	0.32	0.13
Cr	Cr I	24	9	5.64	2.79	−2.85	−0.44	0.14
Cr	Cr II	24	5	5.64	3.34	−2.30	0.11	0.08
Mn	Mn I	25	5	5.39	2.60	−2.79	−0.38	0.1
Co	Co I	27	2	4.92	2.62	−2.30	0.11	0.14
Ni	Ni I	28	11	6.23	3.88	−2.35	0.06	0.15
Zn	Zn I	30	2	4.60	2.35	−2.25	0.16	0.17
Sr	Sr II	38	2	2.92	0.12	−2.8	−0.39	0.12
Ba	Ba II	56	4	2.17	0.045	−2.12	0.28	0.11
Eu	Eu II	63	2	0.52	−1.78	−2.3	0.11	0.1

TABLE C.29: Detailed abundance determination for TYC 1120-1253-1.

Element	species	atomic no.	N-lines	Solar	$A(X)_{syn}$	[X/H]	[X/Fe]	σ
C	CH	6	1	8.39	6.24	−2.15	0.00	0.23
Na	Na I	11	2	6.17	3.61	−2.56	−0.41	0.13
Mg	Mg I	12	5	7.53	5.79	−1.74	0.41	0.15
Si	Si I	14	2	7.51	5.95	-1.56	0.59	0.13
Ca	Ca I	20	8	6.31	4.35	−1.96	0.19	0.16
Sc	Sc II	21	7	3.17	1.18	−1.98	0.162	0.12
Ti	Ti I	22	7	4.90	3.08	−1.82	0.33	0.14
Ti	Ti II	22	12	4.90	3.25	−1.65	0.5	0.04
Cr	Cr I	24	4	5.64	3.13	−2.51	−0.36	0.19
Cr	Cr II	24	3	5.64	3.65	−1.99	0.16	0.08
Mn	Mn I	25	4	5.39	3.11	−2.27	−0.13	0.11
Co	Co I	27	3	4.92	2.60	−2.31	−0.16	0.09
Ni	Ni I	28	6	6.23	4.09	−2.14	0.01	0.16
Zn	Zn I	30	2	4.60	2.80	−1.8	0.35	0.18
Sr	Sr II	38	2	2.92	0.12	−2.8	−0.65	0.09
Ba	Ba II	56	5	2.17	0.11	−2.06	0.09	0.13
Eu	Eu II	63	2	0.52	−1.08	−1.6	0.55	0.09

Table C.30: Detailed abundance determination for TYC 224-475-1.

Element	species	atomic no.	N-lines	Solar	$A(X)_{syn}$	[X/H]	[X/Fe]	σ
C	CH	6	1	8.39	6.16	−2.23	0.1	0.21
Na	Na I	11	2	6.17	4.18	−1.99	0.34	0.01
Mg	Mg I	12	6	7.53	5.69	−1.84	0.49	0.11
Si	Si I	14	2	7.51	5.54	−1.97	0.36	0.13
Ca	Ca I	20	10	6.31	4.36	−1.95	0.38	0.11
Sc	Sc II	21	7	3.17	0.811	−2.35	−0.029	0.10
Ti	Ti I	22	11	4.90	2.77	−2.13	0.2	0.09
Ti	Ti II	22	16	4.90	2.87	−2.03	0.3	0.12
Cr	Cr I	24	7	5.64	3.04	−2.6	−0.27	0.07
Cr	Cr II	24	2	5.64	3.37	−2.27	0.06	0.05
Mn	Mn I	25	6	5.39	2.89	−2.49	−0.16	0.19
Co	Co I	27	2	4.92	2.63	−2.29	0.04	0.24
Ni	Ni I	28	11	6.23	3.98	−2.25	0.08	0.17
Zn	Zn I	30	2	4.60	2.47	−2.13	0.2	0.11
Sr	Sr II	38	2	2.92	0.57	−2.35	−0.02	0.1
Ba	Ba II	56	4	2.17	0.07	−2.1	0.23	0.08
Eu	Eu II	63	2	0.52	−1.38	−1.9	0.43	0.06

Table C.31: Detailed abundance determination for TYC 1741-618-1.

Element	species	atomic no.	N-lines	Solar	$A(X)_{syn}$	[X/H]	[X/Fe]	σ
C	CH	6	1	8.39	5.82	−2.57	0.00	0.22
Na	Na I	11	2	6.17	4.05	−2.12	0.45	0.08
Mg	Mg I	12	7	7.53	5.51	−2.02	0.55	0.18
Si	Si I	14	2	7.51	5.3	−2.21	0.36	0.11
Ca	Ca I	20	10	6.31	4.26	−2.05	0.52	0.19
Sc	Sc II	21	9	3.17	0.568	−2.60	−0.031	0.06
Ti	Ti I	22	7	4.90	2.45	−2.45	0.12	0.07
Ti	Ti II	22	16	4.90	2.72	−2.18	0.39	0.14
Cr	Cr I	24	6	5.64	2.88	−2.76	−0.19	0.10
Cr	Cr II	24	3	5.64	3.10	−2.54	0.03	0.10
Mn	Mn I	25	4	5.39	2.39	−2.99	−0.42	0.12
Co	Co I	27	2	4.92	2.65	−2.26	0.30	0.08
Ni	Ni I	28	6	6.23	3.74	−2.49	0.08	0.14
Zn	Zn I	30	2	4.60	2.36	−2.24	0.33	0.05
Sr	Sr II	38	2	2.92	0.02	−2.9	−0.33	0.05
Ba	Ba II	56	4	2.17	−0.87	−3.04	−0.47	0.12
Eu	Eu II	63	2	0.52	−1.98	−2.5	0.07	0.15

TABLE C.32: Detailed abundance determination for TYC 267-308-1.

Element	species	atomic no.	N-lines	Solar	$A(X)_{syn}$	[X/H]	[X/Fe]	σ
C	CH	6	1	8.39	6.25	−2.14	0.2	0.22
Na	Na I	11	2	6.17	3.79	−2.38	−0.04	0.04
Mg	Mg I	12	7	7.53	5.63	−1.9	0.44	0.17
Si	Si I	14	2	7.51	5.37	−2.14	0.2	0.02
Ca	Ca I	20	11	6.31	4.19	−2.12	0.22	0.12
Sc	Sc II	21	7	3.17	0.865	−2.30	0.035	0.12
Ti	Ti I	22	14	4.90	2.89	−2.01	0.33	0.12
Ti	Ti II	22	26	4.90	2.85	−2.05	0.29	0.06
Cr	Cr I	24	9	5.64	2.96	−2.68	−0.34	0.08
Cr	Cr II	24	2	5.64	3.50	−2.14	0.2	0.04
Mn	Mn I	25	3	5.39	2.64	−2.74	−0.4	0.1
Ni	Ni I	28	5	6.23	3.93	−2.3	0.04	0.09
Zn	Zn I	30	2	4.60	2.48	−2.12	0.22	0.05
Sr	Sr II	38	2	2.92	0.77	−2.15	0.19	0.08
Ba	Ba II	56	5	2.17	0.10	−2.06	0.273	0.13
Eu	Eu II	63	2	0.52	−1.28	−1.8	0.54	0.1

TABLE C.33: Detailed abundance determination for TYC 279-1113-1.

Element	species	atomic no.	N-lines	Solar	$A(X)_{syn}$	[X/H]	[X/Fe]	σ
C	CH	6	1	8.39	7.47	−0.92	0.9	0.21
Na	Na I	11	2	6.17	4.29	−1.88	−0.06	0.17
Mg	Mg I	12	7	7.53	6.2	−1.33	0.49	0.18
Si	Si I	14	2	7.51	6.35	−1.16	0.66	0.13
Ca	Ca I	20	6	6.31	4.78	−1.53	0.29	0.12
Sc	Sc II	21	9	3.17	1.26	−1.9	−0.08	0.09
Ti	Ti I	22	7	4.90	3.25	−1.65	0.17	0.19
Ti	Ti II	22	15	4.90	3.46	−1.44	0.38	0.08
Cr	Cr I	24	5	5.64	3.92	−1.72	0.1	0.19
Cr	Cr II	24	1	5.64	4.04	−1.6	0.22	0.08
Mn	Mn I	25	2	5.39	3.4	−1.99	−0.17	0.07
Co	Co I	27	3	4.92	3.39	−1.53	0.29	0.09
Ni	Ni I	28	6	6.23	4.54	−1.69	0.13	0.07
Zn	Zn I	30	2	4.60	2.88	−1.72	0.1	0.08
Sr	Sr II	38	2	2.92	0.37	−2.55	−0.73	0.11
Ba	Ba II	56	5	2.17	−0.07	−2.24	−0.42	0.05
Eu	Eu II	63	2	0.52	−0.68	−1.2	0.62	0.03